Study of photo induce process by quantum chemistry and quantum dynamics methods

Aurelie Perveaux

NNT : 2015SACLS144

THESE DE DOCTORAT
DE L'UNIVERSITE PARIS-SACLAY,
préparée à l'Université Paris-Sud

ÉCOLE DOCTORALE N°571
Sciences chimiques : molécules, matériaux, instrumentation et biosystèmes

Spécialité de doctorat : Chimie

Par

Mme Aurelie Perveaux

Etude de processus photochimiques par une approche couplant chimie quantique et dynamique quantique

Thèse présentée et soutenue à Orsay, le 8 décembre 2015 :

Composition du Jury :
Mme M. Desouter-Lecomte, Professeur, Université Paris-Sud, Presidente
Mme C. Daniel, Directrice de Recherche, CNRS, Rapporteur
M. G. A. Worth, Professeur, University of Birmingham, Rapporteur
Mme V. Brenner, Directrice de recherche, CEA, Examinatrice
M. M. Boggio-Pasqua, Chargé de recherche, CNRS, Examinateur
M. B. Lasorne, Chargé de recherche, CNRS, Examinateur
M. D. Lauvergnat, Directeur de recherche, CNRS, Directeur de thèse

A la mémoire de mon grand-père

“Si vous n'échouez pas de temps à autres, c’est signe que vous ne faites rien de très innovant.”

Woody Allen

Remerciements

Mon travail de thèse a été réalisé au sein du laboratoire de Chimie Physique d'Orsay ainsi qu'à l'Institut Charles Gerhardt de Montpellier, sous la direction de David Lauvergnat et Benjamin Lasorne.

Je tiens à les remercier tous deux pour leurs encadrements durant ces trois longues (très longues) années de thèse. Ils ont su prendre du temps et leur patience avec moi a été sans faille (et dieu sait qu'il en faut de la patience avec moi). La complémentarité du coté pragmatique de David avec le coté formaliste de Benjamin m'a permis de solidifier mes points forts mais aussi de pouvoir étendre mes capacités dans de nombreux domaines tels que les mathématiques ou la programmation.

Je voudrais particulièrement remercier mon père qui a toujours cru en moi (quand moi-même je n'y croyais plus) et sans qui je n'aurais même pas terminé le lycée.

Je remercie chaleureusement Simon Viallard rencontré en L1 PCST (ma meilleure année à la fac) et qui m'as motivée de la L1 à la dernière année de thèse. Il a su être à l'écoute de tous mes malheurs et de mes « craquages » nerveux mais surtout il a été capable de me supporter pendant toutes ces années !

Je voudrais aussi remercier tous les gens qui ont été présents pendant l'écriture de ce manuscrit, Emmeline Ho, Julien Burgun, Nicolas Lespes, Cecilia Colleta, sans qui j'aurais peut-être démissionné pour partir élever des chèvres dans le Larzac. Je remercie tout particulièrement Geoffrey Brest sans qui je serais clairement morte de faim et sans vêtements propres (parce qu'on ne peut pas écrire sa thèse et faire le ménage… logique). Il a été un soutien très important sur les derniers mois de cette épreuve.

Enfin je voudrais remercier tous les membres des deux laboratoires pour leur accueil et l'ambiance sympathique dans laquelle j'ai pu évoluer pendant trois ans (ou plutôt merci d'avoir supporté le « bordel » que j'ai créé au labo pendant trois ans).

Je suis reconnaissante aux membres du mon jury d'avoir accepté d'examiner mon travail.

Je remercie infiniment ma famille et mes amis pour leur affection et leur sans et sans qui je n'aurais pu braver ce dernier combat (dramaturgie, moi ? jamais).

Contents

Chapter II- Quasidiabatic Model

Chapter III- HydroxyChromone Dyes

Chapter IV- Aminobenzonitrile Intramolecular Charge Transfer

Introduction Générale

Le développement de la technologie laser au cours des dernières décennies a permis la génération de pulses ultracourts de l'ordre de la picoseconde et de la femtoseconde [1] (et même récemment de l'ordre de l'attoseconde [2–4]). Ceci a mené à la conception de nombreuses méthodes expérimentales de spectroscopie ultrarapide [5–7]. En d'autres termes, nous sommes désormais capable de sonder le mouvement des systèmes moléculaires en temps réel et de le contrôler (influencer la réactivité avec un pulse laser optimisé pour atteindre une cible prédéterminée) [8–16]; ce domaine de recherche est appelé femtochimie (pour les réactions considérés comme ultrarapides de l'ordre de la femtoseconde). Ahmed Zewail fut le pionnier de l'utilisation de pulses laser ultracourts pour étudier la dynamique femtoseconde d'états de transition. Il reçut le prix Nobel de Chimie en 1999 pour ses travaux dans le domaine de la spectroscopie ultrarapide [1,17].

L'étude de processus ultrarapides en photochimie a permis l'émergence de nouvelles technologies dans des domaines très hétéroclites tels que : l'élaboration de nouveaux protocoles de synthèse en chimie moléculaire (e.g. réaction de Diels-Alder photoinduite, photopolymerisation), l'obtention de nouveaux matériaux avec des propriétés optiques particulières (e.g. photochromisme, optique non-linéaire), des méthodes d'analyse en biochimie (e.g. marqueurs fluorescents, des traitements médicaux (e.g. photothérapie). L'intérêt et l'utilisation des processus photoinduits dans certains des domaines mentionnés précédemment sont décrits en détail dans les introductions des deux chapitres d'applications portant sur le transfert de proton dans l'état excité du 3-hydroxychromone et le transfert de charge intramoléculaire photoinduit dans l'aminobenzonitrile (respectivement Chapter III et IV). Il est donc capital de pouvoir traiter ce type de réactivité chimique d'un point de vue théorique et ainsi apporter une complémentarité aux expérimentateurs afin de pouvoir déterminer avec précision les mécanismes de ces réactions et, à terme, de les contrôler et/ou d'optimiser les propriétés physicochimiques des systèmes photosensibles (e.g. absorption, émission, rapports de branchement réactif(s)/produit(s)) dans l'optique de développements technologiques [18,19].

La photochimie possède des propriétés mécanistiques tous être explicitées avec des outils standard de chimie quantique et une dynamique reposant sur les lois de la mécanique classique telle que la dynamique moléculaire par exemple. Une réaction photochimique étant une réaction induite par l'absorption d'un photon par le système moléculaire, la réaction va donc se produire en partie ou en totalité sur un ou plusieurs états électroniques excités; on va donc devoir utiliser des méthodes de chimie quantique qui ne sont pas limitées à l'état électronique fondamental (les méthodes utilisées lors de ce travail de thèse pour traiter la structure électronique des systèmes étudiés sont explicitées dans le Chapitre I).

De plus, il existe des géométries particulières où certains états électroniques sont proches en énergie, voire dégénérés (i.e. intersections coniques). Dans les régions proches de ces géométries particulières, l'approximation de Born-Oppenheimer n'est plus valide. Le système chimique est dans un régime de dynamique appelé non-adiabatique (la dynamique des noyaux et des électrons se couple dans ces régions, Cf. Chapitre I). Il est donc nécessaire de traiter le mouvement des noyaux comme évoluant sur plusieurs surfaces d'énergies potentielles couplées entre elles. Ces couplages non-adiabatiques permettent des transferts de population non-radiatifs (sans émission de photon) entre états électroniques de même spin (conversion interne). Ceci suggère que l'état électronique excité après absorption (état initial du point de vue Franck-Condon) n'est pas nécessairement l'état électronique final de la réaction. Ces transferts de population non-radiatifs sont plus efficaces dans les régions ou les états électroniques sont quasi-dégénérés, c'est-à-dire, lorsque le système s'approche d'une région d'intersection conique. Ce point particulier de dégénérescence entres états électroniques joue donc un rôle central dans les processus ultrarapides photoinduits [20–22].

Lors d'une étude de ce type de processus, l'intersection conique est un point qui se doit donc d'être caractérisé et qui peut être vu qualitativement comme le pendant pour la photochimie non-adiabatique d'un état de transition pour les processus thermiques. Cependant ne connaitre que la position et l'énergie de l'intersection conique n'est pas toujours suffisant pour comprendre et déterminer le mécanisme de la réaction. Le

système peut être soumis à plusieurs chemins réactionnels en compétition. A la différence de la réactivité thermique, en photochimie non-adiabatique, il ne suit pas nécessairement le chemin de plus basse énergie. Lors de l'étude d'un processus photochimique ultrarapide, on peut être amené à devoir considérer le système comme pouvant se délocaliser le long de plusieurs chemins réactionnels couplés (ceci est observé et discuté dans les chapitres d'applications étudiées lors de ce travail de thèse Chapitres III et IV). Ceci montre la nécessité d'étudier ce type de réactivité avec des outils de dynamique adaptés.

Ceci est moins crucial pour les processus photochimiques dit adiabatiques, qui sont des processus photoinduits ayant lieu sur un seul état électronique excité considéré comme isolé (séparation importante en énergie par rapport aux autres états électroniques). On peut voir ce type de photoreactivité comme étant similaire aux processus thermiques où le système ne serait pas à l'équilibre dans sont état initial. De plus, comme l'approximation de Born-Oppenheimer reste valide pour ce type de processus, il est plus simple de ce point de vue de décrire leur dynamique car l'intégralité de la réactivité se passe sur la même surface d'énergie potentielle. Il est courant dans ce cas d'utiliser des méthodes de type dynamique moléculaire ab initio (les noyaux sont traités comme des particules classiques évoluant sur un potentiel calculé par une méthode de chimie quantique). Cependant, lors de ces travaux de thèse nous nous sommes principalement concentrés sur l'étude de processus photochimiques non-adiabatiques.

Le développement de méthodes de dynamique adaptées aux processus non-adiabatiques dans des systèmes moléculaires est en plein essor. Différentes approches, quantiques, semi-classiques (ou hybrides) coexistent. Nous allons évoquer certaines d'entre elles dans ce qui suit.

Dans le cas d'une méthode dite semi-classique telle que le « surface hopping » [23], la dynamique du système est décrite par une trajectoire classique. L'énergie potentielle et la force sont calculées « on-the-fly » (au vol). L'efficacité du processus non-radiatif (donc non-adiabatique) est obtenue par la probabilité pour le système de « sauter » d'un état électronique à un autres en fonction de la vitesse de la trajectoire, de la différence d'énergie entre les deux états et de leur couplage. Cette méthode ne permet pas de

rendre compte de la délocalisation quantique du mouvement des noyaux que l'on devrait en toute rigueur représenter par ce que l'on appelle un paquet d'ondes nucléaire (fonction d'onde nucléaire dépendante du temps). Ceci caractérise la capacité du système à avoir une probabilité de présence différente et non nulle pour plusieurs géométries en même temps. Ainsi, les différentes trajectoires calculées ne sont pas couplées (elles évoluent indépendamment les unes des autres). Or, le système se délocalise avec une certaine « cohérence », c'est à dire que les trajectoires ne devraient pas être indépendantes les unes des autres d'un point de vue quantique. Cependant, une approche statistique basée sur un grand nombre de trajectoires est utilisée en échantillonnant les conditions initiales du système pour au moins « mimer » l'état vibrationnel initial dans l'état électronique fondamental (et son énergie de point zéro).

La cohérence quantique peut être vu comme une « force » qui va influencer la délocalisation du paquet d'ondes et ses interférences, ce qui peut être crucial quand, par exemple, il passe à travers la même intersection conique plusieurs fois dans un laps de temps ultracourt. Récemment, des expériences ont suggéré l'existence et l'implication de cohérence quantique pendant un temps long (de l'ordre de la picoseconde) dans des processus biologiques [24,25]. Il est donc préférable de pouvoir représenter le caractère quantique du mouvement des noyaux par un paquet d'ondes.

L'« ab initio multiple spawning » [26,27] s'affranchit du coté classique et statistique de la méthode de « surface hopping » en représentant le paquet d'ondes nucléaire par un ensemble de gaussiennes couplées quantiquement (et dont le nombre augmente quand une intersection conique est rencontrée) mais qui suivent des trajectoires classiques. La description du paquet d'ondes dans cette dernière méthode est donc plus correcte et plus représentative. On peut la considérer comme un ensemble de trajectoires classiques couplées quantiquement. La référence suivante dresse une comparaison entre la méthode « surface hopping » et l'« ab initio multiple spawning » [28].

La méthode DD-vMCG (Direct Dynamics variational MultiConfigurational Gaussian) [29,30] peut être vue d'une certaine façon comme une extension de l'« ab initio multiple spawning », de part le fait que le paquet d'ondes est aussi décrit comme une collection de gaussiennes couplées quantiquement (dont le nombre et les largeurs sont fixés dans

les conditions initiales et ne changent pas au cours du temps dans la plupart des applications) mais qui vont maintenant évoluer en suivant des « trajectoires quantiques » (c'est-à-dire que la position et l'impulsion moyennes des gaussiennes sont obtenues par résolution variationelle de l'équation de Schrödinger dépendante du temps [31]). Ceci permet donc d'avoir besoin de moins de gaussiennes pour converger le paquet d'ondes que dans la méthode précédente (i.e. l'« ab-initio multiple spawning »). Cette méthode prometteuse de dynamique que je considère à mon sens comme étant une dynamique semi-quantique est à l'heure actuelle en plein développement. Ce qui la rend encore limitée dans la taille des systèmes est essentiellement dû à des raisons techniques comme par exemple la nécessité de calculer des dérivées secondes au centre de chaque gaussienne et à chaque pas de la dynamique.

Les méthodes de dynamique quantique sur grille ont pour philosophie de décomposer le paquet d'ondes nucléaire sur une grille de points représentant l'espace des coordonnées nucléaires. Ceci impose de représenter préalablement les surfaces d'énergie potentielle sous forme analytique, à l'inverse des trois méthodes précédemment évoquées ou ce calcul est réalisé « on-the-fly » le long de chaque trajectoire. Le mouvement des noyaux est obtenu par résolution de l'équation de Schrödinger dépendante du temps. Il n'y a donc pas d'approximation dans le traitement de la nature quantique des noyaux (tout comme dans la méthode DD-vMCG). Par ceci, nous entendons que ce type de méthode est en principe exact à convergence pour un hamiltonien donné.

Cependant, ces types de dynamiques sont difficiles à mettre en œuvre pour des systèmes moléculaires de grande taille (nombreux degrés de liberté nucléaires). De par le fait qu'elles coutent cher en termes de temps de calcul (pouvant atteindre plusieurs mois pour converger le paquet d'ondes nucléaire initial) mais aussi car il faut dans un premier temps générer les surfaces d'énergie potentielle et les couplages électroniques sous forme de fonctions analytiques. De plus, comme nous pourrons le voir au cours de cette thèse (Cf. section 2- dans le Chapitre I), selon la méthode de dynamique quantique choisie, il peut y avoir des contraintes sur la forme mathématique des fonctions qui composent la représentation matricielle de l'hamiltonien électronique. Ceci peut s'avérer limitant car, comme déjà mentionné, en photochimie la réactivité implique souvent des paysages énergétiques complexes possédant de nombreux points

stationnaires (minima, états de transition, intersections coniques) et ce pour plusieurs états électroniques. A ceci s'ajoute la description des couplages non-adiabatiques qui comme on le montrera (section 2-1 dans le Chapitre I) n'est pas un problème trivial dans un système multidimensionnel. Toutes ces difficultés font que la représentation des hamiltoniens électroniques en photochimie est une tâche difficile (plus précisément l'obtention des paramètres définissant les fonctions du modèle à partir de données ab initio) et devient bien souvent l'étape limitante dans la description quantique de la dynamique de ce type de systèmes.

C'est pourquoi de nombreuses méthodologies sont encore à l'heure actuelle en cours de développement pour palier à ces difficultés. La première stratégie la plus intuitive est de réduire le nombre de degrés de liberté du système en déterminant les modes les plus importants pour décrire le chemin réactionnel (appelés en général modes actifs dans la littérature) [32–40]. Cependant, ces modèles ne prennent pas en compte la dissipation de l'énergie contenue dans ces modes actifs vers le reste des modes, dit inactifs. Par construction la dissipation vibrationnelle (relaxation vibrationnelle intramoléculaire) n'est pas décrite correctement. Cependant, ces méthodes se justifient en partie de part le fait que dans les processus ultrarapides (ordre de la femtoseconde), le système n'a pas le temps de redistribuer totalement son énergie [41,42]. Ce type de modèles trouve donc sa place dans la description des systèmes où il y a vraiment possibilité de faire une distinction franche entre les coordonnées dites actives et inactives (donc le couplage entre ces deux groupes de coordonnées se doit d'être faible par construction). Cependant, il est judicieux de garder en tête que le passage du paquet d'ondes nucléaire d'une surface d'énergie potentielle à une autre à travers une intersection conique est gouverné par deux directions particulières qui induisent le transfert de population électronique (voir Section 2-2 Chapitre I). Il est donc nécessaire qu'elles soient bien décrites par les modes actifs. Or, puisque la dissipation vibrationnelle du système est sous-estimée, l'énergie contenue dans les modes actifs est surestimée. On va donc augmenter artificiellement la probabilité de transfert de population, ce qui va donc mal décrire la réactivité du système (le transfert de population se fera plus rapidement et plus efficacement) [43]. Dans les cas ou il est nécessaire de prendre en compte cette dissipation vibrationnelle, il a été montré que l'on pouvait hiérarchiser les différentes coordonnées pour décrire la dissipation dans une région d'intersection conique à l'aide

de groupes de trois coordonnées bien spécifiques appelées modes effectifs et dont l'importance décroît de groupe en groupe [44–47].

La méthodologie développée lors des travaux présentés dans cette thèse est différente. Nous avons voulu traiter toutes les dimensions du système au même niveau, c'est à dire sans avoir à les hiérarchiser ou les séparer en groupes de coordonnées. Les paramètres de nos modèles sont obtenus analytiquement, nous permettant d'éviter des procédures de « fit » (parfois non-linéaires) qui sont difficiles à mettre en œuvre pour décrire des systèmes photochimiques de grande taille et impliquant des déformations géométriques de grande amplitude. De plus, ce choix à été motivé par la possibilité d'utiliser une nouvelle méthode de dynamique quantique capable de traiter les systèmes chimiques de grande taille (plus d'une dizaine d'atomes) ; cette méthode, en cours de développement à Heidelberg, est appelée ML-MCTDH (Multilayer MultiConfigurational Time-Dependent Hartree).

Le premier chapitre, *Formalism and Methods,* propose une brève description du formalisme non-adiabatique et des intersections coniques ainsi que des méthodes de chimie quantique et de dynamique quantique utilisées lors de ces travaux. Le deuxième chapitre, *Quasidiabatic Model*, présente la méthodologie mise en place pour obtenir la représentation matricielle de l'hamiltonien électronique (surfaces d'énergie potentielle et couplages électroniques). Les deux derniers chapitres exposent les applications étudiées et sur lesquelles nous avons appliqué notre méthodologie : le chapitre trois concerne le transfert de proton dans l'état excité du 3-hydroxychromone et le quatrieme chapitre porte quant à lui sur le transfert de charge intramoléculaire photoinduit dans l'aminobenzonitrile.

Chapter I- Formalism and Methods

The purpose of this chapter is to give general insights into the formalism and methods used in this thesis.

The first part defines the formal framework of this thesis that is based on concepts that go beyond the Born-Oppenheimer approximation. This chapter does not have for purpose to give a full and detailed description of the concepts presented but enough information and references to understand the applications presented in the second part of this thesis (Chapter III and IV) and the aspects of development presented in the following chapter (Chapter II). The second part of this chapter gives a short description of quantum chemistry and quantum dynamics methods used in the present work.

I- Formalism

The wave functions that are solutions of the molecular Schrödinger equation depend on both the electronic and nuclear degrees of freedom. In most situations, the typical time and energy scales of the light (electrons) and heavy (nuclei) particles differ by a few orders of magnitudes. The full problem can thus be split into two steps: first, upon solving a Schrödinger equation for the electrons with fixed nuclei (quantum chemistry), then, upon solving a Schrödinger equation for the nuclei in the adiabatic mean field created by the electrons (quantum dynamics). This is called the Born-Oppenheimer approximation. This two-step approach can be generalized to a finite set of interacting electronic states if the so-called non-adiabatic couplings (NAC) among them induced by the motion of the nuclei (also called vibronic couplings) are taken into account adequately. Further details are provided in this first part of this chapter.

1- Adiabatic Representation [1,20,48–65]

The formalism used in this thesis excludes relativistic effects such as spin-orbit coupling. Hence, the motion of the molecular system is governed by the time-dependent Schrödinger equation,

$$i\hbar \frac{\partial}{\partial t} \left| \Psi^{\mathrm{mol}}(t, \boldsymbol{\mathcal{R}}) \right\rangle = \hat{H}^{\mathrm{mol}} \left| \Psi^{\mathrm{mol}}(t, \boldsymbol{\mathcal{R}}) \right\rangle \qquad \textbf{Eq. 1}$$

The molecular electronic states are defined by the time-dependent molecular wave function denoted Ψ^{mol} that depend of the nuclei (defined in space by $\boldsymbol{\mathcal{R}}$, the set of Cartesian coordinates) and the electrons (coordinates $\mathbf{r}$, implicit when a "ket" notation is used). The corresponding electrostatic molecular Hamiltonian $\hat{H}^{\mathrm{mol}}$ reads [65,66],

$$\hat{H}^{\mathrm{mol}}(\boldsymbol{\mathcal{R}}, \mathbf{r}) = \hat{T}(\boldsymbol{\mathcal{R}}) + \hat{T}_{\mathrm{e}}(\mathbf{r}) + \hat{V}_{\mathrm{N-N}}(\boldsymbol{\mathcal{R}}) + \hat{V}_{\mathrm{e-e}}(\mathbf{r}) + \hat{V}_{\mathrm{N-e}}(\boldsymbol{\mathcal{R}}, \mathbf{r}) \qquad \textbf{Eq. 2}$$

where $\hat{T}$ and $\hat{T}_{\mathrm{e}}$ are the kinetic energy operator for nuclei and electrons, respectively. $\hat{V}_{\mathrm{N-N}}$ is the Coulomb repulsion between nuclei, $\hat{V}_{\mathrm{e-e}}$ is the Coulomb repulsion between electrons, and $\hat{V}_{\mathrm{N-e}}$ is the Coulomb attraction between nuclei and electrons.

Since nuclei are much heavier than electrons, they move more slowly. Hence, one can consider, as a first approximation, the electrons in a molecular system to be moving in the field of fixed nuclei. Another consequence is that electrons respond faster than nuclei to a perturbation. Therefore, it is often an adequate description to consider electron as following adiabatically the motion of the nuclei that, in turn, move in the mean field created by the electrons (concept of potential energy surface). Thus, as already mentioned, the molecular problem can be split in two: first the electronic problem and then the nuclear problem within the previously defined mean field of the electrons. This is known as the adiabatic or Born-Oppenheimer approximation.

Hence, within this approximation one first write an electronic Hamiltonian, which describes the electronic motion with fixed nuclei (thus, the kinetic energy operator of the nuclei is equal to zero),

$$\hat{H}^{\mathrm{elec}}(\boldsymbol{\mathcal{R}}, \mathbf{r}) = \hat{T}_{\mathrm{e}}(\mathbf{r}) + \hat{V}_{\mathrm{N-N}}(\boldsymbol{\mathcal{R}}) + \hat{V}_{\mathrm{e-e}}(\mathbf{r}) + \hat{V}_{\mathrm{N-e}}(\boldsymbol{\mathcal{R}}, \mathbf{r}) \qquad \textbf{Eq. 3}$$

In practice, quantum chemistry methods provide the adiabatic energy, V_α, of a given adiabatic electronic state, α, upon solving the following time-independent Schrödinger equation for each position of the nuclei (i.e. each value of $\boldsymbol{\mathcal{R}}$), where Ψ_α is the wave function of the corresponding electronic eigenstate,

$$\hat{H}^{\mathrm{elec}}(\boldsymbol{\mathcal{R}}, \mathbf{r})|\Psi_\alpha; \boldsymbol{\mathcal{R}}\rangle = V_\alpha(\boldsymbol{\mathcal{R}})|\Psi_\alpha; \boldsymbol{\mathcal{R}}\rangle \qquad \textbf{Eq. 4}$$

One can notice that the electronic Hamiltonian and the adiabatic electronic states depend explicitly on the electronic coordinates and only parametrically on the nuclear coordinates (the eigenvalues, i.e. the adiabatic energies, only depend on the nuclear coordinates).

In order to describe the motion of the nuclei, one must then reintroduce the corresponding kinetic energy operator. As will be explained in the next section, this will induce vibronic non-adiabatic couplings. Considering only one state (which means neglecting these couplings) is, in effect, the adiabatic or Born-Oppenheimer approximation, where $V_\alpha(\boldsymbol{\mathcal{R}})$ is considered as the potential energy for the nuclei (strictly speaking, the Born-Oppenheimer approximation does not consider any second-order diagonal term whereas the adiabatic approximation, sometimes called Born-Huang approximation, includes them as a non-adiabatic correction; note that this terminology is not always consistent in the literature).

Photoinduced processes (photochemical and photophysical) often involve vibronic couplings that are responsible of ultrafast decay processes (typically, internal conversion, between same-spin electronic states, or intersystem crossing for different spins) from an excited electronic state to a lower-energy one. In such a situation, the excess energy given to the molecule through light absorption and electronic excitation is transformed into vibrational excitation. Chemiluminescence (situation not studied in this thesis) occurs in the reverse situation, when vibrational excitation (heat) is transformed into electronic excitation through internal conversion to a higher-energy electronic state that further relaxes upon light emission. Such processes are governed by so-called non-adiabatic couplings between the electronic structure and the nuclear motion that are, by definition, beyond the Born-Oppenheimer (adiabatic) approximation [1,21,48,67,68]. Their effect becomes significant when the energy difference between two electronic states is of the same order of magnitude as vibrational energies. As will be shown below, they even diverge when the energy difference vanishes, i.e., when two electronic states are degenerate at what is called a conical intersection.

2- Beyond the Born-Oppenheimer Approximation [20,22,69]

2-1. Non-Adiabatic Couplings

The usual approach for treating a problem beyond the Born-Oppenheimer approximation consists in choosing a relevant finite set of Born-Oppenheimer (adiabatic) eigenstates of the electronic Hamiltonian (as defined in the previous Section), and in considering the non-adiabatic couplings among them explicitly (the couplings with the remaining irrelevant states are neglected); this is called the group Born-Oppenheimer approximation. The time-dependent molecular wave packet (made of more than one nuclear wave functions, by definition, when more than one electronic states are considered) is expanded in an electronic basis set where the nuclear expansion coefficients (i.e. $\psi_\alpha^{\text{nuclear}}$) are time-dependent,

$$|\Psi^{\text{mol}}(t,\boldsymbol{\mathcal{R}})\rangle = \sum_\alpha \psi_\alpha^{\text{nuclear}}(t,\boldsymbol{\mathcal{R}})|\Psi_\alpha;\boldsymbol{\mathcal{R}}\rangle \qquad \textbf{Eq. 5}$$

where α is the label of the adiabatic electronic states within the chosen set and $\boldsymbol{\mathcal{R}}$ is still the set of nuclear coordinates. The factors $\psi_\alpha^{\text{nuclear}}(t,\boldsymbol{\mathcal{R}})$ are considered as coupled nuclear wave packets while the kets $|\Psi_\alpha;\boldsymbol{\mathcal{R}}\rangle$ are the Born-Oppenheimer (adiabatic) electronic eigenstates that depend parametrically on $\boldsymbol{\mathcal{R}}$, as defined in the previous section. In practice, and in particular in this thesis, the adiabatic electronic states and their energies are obtained from quantum chemistry calculations (using methods such as those presented in Section 1- Chapter I — **Eq. 4**). For each electronic eigenstate, the adiabatic potential energy surface is identified to the electronic eigenvalue for all values of $\boldsymbol{\mathcal{R}}$.

Now, let us consider the nuclear kinetic energy operator (in Cartesian coordinates),

$$\hat{T}(\boldsymbol{\mathcal{R}}) = -\frac{\hbar^2}{2}\sum_I \frac{1}{M_I}\frac{\partial^2}{\partial \mathcal{R}^{I\,2}} \qquad \textbf{Eq. 6}$$

where M_I are the atomic nuclear masses (with indices made consistent with respect to the three coordinates of each nucleus). The molecular Schrödinger equation from **Eq. 1** can be recast as a set of coupled equations for the nuclear wave packets, $\psi_\alpha^{\text{nuclear}}(t,\boldsymbol{\mathcal{R}}) = \langle \Psi_\alpha;\boldsymbol{\mathcal{R}} | \Psi^{\text{mol}}(t,\boldsymbol{\mathcal{R}}) \rangle$ (upon integrating over electronic coordinates only), such that

$$i\hbar\frac{\partial}{\partial t}\psi_\alpha^{\text{nuclear}}(t,\boldsymbol{\mathcal{R}}) = \sum_\beta \left[\delta_{\alpha\beta}\hat{T}(\boldsymbol{\mathcal{R}}) + \delta_{\alpha\beta}V_\alpha(\boldsymbol{\mathcal{R}}) + \hat{\Lambda}_{\alpha\beta}(\boldsymbol{\mathcal{R}})\right]\psi_\beta^{\text{nuclear}}(t,\boldsymbol{\mathcal{R}}) \qquad \textbf{Eq. 7}$$

where the kinetic coupling operator between the α and β adiabatic electronic states reads

$$\hat{\Lambda}_{\alpha\beta}(\boldsymbol{\mathcal{R}}) = -\frac{\hbar^2}{2}\sum_I \frac{1}{M_I}\left[2D_{\alpha\beta}^I(\boldsymbol{\mathcal{R}})\frac{\partial}{\partial \mathcal{R}^I} + C_{\alpha\beta}^I(\boldsymbol{\mathcal{R}})\right], \qquad \textbf{Eq. 8}$$

and the first- and second-order non-adiabatic couplings are defined as [21,68,70,71]

$$D_{\alpha\beta}^I(\boldsymbol{\mathcal{R}}) = \left\langle \Psi_\alpha;\boldsymbol{\mathcal{R}} \middle| \frac{\partial}{\partial \mathcal{R}^I}\Psi_\beta;\boldsymbol{\mathcal{R}} \right\rangle, \qquad \textbf{Eq. 9}$$

and

$$C_{\alpha\beta}^I(\boldsymbol{\mathcal{R}}) = \left\langle \Psi_\alpha;\boldsymbol{\mathcal{R}} \middle| \frac{\partial^2}{\partial \mathcal{R}^{I2}}\Psi_\beta;\boldsymbol{\mathcal{R}} \right\rangle. \qquad \textbf{Eq. 10}$$

These coupling terms simply reflect the action of the second derivative, $\frac{\partial}{\partial \mathcal{R}^I}\frac{\partial}{\partial \mathcal{R}^I}$, on a product of two functions of $\boldsymbol{\mathcal{R}}$: the nuclear wave packet and the electronic wave function. Neglecting them yields the Born-Oppenheimer approximation for a given adiabatic electronic state α, as defined in the previous section,

$$i\hbar\frac{\partial}{\partial t}\psi_\alpha^{\text{nuclear}}(t,\boldsymbol{\mathcal{R}}) = \left[\hat{T}(\boldsymbol{\mathcal{R}}) + V_\alpha(\boldsymbol{\mathcal{R}})\right]\psi_\alpha^{\text{nuclear}}(t,\boldsymbol{\mathcal{R}}) \qquad \textbf{Eq. 11}$$

2-2. Conical Intersection [22,72,73]

Until now, we have considered the $3N$ Cartesian coordinates of the nuclei as the set of parameters that define the geometry of the molecule when solving the electronic problem (where N is the number of atoms). In fact, only the $3N-6$ internal degrees of freedom ($3N-5$ in the collinear case) that define the relative positions of the nuclei have an effect on the electronic Hamiltonian and its eigenstates and eigenenergies. More details will be given later about the separation of coordinates into translations, rotations and internal deformations. For the sake of simplicity, we simply assume here that only a subset of $3N-6$ (or $3N-5$) internal coordinates is relevant in $\boldsymbol{\mathcal{R}}$.

In this thesis, we will assume that only two electronic states, *state 1* and *state 2*, are coupled and are energetically well separated from the rest. Thus, we will limit our discussion to possible intersections of only two electronics states. Nevertheless, in general, a molecule with N atoms can give rise to up to n-fold intersections (n degenerate states), where n is the largest integer satisfying $\frac{(n-1)(n+2)}{2} \leq 3N-6$ [74]. Indeed, recently, intersections of three [75,76] and four [77] electronic states have been reported.

2-2-1 Two-State Electronic Hamiltonian Matrix

Let us consider a basis set made of a pair of orthonormal electronic states, $|\overline{\Phi}_1;\boldsymbol{\mathcal{R}}\rangle$ and $|\overline{\Phi}_2;\boldsymbol{\mathcal{R}}\rangle$, which are assumed to be known and to span the same space as the two adiabatic eigenstates of interest, $|\Psi_1;\boldsymbol{\mathcal{R}}\rangle$ and $|\Psi_2;\boldsymbol{\mathcal{R}}\rangle$. The latter can be obtained from a rotation of the former through a mixing angle $\varphi_X(\boldsymbol{\mathcal{R}})$ at each $\boldsymbol{\mathcal{R}}$ [20,21,62,63,68,78,79],

$$|\Psi_1;\boldsymbol{\mathcal{R}}\rangle = \cos\varphi_X(\boldsymbol{\mathcal{R}})\,|\overline{\Phi}_1;\boldsymbol{\mathcal{R}}\rangle + \sin\varphi_X(\mathbf{R})\,|\overline{\Phi}_2;\boldsymbol{\mathcal{R}}\rangle, \qquad \textbf{Eq. 12}$$
$$|\Psi_2;\boldsymbol{\mathcal{R}}\rangle = -\sin\varphi_X(\boldsymbol{\mathcal{R}})\,|\overline{\Phi}_1;\boldsymbol{\mathcal{R}}\rangle + \cos\varphi_X(\boldsymbol{\mathcal{R}})\,|\overline{\Phi}_2;\boldsymbol{\mathcal{R}}\rangle,$$

The matrix representation of $\widehat{H}^{\text{elec}}(\boldsymbol{\mathcal{R}})$ in this basis set is not necessarily diagonal. If the states are chosen real-valued, the Hamiltonian matrix is real symmetric,

$$\mathbf{H}(\boldsymbol{\mathcal{R}}) = \begin{bmatrix} H_{11}(\boldsymbol{\mathcal{R}}) & H_{12}(\boldsymbol{\mathcal{R}}) \\ H_{21}(\boldsymbol{\mathcal{R}}) & H_{22}(\boldsymbol{\mathcal{R}}) \end{bmatrix} = S(\boldsymbol{\mathcal{R}})\mathbf{1} + \begin{bmatrix} -\Delta H(\boldsymbol{\mathcal{R}}) & H_{12}(\boldsymbol{\mathcal{R}}) \\ H_{21}(\boldsymbol{\mathcal{R}}) & \Delta H(\boldsymbol{\mathcal{R}}) \end{bmatrix}, \quad \textbf{Eq. 13}$$

where the following notation is used,

$$H_{ij}(\boldsymbol{\mathcal{R}}) = \left\langle \overline{\Phi}_i; \boldsymbol{\mathcal{R}} \middle| \widehat{H}_{\mathrm{el}}(\boldsymbol{\mathcal{R}}) \middle| \overline{\Phi}_j; \boldsymbol{\mathcal{R}} \right\rangle \quad \textbf{Eq. 14}$$

and

$$S(\boldsymbol{\mathcal{R}}) = \frac{H_{11}(\boldsymbol{\mathcal{R}}) + H_{22}(\boldsymbol{\mathcal{R}})}{2}, \quad \textbf{Eq. 15}$$
$$\Delta H(\boldsymbol{\mathcal{R}}) = \frac{H_{22}(\boldsymbol{\mathcal{R}}) - H_{11}(\boldsymbol{\mathcal{R}})}{2},$$
$$H_{12}(\boldsymbol{\mathcal{R}}) = H_{21}(\boldsymbol{\mathcal{R}}).$$

The mixing angle that makes this matrix diagonal can be defined explicitly as [21,62,63,68,75,78–80],

$$\tan 2\varphi_X(\boldsymbol{\mathcal{R}}) = -\frac{H_{12}(\boldsymbol{\mathcal{R}})}{\Delta H(\boldsymbol{\mathcal{R}})} \quad \textbf{Eq. 16}$$

The minus sign is here to ensure $V_2 \geq V_1$. The two adiabatic potential energy surfaces, V_1 and V_2, for the two states, *state 1* and *state 2*, correspond to the eigenvalues of the two-state potential energy matrix $\mathbf{H}(\boldsymbol{\mathcal{R}})$ of Eq. 13,

$$V_{1,2}(\boldsymbol{\mathcal{R}}) = \frac{V_2(\boldsymbol{\mathcal{R}}) + V_1(\boldsymbol{\mathcal{R}})}{2} \pm \left(\frac{V_2(\boldsymbol{\mathcal{R}}) - V_1(\boldsymbol{\mathcal{R}})}{2} \right) \quad \textbf{Eq. 17}$$
$$= S(\boldsymbol{\mathcal{R}}) \pm \sqrt{[\Delta H(\boldsymbol{\mathcal{R}})]^2 + [H_{12}(\boldsymbol{\mathcal{R}})]^2}$$

2-2-2 Condition for a Conical Intersection

We now consider the situation where the two electronic states are degenerate at some given geometry, $\boldsymbol{\mathcal{R}_0}$ [22,55,62,63,68,75].

For $\boldsymbol{\mathcal{R}} = \boldsymbol{\mathcal{R}_0}$ to be the locus of a conical intersection between the pair of adiabatic electronic states, *state 1* and *state 2*, it must be such that the difference in energy between these two states is zero, i.e $V_2(\boldsymbol{\mathcal{R}_0}) = V_1(\boldsymbol{\mathcal{R}_0})$, thus,

$$\Delta V(\boldsymbol{\mathcal{R}_0}) = \frac{V_2(\boldsymbol{\mathcal{R}_0}) - V_1(\boldsymbol{\mathcal{R}_0})}{2} = \sqrt{[\Delta H(\boldsymbol{\mathcal{R}_0})]^2 + [H_{12}(\boldsymbol{\mathcal{R}_0})]^2} = 0. \qquad \textbf{Eq. 19}$$

This is achieved if and only if both

$$\Delta H(\boldsymbol{\mathcal{R}_0}) = H_{12}(\boldsymbol{\mathcal{R}_0}) = 0. \qquad \textbf{Eq. 20}$$

The function $\Delta V(\boldsymbol{\mathcal{R}})$ is singular at $\boldsymbol{\mathcal{R}}_0$ because of the square-root (it cannot be differentiated: $\frac{\partial}{\partial \mathcal{R}^I}\Delta V(\boldsymbol{\mathcal{R}_0})$ is ill-defined). In other words, the shapes of the potential energy surfaces in the vicinity of $\boldsymbol{\mathcal{R}_0}$ show a cusp that cannot be described in terms of ordinary local derivatives. Hence, the potential energy surface at the crossing point shows a double cone as illustrated in Fig. 1 (in this figure the conical intersection is located at the origin of the Cartesian frame).

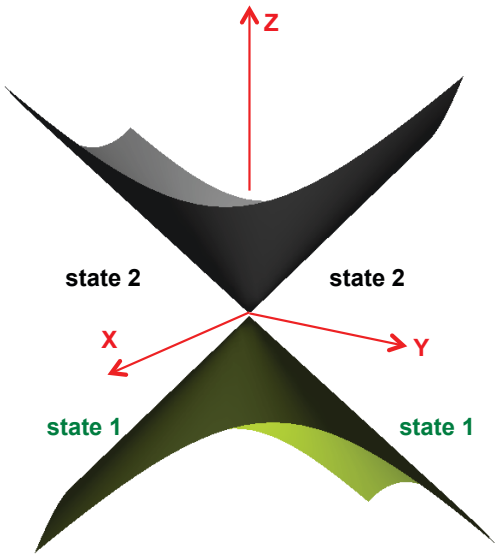

Fig. 1 Scheme of the double cone of a conical intersection between two potential energy surfaces in a Cartesian frame: *z* axis: energy, *x* and *y* axes are specific coordinates that will be defined in the following.

As mentioned above, achieving $\Delta V(\boldsymbol{\mathcal{R}_0}) = 0$ (the degeneracy of the electronic states) implies the two following conditions: $\Delta H(\boldsymbol{\mathcal{R}_0}) = 0$ and $H_{12}(\boldsymbol{\mathcal{R}_0}) = 0$. As a consequence, since $\mathbf{H}(\boldsymbol{\mathcal{R}_0}) = S(\boldsymbol{\mathcal{R}_0})\mathbf{1}$ is now diagonal (where $S(\boldsymbol{\mathcal{R}_0}) = V_2(\boldsymbol{\mathcal{R}_0}) = V_1(\boldsymbol{\mathcal{R}_0})$), both $|\overline{\Phi}_1; \boldsymbol{\mathcal{R}_0}\rangle$ and $|\overline{\Phi}_2; \boldsymbol{\mathcal{R}_0}\rangle$ also form a pair of degenerate eigenstates. The mixing angle $\varphi_X(\boldsymbol{\mathcal{R}_0})$ is now arbitrary and can take any value (any linear combination of degenerate eigenstates is also an eigenstate).

Now, fulfilling these two conditions implies to be able to vary two independent degrees of freedom among the $(3N-6)$ internal degrees of freedom. Reciprocally, degeneracy can be preserved within a subspace of $(3N-6)-2 = 3N-8$ internal degrees of freedom [21,51,68,71,74,78,81,82]. This means that the crossing points are not isolated, but rater they are all connected along a $(3N-8)$-dimensional hyperline, often referred to as the intersection seam, as illustrated in Fig. 2 [21,63,68,71,83].

The study of the photoinduced intramolecular charge transfer of aminobenzonitrile presented in this thesis (Chapter IV) and other recent studies have shown that decay does not always occur near the lowest energy conical intersection (as could be thought intuitively) but can involve more preferentially some other regions within the seam [84–87].

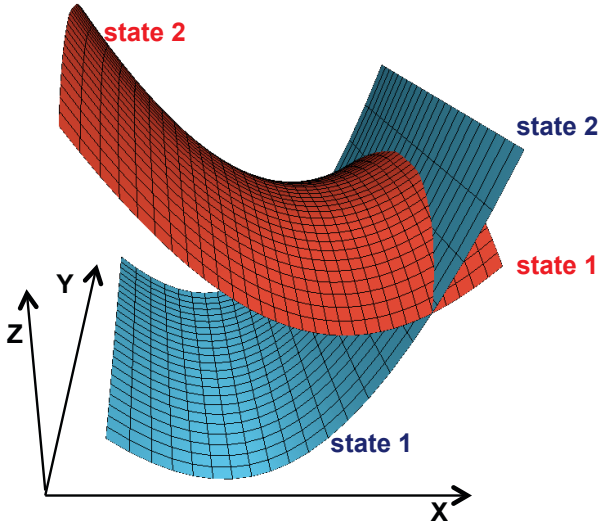

Fig. 2 Scheme of a crossing hyperline between *state 1* and *state 2* along two relevant coordinates *X* and *Y*. *Z* is the energy.

In addition, if $\Delta V(\boldsymbol{\mathcal{R}_0}) = 0$, the first-order non-adiabatic coupling diverges. Indeed, as defined in **Eq. 9**,

$$D_{12}^{I}(\boldsymbol{\mathcal{R}}) = \frac{\left\langle \Psi_1;\boldsymbol{\mathcal{R}} \middle| \frac{\partial}{\partial \mathcal{R}^I} \widehat{H}^{\text{elec}}(\boldsymbol{\mathcal{R}}) \middle| \Psi_2;\boldsymbol{\mathcal{R}} \right\rangle}{2\Delta V(\boldsymbol{\mathcal{R}})} = \frac{\left\langle \Psi_1;\boldsymbol{\mathcal{R}} \middle| \frac{\partial}{\partial \mathcal{R}^I} \widehat{H}^{\text{elec}}(\boldsymbol{\mathcal{R}}) \middle| \Psi_2;\boldsymbol{\mathcal{R}} \right\rangle}{V_2(\boldsymbol{\mathcal{R}}) - V_1(\boldsymbol{\mathcal{R}})}, \qquad \textbf{Eq. 21}$$

The numerator can be finite, but the denominator tends to zero when $\boldsymbol{\mathcal{R}}$ tends to $\boldsymbol{\mathcal{R}_0}$.

The singular behavior of both $\frac{\partial}{\partial \mathcal{R}^I}\Delta V(\boldsymbol{\mathcal{R}})$ and $D_{12}^{I}(\boldsymbol{\mathcal{R}})$ at $\boldsymbol{\mathcal{R}_0}$ can be understood more intuitively in the spirit of electronic state correlation diagrams: it is due essentially to the fact that both adiabatic electronic states with their labels 1 and 2 defined from the energy order ($V_2 \geq V_1$) swap brutally in terms of their "chemical nature" when $\boldsymbol{\mathcal{R}}$ varies such that it goes smoothly across a conical intersection. This will be made clearer below.

Before going further, let us make an important remark: the above equation shows that the non-adiabatic coupling term becomes large (infinite) when $\Delta V(\boldsymbol{\mathcal{R}})$ becomes small (zero); in other word, the more the electronic states come close to each other the more the non-adiabatic coupling term becomes large. Hence, the kinetic energy operator of

the nuclei can no longer be considered as a small perturbation of the electronic system. This is the reason why the Born-Oppenheimer approximation breaks down when approaching regions where electronic states get close in energy. Conical intersections are thus geometries that are representative of regions where significant probability of transfer of electronic population can occur through ultrafast radiationless decay. As such, these points are key for describing non-adiabatic photochemical mechanisms.

2-2-3 Definition of the Conical intersection Branching Space

As first shown by Davidson [61] and Atchity et al. [34, 36], and already mentioned in the previous section, the space of $3N-6$ internal degrees of freedom can be partitioned into two subspaces. The first subspace is two-dimensional and spanned by two collective coordinates (specific combinations of the internal degrees of freedom) along which degeneracy is lifted to first order. This is called the branching space (or branching plane) and the expressions of its pair of vectors are given further along this thesis. The second subspace is locally orthogonal and complementary to the branching space (BS) and, therefore, has a dimensionality of $3N-8$. In this subspace the degeneracy is retained and it is referred to as the intersection space or seam.

As degeneracy is lifted to first order from $\boldsymbol{\mathcal{R}_0}$ within the two-dimensional plane spanned by the branching space vectors, the local shape of both potential energy surfaces within this plane is thus a double cone the apex of which is at $\boldsymbol{\mathcal{R}_0}$, which justifies the name conical intersection. More specifically, the shape is determined from the two conditions mentioned in the previous section for achieving degeneracy: $\Delta H(\boldsymbol{\mathcal{R}_0}) = 0$ and $H_{12}(\boldsymbol{\mathcal{R}_0}) = 0$. Thus, lifting degeneracy occurs to first order when following the gradients of $\Delta H(\boldsymbol{\mathcal{R}})$ and $H_{12}(\boldsymbol{\mathcal{R}})$ at the crossing point.

Let us examine these two gradients in more detail within the formal framework used in the previous section for a two-state problem. We now assume that we know a specific pair of orthogonal degenerate eigenstates (for example as the result of an actual quantum chemistry calculation) and denote them $|\Psi_1^0; \boldsymbol{\mathcal{R}_0}\rangle$ and $|\Psi_2^0; \boldsymbol{\mathcal{R}_0}\rangle$. Any pair of rotated states with respect to these specific degenerate eigenstates (for any angle θ_{12}) is eigenstate as well,

$$\left|\Psi_1^{\theta_{12}};\boldsymbol{\mathcal{R}_0}\right\rangle = \cos\theta_{12}\left|\Psi_1^0;\boldsymbol{\mathcal{R}_0}\right\rangle + \sin\theta_{12}\left|\Psi_2^0;\boldsymbol{\mathcal{R}_0}\right\rangle, \qquad \textbf{Eq. 22}$$
$$\left|\Psi_2^{\theta_{12}};\boldsymbol{\mathcal{R}_0}\right\rangle = -\sin\theta_{12}\left|\Psi_1^0;\boldsymbol{\mathcal{R}_0}\right\rangle + \cos\theta_{12}\left|\Psi_2^0;\boldsymbol{\mathcal{R}_0}\right\rangle.$$

Now, let us get back to the pair of states $|\overline{\Phi}_1;\boldsymbol{\mathcal{R}}\rangle$ and $|\overline{\Phi}_2;\boldsymbol{\mathcal{R}}\rangle$ involved in the matrix $\mathbf{H}(\boldsymbol{\mathcal{R}})$. As already mentioned, they are eigenstates when $\boldsymbol{\mathcal{R}} = \boldsymbol{\mathcal{R}_0}$. We can thus fix them such that $|\overline{\Phi}_1;\boldsymbol{\mathcal{R}_0}\rangle = |\Psi_1^0;\boldsymbol{\mathcal{R}_0}\rangle$ and $|\overline{\Phi}_2;\boldsymbol{\mathcal{R}_0}\rangle = |\Psi_2^0;\boldsymbol{\mathcal{R}_0}\rangle$. Note, however, that there is no reason for them to be eigenstates elsewhere. We now make the hypothesis that $|\overline{\Phi}_1;\boldsymbol{\mathcal{R}}\rangle$ and $|\overline{\Phi}_2;\boldsymbol{\mathcal{R}}\rangle$ do not vary with $\boldsymbol{\mathcal{R}}$ from $\boldsymbol{\mathcal{R}_0}$, i.e. $|\overline{\Phi}_1;\boldsymbol{\mathcal{R}}\rangle \equiv |\Psi_1^0;\boldsymbol{\mathcal{R}_0}\rangle$ and $|\overline{\Phi}_2;\boldsymbol{\mathcal{R}}\rangle \equiv |\Psi_2^0;\boldsymbol{\mathcal{R}_0}\rangle$ for any $\boldsymbol{\mathcal{R}}$ (at least to first order). Such states are often referred to as "crude adiabatic" [88], as they are adiabatic states (eigenstates) for $\boldsymbol{\mathcal{R}} = \boldsymbol{\mathcal{R}_0}$ but not elsewhere. As a consequence, in the spirit of the Hellmann-Feynman theorem (extended to a degenerate situation [89]), one can write the derivatives of $\Delta H(\boldsymbol{\mathcal{R}})$ and $H_{12}(\boldsymbol{\mathcal{R}})$ at $\boldsymbol{\mathcal{R}} = \boldsymbol{\mathcal{R}_0}$ (defined in and **Eq. 15**) from adiabatic derivatives,

$$\frac{\partial}{\partial\mathcal{R}^I}\Delta H(\boldsymbol{\mathcal{R}_0}) = x_I^{0(12)1}(\boldsymbol{\mathcal{R}_0}) \qquad \textbf{Eq. 23}$$

$$= \frac{\left\langle\Psi_2^0;\boldsymbol{\mathcal{R}_0}\right|\frac{\partial}{\partial\mathcal{R}^I}\widehat{H}^{\text{elec}}(\boldsymbol{\mathcal{R}_0})\left|\Psi_2^0;\boldsymbol{\mathcal{R}_0}\right\rangle - \left\langle\Psi_1^0;\boldsymbol{\mathcal{R}_0}\right|\frac{\partial}{\partial\mathcal{R}^I}\widehat{H}^{\text{elec}}(\boldsymbol{\mathcal{R}_0})\left|\Psi_1^0;\boldsymbol{\mathcal{R}_0}\right\rangle}{2},$$

$$\frac{\partial}{\partial\mathcal{R}^I}H_{12}(\boldsymbol{\mathcal{R}_0}) = x_I^{0(12)2}(\boldsymbol{\mathcal{R}_0}) = \left\langle\Psi_1^0;\boldsymbol{\mathcal{R}_0}\right|\frac{\partial}{\partial\mathcal{R}^I}\widehat{H}^{\text{elec}}(\boldsymbol{\mathcal{R}_0})\left|\Psi_2^0;\boldsymbol{\mathcal{R}_0}\right\rangle.$$

The two gradient vectors, $\frac{\partial}{\partial\mathcal{R}^I}\Delta H(\boldsymbol{\mathcal{R}_0})$ (denoted $x_I^{0(12)1}$) and $\frac{\partial}{\partial\mathcal{R}^I}H_{12}(\boldsymbol{\mathcal{R}_0})$ (denoted $x_I^{0(12)2}$), are usually called Gradient Difference (GD) and Derivative Coupling (DC). They span the so-called branching space (or branching plane) over which degeneracy is lifted to first order in $\boldsymbol{\mathcal{R}}$ from $\boldsymbol{\mathcal{R}_0}$. In general, these vectors are simply denoted $\mathbf{x}^1$ and $\mathbf{x}^2$ in the literature. Here, we use a subscript 0 to make apparent that they are defined for $\theta_{12} = 0$ while (12) specifies the labels of the electronic states. Also, note that the plane spanned by the branching space vectors is sometimes referred to as the g-h plane in the literature [21,68,71].

Before going further, let us make an important remark. The working basis set was chosen as a pair of crude adiabatic states for which $\theta_{12} = 0$ corresponded by definition to a specific pair of adiabatic states obtained from an actual calculation, Ψ_α^0. Often, this arbitrary angle occurs to get fixed in practice through symmetry considerations: when both degenerate states potentially belong to different irreducible representations, then the GD will be a vector that conserve the symmetry while the DC will be a vector that breaks the symmetry of the molecule, thus, θ_{12} becomes determined according to this additional condition (up to unphysical signs of the states). However, in a general situation, the value of θ_{12} can be viewed as a gauge condition that requires an extra constraint to be determined according to context. In a general situation, the value of θ_{12} can be fixed upon imposing $H_{12}(\boldsymbol{\mathcal{R}}_{\text{ref}}) = 0$ at some reference geometry, $\boldsymbol{\mathcal{R}} = \boldsymbol{\mathcal{R}}_{\text{ref}}$, where the states are not degenerate (for example at a given minimum). This will be reminded in the following chapter, i.e. Chapter II.

A rigorous treatment of the aspect presented in this section can be derived from a generalization of the Hellmann-Feynman theorem to degenerate situations [89] or, similarly, within the framework of degenerate perturbation theory [68].

2-2-4 Conical Intersection Classification

Generally the local topography of a conical intersection (i.e. the shapes of the potential energy surfaces in the vicinity of the crossing point) can be classified as sloped or peaked; this nomenclature was proposed by Atchity et al. [90]. Sloped conical intersections arise when the gradients of the two potential energy surfaces point approximately in the same direction (often the reactant), as shown by the red arrows in the left panel of Fig. 3. An actual example of this situation is considered in Chapter IV. On the other hand, a peaked conical intersection occurs when the gradients of the potential energy surfaces on both sides of the conical intersection are directed towards different directions (i.e. species A and species B), such as in the right panel of Fig. 3 and in both applications presented in Chapter III and IV.

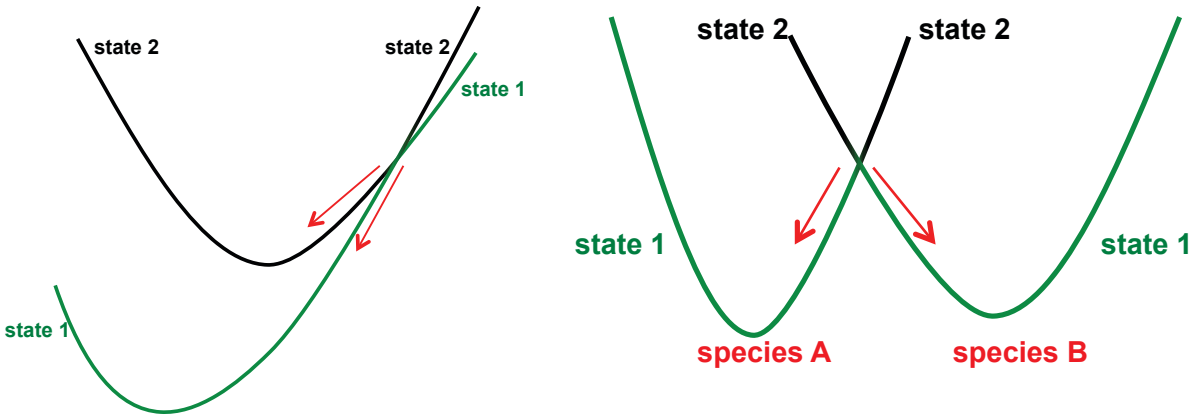

Fig. 3 Left panel: scheme of a sloped conical intersection between *state 1* and *state 2*. Right panel: scheme of a peaked conical intersection between *state 1* and *state 2*.

3- Adiabatic-to-Diabatic Transformation

As already mentioned above, the components of the first-order non-adiabatic coupling vector, $\mathbf{D}_{\alpha\beta}(\boldsymbol{\mathcal{R}})$ (**Eq. 9**), diverge when getting close to regions of the potential energy surfaces where two adiabatic electronic states, α and β, are getting closer to each other (i.e. the difference in energy between these two adiabatic electronic states is getting smaller). As a consequence, although the adiabatic representation is the "practical" representation of the quantum chemist (the data obtained with quantum chemistry calculations are in the adiabatic representation), it often happens to be impractical for quantum dynamics simulations when the effect of a conical intersection and non-adiabatic couplings are to be considered. Smoother functions, easier to handle numerically, can be obtained upon considering an alternative electronic basis set called diabatic. Transformations from adiabatic states to diabatic states are called diabatizations.

Formally, diabatic states are defined such that the corresponding kinetic coupling operator, $\widehat{\Lambda}_{\alpha\beta}(\boldsymbol{\mathcal{R}})$ (defined in **Eq. 8**), vanishes. Instead, the electronic Hamiltonian matrix of **Eq. 3** is no longer diagonal, as the diabatic states (further denoted Φ_i) are not eigenstates (in contrast with the adiabatic states). The electronic couplings between the electronic states are now represented by the off-diagonal entries,

$$H_{ij}^{\text{diab}}(\boldsymbol{\mathcal{R}}) = \left\langle \Phi_i; \boldsymbol{\mathcal{R}} \middle| \widehat{H}^{\text{elec}}(\boldsymbol{\mathcal{R}}) \middle| \Phi_j; \boldsymbol{\mathcal{R}} \right\rangle. \qquad \textbf{Eq. 24}$$

For this reason, they are called potential couplings, as opposed to the kinetic couplings that arise in the adiabatic representation. This concept was introduced in 1935 by Polanyi [91] and Hellmann and Syrkin [92] and further generalised by Smith and Baer [93,94]. Originally used essentially in the context of inelastic scattering in molecular physics, diabatic states have gradually become essential tools in non-adiabatic photochemistry.

As opposed to adiabatic states, diabatic states are not the eigenstates of any electronic operator in particular. Their definition is not unique and, as shown by Mead and Truhlar [95], the diabatic criterion (see below), which is a local condition, cannot be achieved globally (except for a diatom or for the ideal two-state model). In the general case, a complete (thus infinite) basis set of electronic states is required for integrating the condition of diabaticity over the whole nuclear coordinates space. However, it is possible to find states that make the non-adiabatic couplings negligible and with no significant effect on the dynamics of the molecule; such states are called quasidiabatic and often referred to as diabatic for simplicity [96–100].

Formally, the diabatic and adiabatic basis sets can be considered both as orthonormal and spanning the same space at all geometries. They are thus transformed into each other through a unitary transformation, $\mathbf{U}(\boldsymbol{\mathcal{R}})$,

$$\mathbf{U}^{\dagger}(\boldsymbol{\mathcal{R}})\mathbf{U}(\boldsymbol{\mathcal{R}}) = \mathbf{U}(\boldsymbol{\mathcal{R}})\mathbf{U}^{\dagger}(\boldsymbol{\mathcal{R}}) = \mathbf{1}, \qquad \textbf{Eq. 25}$$

such that both Hamiltonian matrices are related through a similarity transformation,

$$\mathbf{V}(\boldsymbol{\mathcal{R}}) = \mathbf{U}^{\dagger}(\boldsymbol{\mathcal{R}})\mathbf{H}^{\text{diab}}(\boldsymbol{\mathcal{R}})\mathbf{U}(\boldsymbol{\mathcal{R}}), \qquad \textbf{Eq. 26}$$

where $\mathbf{V}(\boldsymbol{\mathcal{R}})$ is diagonal (i.e. the matrix representation of $\widehat{H}^{\text{elec}}(\boldsymbol{\mathcal{R}})$ in the adiabatic basis set). In this definition, the columns of $\mathbf{U}(\boldsymbol{\mathcal{R}})$ correspond to the components of the adiabatic states in the diabatic basis set. $\mathbf{D}_{\alpha\beta}(\boldsymbol{\mathcal{R}})$ is the first-order non-adiabatic

coupling matrix between states α and β in the adiabatic basis set and $\mathbf{D}_{ij}^{\mathrm{diab}}(\boldsymbol{\mathcal{R}})$ the same quantity between states i and j in the diabatic basis set. For each coordinate $\mathcal{R}^I$ the electronic matrices transform into each other according to

$$\mathbf{D}^I(\boldsymbol{\mathcal{R}}) = \mathbf{U}^\dagger(\boldsymbol{\mathcal{R}})\mathbf{D}^{\mathrm{diab},I}(\boldsymbol{\mathcal{R}})\mathbf{U}(\boldsymbol{\mathcal{R}}) + \mathbf{U}^\dagger(\boldsymbol{\mathcal{R}})\frac{\partial}{\partial \mathcal{R}^I}\mathbf{U}(\boldsymbol{\mathcal{R}}). \qquad \textbf{Eq. 27}$$

The diabatic criterion of Smith and Baer reads

$$\mathbf{D}^{\mathrm{diab}}(\boldsymbol{\mathcal{R}}) \approx \mathbf{0}, \qquad \textbf{Eq. 28}$$

so that the unitary transformation, $\mathbf{U}(\boldsymbol{\mathcal{R}})$, must fulfill

$$\mathbf{D}^I(\boldsymbol{\mathcal{R}}) \approx \mathbf{U}^\dagger(\boldsymbol{\mathcal{R}})\frac{\partial}{\partial \mathcal{R}^I}\mathbf{U}(\boldsymbol{\mathcal{R}}). \qquad \textbf{Eq. 29}$$

In the two-state case exposed in the previous section, we had considered a real rotation through an angle $\varphi_X(\boldsymbol{\mathcal{R}})$ between two adiabatic states, $|\Psi_1;\boldsymbol{\mathcal{R}}\rangle$ and $|\Psi_2;\boldsymbol{\mathcal{R}}\rangle$, and two states, $|\overline{\Phi}_1;\boldsymbol{\mathcal{R}}\rangle$ and $|\overline{\Phi}_2;\boldsymbol{\mathcal{R}}\rangle$, not necessarily specified as adiabatic or diabatic. In other words, the angle $\varphi_X(\boldsymbol{\mathcal{R}})$ was not further specified. Now, in this situation, the previous diabatic criterion applied to a unitary transformation chosen as a real rotation through an angle $\varphi'(\boldsymbol{\mathcal{R}})$,

$$\mathbf{U}(\boldsymbol{\mathcal{R}}) = \begin{bmatrix} \cos\varphi'(\boldsymbol{\mathcal{R}}) & -\sin\varphi'(\boldsymbol{\mathcal{R}}) \\ \sin\varphi'(\boldsymbol{\mathcal{R}}) & \cos\varphi'(\boldsymbol{\mathcal{R}}) \end{bmatrix}, \qquad \textbf{Eq. 30}$$

i.e.

$$\begin{aligned} |\Psi_1;\boldsymbol{\mathcal{R}}\rangle &= \cos\varphi'(\boldsymbol{\mathcal{R}})\,|\Phi_1;\boldsymbol{\mathcal{R}}\rangle + \sin\varphi'(\boldsymbol{\mathcal{R}})\,|\Phi_2;\boldsymbol{\mathcal{R}}\rangle, \\ |\Psi_2;\boldsymbol{\mathcal{R}}\rangle &= -\sin\varphi'(\boldsymbol{\mathcal{R}})\,|\Phi_1;\boldsymbol{\mathcal{R}}\rangle + \cos\varphi'(\boldsymbol{\mathcal{R}})\,|\Phi_2;\boldsymbol{\mathcal{R}}\rangle. \end{aligned} \qquad \textbf{Eq. 31}$$

yields

$$\mathbf{D}^I(\boldsymbol{\mathcal{R}}) \approx -\frac{\partial\varphi'(\boldsymbol{\mathcal{R}})}{\partial\mathcal{R}^I}\begin{bmatrix} 0 & 1 \\ -1 & 0 \end{bmatrix}, \qquad \textbf{Eq. 32}$$

i.e.

$$D_{12}^{\boldsymbol{I}}(\boldsymbol{\mathcal{R}}) = -D_{21}^{\boldsymbol{I}}(\boldsymbol{\mathcal{R}}) \approx -\frac{\partial\varphi'(\boldsymbol{\mathcal{R}})}{\partial\mathcal{R}^I}. \qquad \textbf{Eq. 33}$$

Thus, we get $|\Phi_1;\boldsymbol{\mathcal{R}}\rangle$ and $|\Phi_2;\boldsymbol{\mathcal{R}}\rangle$ as states that are "as diabatic as possible" if we can determine $\varphi'(\boldsymbol{\mathcal{R}})$ such that its gradient satisfies the previous equation to some extent.

The development of various diabatization formalisms was an active field of research in the 1980s and has recently become central again with the advent of quantum dynamics methods able to treat large molecular systems. Many approaches, based on different criteria, have been proposed to build quasidiabatic states and/or Hamiltonians [20,73,100–102]. A detailed review of diabatization methods is beyond the scope of this thesis, thus, we suggest to refer to the following references for more details and applications [54,73,103–109].

4- Vibronic Coupling Hamiltonian Models

Methods known as diabatizations by Ansatz are based on assuming mathematical expressions for the functions entering the diabatic Hamiltonian matrix $\mathbf{H}^{\text{diab}}(\boldsymbol{\mathcal{R}})$, **Eq. 24**, where each function is defined by a set of parameters. The values of the various parameters are adjusted through a fitting procedure so that the eigenvalues of $\mathbf{H}^{\text{diab}}(\boldsymbol{\mathcal{R}})$, are as close as possible to the ab-initio (i.e. adiabatic) energies over a sample of relevant molecular geometries. The functions $H_{ij}^{\text{diab}}(\boldsymbol{\mathcal{R}})$ must depend as smoothly as possible on the nuclear coordinates. This ensures indirectly that the states vary as little as possible with $\boldsymbol{\mathcal{R}}$. Indeed, there is no control over $\widehat{H}^{\text{elec}}(\boldsymbol{\mathcal{R}})$ (which, in any case, varies smoothly with $\boldsymbol{\mathcal{R}}$). So, abrupt variations of $\langle\Phi_i;\boldsymbol{\mathcal{R}}|\widehat{H}^{\text{elec}}(\boldsymbol{\mathcal{R}})|\Phi_j;\boldsymbol{\mathcal{R}}\rangle$ are to be attributed to large values of $D_{ij}^{\text{diab},I}(\boldsymbol{\mathcal{R}}) = \left\langle\Phi_i;\boldsymbol{\mathcal{R}}\middle|\frac{\partial}{\partial\mathcal{R}^I}\Phi_j;\boldsymbol{\mathcal{R}}\right\rangle$, and reciprocally (small couplings in the diabatic representation yield smooth Hamiltonian functions).

Note that the non-adiabatic couplings are not explicitly used. However, if the double cone around a conical intersection is described correctly to first order in the model, the first-order non-adiabatic coupling at this point will be correct by construction. Indeed, as already shown, the adiabatic gradient difference and non-adiabatic coupling span the branching plane. This ensures that the effect of the non-adiabatic couplings will be treated adequately in regions where they are significant (around conical intersections).

A particular case of diabatization by Ansatz is known as the Vibronic-Coupling Hamiltonian (VCH) model [20,110–112]. Usually, its entries are expressed as linear (Linear Vibronic Coupling model – LVC) or quadratic (Quadratic Vibronic Coupling model – QVC) functions of normal Cartesian coordinates originated from the ground-state equilibrium geometry (Franck-Condon point). This is the type of approach that we used in the present work. However, the main originality of the approach that we developed (detailed in the next chapter – Chapter II) is that we explicitly used analytical relationships between adiabatic data and diabatic parameters to obtain them automatically. Therefore, we avoid the numerical fitting procedure that, in some cases, can occur to be time consuming and a tedious task from a technical perspective.

II- Methods

In this part we present the method used first to calculate the electronic energy of the system (quantum chemistry methods) such as the multiconfigurational self-consistent field (MCSCF) or the time-dependent density functional methods that are adapted to describe the electronic structure of excited states. As well we present the polarizable continuum model method as we used it in the application on 3-hydroxychromone dyes to describe the effect of the solvent over the potential energy surfaces. Then, we describe the method used to describe the quantum motion of the system during the photoprocess, the multilayer multiconfigurational time-dependent hartree method (ML-MCTDH), that is currently a method in development and let us run quantum dynamics calculations of large system (more than tens degrees of freedom) on coupled potential energy surfaces.

1- Quantum Chemistry

1-1 The MultiConfigurational Self-Consistent Field Methods

Let us consider a closed-shell system such as H_2. Around its equilibrium geometry, a Hartree-Fock description is known to be adequate. However, more than one Slater determinants are required for describing correctly the dissociation of this molecule when using molecular orbitals. This is known as a lack of left-right static correlation in the Hartree-Fock description. There are different kinds of static correlation and no strict definition. Generally speaking, static correlation reflects the necessity to include more than one Slater determinant to get a qualitatively correct description of the wave function. Taking this into account is essential for example in situations where electronic states are close enough to interact significantly with each other or even degenerate such as at a conical intersection.

The multiconfigurational self-consistent field methods [113–117] express the wave function as a linear combination of Slater determinants whereby both the coefficients of each Slater determinant in the expansion and the coefficients of each molecular orbital (expressed as linear combinations of atomic orbitals) are optimized. When the total electron spin is specified, the expansion is usually made more compact upon first combining Slater determinants into so-called configuration-state functions according to spin symmetry (configuration-state functions are eigenstates of both S^2 and S_z whereas Slater determinants are eigenfunctions of S_z only). In this case, the coefficients that are optimized are those of the configuration-state functions.

When the molecular orbitals are not optimized but come from a previous calculation, this type of expansion is known as a configuration interaction. On the other hand, if only one Slater determinant is used but the molecular orbitals are optimized, one obtains a Hartree-Fock wave function. In other words, MCSCF methods can be viewed as a “mixture” of configuration interaction and Hartree-Fock.

In practice, there are various types of MCSCF approaches, according to the definition and construction of the space of configurations (either Slater determinants or configuration-state functions) used in the configuration interaction expansion. They can be selected "by hand", which is the original implementation of MCSCF in quantum chemistry programs but is quite delicate to handle numerically. The most usual implementation of MCSCF is known as the Complete Active Space SCF (CASSCF) method. Here, the user must define a number of active electrons and a set of active orbitals that are expected to have an average occupation number that is significantly different from 0 or 2 in the wave function. The configuration space is generated by considering all possible distributions of the active electrons in the active orbitals. The active orbitals are identified either from a previous Hartree-Fock calculation or from another CASSCF calculation (for example with a small basis set of at neighboring geometry). The molecular orbital are thus separated into the three following categories.

(i) The inactive orbitals are optimized but they are kept doubly occupied in all determinants.

(ii) The active orbitals are optimized and all possible excitations and occupations are used according to the number of active electrons to obtain the set of configurations for the MCSCF expansion (the active space).

(iii) The remaining orbitals are not occupied. As they are not part of the wave function, they are not optimized.

The choice of active orbitals is user dependent and can be a very tedious task. Often, chemical intuition helps. See Ref. [115] for a detailed discussion on the choice of an active space.

MCSCF methods optimize iteratively the orbital and configuration coefficients using a self-consistent procedure. The configuration coefficients are obtained from a diagonalization of the electronic Hamiltonian matrix expressed in the configuration space. As a consequence, MCSCF methods are capable of providing excited states because several eigenstates and eigenenergies can be obtained. It is thus possible to determine for which state the orbitals are to be optimized (state specific calculation). In some situations (in particular for conical intersections) it is better to optimize the orbitals for a group of states with weights provided by the used (state average calculation).

CASSCF calculations are often made with the objective of considering static correlation in the wave function. In practice, this means that the set of active orbitals is minimal and chosen so as to yield the smallest number of interacting configurations required to get a qualitatively correct wave function. For example, a valence active space will provide qualitatively correct valence states but will not be adapted for a correct description of ionic states or Rydberg states. In the case of ionic states, the probability of finding a pair of electrons simultaneously in the same region of space is high, which can produce an overestimation of the electron repulsion if the wave function is not flexible enough. This is known as a lack of dynamic correlation. A correct treatment of such a situation requires considering excitations to a larger number of virtual orbitals. Intuitively, both electrons will thus be able to be in the same region of space but described by orthogonal orbitals. In other words, including dynamic correlation corresponds to considering additional configurations, not necessarily close in energy to the configurations generated by the active space but still required to get quantitative results. Increasing the size of the active space is a possibility but not the most usual one. Often, dynamic correlation is accounted for by using the complete active space with second-order perturbation theory (e.g. CASPT2) method [118–124]. In this approach, the effect of the extra configurations (those missing from the configuration space used to calculate the CASSCF wavefunctions) is calculated from a second-order perturbation theory treatment.

1-2 The (Time-Dependent) Density Functional Theory [125–131]

The Density Functional Theory (DFT), is an alternative formulation of the electronic problem that avoids the explicit use of wave functions. In practice, as a method, it provides the ground state energy of the electronic Hamiltonian from the one-electron density rather than from the all-electron wave function that is used in HF and post-HF methods. The one-electron density of a system with N electrons is a function that depends on the coordinates of a single electron among N (defined in space by the vector $\mathbf{r}$). Its physical meaning is the density of probability of finding any of the N electrons at the position $\mathbf{r}$. It is obtained upon fixing the position of each electron and integrating the all-electron density over the coordinates of the remaining $N-1$

electrons. As the electrons are indistinguishable, it is in practice calculated by particularising one given electron (in general the first one) and by multiplying the result by N, which reads

$$\rho(\mathbf{r}) = N \int \cdots \int |\Psi(\mathbf{r}_1 = \mathbf{r}, \mathbf{r}_2, \cdots, \mathbf{r}_N)|^2 \, d\mathbf{r}_2 \cdots d\mathbf{r}_N \qquad \textbf{Eq. 34}$$

Hence, in this formalism, the electronic energy will be expressed as a functional of $\rho(\mathbf{r})$, denoted $E[\rho]$, where $\rho(\mathbf{r})$ depends only on three variables, $\mathbf{r}$, and this for any number of electrons, N. In contrast, in the wave function formalism we have a $(3N)$-dimensional dependence. Therefore, using DFT-based methods gives us access to treating systems with a large number of electrons such as materials (for example, solid state metals).

The first Hohenberg-Kohn theorem [132] deals with the external potential, $v_{ext}(\mathbf{r})$ (reflecting for one electron the effect of V_{N-e}, the electrostatic potential between nuclei and one electron); its contribution to the energy, $E[\rho]$, is obtained as a unique functional of $\rho(\mathbf{r})$: $\mathcal{V}_{N-e}[\rho] = \int \rho(\mathbf{r}) v_{ext}(\mathbf{r}) d\mathbf{r}$ (integrating over the coordinate of a single electron). The remaining terms in the electronic Hamiltonian, **Eq. 3**, are universal for a system of N electrons: they do not depend on the positions of the nuclei, i.e. are unrelated to the structure and nature of the molecule (note that we omit here the effect of V_{N-N}, which is a constant term that does not affect the wave function or the density and that can be added at the end of the calculation). In other words, the external potential is the only term that is "molecule-dependent" in the electronic Hamiltonian. The remaining terms reflect the effect of T_e and V_{e-e}, the kinetic and potential energies of the N interacting electrons, for a given $\rho(\mathbf{r})$. Their contributions to the energy are also represented with unique functionals of $\rho(\mathbf{r})$: $\mathcal{T}_e[\rho]$ and $\mathcal{V}_{N-e}[\rho]$. Hence, the electronic energy is a unique functional of $\rho(\mathbf{r})$ and reads

$$E[\rho] = \mathcal{T}_e[\rho] + \mathcal{V}_{e-e}[\rho] + \mathcal{V}_{N-e}[\rho] \qquad \textbf{Eq. 35}$$

In principle, the electronic energy of the ground state can be obtained variationally. Unfortunately, the first two terms do not have explicit expressions as functionals of $\rho(\mathbf{r})$ in the case of N interacting electrons. To simplify this problem, Kohn-Sham [132,133]

proposed to obtain $\rho(\mathbf{r})$ for an *N*-electrons system from the electron density of one electron living in a one-body potential (homogenous free electrons gas).

Then, the total electronic energy, $E[\rho]$, is well defined and all the terms have now an explicit expression except for the exchange and correlation contributions. In addition, this one-electron density is expanded as a sum of squared monoelectronic functions called Kohn-Sham orbitals. Those orbitals are obtained and optimized using a self-consistent procedure solving the Kohn-Sham monoelectronic equation. The exchange and correlation contributions to the total electronic energy are obtained with functionals expressed as Taylor-expansions of the one-electron density at a given point: the Local Density Approximation (LDA) is the zero order, based only on the value of $\rho(\mathbf{r})$ at this point. The Generalized Gradient Approximation (GGA) is the first order, based on the $\rho(\mathbf{r})$ and its gradient [134]. Nowadays, it is usual to use hybrid functionals [135,136], such as B3LYP or PBE0 (used to study 3-hydroxychromone dyes in Chapter III), where the exchange terms is partly based on the same expression as in a HF calculation and the remaining part comes from a local or semi-local approximation of the one-electron density (LDA, GGA, ….), which improves the description.

One should keep in mind that this method is only used to calculate the energy of the ground state. The most common DFT-based approach to compute the energies of excited states is the Time-Dependent DFT (TD-DFT) method [137–143]. It essentially is a DFT treatment with a time-dependent external potential. Now, the external potential is the electrostatic potential with a small external perturbation that evolves in time. Let us first picture simply what is an excited state is terms of electronic density. We apply an external perturbation to a system in its ground state with a given electronic density; this electronic density is going to oscillate (it gets excited) with respect to this external perturbation. How the electronic density is going to respond to the external perturbation defines a new repartition of the electrons in space, hence, a new electronic density, which involves excited electronic states. Therefore, we will obtain the excitation energies of these excited electronic states. This general idea is called linear response TD-DFT and it is a great advantage, as the variation of the system will depend only on the electronic density of the ground state so that we can simply use all the properties of the DFT method.

1-3 The Polarizable Continuum Model Method [144–146]

In order to evaluate the effect of the solvent on the electronic energy of a molecule (i.e. the potential energy for the nuclei) we used the Polarizable Continuum Model (PCM) method implemented in Gaussian09 package.

The PCM model is an extension of the Onsager solvation model [147] where the solute is placed inside a cavity (which can have different shapes, such as spherical, ellipsoidal, etc.) embedded in a surrounding polarizable dielectric continuum that describes the solvent implicitly. The solute dipole induces a reaction field felt by the surrounding medium, which in turn induces a new electric field in the cavity (back reaction field), which interacts with the solute dipole again; the final resulting interaction is obtained from a self-consistent process. The interaction between the solvent and the solute is then represented by a solvent reaction potential introduced into the electronic Hamiltonian that will be solved with the quantum chemistry method chosen by the user.

For excited state calculations in solution, there is a distinction to make between the solvent being at equilibrium or not with respect to the geometry and the electronic state considered in the calculation. The solvent responds in two different ways to changes in the state of the solute: (i) it polarizes the electron distribution of the solute, which is a very rapid process (10^{-15}s), (ii) and the solvent molecules reorient themselves, which is a much slower process (10^{-12} – 10^{-8}s) [148]. A calculation where the solvent is in its equilibrium state describes a situation where the solvent had time to fully respond to the solute. This is adapted to describing a process that is slower than the solvent relaxation. If the process under study is faster than the solvent relaxation, it is then a situation where the solvent should be considered in a non-equilibrium state, such as when calculating a vertical electronic transition energy. Therefore, when computing an absorption energy in solution, we will use a solvent in its equilibrium state for the ground state and in a non-equilibrium state for the excited state. To compute the emission energy, the general idea is the same but reversed: the solvent is in its equilibrium state for the excited state and in a non-equilibrium state for the ground state.

This method is adapted only to describe electrostatic interaction between the solute and the solvent (i.e. for an aprotic solvent). In other words, one cannot represent interactions with significant chemical character between molecules of the solute-solvent supersystem (e.g. hydrogen bonds or, even worse, proton transfers within protic solvents). This would require an explicit treatment of the solvent molecules surrounding the solute.

In addition, the PCM model, as it is, does not describe the dynamics of the solvent (as already mentioned, it is considered in a static state, either at equilibrium or not). However, if the dynamics of the process under study has a similar time scale as the solvent relaxation, hence, the dynamics of solvation can play a non-negligible role on the process dynamics. To achieve this description one would need a time dependent PCM model and expand it over the whole nuclear grid (i.e. numerical description). This type of model is not trivial and requires developments that we did not focus on. Note that, in the application case that we treated with the PCM model to run nuclear dynamics (aminobenzonitrile; see Chapter IV), it is sensible to assume that the first few femtoseconds of the photoinduced process are better described with the solvent in the equilibrium state for the ground state. However, for longer times, this choice becomes questionable, which is why we also considered the case where the solvent in the equilibrium state for the excited state.

2- Quantum Dynamics

Quantum dynamics determines the motion of the nuclei using a quantum mechanical approach to take into account the quantum character of the internuclear degrees of freedom (in cases where this is relevant), $\boldsymbol{\mathcal{R}}$, when solving the time-dependent molecular Schrödinger equation (already express in **Eq. 1** but to remind),

$$i\hbar\frac{\partial}{\partial t}\left|\Psi^{\mathrm{mol}}(t,\boldsymbol{\mathcal{R}})\right\rangle = \hat{H}^{\mathrm{mol}}\left|\Psi^{\mathrm{mol}}(t,\boldsymbol{\mathcal{R}})\right\rangle \qquad \textbf{Eq. 36}$$

The molecular wave packet, $\left|\Psi^{\mathrm{mol}}(t,\boldsymbol{\mathcal{R}})\right\rangle$, can be identified to a single nuclear wave packet where only one electronic state is involved (Born-Oppenheimer approximation).

When several electronic states are coupled, $\left|\Psi^{\mathrm{mol}}(t,\boldsymbol{\mathcal{R}})\right\rangle$ is expanded into this electronic basis set at each $\boldsymbol{\mathcal{R}}$ with coefficients considered as coupled nuclear wave packets (see **Eq. 5**).

Before solving the time-dependent Schrodinger equation, we need to specify the degrees of freedom that describe the positions of the nuclei in space, which is achieved by the definition of a set of coordinates. In our case, as discussed in the following, we chose to work with curvilinear internal coordinates denote **Q**. Then, one must express the nuclear Kinetic Energy Operator (KEO) in terms of this set of coordinates and finally generate the corresponding representation of the electronic Hamiltonian (i.e. a single potential energy surface within the Born-Oppenheimer approximation or a matrix of potential energy surfaces and couplings in the non-adiabatic case; see Section 2- Chapter I).

To solve the time-dependent Schrödinger equation we used the ML-MCTDH method, presented in the following. This method corresponds to a very compact representation of the nuclear wave function that makes possible quantum dynamics calculations with numerous degrees of freedom.

2-1. Coordinates

In classical dynamics, calculations are usually made using Cartesian coordinates. In contrast, in quantum dynamics, one must carefully choose a set of coordinates adapted to the process that one wants to describe. This difference is due to the fact that the trajectory of a particle is represented as a point in classical mechanics, while, in quantum mechanics, it is a delocalized wave function. i.e. a function that depends on all nuclear coordinates with more or less correlation according to the choice of coordinates. Therefore, in classical mechanics, the set of coordinates does not influence the quality of the description, whereas, in quantum dynamics the number of terms required to express accurately the wave function depends on the set of coordinate. If the coordinates are well chosen in the sense that they describe adequately the molecule internal motions,

with as little coupling (correlation) as possible, hence, one can use a compact expression of the nuclear wave function.

This is illustrated in the following example with a single electronic state (Born-Oppenheimer approximation) and two Cartesian nuclear coordinates, *x* and *y*. We consider a two-dimensional harmonic oscillator model centered at the origin of the framework with $\boldsymbol{f}$ the Hessian matrix. The nuclear Hamiltonian reads

$$\hat{H}(x,y) = V(x,y) + \hat{T}(x,y) \qquad \textbf{Eq. 37}$$

$$\hat{H}(x,y) = \frac{1}{2}f^{xx}x^2 + \frac{1}{2}f^{yy}y^2 + f^{xy}xy - \frac{\hbar^2}{2m}\frac{\partial^2}{\partial x^2} - \frac{\hbar^2}{2m}\frac{\partial^2}{\partial y^2}$$

One can notice in **Eq. 37**, the presence of a coupling term between the *x* and *y* coordinates in the potential energy, i.e. $f^{xy}xy$.

In the case of a symmetric oscillator, $f^{xx} = f^{yy}$, the following linear combination of the previous set of coordinates,

$$\begin{cases} x' = \frac{1}{2}(x+y) \\ y' = \frac{1}{2}(x-y) \end{cases} \qquad \textbf{Eq. 38}$$

diagonalises the $\boldsymbol{f}$ matrix, such that the nuclear Hamiltonian now reads

$$\hat{H}(x',y') = \frac{1}{2}f^{x'x'}x'^2 + \frac{1}{2}f^{y'y'}y'^2 - \frac{\hbar^2}{2m'}\frac{\partial^2}{\partial x'^2} - \frac{\hbar^2}{2m'}\frac{\partial^2}{\partial y'^2} \qquad \textbf{Eq. 39}$$

One can notice in **Eq. 39**, that there is no longer any coupling term between the *x*' and *y*' coordinates, as they are the equivalent to the normal coordinates (the potential energy is now separable as a sum of two one-dimensional terms).

Let us just make a short parenthesis about normal coordinates [149–151]. Normal

coordinates are obtained from a rotation of the original set of Cartesian displacements from a stationary point under the constraint that the potential energy must be separable to second order (in other words, the mass-weighted Hessian matrix must be diagonalized). If the previous example were not symmetrical (i.e. $f^{xx} \neq f^{yy}$), the relationship between both sets of coordinates expressed in **Eq. 38** would not be compatible with **Eq. 39** (it would not diagonalize the Hessian matrix). However, another rotation angle could be expressed to provide the correct normal coordinates. In addition, if we were using curvilinear coordinates [150,152,153], the KEO in **Eq. 37** would not be diagonal. Therefore, if one wants to generate the curvilinear normal coordinates at a reference geometry (usually a minimum), first, we need to diagonalize the KEO (to generate an intermediate set of curvilinear coordinates), and then, as for rectilinear normal coordinates, with this intermediate set of curvilinear coordinates, we could diagonalize the new Hessian matrix to obtain the curvilinear normal coordinates (this type of coordinates were used for technical reasons during the quantum dynamics study of 3-HC, see Chapter III).

Often, to solve the time-dependent Schrödinger equation, the nuclear wave packet is expanded into a basis set made of products of low-dimensional functions. Hence, removing artificial correlation will imply that fewer basis functions are required to converge the nuclear wave function. This is the case when using the second set of coordinates (i.e. x' and y'), which is more adapted than the first set (i.e. x and y) in the previous example. In the case of the original set of coordinates, the coupling term in the potential energy requires more basis functions for the wave packet expression to be flexible enough to account for the presence of the off-diagonal term (i.e. xy).

Therefore, in quantum dynamics the choice of coordinates is crucial, and allows a compact representation of the nuclear wave function. This has an impact on the possibility to run or not quantum dynamics calculations in practice.

The choice of an adequate coordinate system depends on the process under study. In particular, for molecular systems with large-amplitude motions, normal mode coordinates are not adequate to describe motions leading far from the equilibrium position [154]. Therefore, it is often advantageous to describe the molecular system

with curvilinear coordinates, i.e., distances and angles since they describe large-amplitude motions such as for example torsions in a more natural way; in other words, they will give a simpler expression of the potential energy surface. Unfortunately, the use of curvilinear coordinates can lead to very complicated expressions of the KEO (discussed in Section 2-2 Chapter I), which can be expressed numerically (but exactly) or analytically. An analytical approach is more practical, as there is no need to compute the numerical KEO on a grid and then fit the results or make further approximations (for example by considering Taylor expansions). However, an analytical expression of the KEO is not always compatible with an "MCTDH format" (see below), where operators must be written as sums of products of low-dimensional functions. Some specific types of coordinates allow this condition to be fulfilled, in particular so-called polyspherical coordinates [155,156], which were used in Chapter III and IV and discussed in the following.

2-1-1- Polyspherical Coordinates General Approach

In the framework of the polyspherical approach [154,155,157–161],the choice of an optimal set of coordinates proceeds in four steps:

(i) Choose a well-adapted vector parameterization for a given molecular system, i.e., a set of vectors describing the shape of the molecule such as valence, Jacobi, or Radau vectors. In Fig. 4, we choose a set of vectors ($\mathbf{R_1}$ and $\mathbf{R_2}$) defined along the chemical bonds between the oxygen and both hydrogens, so-called valence vectors.

(ii) Define a frame, so called Body-Fixe (BF) frame with respect to the center of mass of the system. Its orientation with respect to the Laboratory-Fixed (LF) frame is determined by three Euler angles (α, β, and γ).

The BF is defined in a particular way using two vectors such that the $\boldsymbol{z}_{\mathrm{BF}}$ axis is parallel to $\mathbf{R_1}$ (this choice is done by the user), and $\mathbf{R_2}$ defines the half-plane ($\boldsymbol{x}_{\mathrm{BF}},\boldsymbol{z}_{\mathrm{BF}}$) with $x_{\mathrm{BF}} > 0$ [162,163]. This is illustrated in Fig. 4 (note that the origin of BF is not indicated but is at the center of mass). The $\mathbf{R_1}$ vector connects the oxygen to H_1. It defines the $\mathbf{z}_{\mathrm{BF}}$ axis such that its BF components read (0,0, $z_{1,\mathrm{BF}} > 0$). The $\mathbf{R_2}$ vector

connects the oxygen to H_2. It defines the half-plane $(\boldsymbol{x}_{\mathrm{BF}},\boldsymbol{z}_{\mathrm{BF}})$ with $x_{\mathrm{BF}} > 0$ such that its BF components read $(x_{2,\mathrm{BF}} > 0{,}0, z_{2,\mathrm{BF}})$.

The orientation of the BF frame with respect to the LF frame is determined by the three Euler angles that characterize the overall rotation of the molecular system. This is achieved in three steps (Fig. 4): first, we rotate with an $\alpha \in [0; 2\pi]$ angle the $\boldsymbol{x}_{\mathrm{LF}},\boldsymbol{y}_{\mathrm{LF}}$ axes around the $\boldsymbol{z}_{\mathrm{LF}}$ axis. This defines a new frame: $\boldsymbol{x}', \boldsymbol{y}', \boldsymbol{z}' = \boldsymbol{z}_{\mathrm{LF}}$. In a second step, we rotate with a $\beta \in [0; \pi]$ angle the $\boldsymbol{x}', \boldsymbol{z}'$ axes around the $\boldsymbol{y}'$ axis. This defines again a new frame: $\boldsymbol{x}'', \boldsymbol{y}'' = \boldsymbol{y}', \boldsymbol{z}''$. In a third and last step, we rotate with a $\gamma \in [0; 2\pi]$ angle the $\boldsymbol{x}'', \boldsymbol{y}'' = \boldsymbol{y}'$ axes around the $\boldsymbol{z}''$ axis. This finally defines the BF frame $\boldsymbol{x}_{\mathrm{BF}},\boldsymbol{y}_{\mathrm{BF}}, \boldsymbol{z}'' = \boldsymbol{z}_{\mathrm{BF}}$.

(iii) If subsystems are needed, define them. The subsystems approach is discussed in the following Section.

(iv) Express the vectors themselves in a well-chosen set of coordinates; in terms of bond lengths, R, polar angles, θ, azimuthal angles, φ (i.e. spherical coordinates). In our given example, $\mathbf{R_1}$ vector is defined in the set of polyspherical coordinates as R_1, β, α, and $\mathbf{R_2}$ vector as R_2, θ, γ. The three Euler angles β, α, and γ defined the BF frame, thus, they are not deformation coordinates as are the two bond lengths R_1 and R_2 and the valence angle θ. One needs at least three vectors to have a φ angle that represents an out-of-plane motion within the molecule, which explains its absence in this example.

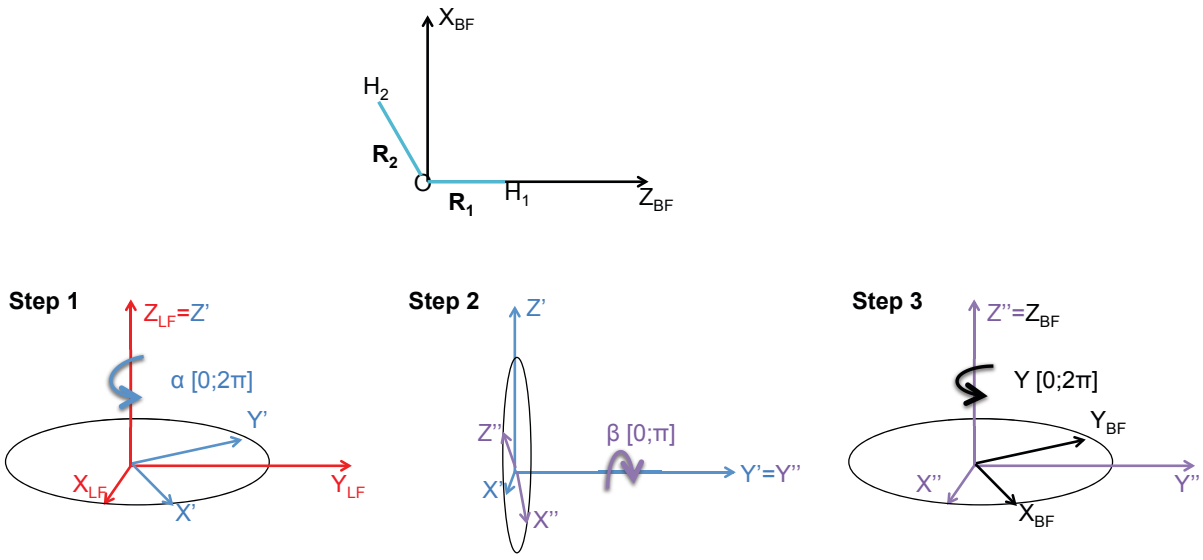

Fig. 4 Definition of the Euler angles defining the orientation of BF with respect to LF in three steps.

2-1-2- Separation into subsystems

Let us now introduce some subsystems in the polyspherical approach. A subsystem can be seen as a bunch of vectors attached to an intermediate frame that is embedded into another frame that is the BF or another intermediate frame and so on [154,155,159]. One can see the subsystem as "multi-layer" strategy to define coordinates.

In order to correctly describe the hierarchy (i.e. layering) between various embedded subsystems, it is necessary to resort to an extended notation that is explained in details in [160]. In the following, we will explain the general idea of the subsystem notation upon applying it to a specific example, i.e. the set of aminobenzonitrile polyspherical coordinates (used in Chapter IV), depicted in Fig. 5.

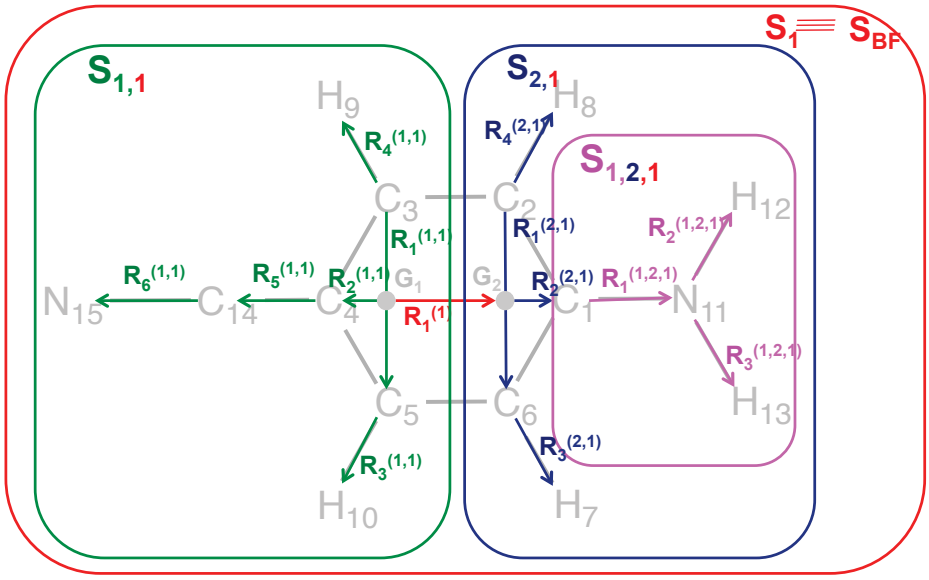

Fig. 5 Set of polyspherical coordinates and subsystems of aminobenzonitrile.

One can notice on Fig. 5, that the total system is called S_1, which is the BF frame. Within S_1, there is a first layer of subsystems: $S_{1,1}$ and $S_{2,1}$. In addition, embedded within the $S_{2,1}$ subsystem, there is a second layer made of one subsystem: $S_{1,2,1}$. One can start to see the logic behind the notation of the subsystems. S_1 will always be the first subsystem (the system), the first layer will always be $S_{i,1}$ with *i* the number of the first layer subsystem (i.e. first, second, etc..) et *1* represent the S_1. If there is a second layer of subsystem embedded in a previous subsystem, hence, the notation will be $S_{j,i,1}$ with *j* the number of the second layer subsystem, *i* is the number of the first layer subsystem that posses a second layer of subsystem and *1* is still the BF frame.

The main advantage of splitting a system into several smaller subsystems is that one can introduce many different sets of coordinates that may be more adapted to the physics of the problem than the standard (without subsystems) polyspherical coordinates; in other words, that gives a higher flexibility in the choice of the set of coordinates. In addition, parameterization with subsystems allows us to still use direct products of one-dimensional basis sets while avoiding the singularity problem that will be explained in the next section. It also leads to a reduced coupling between the parameterizing vectors.

In summary the polyspherical approach can be applied to any set of vector parameterization and whatever the number of atoms. One of the advantages is the

possibility to split large systems into several small subsystems. Another crucial advantage is that this approach gives a general analytical form of the KEO for any set of polyspherical coordinates, which is adapted to the "MCTDH format" and can be obtained automatically [153,155,159,160].

2-2. Kinetic Energy Operator

In Cartesian coordinates the KEO is well known and simple to express. However, in curvilinear coordinates (denoted **Q** in the following) its expression becomes complicated [155,162–164]. The general expression of the KEO (for the $3N$ curvilinear coordinates: translations, rotations, and deformations; note here that the three translation coordinates are not curvilinear but the other ones are), $\hat{T}(\mathbf{Q})$, and the volume element, $d\tau$, can be expressed as follows:

$$\hat{T}(\mathbf{Q}) = -\frac{\hbar^2}{2}\sum_{K=1}^{3N}\sum_{L=1}^{3N}\rho_{KEO}^{-1}\frac{\partial}{\partial Q_K}G^{KL}(\mathbf{Q})\,\rho_{KEO}\frac{\partial}{\partial Q_L} + V_{\text{extra}}(\mathbf{Q}) \qquad \textbf{Eq. 40}$$

$$d\tau = d\tau_{deformation}d\tau_{translation}d\tau_{rotation} = \rho_{KEO}(\mathbf{Q})dQ_1dQ_2\ldots dQ_{3N}$$

The expression of the KEO requires knowing the expressions of the Cartesian coordinates ($\boldsymbol{\mathcal{R}}$) as functions of the internal coordinates (**Q**); in other words one must compute the contravariant components of the mass-weighted metric tensor (i.e. $G^{KL}(\mathbf{Q})$). The volume element of translation is associated to the center of mass of the molecule and the volume element of rotation is involves the three Euler angles (α, β, γ) (defined in the previous section). The function $\rho_{KEO}(\mathbf{Q})$ is used to determine the normalization convention of the wave functions and can be changed for convenient reasons. It is often restricted to the $3N-6$ deformation coordinates only. When a non-Euclidian normalization convention is considered (i.e. when $\rho_{KEO}(\mathbf{Q})$ is not equal to the standard Jacobian determinant of the coordinate transformation), there may appear a function $V_{\text{extra}}(\mathbf{Q})$ called the extrapotential term. The explicit expression of this term with respect to the normalization convention can be found in Refs. [163,165].

The contravariant components of the mass-weighted metric tensor can be defined as

$$\mathbf{G}(\mathbf{Q}) = \mathbf{g}^{-1}(\mathbf{Q}) \qquad \textbf{Eq. 41}$$

where,

$$g_{KL}(\mathbf{Q}) = \sum_{I=1}^{3N} M_I \left(\frac{\partial \mathcal{R}^I(\mathbf{Q})}{\partial Q_K}\right)\left(\frac{\partial \mathcal{R}^I(\mathbf{Q})}{\partial Q_L}\right) \qquad \textbf{Eq. 42}$$

M_I is the atomic mass associated to the I^{th} coordinate. One should keep in mind that in a Cartesian frame each nuclear position is defined in space by three coordinates, hence, the various masses will appear three times (for three consecutive coordinates). For example, in a diatomic system AB at a given geometry, nucleus A is located in the framework by the position vector ($X_A = \mathcal{R}^1, Y_A = \mathcal{R}^2, Z_A = \mathcal{R}^3$) and equivalently for nucleus B ($X_B = \mathcal{R}^4, Y_B = \mathcal{R}^5, Z_B = \mathcal{R}^6$). Therefore, the mass associated to the first three Cartesian coordinates is the same (mass of A) and the same is true for the last three ones (mass of B). In other words, $M_1 = M_2 = M_3$ and $M_4 = M_5 = M_6$.

The calculation of the KEO (in particular of the matrix $\mathbf{G}(\mathbf{Q})$) has been automatized thanks to the development of the Tnum [165] and Tana [159,160] programs by Dr. David Lauvergnat and Dr. Mamadou Ndong from the Laboratoire de Chimie Physique d'Orsay, France. Tnum gives the numerical (but exact) values of the KEO at any point while Tana gives its analytical expression. A technical comment must be made here: we never used the total KEO (for the $3N$ coordinates: translations, rotations, and deformations) but a restriction of it, where we only took into account the $3N - 6$ degrees of freedom describing the deformations (separation of the translations and rotations) in the matrix $\mathbf{G}(\mathbf{Q})$. This separation is rigorous when assuming implicitly that the total angular momentum is zero ($J = 0$), which will be the case in all applications presented in this thesis.

As already mentioned, one of the main advantages of the polyspherical coordinate approach is that it is compatible with a general analytical expression of the KEO in "MCTDH format" using Tana. However, the KEO is not the only operator that must be

expressed to run quantum dynamics calculation. One needs to give an analytical expression of the potential energy surfaces (Section 2-3 Chapter I) and in the "MCTDH format" (i.e. sums of products of one-dimensional functions). The methodology we developed to generate potential energy surfaces automatically is exposed in this thesis. We sometimes had to change the set of original polyspherical coordinates to generate a new set from linear combinations of the former. Unfortunately, although this set of linear combinations of polyspherical coordinates will give an "MCTDH format" expression of the potential energy surfaces (discussed in Section 2-2 Chapter I), this is no longer the case for the KEO.

This last point can be illustrated with the following example. Let us consider the Jacobi coordinates (**Q**) of H-CN depicted in Fig. 6 [166–168].

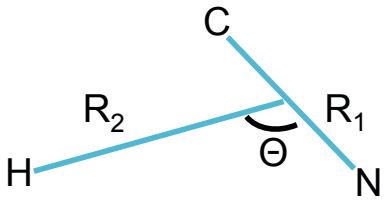

Fig. 6 Jacobi coordinates of H-CN

The deformation KEO with a non-Euclidean normalization convention reads [169],

$$\hat{T}_{deformation}(\mathbf{Q}) = -\frac{\hbar^2}{2M_1}\frac{\partial^2}{\partial {R_1}^2} - \frac{\hbar^2}{2M_2}\frac{\partial^2}{\partial {R_2}^2} - \frac{\hbar^2}{2}\left(\frac{1}{M_1 {R_1}^2} + \frac{1}{M_2 {R_2}^2}\right)\left(\frac{1}{sin\theta}\frac{\partial}{\partial\theta} sin\theta \frac{\partial}{\partial\theta}\right) \quad \textbf{Eq. 43}$$

$$d\tau_{deformation} = dR_1 dR_2 \sin\theta d\theta = \rho_{KEO}(\theta) dR_1 dR_2 d\theta$$

where $\rho_{KEO}(\theta) = \sin\theta$. One can notice that the KEO in **Eq. 43** is a sum of products of one-dimensional functions; hence, this is an "MCTDH format" KEO (in practice, for MCTDH, $\rho_{KEO}(\mathbf{Q})$ must be equal to one, which is achieving when using $u = \cos\theta$ instead of θ as a variable).

Symmetrized coordinates are often useful in situations where symmetry can be used to simplify the expression of the potential energy and of the KEO (there are fewer terms

because some "couplings" vanish for symmetry reasons). One can also want to consider linear combinations of coordinates for practical reasons (this will be the case in most applications treated in this thesis). Unfortunately, this often leads to a non-separable KEO. In the above example, if we consider the following linear combinations of the original set of Jacobi coordinates (note that this new set of coordinates may seem absurd to describe the physics of the problem but it just here to illustrate the above remark),

$$\begin{cases} R^+ = \frac{1}{2}(R_1 + R_2) \\ R^- = \frac{1}{2}(R_1 - R_2) \\ \theta' = \theta \end{cases} \qquad \textbf{Eq. 44}$$

the corresponding KEO reads (the new extrapotential term and volume element are also different, but this is not the point here),

$$\hat{T}_{deformation}(\mathbf{Q}) = \qquad \textbf{Eq. 45}$$
$$-\frac{\hbar^2}{2M_1}\frac{\partial^2}{\partial(R^+ + R^-)^2} - \frac{\hbar^2}{2M_2}\frac{\partial^2}{\partial(R^+ - R^-)^2}$$
$$-\frac{\hbar^2}{2}\left(\frac{1}{M_1(R^+ + R^-)^2} + \frac{1}{M_2(R^+ - R^-)^2}\right)\left(\frac{1}{sin\theta'}\frac{\partial}{\partial\theta'}sin\theta'\frac{\partial}{\partial\theta'}\right)$$
$$+ V'_{\text{extra}}(\mathbf{Q}).$$

This expression highlights the non-separability issue resulting from using linear combinations of coordinates: the last term, $\left(\frac{1}{M(R^+-R^-)^2} + \frac{1}{M(R^+-R^-)^2}\right)\left(\frac{1}{sin\theta'}\frac{\partial}{\partial\theta'}sin\theta'\frac{\partial}{\partial\theta'}\right)$, cannot be expressed as a sum of products of one-dimensional operators, in contrast with the first two terms. Therefore, this analytical expression of the KEO in this specific set of coordinates is not "MCTDH compatible" and cannot be used as it is for our quantum dynamics calculations. In that situation one must use a numerical KEO.

Let us now clarify another practical issue that has already been mentioned about why subsystems of polyspherical coordinates help avoiding singularities in the KEO. For example, terms in $\frac{1}{\sin\theta}$ (**Eq. 43**) induce singularities (divergences) when $\theta = 0$ or π, i.e. when vectors are parallel to the $\boldsymbol{z}$ axis of the frame in which θ is defined (BF or any

subsystem), [159]. Thus, subsystems allow us to change the parameterization of the polyspherical coordinates and reduce the possibility of occurrence of these singularities. However, for a large molecule, removing all possible singularities cannot always be achieved easily. This can be illustrated with the set of polyspherical coordinates used to study the dynamics of aminobenzonitrile already depicted in Fig. 5 and redepicted in the Fig. 7 for the sake of clarity. If no subsystem were used (i.e. $S_1 \equiv S_{BF}$ is the only subsystem), the $\mathbf{R_2^{(1,1)}}$ and $\mathbf{R_2^{(2,1)}}$ vectors would be parallel to the $\mathbf{R_1^{(1)}}$ vector (that defines the $\mathbf{z_{BF}}$ axis). Therefore, this will create singularities within the deformation KEO. In order to remove these singularities, two subsystems were created, $S_{1,1}$ and $S_{2,1}$, where $\mathbf{R_2^{(1,1)}}$ and $\mathbf{R_2^{(2,1)}}$ are no longer parallel to the $\mathbf{z}$ axes (of their respective subsystem) defined now by the $\mathbf{R_1^{(1,1)}}$ and $\mathbf{R_1^{(2,1)}}$ vectors. Nevertheless, one should notice that $\mathbf{R_3^{(1,1)}}$ and $\mathbf{R_4^{(1,1)}}$ in the $S_{1,1}$ subsystem are not parallel to $\mathbf{R_1^{(1,1)}}$ at the equilibrium geometry (represented in the Fig. 5 and used to compute the metric tensor of the KEO). Hence, those vectors at this given geometry are not problematic (do not create numerical singularities). However, during the dynamics of the molecule, one could expect in-plane bending motion of $\mathbf{R_3^{(1,1)}}$ or $\mathbf{R_4^{(1,1)}}$, such that those vectors could occur to become parallel to $\mathbf{R_1^{(1,1)}}$ ($\boldsymbol{z}$ axis of $S_{1,1}$), thus producing extra singularities in the KEO (one can make the same observation in the $S_{2,1}$ subsystem).

If so, a zero-approximation of the KEO calculated numerically at a given geometry with no singularity can be a practical solution that was used in the application cases treated in this present work.

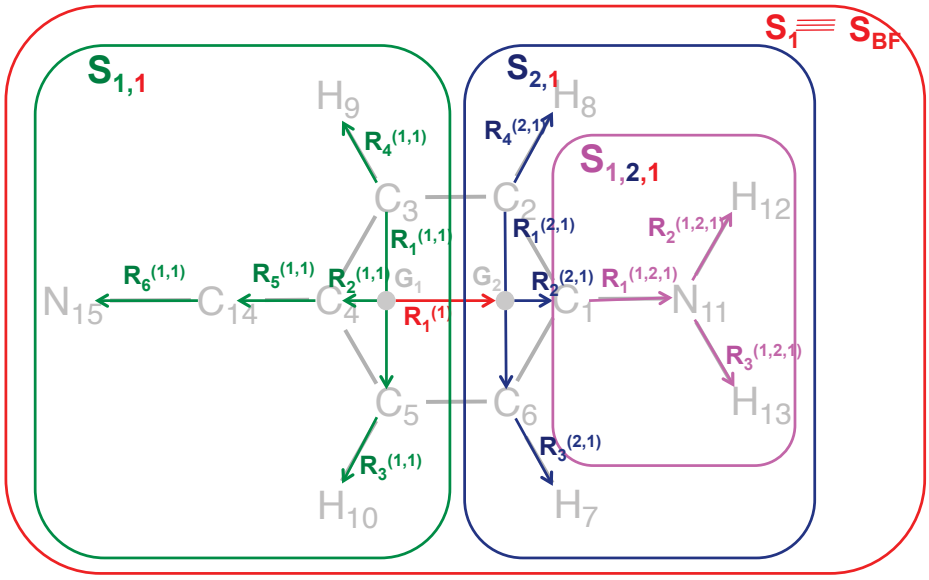

Fig. 7 Set of polyspherical coordinates and subsystems of aminobenzonitrile.

The numerical approach of the KEO in internal coordinate is well known [165,170–177] A possible approach for using a numerical KEO procedure consists in expressing the $\mathbf{G}(\mathbf{Q})$ matrix as a Taylor expansion around a given $\mathbf{Q}$ (terms can be computed up to second order with Tnum). In this thesis, we only used a zero-order approximation of $\mathbf{G}(\mathbf{Q})$ (note that it is "MCTDH compatible" by construction). In other words, the $\mathbf{G}$ matrix will be considered constant all over the coordinate grid. This approximation was made for the reasons mentioned above (linear combinations and singularities) and also to reduce the number of terms in the KEO. Indeed, in $\mathbf{G}(\mathbf{Q})$ up to second order there are about $\frac{(3N-6)^4}{4}$ terms while only $\frac{(3N-6)^2}{2}$ terms appear in the zero-order approximation, which reduces the computation time significantly. This was proved to be a decent approximation in previous studies [178].

2-3. Solving the Time-Dependent Schrödinger Equation

2-3-1- General Overview

The most direct way to solve the time-dependent Schrödinger equation is to expand the wave function into a direct-product basis and to solve the resulting equations of motion. An M-dimensional nuclear wave function, ψ^{nuclear}, is hence expanded as,

$$\psi^{\text{nuclear}}(Q_1,\ldots,Q_M,t)=\sum_{j_1=1}^{N_1}\ldots\sum_{j_M=1}^{N_M}C_{j_1,\ldots,j_M}(t)\prod_{K=1}^{M}\chi_{j_K}^{(K)}(Q_K) \qquad \textbf{Eq. 46}$$

with N_K the number of basis functions ($\chi_{j_K}^{(K)}$) per nuclear degree of freedom (Q_K) and $C_{j_1,\ldots,j_M}(t)$ the time-dependent coefficient of each nuclear configuration (a configuration being one of the M-dimensional products of one-dimensional functions that appear in this sum).

In order to fully understand the meaning of this equation (and the followings), we will apply them to a simple example: H_2O. If we choose a set of valence coordinates (both bonds lengths, i.e. R_1 and R_2, and the valence bending angle, i.e. θ), we have a three-dimensional nuclear wave function where $Q_1 = R_1$, $Q_2 = R_2$, and $Q_3 = \theta$ (as already mentioned, one should remember that technically within the "MCTDH format", we use the variable $u = \cos\theta$ instead of θ) (see Fig. 8).

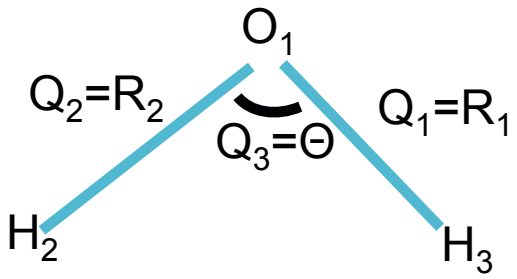

Fig. 8 Scheme of the triatomic system used as an illustrative example for this section.

Let us consider two basis functions per dimension. The corresponding 3-dimensional nuclear wave function of **Eq. 46** reads

$$\psi^{nuclear}(Q_1, Q_2, Q_3, t) \qquad \textbf{Eq. 47}$$

$$\begin{aligned}
&= C_{1,1,1}(t)\chi_1^{(1)}(Q_1)\chi_1^{(2)}(Q_2)\chi_1^{(3)}(Q_3) \\
&+ C_{1,1,2}(t)\chi_1^{(1)}(Q_1)\chi_1^{(2)}(Q_2)\chi_2^{(3)}(Q_3) \\
&+ C_{1,2,1}(t)\chi_1^{(1)}(Q_1)\chi_2^{(2)}(Q_2)\chi_1^{(3)}(Q_3) \\
&+ C_{1,2,2}(t)\chi_1^{(1)}(Q_1)\chi_2^{(2)}(Q_2)\chi_2^{(3)}(Q_3) \\
&+ C_{2,1,1}(t)\chi_2^{(1)}(Q_1)\chi_1^{(2)}(Q_2)\chi_1^{(3)}(Q_3) \\
&+ C_{2,1,2}(t)\chi_2^{(1)}(Q_1)\chi_1^{(2)}(Q_2)\chi_2^{(3)}(Q_3) \\
&+ C_{2,2,1}(t)\chi_2^{(1)}(Q_1)\chi_2^{(2)}(Q_2)\chi_1^{(3)}(Q_3) \\
&+ C_{2,2,2}(t)\chi_2^{(1)}(Q_1)\chi_2^{(2)}(Q_2)\chi_2^{(3)}(Q_3)
\end{aligned}$$

Each term of the sum is a nuclear configuration multiplied by a time-dependent coefficient and each configuration is equivalent to a Slater determinant in quantum chemistry. Hence, **Eq. 47** highlights that the nuclear wave function is a linear combination of all the possible nuclear configurations expanded in a given basis (later called primitive basis). At this point, a parallel can be made between quantum dynamics and quantum chemistry: the nuclear wave function written in **Eq. 46** (and **Eq. 47**) is somewhat equivalent to the full Configuration Interaction (full CI) expansion of an electronic wave function in a given basis. In this standard method (as in a full CI), the basis function coefficients (i.e. $C_{j_1,\ldots,j_M}(t)$) are optimized (according to the relevant variational principle, either time-dependent or time-independent) but not the basis functions themselves ($\chi_{j_K}^{(K)}$). Hence, one can rapidly have to use a large amount of basis functions to converge the nuclear wave function, which limits this approach to small systems (in general, no more than four atoms).

The solution of the time-dependent Schrödinger equation in a direct-product basis (primitive basis) scales exponentially (typically as N^M if $N_K = N$ is the number of primitive basis functions for each degree of freedom). In the MultiConfiguration Time-Dependent Hartree (MCTDH) method presented in the following, one introduces an optimal time-dependent basis for each degree of freedom. This new basis can be kept smaller than the primitive basis, leading to a better scaling of the number of nuclear

configurations. This feature makes the MCTDH method more efficient than the above-mentioned standard method.

2-3-2- *(MultiLayer) MultiConfiguration Time-Dependent Hartree*

The MCTDH method [31,179–182] has become over the last decade the tool of choice to accurately describe the dynamics of complex multidimensional quantum mechanical systems. Many successful applications have been achieved, dealing with molecular spectroscopy [183–186], photo-isomerization and Intramolecular Vibrational energy Redistribution (IVR) [187,188], inelastic and reactive scattering [189–192], and scattering of atoms or molecules at surfaces [190,193,194].

2-3-2-1- MCTDH Wave Function Ansatz

The principle of the MCTDH method is the use of the following wave function Ansatz to solve the time-dependent Schrödinger equation for a system with M degrees of freedom described with Q_M coordinates. The nuclear wave function is expanded in terms of time-dependent direct products of orthonormal time-dependent Single Particle Functions (SPFs), denoted $\varphi_{j_K}^{(K)}$, where both the coefficients and the basis functions are optimized (as in an MCSCF electronic wave function).

$$\psi^{\text{nuclear}}(Q_1,\dots,Q_M,t) = \sum_{j_1=1}^{n_1} \dots \sum_{j_M=1}^{n_M} A_{j_1,\dots,j_M}(t) \prod_{K=1}^{M} \varphi_{j_K}^{(K)}(Q_K,t) \qquad \textbf{Eq. 48}$$

The SPFs are themselves expanded in terms of primitive basis functions,

$$\varphi_{j_K}^{(K)}(Q_K,t) = \sum_{v_K=1}^{N_K} C_{j_K;v_K}^{(K)}(t)\, \chi_{v_K}^{(K)}(Q_K) \qquad \textbf{Eq. 49}$$

Therefore, MCTDH can be seen as a two-layer scheme with time-dependent coefficients: $A_{j_1,\dots,j_M}(t)$ at the top layer, and sets of second layer time-dependent coefficients $C_{j_K;v_K}^{(K)}(t)$

for each degree of freedom. We usually refer to the one-layer scheme as the standard method (primitive basis), to the two-layer scheme simply as MCTDH, and to deeper layering schemes as ML-MCTDH (more details about the latter method are given in the following).

Let us apply this MCTDH Ansatz, to the previous three-dimensional example. Here, for the sake of clarity, we consider one SPF basis function per coordinate and keeping two primitive basis functions per dimensions; this particular situation corresponds to a single configuration, i.e. to the Time-Dependent Hartree method (TDH) also called the Time-Dependent SCF method (TDSCF) [195–199] and MCTDH is its multiconfigurational extension (more than one SPF, which yields more than one configuration). The corresponding nuclear wave function expanded in the SPF basis reads (note that when there are more than one SPF basis function the way to handle the coefficients is similar to **Eq. 47**)

$$\psi^{\text{nuclear}}(Q_1, Q_2, Q_3, t) = A_{1,1,1}(t)\varphi_1^{(1)}(Q_1, t)\varphi_1^{(2)}(Q_2, t)\varphi_1^{(3)}(Q_3, t) \qquad \textbf{Eq. 50}$$

The SPFs are in turn expanded in the primitive basis with time-dependent coefficients. For example, for a two-function basis, we get

$$\varphi_1^{(1)}(Q_1, t) = C_{1;1}^{(1)}(t)\chi_1^{(1)}(Q_1) + C_{1;2}^{(1)}(t)\chi_2^{(1)}(Q_1) \qquad \textbf{Eq. 51}$$

$$\varphi_1^{(2)}(Q_2, t) = C_{1;1}^{(2)}(t)\chi_1^{(2)}(Q_2) + C_{1;2}^{(2)}(t)\chi_2^{(2)}(Q_2)$$

$$\varphi_1^{(3)}(Q_3, t) = C_{1;1}^{(3)}(t)\chi_1^{(3)}(Q_3) + C_{1;2}^{(3)}(t)\chi_2^{(3)}(Q_3)$$

The computational gain of MCTDH with respect to the standard method (presented in the previous section) arises from the expansion orders, n_K, being in general smaller than the size of the primitive basis N_K, which leads to a smaller number of configurations, hence a smaller number of time-dependent coefficients to be propagated. However, the total number of time-dependent coefficients is given by $\prod_{K=1}^{M} n_K$, and therefore the computational effort still rises exponentially with the number of degrees of freedom.

Thus, MCTDH does not eliminate the exponential scaling but reduces the size of the basis over which the scaling occurs.

The size of the SPF basis can be further reduced by combining the physical coordinates $Q_1, \ldots, Q_M$ into logical coordinates (also called combined modes) $Q_1^1, \ldots, Q_P^1$, such that each logical coordinate comprises one or several of the physical coordinates, as $Q_K^1 = \{Q_{1_K}, \ldots, Q_{d_K}\}$. The superscript 1 in the notation represents the layer number of the combined modes (notation introduced to facilitate the multilayer formulation expressed in the following).

The MCTDH nuclear wave function with combined modes reads

$$\psi^{\text{nuclear}}(Q_1^1, \ldots, Q_P^1, t) = \sum_{j_1=1}^{n_1} \ldots \sum_{j_P=1}^{n_P} A_{1;j_1,\ldots,j_P}^1(t) \prod_{K=1}^{P} \varphi_{j_K}^{(1;K)}(Q_K^1, t) \qquad \textbf{Eq. 52}$$

The time-dependent basis functions $\varphi_{j_K}^{(1;K)}$ is now multidimensional. Introducing mode combination implies that the computational effort is transferred from the propagation of a large vector of $A_{1;j_1,\ldots,j_P}^1(t)$ coefficients with one-dimensional SPFs, to a shorter vector of coefficients but multidimensional SPFs. Some experience and knowledge of the system under study is required to find an efficient mode-combination scheme for the study. For example, combining modes with similar frequencies is a possible strategy, as shown by O. Vendrell et al. [200].

The mode-combined SPFs expressed in the primitive basis are given by,

$$\varphi_{j_K}^{(1;K)}(Q_K^1, t) = \sum_{v_{1_K}}^{N_{1_K}} \ldots \sum_{v_{d_K}}^{N_{d_K}} C_{j_K;v_{1_K}\ldots v_{d_K}}^{(2;K)}(t) \prod_{i=1}^{d_K} \chi_{v_{i_K}}^{(K,i_K)}(Q_{i_K}) \qquad \textbf{Eq. 53}$$

Let us apply this MCTDH Ansatz with combined modes to the previous three-dimensional example. First, we consider one SPF basis function per combined mode. They are defined as $Q_1^1 = \{Q_1, Q_2\}$ and $Q_2^1 = \{Q_3\}$. Q_1 and Q_2 are combined together as they are both bond lengths of the triatomic molecule (see Fig. 8) and Q_3 represent the

valence in-plane angle. The corresponding nuclear wave function expanded in the SPF basis reads

$$\psi^{\text{nuclear}}(Q_1^1, Q_2^1, t) = A_{1;11}^1(t)\varphi_1^{(1;1)}(Q_1^1, t)\varphi_1^{(1;2)}(Q_2^1, t) \qquad \textbf{Eq. 54}$$

Expressing the SPFs in a two- function primitive basis, we get

$$\begin{aligned}\varphi_1^{(1;1)}(Q_1^1, t) = {} & C_{1;11}^{(2,1)}(t)\chi_1^{(1;1)}(Q_1)\chi_1^{(1;2)}(Q_2) + C_{1;12}^{(2;1)}(t)\chi_1^{(1;1)}(Q_1)\chi_2^{(1;2)}(Q_2) \\ & + C_{1;21}^{(2;1)}(t)\chi_2^{(1;1)}(Q_1)\chi_1^{(1;2)}(Q_2) + C_{1;22}^{(2;1)}(t)\chi_2^{(1;1)}(Q_1)\chi_2^{(1;2)}(Q_2)\end{aligned} \qquad \textbf{Eq. 55}$$

$$\varphi_1^{(1;2)}(Q_2^1, t) = C_{1;1}^{(2,2)}(t).\chi_1^{(1;3)}(Q_3) + C_{1;2}^{(2,2)}(t).\chi_2^{(1;3)}(Q_3)$$

As already mentioned, the MCTDH method can be seen as a two-layer scheme: one layer of time-dependent SPF functions decomposed directly into a time-independent primitive basis. The multi-layer MCTDH method, which we present in the following, is an extension of the combined-mode MCTDH method expressed by **Eq. 52** and Eq. 53, which is capable to propagate the nuclear wave functions of high dimensional systems (more than ten degrees of freedom) upon adding more time-dependent layers of SPF functions.

2-3-2-2- ML-MCTDH General Principal

In a high-dimensional system one should combine groups of degrees of freedom into high-dimensional SPFs in order to make the size of the vector of coefficients in **Eq. 52** manageable (i.e. to get a wave function propagation that is reasonable in terms of computation time). However, the combined SPFs are too large to be efficiently propagated. The ML-MCTDH layering scheme is a very flexible way of dealing with this issue. One treats the combined mode as a “sub-configuration” involving smaller groups of logical coordinates. This introduces a new layer of coefficients, whose size is manageable. The procedure can be repeated over and over until the primitive degrees of freedom are reached.

The general mathematical expression of the ML-MCTDH method is very complicated at first sight due to the flexibility regarding the amount of layers that one can use to express the nuclear wave function. Here, we will apply directly the general principal of the ML-MCTDH method to the three-dimensional system that we have used as an example since the beginning of this section, with one SPF per layer and per combined mode. This will give a concrete insight into the ML-MCTDH formulation with respect to the MCTDH Ansatz with combined mode given in **Eq. 52** and Eq. 53.

First, we will express the nuclear wave function into a three-layer scheme. In addition we consider one SPF basis function per combined mode defined as $\mathrm{Q}_1^1 = \{\mathrm{Q}_1^2, \mathrm{Q}_2^2\}$ and $\mathrm{Q}_2^1 = \{\mathrm{Q}_3^2\}$. $\mathrm{Q}_1^2, \mathrm{Q}_2^2$, and Q_3^2 are the second-layer combined modes. The corresponding nuclear wave function expanded in the first layer SPF basis functions reads

$$\psi^{\mathrm{nuclear}}(Q_1^1, Q_2^1, t) = A_{1;11}^1(t)\varphi_1^{(1;1)}(Q_1^1, t)\varphi_1^{(1;2)}(Q_2^1, t) \qquad \textbf{Eq. 56}$$

Where the first-layer time-dependent SPFs are expressed into a second layer of time-dependent SPF basis with one SPF basis function per mode, which reads

$$\varphi_1^{(1;1)}(Q_1^1, t) = A_{1;11}^{(2,1)}(t).\varphi_1^{(2;1)}(Q_1^2, t).\varphi_1^{(2;2)}(Q_2^2, t) \qquad \textbf{Eq. 57}$$

$$\varphi_1^{(1;2)}(Q_2^1, t) = A_{1;11}^{(2,2)}(t).\varphi_1^{(2;3)}(Q_3^2, t)$$

This second layer of time-dependent SPF basis is decomposed over the primitive basis on a third layer with two primitive basis functions per mode. Note that $\mathrm{Q}_1^2, \mathrm{Q}_2^2$, and Q_3^2 could, in principle, be second-layer combined modes but in this example they identify to the physical coordinates: $\mathrm{Q}_1^2 = \{\mathrm{Q}_1\}, \mathrm{Q}_2^2 = \{\mathrm{Q}_2\}$, and $\mathrm{Q}_3^2 = \{\mathrm{Q}_3\}$. Thus, this second layer expressed in terms of primitive basis functions (third layer) reads

$$\varphi_1^{(2;1)}(Q_1^2, t) = C_{1;1}^{(3,1)}(t)\chi_1^{(3;1)}(Q_1) + C_{1;2}^{(3;1)}(t)\chi_2^{(3;1)}(Q_1) \qquad \textbf{Eq. 58}$$

$$\varphi_1^{(2;2)}(Q_2^2, t) = C_{2;1}^{(3,2)}(t)\chi_1^{(3;2)}(Q_2) + C_{2;2}^{(3;2)}(t)\chi_2^{(3;2)}(Q_2)$$

$$\varphi_1^{(2;3)}(Q_3^2, t) = C_{1;1}^{(3,3)}(t)\chi_1^{(3;3)}(Q_3) + C_{1;2}^{(3;3)}(t)\chi_2^{(3;3)}(Q_3)$$

One can notice in this specific example that in the ML-MCTDH formulation there is one layer more than in the MCTDH method. However, one must keep in mind that the number of layers in the ML-MCTDH formulation can be larger than in this example.

Owing to the flexibility of the layering scheme and to the fact that ML-MCTDH wave functions can be "many-layer deep", it is convenient to introduce a diagrammatic notation to represent them, such as in Fig. 9 for our specific example [201]. In this notation the nuclear wave function is represented by a "tree". Each node (circle) in the tree represents a set of vectors of coefficients for SPF basis functions. The final squares correspond to the primitive basis functions and the physical coordinates.

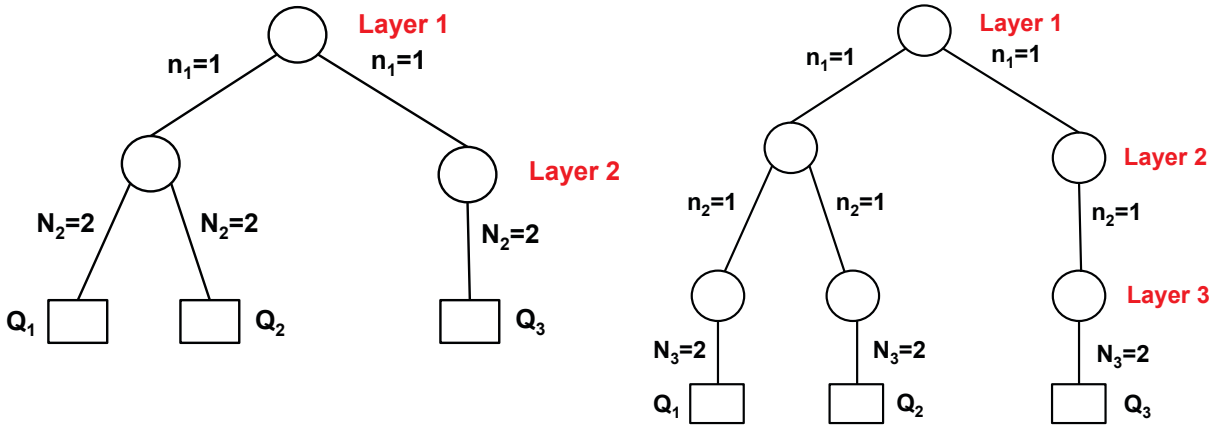

Fig. 9 Tree structure for the MCTDH and ML-MCTDH nuclear wave function of the three-dimensional system used as example. Left: MCTDH nuclear wave function tree, in which the coordinates are combined (N_2 refer in this particular case to the numbers of primitive basis functions and n_1 to the numbers of SPF basis functions). Right: ML-MCTDH tree (n_1 and n_2 are the numbers of SPF basis functions and N_3 represent the numbers of primitive basis functions).

As seen on Fig. 9, the ML-MCTDH tree of our three-dimensional system is composed of two layers of nodes that picture the two layers of time-dependent SPF functions and one layer of squares for the primitive basis. This representation of the wave function gives: the number of basis functions used for each mode in each layer and the combination of modes at each stage. This figure gives a direct insight into the difference between the

MCTDH and the ML-MCTDH formulations beyond two layers. While MCTDH will always have two layers, the number of layers with ML-MCTDH is let to the user choice.

The ML-MCTDH method is helpful when the number of degrees of freedom is large (48 and 39 dimensions in this thesis). However, this raises another issue: choosing the ML-tree can become a tedious task but it is a key step that can make the calculation possible or not (in terms of computation time) [200,202,203]. For example, for 3-hydroxychromone (Chapter III), with the same number of SPF basis functions and the same set of coordinates, an ML-tree chosen randomly made the relaxation calculation take 546 hours against 10 hours with a well-chosen ML-tree. However, we did not focus on automatizing the methodology to optimize the ML-tree. Our strategy was to combine coordinates that are the most coupled to each other in the ground state; in other words, we combined coordinates that correspond to large values of the off-diagonal elements in the ground-state Hessian at the minimum. This analysis "by hand" was helped also with some physical intuition (for example, avoiding to combine in-plane coordinates with out-of-plane ones). We chose to use the ground state Hessian in order to reduce the computation time of the nuclear wave function relaxation (i.e. generation of the initial wave function). Indeed, the generation of the initial wave function in the ground state takes more time than propagating it on the reactive potential energy surfaces. This is due to some technical limitations within the ML-MCTDH code that is currently in development, such as the impossibility to restart a calculation from a previous nuclear wave function converged with a different number of SPF basis functions.

One of the other parameters that have to be determined by the user is the number of SPF basis functions to reach convergence within some tolerance threshold. In the ML-MCTDH formulation, one must use a large number of SPF basis functions to converge the initial nuclear wave function [200,204]. However, increasing it will increase the time of the calculation; for example in 3-hydroxychromone with the same ML-tree and the same set of coordinates, increasing the number of SPF basis functions by a factor two for each mode and layer increased the time of the relaxation by a factor 2.5. Relaxing to a very accurate wave function can easily become too much time consuming. Hence, one must often make a compromise between computation time and level of convergence for the initial nuclear wave function. This depends on the purpose of the study. In this thesis, we

used quantum dynamics calculations to investigate the mechanisms of photochemical reactions, specifically in non-adiabatic regions (i.e. conical intersection regions). Our purpose was to obtain relevant information about the nuclear motion (what are the relevant regions for the mechanism and how fast are they accessed) and about the transfers of electronic population through internal conversion, but not to compute high-resolution spectra that require a very accurate description of the vibrational levels of the molecule. Therefore, the initial wave packet can be less accurate (converged within 10^{-1}-10^{-2} eV) than for computing an infrared spectrum for example (converged within 10^{-4}-10^{-6} eV).

Chapter II- Quasidiabatic Model

One of the main focuses of this thesis is to develop a systematic methodology, as automatic as possible, to generate non-adiabatically coupled potential energy surfaces in full dimensionality to be used in quantum dynamics calculations in order to investigate photochemical processes in large molecules efficiently and with no reduction of dimensionality.

The first part of this chapter addresses the formalism of the vibronic coupling Hamiltonian model and how our analytical potential energy surface models are built from explicit relationships between the adiabatic data at a regular point and at a conical intersection. One should notice that some of the underlying formalism has already been presented in the previous chapter; however, we mention some useful expressions again in the present chapter for the sake of clarity. The second part is focused on how to map the ab-initio data with the model parameters. A third part will regard the methodology that we specifically developed to treat more difficult cases where anharmonicity plays a significant role or when several conical intersections must be considered together.

I. Introduction

Our strategy is based on the well-known Vibronic-Coupling Hamiltonian (VCH) model [20,110–112] that we briefly mentioned in the previous Chapter (Chapter I). We extended it in a similar fashion to the developments previously carried out in Montpellier by Loïc Joubert-Doriol and Joaquim Jornet-Somoza [205–207].
The originality of the present work is to avoid being dimension (number of nuclear degrees of freedom) dependent. In other words, we do not want a methodology where the dimensionality of the system is the limiting step. In contrast, in a fitting procedure (usually used to obtain the parameters of the model) the number of parameters to be fitted explodes with the dimensionality of the system (e.g. for a 12-dimensional system in a two-state problem, if one uses a fourth-order polynomial expression for the PESs and a linear expression (first-order polynomial expression) for the electronic coupling the number of parameters required is 1924 [208]).

To achieve this purpose, we established fully analytical relationships between the Hamiltonian matrices and their derivatives represented in both the quasidiabatic basis (to be generated for quantum dynamics) and the adiabatic basis (obtained from quantum chemistry). Therefore, once the required quantum chemistry calculations are made, the production of the quasidiabatic potential energy surfaces parameters is automatic and immediate upon using the PAnDA (Potentiel Analytique Diabatique Adiabatique) program developed during this thesis (Fig. 10).

The philosophy of PAnDA is summarized below in Fig. 10. Further details will be provided in the section called mapping. The input data are obtained from ab-initio calculations and transformed into parameters used for building the quasidiabatic electronic Hamiltonian, which is the output. The data of the conical intersection are involved in the generation of the gradient of the electronic coupling (1 in Fig. 10) while the data of the minima and the electronic coupling are used to generate the Hessians of the quasidiabatic potential energy surfaces (2 in Fig. 10). The description of complicated shapes of some potential energy surfaces will require modifications of the general vibronic coupling Hamiltonian model along specific directions (6 and 7 in Fig. 10) and the definition of additional parameters. The different strategies developed to achieve

this purpose are detailed further along this section. Then, once all the parameters of the models are obtained one can generate the analytical expression of the vibronic coupling Hamiltonian model, i.e. the multidimensional coupled potential energy surfaces to be used to run quantum dynamics calculations with the ML-MCTDH method.

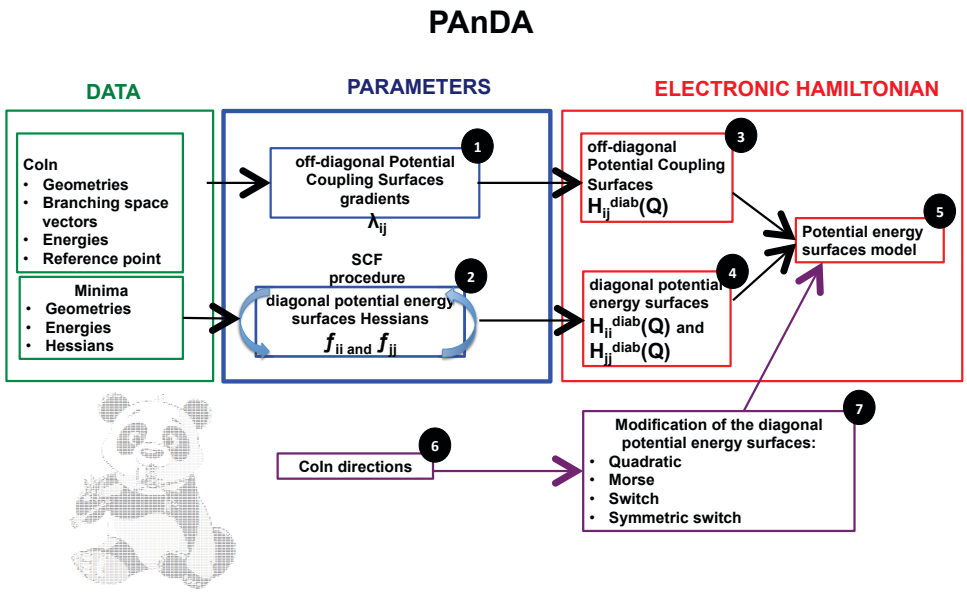

Fig. 10 Scheme of PAnDA philosophy.

II. Vibronic-Coupling Hamiltonian Model

As already defined in the previous chapter, the effective quasidiabatic electronic states (i.e. Φ_i) used in our Vibronic-Coupling Hamiltonian (VCH) model are assumed real-valued. The matrix representation of the electronic Hamiltonian in the quasidiabatic basis set,

$$H_{ij}^{\mathrm{diab}}(\mathbf{Q}) = \left\langle \Phi_i; \mathbf{Q} \middle| \widehat{H}^{\mathrm{elec}}(\mathbf{Q}) \middle| \Phi_j; \mathbf{Q} \right\rangle \qquad \textbf{Eq. 59}$$

is thus real-valued and symmetric. Here, we specifically use a set of curvilinear coordinates denoted $\mathbf{Q}$.

The diagonal potential energy surfaces are approximated by quadratic forms with minima at $\mathbf{Q} = \mathbf{Q}_{ii}$, where by definition the first order (gradient) is zero.

$$H_{ii}^{\text{diab}}(\mathbf{Q}) = e_{ii} + \frac{1}{2}\sum_{M}\sum_{L}(Q^M - Q_{ii}^M) f_{ii}^{ML}(Q^L - Q_{ii}^L) \qquad \textbf{Eq. 60}$$

The Hessian matrices, $\boldsymbol{f}_{ii}$, are symmetric with respect to the coordinate indices, *M* and *L*.

The off-diagonal Potential Coupling Surfaces (PCS) are considered as linear forms with zeros at $\mathbf{Q} = \mathbf{Q}_{ij}$ (crossing geometries),

$$H_{ij}^{\text{diab}}(\mathbf{Q}) = H_{ji}^{\text{diab}}(\mathbf{Q}) = \sum_{M}\left(Q^M - Q_{ij}^M\right)\lambda_{ij}^M \qquad \textbf{Eq. 61}$$

for $i \neq j$ (note that $Q_{ij}^M = Q_{ji}^M$ and $\lambda_{ij}^M = \lambda_{ji}^M$).

$H_{ij}^{diab}(\mathbf{Q})$ vanishes when $\mathbf{Q} - \mathbf{Q}_{ij}$ is perpendicular to $\boldsymbol{\lambda}_{ij}$, i.e. for all $\mathbf{Q}$ that belong to a hyperplane containing $\mathbf{Q}_{ij}$ and perpendicular to $\boldsymbol{\lambda}_{ij}$. Additional conditions will be provided later on.

The quasidiabatic gradients read,

$$\frac{\partial H_{ii}^{\text{diab}}(\mathbf{Q})}{\partial Q^M} = \sum_{L} f_{ii}^{ML}\,(Q^L - Q_{ii}^L) \qquad \textbf{Eq. 62}$$

and, for $i \neq j$,

$$\frac{\partial H_{ij}^{\text{diab}}(\mathbf{Q})}{\partial Q^M} = \lambda_{ij}^M \qquad \textbf{Eq. 63}$$

The quasidiabatic second derivatives are constant,

$$\frac{\partial^2 H_{ii}^{\text{diab}}(\mathbf{Q})}{\partial Q^M \partial Q^L} = f_{ii}^{ML} \qquad \textbf{Eq. 64}$$

and, for $i \neq j$,

$$\frac{\partial^2 H_{ij}^{\text{diab}}(\mathbf{Q})}{\partial Q^M \partial Q^L} = 0 \qquad \textbf{Eq. 65}$$

1. Adiabatic Data at a Regular Point

The adiabatic electronic states (i.e. Ψ_α) are the eigenstates of the electronic Hamiltonian and thus satisfy

$$\left\langle \Psi_\alpha; \boldsymbol{\mathcal{R}} \middle| \widehat{H}^{\text{elec}}(\boldsymbol{\mathcal{R}}) \middle| \Psi_\beta; \boldsymbol{\mathcal{R}} \right\rangle = V_\alpha(\boldsymbol{\mathcal{R}}) \delta_{\alpha\beta}.$$

where $\boldsymbol{\mathcal{R}}$ denote the Cartesian coordinates of the nuclei.

The non-adiabatic coupling vectors are defined as (see **Eq. 9**)

$$D_{\alpha\beta}^I(\boldsymbol{\mathcal{R}}) = \left\langle \Psi_\alpha; \boldsymbol{\mathcal{R}} \middle| \frac{\partial}{\partial \mathcal{R}^I} \Psi_\beta; \boldsymbol{\mathcal{R}} \right\rangle. \qquad \textbf{Eq. 66}$$

In what follows, we assume differentiability of the adiabatic states with respect to the nuclear coordinates (in particular, we are at a geometry that is not the locus of any degeneracy, i.e. $\boldsymbol{\mathcal{R}} \neq \boldsymbol{\mathcal{R}_0}$), such that the non-adiabatic coupling vectors are regular. The twofold-degenerate case of a conical intersection between two states will be treated below in Section 2.

For the sake of clarity, let us recall here the Hellmann-Feynman theorems (diagonal and off-diagonal) [89] (see Chapter I): the adiabatic gradients and non-adiabatic coupling vectors satisfy,

$$\frac{\partial V_\alpha(\boldsymbol{\mathcal{R}})}{\partial \mathcal{R}^I} = \left\langle \Psi_\alpha; \boldsymbol{\mathcal{R}} \middle| \frac{\partial \widehat{H}^{\text{elec}}(\boldsymbol{\mathcal{R}})}{\partial \mathcal{R}^I} \middle| \Psi_\alpha; \boldsymbol{\mathcal{R}} \right\rangle, \qquad \textbf{Eq. 67}$$

and, for $\alpha \neq \beta$,

$$D^I_{\alpha\beta}(\boldsymbol{\mathcal{R}}) = \frac{\left\langle \Psi_\alpha;\boldsymbol{\mathcal{R}} \middle| \frac{\partial \widehat{H}^{\text{elec}}(\boldsymbol{\mathcal{R}})}{\partial \mathcal{R}^I} \middle| \Psi_\beta;\boldsymbol{\mathcal{R}} \right\rangle}{V_\beta(\boldsymbol{\mathcal{R}}) - V_\alpha(\boldsymbol{\mathcal{R}})} \qquad \textbf{Eq. 68}$$

The numerators are called derivative coupling vectors.

Similarly, the adiabatic Hessians read,

$$\frac{\partial^2 V_\alpha(\boldsymbol{\mathcal{R}})}{\partial \mathcal{R}^I \partial \mathcal{R}^J} = \left\langle \Psi_\alpha;\boldsymbol{\mathcal{R}} \middle| \frac{\partial^2 \widehat{H}^{\text{elec}}(\boldsymbol{\mathcal{R}})}{\partial \mathcal{R}^I \partial \mathcal{R}^J} \middle| \Psi_\alpha;\boldsymbol{\mathcal{R}} \right\rangle - 2\Re \sum_{\beta\neq\alpha} \left[V_\alpha(\boldsymbol{\mathcal{R}}) - V_\beta(\boldsymbol{\mathcal{R}})\right] D^I_{\alpha\beta}(\boldsymbol{\mathcal{R}}) D^J_{\beta\alpha}(\boldsymbol{\mathcal{R}}), \qquad \textbf{Eq. 69}$$

or, equivalently,

$$\frac{\partial^2 V_\alpha(\boldsymbol{\mathcal{R}})}{\partial \mathcal{R}^I \partial \mathcal{R}^J} = \left\langle \Psi_\alpha;\boldsymbol{\mathcal{R}} \middle| \frac{\partial^2 \widehat{H}^{\text{elec}}(\boldsymbol{\mathcal{R}})}{\partial \mathcal{R}^I \partial \mathcal{R}^J} \middle| \Psi_\alpha;\boldsymbol{\mathcal{R}} \right\rangle - 2\Re \sum_{\beta\neq\alpha} \frac{\left\langle \Psi_\alpha;\boldsymbol{\mathcal{R}} \middle| \frac{\partial \widehat{H}^{\text{elec}}(\boldsymbol{\mathcal{R}})}{\partial \mathcal{R}^I} \middle| \Psi_\beta;\boldsymbol{\mathcal{R}} \right\rangle \left\langle \Psi_\beta;\boldsymbol{\mathcal{R}} \middle| \frac{\partial \widehat{H}^{\text{elec}}(\boldsymbol{\mathcal{R}})}{\partial \mathcal{R}^J} \middle| \Psi_\alpha;\boldsymbol{\mathcal{R}} \right\rangle}{V_\beta(\boldsymbol{\mathcal{R}}) - V_\alpha(\boldsymbol{\mathcal{R}})} \qquad \textbf{Eq. 70}$$

which is a manifestation of what is called second-order Jahn-Teller effect [209–212] (i.e. the effect of the non-adiabatic coupling on the curvature of the potential energy surface).

2. Adiabatic Data at a Conical Intersection

Let us now consider the case of a conical intersection between two adiabatic potential energy surface, $V_\alpha(\boldsymbol{\mathcal{R}})$ and $V_\beta(\boldsymbol{\mathcal{R}})$, at $\boldsymbol{\mathcal{R}} = \boldsymbol{\mathcal{R}}_\mathbf{0}$ where $V_\alpha(\boldsymbol{\mathcal{R}}_\mathbf{0}) = V_\beta(\boldsymbol{\mathcal{R}}_\mathbf{0})$. The corresponding formalism has been exposed in Chapter I but let us recall here some relationships that are relevant in the present context. As already mentioned, two degenerate eigenstates are determined only up to an arbitrary mixing angle $\theta_{\alpha\beta}$ (and, as usual, up to an arbitrary complex phase for each, which is irrelevant here). We will denote them $\left|\Psi_\alpha^{\theta_{\alpha\beta}};\boldsymbol{\mathcal{R}}_\mathbf{0}\right\rangle$ and $\left|\Psi_\beta^{\theta_{\alpha\beta}};\boldsymbol{\mathcal{R}}_\mathbf{0}\right\rangle$ in what follows; they will be assumed real an

orthogonal. In practice, $\theta_{\alpha\beta} = 0$ can be attributed to the states actually calculated in quantum chemistry, $|\Psi_\alpha^0; \boldsymbol{\mathcal{R}_0}\rangle$ and $|\Psi_\beta^0; \boldsymbol{\mathcal{R}_0}\rangle$. From the latter, we can produce the gradient-half-difference (GD) vector (tuning mode), $\boldsymbol{x}^{0(\alpha\beta)1}$, and the DC vector (coupling mode), $\boldsymbol{x}^{0(\alpha\beta)2}$. Both span the Branching Space (BS), i.e. the plane over which degeneracy is lifted to first order. If now one considers a pair of rotated states, $|\Psi_\alpha^{\theta_{\alpha\beta}}; \boldsymbol{\mathcal{R}_0}\rangle$ and $|\Psi_\beta^{\theta_{\alpha\beta}}; \boldsymbol{\mathcal{R}_0}\rangle$, we get

$$x_I^{\theta_{\alpha\beta}(\alpha\beta)1} = \cos 2\theta_{\alpha\beta}\, x_I^{0(\alpha\beta)1} - \sin 2\theta_{\alpha\beta}\; x_I^{0(\alpha\beta)2}, \qquad \textbf{Eq. 71}$$

$$x_I^{\theta_{\alpha\beta}(\alpha\beta)2} = \sin 2\theta_{\alpha\beta}\, x_I^{0(\alpha\beta)1} + \cos 2\theta_{\alpha\beta}\; x_I^{0(\alpha\beta)2}. \qquad \textbf{Eq. 72}$$

The GD and DC vectors rotate within this plane through an angle $-2\theta_{\alpha\beta}$ and are thus also determined only up to an arbitrary angle in principle. It is to be understood that these quantities are well defined in practice because actual calculations are based on well-determined states (those for which we have defined $\theta_{\alpha\beta} = 0$). We will show later that setting a convenient value to this angle can help when generating the quasidiabatic model from the adiabatic data. Also, note that the GD vector is sometimes defined in the literature as the actual gradient difference (i.e., not halved).

III. Mapping

In our vibronic coupling Hamiltonian model, we consider two interacting real-valued quasidiabatic states (1, 2) assumed to form a complete basis set with respect to the two adiabatic states (S_0, S_1) at any point**.** Our objective is to map the quasidiabatic parameters to adiabatic data produced by quantum-chemical calculations (using various methods such as CASSCF or TD-DFT). To this end, we consider the off-diagonal potential couplings between pairs of states for which a conical intersection occurs along the photoreaction coordinate. We make a particular choice of quasidiabatic states: we assume that they nearly coincide with some particular adiabatic states at three selected points along the schematic interpolation pathway shown on Fig. 11. (In fact, they are

chosen to strictly coincide at the crossing point). This last comment will be enlightened in the following.

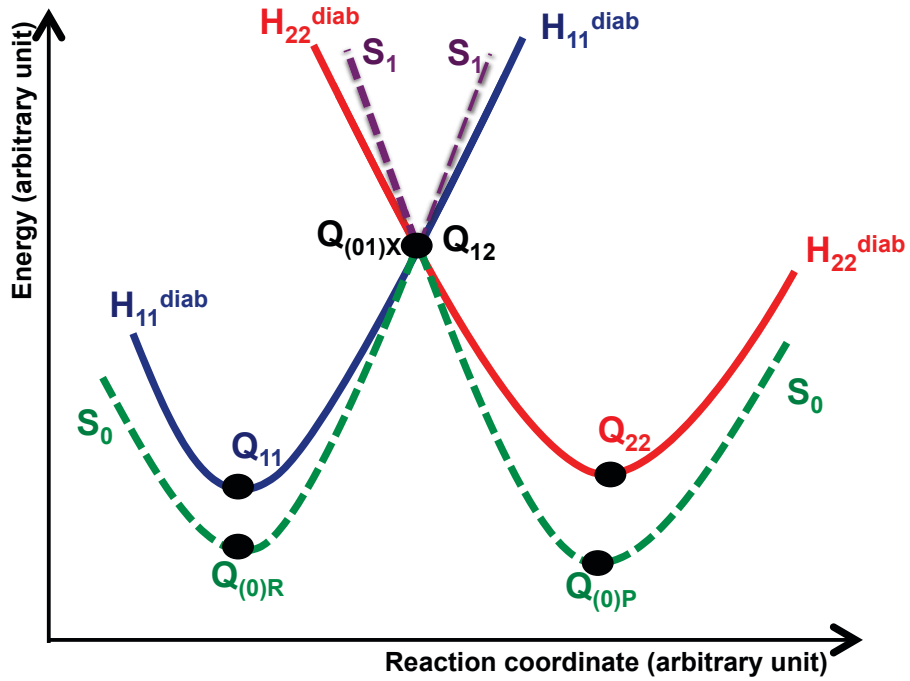

Fig. 11. Scheme illustrating the coincidence of the quasidiabatic and adiabatic representations at a conical intersection. Dashed lines: adiabatic potential energy surfaces. Plain lines: diagonal quasidiabatic potential energy surfaces.

1. Parameters and Data

We recall here that the quasidiabatic model is expressed in terms of internal nuclear coordinates, **Q** (we will reserve indices M and L for them). For $n = (3N - 6)$, the number of quasidiabatic parameters in our model is thus:

- $3n$ nuclear coordinates: $Q_{11}^L, Q_{22}^L, Q_{12}^L$. ($n$ coordinates per particular point we selected: one particular point per quasidiabatic state and one point for the conical intersection);
- 2 energies: e_{11}, e_{22} (one energy per quasidiabatic states);
- n off-diagonal (coupling) gradient components: λ_{12}^L (one off-diagonal gradient per conical intersection);

- $2\ \frac{n(n+1)}{2}$ Hessian components: f_{11}^{ML}, f_{22}^{ML} (one Hessian per quasidiabatic states).

Note that there is an irrelevant parameter, as the energy origin is an arbitrary offset (e.g., $e_{11} = 0$).

Our objective is to establish a direct mapping based on the same number of adiabatic data. A possibility is to use the following adiabatic data obtained from quantum chemistry calculations:

- geometries: $\mathcal{R}_{(0)R}^{I}, \mathcal{R}_{(0)P}^{I}, \mathcal{R}_{(01)X}^{I}$ (optimized geometries of both S_0 minima on the reactant and product sides, and the most relevant S_0/S_1 conical intersection for the problem under study, respectively);
- energies: $V_0(\boldsymbol{\mathcal{R}}_{(0)R}), V_0(\boldsymbol{\mathcal{R}}_{(0)P})$ (of the optimized geometries of the two S_0 minima, reactant and product, respectively);
- branching space vectors: $x_I^{0(01)1}, x_I^{0(01)2}$ (calculated at the S_0/S_1 conical intersection mentioned above);
- Hessians: $\frac{\partial^2 V_0\ \left(\boldsymbol{\mathcal{R}}_{(0)R}\right)}{\partial \mathcal{R}^I \partial \mathcal{R}^J}, \frac{\partial^2 V_0\ \left(\boldsymbol{\mathcal{R}}_{(0)P}\right)}{\partial \mathcal{R}^I \partial \mathcal{R}^J}$ (calculated at the optimized geometries of the two S_0 minima, reactant and product, respectively).

Note that the BS vectors are calculated with analytic gradient techniques when possible (this is the case for CASSCF wavefunctions). However, they are not available in all quantum chemistry methods, for example TD-DFT (used to study 3-HC derivatives in Chapter III). In the latter situation, we had to develop a numerical method to obtain them (see Appendix B).

An important remark must be made at this stage. The adiabatic data are produced in terms of body-frame Cartesian coordinates (indices *I* and *J* below) while the quasidiabatic parameters correspond to curvilinear coordinates. As already mentioned in Chapter I, geometries are converted directly by direct numerical evaluation of $\mathbf{Q}(\boldsymbol{\mathcal{R}})$ or $\boldsymbol{\mathcal{R}}(\mathbf{Q})$ with the Tnum program. Branching space vectors (with *i* equals 1 or 2 below) and gradients are transformed from the body-frame Cartesian components into curvilinear components according to [213],

$$x_M^{0(\alpha\beta)i} = \sum_{I=1}^{3N} \left(\frac{\partial \mathcal{R}^I(\mathbf{Q}_{(\alpha\beta)X})}{\partial Q^M} \right) x_I^{0(\alpha\beta)i} \qquad \textbf{Eq. 73}$$

and,

$$\frac{\partial V(\mathbf{Q})}{\partial Q^M} = \sum_{I=1}^{3N} \left(\frac{\partial V(\boldsymbol{\mathcal{R}})}{\partial \mathcal{R}^I} \right) \left(\frac{\partial \mathcal{R}^I(\mathbf{Q})}{\partial Q^M} \right) \qquad \textbf{Eq. 74}$$

The general transformation for a Hessian evaluated at a non-stationary point reads

$$\frac{\partial^2 V(\mathbf{Q})}{\partial Q^M \partial Q^L} = \sum_{I=1}^{3N} \left(\frac{\partial V(\boldsymbol{\mathcal{R}})}{\partial \mathcal{R}^I} \right) \left(\frac{\partial^2 \mathcal{R}^I(\mathbf{Q})}{\partial Q^M \partial Q^L} \right) + \sum_{I,J=1}^{3N} \left(\frac{\partial^2 V(\boldsymbol{\mathcal{R}})}{\partial \mathcal{R}^I \partial \mathcal{R}^J} \right) \left(\frac{\partial \mathcal{R}^I(\mathbf{Q})}{\partial Q^M} \right) \left(\frac{\partial \mathcal{R}^J(\mathbf{Q})}{\partial Q^L} \right) \qquad \textbf{Eq. 75}$$

All these quantities (i.e. geometries, gradients, Hessians) are transformed from body-fixed frame Cartesian coordinates (indices *I* and *J*) to internal coordinates (indices *L* and *M*) with the Tnum program developed by D. Lauvergnat (Laboratoire de Chimie Physique, Orsay, France) [165].

This leads to

- $3n$ coordinates: $Q^L_{(0)R}, Q^L_{(0)P}, Q^L_{(01)X}$;
- 2 energies: $V_0(\mathbf{Q}_{(0)R}), V_0(\mathbf{Q}_{(0)P})$;
- $2n$ BS vector components: $x_L^{0(01)1}, x_L^{0(01)2}$;
- $2\,\frac{n(n+1)}{2}$ diagonal Hessian components: $\frac{\partial^2 V_0\,(\mathbf{Q}_{(0)\mathrm{R}})}{\partial Q^M \partial Q^L}, \frac{\partial^2 V_0\,(\mathbf{Q}_{(0)\mathrm{P}})}{\partial Q^M \partial Q^L}$.

The number of parameters and data is thus identical and from now on we will only work in terms of internal coordinates.

Note that there are other potentially available adiabatic data that are not used in this mapping because the problem would become over-determined and then possibly not flexible enough to posses a solution. These are:

- 3 energies: $V_1(\mathbf{Q}_{(0)R}), V_1(\mathbf{Q}_{(0)P}), V_0(\mathbf{Q}_{(01)X}) = V_1(\mathbf{Q}_{(01)X})$ (adiabatic, i.e. ab-initio, energies of the first excited state, S_1, at the S_0 optimized geometries on the side of the reactant and on the side of the product, and energy of the conical intersection, respectively);
- $2n$ gradient components: $\frac{\partial V_1\ (\mathbf{Q_{(0)R}})}{\partial Q^M}, \frac{\partial V_1\ (\mathbf{Q_{(0)P}})}{\partial Q^M}$ (non-zero gradients of the first excited state at the S_0 optimized geometries on the side of the reactant and on the side of the product, respectively);
- n average gradient components at the conical intersection (to be used in complement of the gradient difference if one wants to get the individual gradients at this point).

A few warning remarks must be made at this stage. The quasidiabatic model does not depend on enough parameters to make sure that these latter quantities will have their right values, especially in the case of a strongly anharmonic problem such as a ring-opening process (i.e. large amplitude motion). Getting incorrect energies for the conical intersection (which is a crucial point of the surface and for the photoreactivity) is perhaps the biggest issue. We thus implemented a set of strategies that ensure this point to be treated correctly. They are based on various curvature modification procedures (upon using Morse, quadratic, or switch functions). This aspect will be developed later on. Finally, when the crossing point, $\mathbf{Q}_{(01)X}$, is assumed to be the minimum-energy conical intersection within its seam, the projections of the gradients out of the branching space spanned by $\boldsymbol{x}^{0(01)1}$ and $\boldsymbol{x}^{0(01)2}$ should vanish. However, the actual gradients extrapolated from the Hessians at the minima may not fulfill these conditions.

Note that we consider S_1 energies and gradients unknown except at $\mathbf{Q}_{(01)X}$. This is in the case of a peaked conical intersection, such as on Fig. 11. For a sloped conical intersection, the same type of relationships can be derived, except that $\boldsymbol{\mathcal{R}}_{(0)P}$ is changed for $\boldsymbol{\mathcal{R}}_{(1)P}$ (the S_1 minimum) and the energy labels are also changed accordingly.

2. Determination of the Off-Diagonal Parameters.

In this section, we present analytical relationships between the adiabatic basis and the quasidiabatic basis at the conical intersection geometry. These will determine the off-diagonal parameters, Q_{12}^{M} and λ_{12}^{M}, involved in the potential coupling surface, i.e. the off-diagonal part of the quasidiabatic electronic Hamiltonian.

In what follows, we assume the adiabatic states real-valued. Strict coincidence is forced by definition between quasidiabatic and adiabatic states (up to a mixing angle) at the S_1/S_0 conical intersection due to the absence of electronic coupling at the degeneracy point,

$$\left|\Phi_2; \mathbf{Q}_{(01)\mathrm{X}}\right\rangle = \left|\Psi_0^{\theta_{01}}; \mathbf{Q}_{(01)\mathrm{X}}\right\rangle ,$$
$$\left|\Phi_1; \mathbf{Q}_{(01)\mathrm{X}}\right\rangle = \left|\Psi_1^{\theta_{01}}; \mathbf{Q}_{(01)\mathrm{X}}\right\rangle,$$

where θ_{01} remains to be determined according to some additional constraints discussed further below.

The degeneracy of both quasidiabatic states sets two relationships:

$$\begin{aligned} H_{11}^{\mathrm{diab}}\left(\mathbf{Q}_{(01)X}\right) &= H_{22}^{\mathrm{diab}}\left(\mathbf{Q}_{(01)X}\right) \\ &= e_{11} \\ &+ \frac{1}{2}\sum_{M}\sum_{L}\left(Q_{(01)X}^{M} - Q_{11}^{M}\right) f_{11}^{ML}\left(Q_{(01)X}^{L} - Q_{11}^{L}\right) \\ &= e_{22} + \frac{1}{2}\sum_{M}\sum_{L}\left(Q_{(01)X}^{M} - Q_{22}^{M}\right) f_{22}^{ML}\left(Q_{(01)X}^{L} - Q_{22}^{L}\right) \end{aligned}$$

hence,

$$\begin{aligned} e_{11} - e_{22} + \frac{1}{2}\sum_{M}\sum_{L}\left(Q_{(01)X}^{M} - Q_{11}^{M}\right) f_{11}^{ML}\left(Q_{(01)X}^{L} - Q_{11}^{L}\right) - \left(Q_{(01)X}^{M} - Q_{22}^{M}\right) f_{22}^{ML}\left(Q_{(01)X}^{L} - Q_{22}^{L}\right) \\ = 0 \end{aligned}$$

and,

$$H_{12}^{\text{diab}}\left(\mathbf{Q}_{(01)X}\right) = 0,$$

thus,

$$\sum_{M} \lambda_{12}^{M}\left(Q_{(01)X}^{M} - Q_{12}^{M}\right) = 0$$

A trivial solution for choosing Q_{12}^{M} is

$$Q_{12}^{M} = Q_{(01)X}^{M}$$

The branching space vectors, $\boldsymbol{x}^{0(01)1}$ and $\boldsymbol{x}^{0(01)2}$, are available at the conical-intersection points (for $\theta_{01} = 0$ by convention). The off-diagonal gradient can be identified to a rotated $\boldsymbol{x}^{\theta_{01}(01)2}$ (see **Eq. 63** and **Eq. 72**)

$$\frac{\partial H_{12}^{\text{diab}}\left(\mathbf{Q}_{(01)X}\right)}{\partial Q^{M}} = x_{M}^{\theta_{01}(01)2}\,. \qquad \textbf{Eq. 76}$$

i.e.

$$\lambda_{12}^{M} = \sin 2\theta_{01}\, x_{M}^{0(01)1} + \cos 2\theta_{01}\, x_{M}^{0(01)2}\,. \qquad \textbf{Eq. 77}$$

The rotation angle θ_{01} is fixed by imposing an extra condition on the off-diagonal term: it has to vanish at some particular reference point, $\mathbf{Q}_{(01)\text{ref}} \neq \mathbf{Q}_{(01)\text{X}}$, such that

$$H_{12}^{\text{diab}}\left(\mathbf{Q}_{(01)\text{ref}}\right) = \sum_{M} \lambda_{12}^{M}\left(Q_{(01)\text{ref}}^{M} - Q_{12}^{M}\right) = \sum_{M} \lambda_{12}^{M}\left(Q_{(01)\text{ref}}^{M} - Q_{(01)X}^{M}\right) = 0. \qquad \textbf{Eq. 78}$$

With the above relationships, this leads to

$$\sin 2\theta_{01} \sum_{M}\left(Q_{(01)\text{ref}}^{M} - Q_{(01)X}^{M}\right)x_{M}^{0(01)1} + \cos 2\theta_{01} \sum_{M}\left(Q_{(01)\text{ref}}^{M} - Q_{(01)X}^{M}\right)x_{M}^{0(01)2} = 0, \qquad \textbf{Eq. 79}$$

i.e.,

$$\sin 2\theta_{01} = -\frac{\sum_L \left(Q^L_{(01)\text{ref}} - Q^L_{(01)X}\right) x_L^{0(01)2}}{\sqrt{\left[\sum_L \left(Q^L_{(01)\text{ref}} - Q^L_{(01)X}\right) x_L^{0(01)1}\right]^2 + \left[\sum_L \left(Q^L_{(01)\text{ref}} - Q^L_{(01)X}\right) x_L^{0(01)2}\right]^2}}, \quad \textbf{Eq. 80}$$

$$\cos 2\theta_{01} = \frac{\sum_L \left(Q^L_{(01)\text{ref}} - Q^L_{(01)\text{X}}\right) x_L^{0(01)1}}{\sqrt{\left[\sum_L \left(Q^L_{(01)\text{ref}} - Q^L_{(01)X}\right) x_L^{0(01)1}\right]^2 + \left[\sum_L \left(Q^L_{(01)\text{ref}} - Q^L_{(01)X}\right) x_L^{0(01)2}\right]^2}}.$$

Inserting **Eq. 80** into **Eq. 77** yields

$$\lambda_{12}^M = \frac{-\left[\sum_L \left(Q^L_{(01)\text{ref}} - Q^L_{(01)X}\right) x_L^{0(01)2}\right] x_M^{0(01)1} + \left[\sum_L \left(Q^L_{(01)\text{ref}} - Q^L_{(01)X}\right) x_L^{0(01)1}\right] x_M^{0(01)2}}{\sqrt{\left[\sum_L \left(Q^L_{(01)\text{ref}} - Q^L_{(01)X}\right) x_L^{0(01)1}\right]^2 + \left[\sum_L \left(Q^L_{(01)\text{ref}} - Q^L_{(01)X}\right) x_L^{0(01)2}\right]^2}}. \quad \textbf{Eq. 81}$$

The choice of the reference point is arbitrary in principle but occurs to be of prime importance in practice. However, it is safer to choose it as a point where one wants the model to be as correct as possible. This is where coincidence is achieved between the adiabatic and the quasidiabatic representations, such that the mapping procedure is less approximate at this point. In our model, we will always choose the minimum of one of the quasidiabatic state as reference points: $\mathbf{Q}_{(01)\text{ref}} = \mathbf{Q}_{(11)}$ or $\mathbf{Q}_{(01)\text{ref}} = \mathbf{Q}_{(22)}$ because we consider that the potential electronic coupling should be negligible in those regions. This choice of reference point will be discussed further along in practical situations, for the various application cases presented in this work.

We have thus set $2n$ relationships that determine Q_{12}^M and λ_{12}^M (**Eq. 81**) explicitly. Note that we implemented into the PAnDA program a general treatment for any pair of electronic states within a set that can be made of more than two states.

An important remark should be made at this stage: our objective is to achieve coincidence of the quasidiabatic and adiabatic representations at the conical

intersection; the electronic coupling is set to zero by construction as expected, but there is no direct control over the behavior of the diagonal elements. This aspect will be discussed in the last section of the present chapter.

Now that we are able to calculate the off-diagonal part of the quasidiabatic electronic Hamiltonian let us focus on the diagonal one.

3. Determination of the Diagonal Potential Energy Surface Parameters

In this section, we present analytical relationships up to second order between the Hamiltonian matrices both in the adiabatic basis and the quasidiabatic basis at the geometries of the minima. These will determine the diagonal parameters of the potential energy surfaces (i.e. Q_{11}^{M}, Q_{22}^{M}, f_{11}^{ML}, and f_{22}^{ML}).

Let us consider again the case of a peaked conical intersection. If we assume, as a starting point, that coincidence is achieved both at the adiabatic ground-state (S_0) minimum corresponding to the reactant,

$$\left|\Phi_1; \mathbf{Q}_{(0)R}\right\rangle = \left|\Psi_0; \mathbf{Q}_{(0)R}\right\rangle,$$
$$\left|\Phi_2; \mathbf{Q}_{(0)R}\right\rangle = \left|\Psi_1; \mathbf{Q}_{(0)R}\right\rangle.$$

and at the adiabatic ground-state (S_0) minimum corresponding to the product,

$$\left|\Phi_2; \mathbf{Q}_{(0)P}\right\rangle = \left|\Psi_0; \mathbf{Q}_{(0)P}\right\rangle,$$
$$\left|\Phi_1; \mathbf{Q}_{(0)P}\right\rangle = \left|\Psi_1; \mathbf{Q}_{(0)P}\right\rangle,$$

then the off-diagonal elements satisfy the two following relationships,

$$H_{12}^{\text{diab}}\left(\mathbf{Q}_{(0)R}\right) = \sum_{M} \lambda_{12}^{M}\left(Q_{(0)R}^{M} - Q_{12}^{M}\right) = 0, \qquad \textbf{Eq. 82}$$

$$H_{12}^{\mathrm{diab}}\left(\mathbf{Q}_{(0)P}\right)=\sum_{M}\lambda_{12}^{M}\left(Q_{(0)P}^{M}-Q_{12}^{M}\right)=0.$$

The validity of the approximation that adiabatic and quasidiabatic states coincide at the minima is determined by the extent to which the latter relationships are satisfied. We may want to use them as constraints to build the quasidiabatic models. Using $\mathbf{Q}_{(01)\mathrm{ref}}$ to rotate $\boldsymbol{\lambda}_{12}$ conveniently (see previous section) makes it possible to achieve one of the two conditions but not both. Indeed, there is no reason for $\mathbf{Q}_{(0)R}$, $\mathbf{Q}_{(0)P}$, and $\mathbf{Q}_{(01)X}$ to belong to the same hyperplane orthogonal to $\boldsymbol{\lambda}_{12}$, except in cases where symmetry ensures this (or, of course, by accident). However, making this assumption allows approximate relationships to be derived for the parameters that remain to be determined. They can be used as such to build a crude model or may be further refined by serving as a guess in a self-consistent fitting procedure.

More specifically, let us consider as an example that $\mathbf{Q}_{(01)\mathrm{ref}}=\mathbf{Q}_{(0)R}$. Here, $H_{12}^{\mathrm{diab}}\left(\mathbf{Q}_{(0)R}\right)=0$ by construction, and the model should reproduce the adiabatic data correctly up to second order after diagonalization. However, since, $H_{12}^{\mathrm{diab}}\left(\mathbf{Q}_{(0)P}\right)\neq 0$, one does not have as much control over the adiabatic potential at this point. The quasidiabatic and adiabatic minima will not be coincident if the electronic coupling is too strong. In the worst-case scenario, we can even get what is called a “hole”, a situation where the adiabatic minimum obtained after diagonalization is not physical, with a depth in energy that depends on the magnitude of the off-diagonal term. If such a problem occurs, it could also mean that the mathematical expression chosen for the quasidiabatic potential energy surface is not adequate and should be re-investigated.

Coincidence between quasidiabatic and adiabatic potential energy surfaces at both minima sets $2n+2$ relationships,

$$Q_{11}^{M} = Q_{(0)R}^{M},$$
$$Q_{22}^{M} = Q_{(0)P}^{M},$$
$$e_{11} = V_0\left(\mathbf{Q}_{(0)R}\right),$$
$$e_{22} = V_0\left(\mathbf{Q}_{(0)P}\right).$$

Finally, the quasidiabatic Hessian components satisfy $2\frac{n(n+1)}{2}$ relationships expressed in **Eq. 69** read

$$f_{11}^{ML} = \frac{\partial^2 V_0\left(\mathbf{Q}_{(0)R}\right)}{\partial Q^M \partial Q^L} + \frac{2\lambda_{12}^{M}\lambda_{12}^{L}}{V_0\left(\mathbf{Q}_{(0)P}\right) - V_0\left(\mathbf{Q}_{(0)R}\right) + \frac{1}{2}\sum_M \sum_L \left(Q_{(0)R}^{M} - Q_{(0)P}^{M}\right) f_{22}^{ML} \left(Q_{(0)R}^{L} - Q_{(0)P}^{L}\right)}, \quad \textbf{Eq. 83}$$

$$f_{22}^{ML} = \frac{\partial^2 V_0\left(\mathbf{Q}_{(0)P}\right)}{\partial Q^M \partial Q^L} + \frac{2\lambda_{12}^{M}\lambda_{12}^{L}}{V_0\left(\mathbf{Q}_{(0)R}\right) - V_0\left(\mathbf{Q}_{(0)P}\right) + \frac{1}{2}\sum_M \sum_L \left(Q_{(0)P}^{M} - Q_{(0)R}^{M}\right) f_{11}^{ML} \left(Q_{(0)P}^{L} - Q_{(0)R}^{L}\right)}$$

Such expressions reflect the so-called second order jahn-Teller effect. One can appreciate that a self-consistent procedure is required from how f_{11}^{ML} and f_{22}^{ML} mutually depend on each other. We implemented this into the PAnDA program accordingly.

Note, again, that in the case of a sloped conical intersection, we would have $\mathbf{Q}_{(1)P}$ in S_1. If so, there would be a minus instead of a plus sign in front of the second term (second-order Jahn-Teller effect in the upper state).

We have thus set $2 + 2n + 2\frac{n(n+1)}{2}$ relationships that determine e_{11}, e_{22}, Q_{11}^{M}, Q_{22}^{M}, f_{11}^{ML}, and f_{11}^{ML} (**Eq. 83**) explicitly.

Up to this point we defined a vibronic coupling Hamiltonian model where:

- The diagonal quasidiabatic potential energy surfaces are expressed as quadratic expansions centered at the optimized ab-initio geometries of the adiabatic potential energy surfaces.
- There is an off-diagonal potential coupling surface for each quasidiabatic electronic state crossing point. We express it as linear expansion centered on the conical intersection.
- All the quasidiabatic parameters of the vibronic coupling Hamiltonian model are defined by the ab-initio data.

However, as already mentioned, there is no control over some relevant features: the energy at the conical intersection, the topography of the cone along the gradient difference, and the adiabatic electronic state minima. In addition, our quasidiabatic diagonal potential energy surfaces are harmonic (quadratic expansions based on ab-initio force constants corrected by the second-order Jahn-Teller effect induced by the non-adiabatic coupling). After diagonalization, this type of model will induce some anharmonicity (the adiabatic potential energy surfaces are not quadratic) but will probably not account for all types of anharmonicity. For example, bond dissociations often result in Morse-type curves, which is not due to an electronic coupling between quasidiabatic states. In other words, the quasidiabatic surfaces should already present this type of shape. In addition, this lack of flexibility may result in a conical intersection that is not at the right position and/or energy compared to the actual ab-initio one, whereas we want this condition to be achieved for making sure that the photoprocess is described adequately.

From now on, we will call intrinsic anharmonicity the difference between the actual adiabatic potential energy surfaces obtained after the diagonalization of our analytically parameterized quadratic quasidiabatic vibronic coupling Hamiltonian model (which already takes into account some small anharmonicity due to non-adiabatic couplings) and the ab-initio adiabatic potential energy surfaces obtained with quantum chemistry calculations (Fig. 12).

To be able to get some control over the conical intersection position and energy, we modified the original vibronic coupling Hamiltonian model presented above with n-

dimensional functions along specific directions (e.g. from the minimum of the diagonal quasidiabatic electronic potential energy surface to the corresponding conical intersection). This strategy is described in the following section. It was first tested on the photoinduced benzopyran ring-opening process that presents a strong anharmonicity. The results regarding this application are not presented in this thesis. Our improved strategy occurred not to be the most suitable in this situation for which a three-state description should be more adequate. Nevertheless, our models were used with success to study two others cases such as excited-state proton transfer in 3-hydroxychromone dyes and ultrafast excited-state intramolecular charge transfer in aminobenzonitrile derivatives.

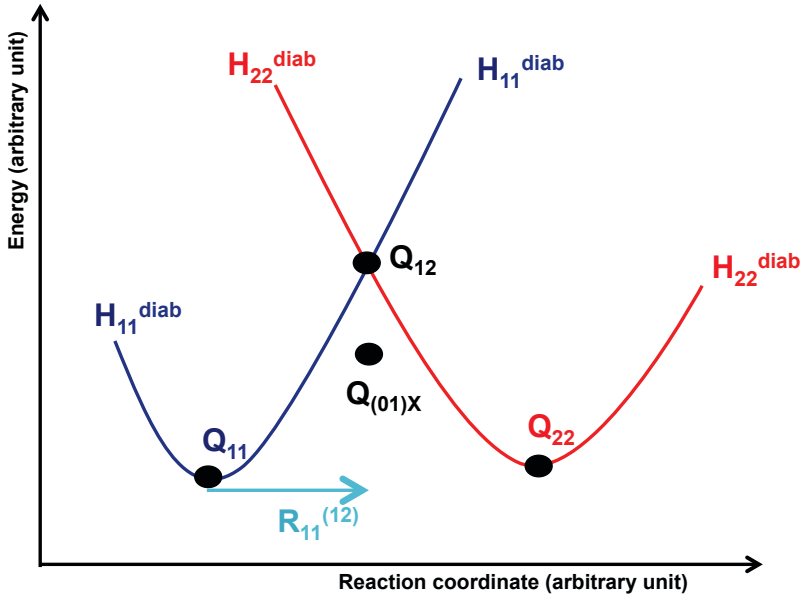

Fig. 12. Illustration of the intrinsic anharmonicity problem. Q_{12} is the energy of the conical intersection obtained with the quadratic diagonal quasidiabatic potential energy surfaces. $Q_{(01)X}$ is the ab-initio energy of the conical intersection (targeted).

IV. Description of the Anharmonicity

The purpose of this section is to define the strategy that we implemented to account for the lack of anharmonicity of the quadratic model and its possible consequence on the position and/or energy of the crossing point with respect to the ab-initio conical intersection. To solve this problem, we considered various strategies that change the curvature along the direction linking a minimum to the crossing point so that the crossing point occurs at the correct position and energy.

We define $\mathbf{R}_{ii}^{(ij)}$ the normalized vector between the diagonal quasidiabatic potential energy surface minimum $\mathbf{Q}_{ii}$ (state $i = 1$ or 2) chosen as a starting point and the conical intersection $\mathbf{Q}_{ij} = \mathbf{Q}_{(\alpha\beta)\mathrm{X}}$ (between states $i = 1$ or 2 and $j = 2$ or 1) that is to be targetted (Fig. 12),

$$\mathbf{R}_{ii}^{(ij)} = \frac{\mathbf{Q}_{ij} - \mathbf{Q}_{ii}}{\left\| \mathbf{Q}_{ij} - \mathbf{Q}_{ii} \right\|} \qquad \textbf{Eq. 84}$$

Note that i and j could take other values than 1 and 2 in the general case.

The corresponding coordinate for a given point $\mathbf{Q}$ along this collective direction (i.e. the projection of $\mathbf{Q} - \mathbf{Q}_{ii}$ on $\mathbf{R}_{ii}^{(ij)}$) is denoted $\varepsilon_{ii}^{(ij)}$ (Fig. 13),

$$\varepsilon_{ii}^{(ij)} = \left(\mathbf{Q} - \mathbf{Q}_{ii}\right) \cdot \mathbf{R}_{ii}^{(ij)} \qquad \textbf{Eq. 85}$$

where the dot symbol used in the scalar product means implicitly that the left vector is transposed.

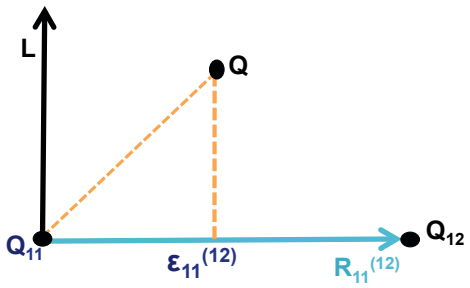

Fig. 13. Two-dimensional illustration of the projection of a point Q along the direction $\mathbf{R}_{ii}^{(ij)}$.

Defining this coordinate will allow the original curvature along the $\mathbf{R}_{ii}^{(ij)}$ direction to be either changed for a new curvature to reach the actual energy of the conical intersection or replaced by a coordinate-dependent curvature to also account for intrinsic anharmonicity.

The first strategy we will present is adapted to harmonic-like systems. The idea is to keep the quadratic form of the curvature but to change its value in order to constrain the conical intersection energy. The second strategy uses a Morse potential, which is the most "natural" function to describe anharmonicity. However, we will highlight the limitation of such a function to describe coupled potential energy surfaces. The third strategy is the most flexible one with the use of a switch function and it is proved to be capable of describing correctly several different systems (Chapter IV). However, the drawback of this latter strategy is that it is not directly "MCTDH compatible" in the original set of coordinates because $\varepsilon_{ii}^{(ij)}$ is now a collective coordinate involved in a function that is not a simple polynomial. It thus, requires some further modifications (this aspect is further detailed in the following and applied in Chapter III and IV). All these strategies have been implemented into the PAnDA program.

1. Quadratic Potential

Our first strategy is based on a very simple idea. Along the $\mathbf{R}_{ii}^{(ij)}$ direction we remove the previous quadratic contribution, $f_{ii,R}^{(ij)}$, to replace it with a new quadratic contribution, $\tilde{f}_{ii,R}^{(ij)}$, the value of which is chosen to constrain the conical intersection to have the correct energy at its position (i.e. to match the ab-initio data).

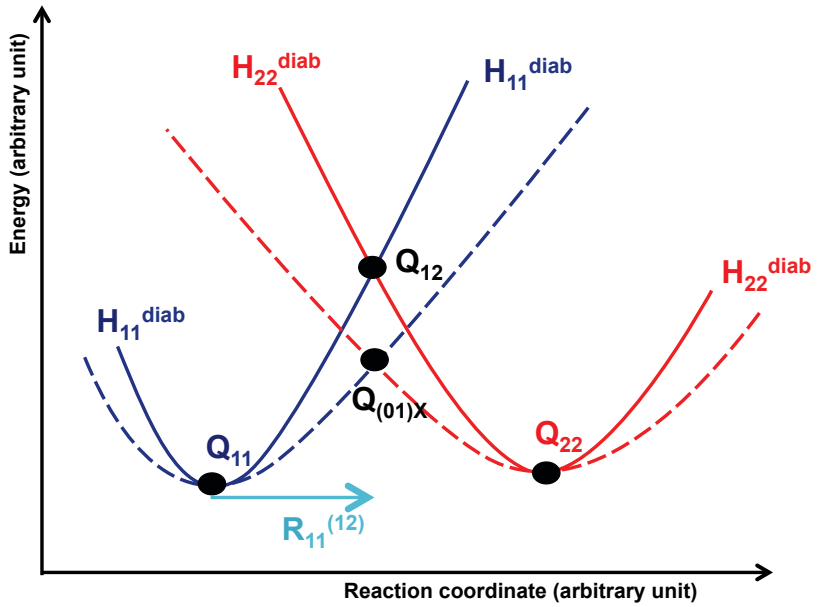

Fig. 14 Illustration of the quadratic modification strategy. Plain lines: original quadratic curvature. Dashed lines: quadratic curvature obtained once the modification has been applied.

The quadratic modified diagonal quasidiabatic potential energy surface reads

$$H_{ii}^{\text{diab,Quadra}}(\mathbf{Q}) = H_{ii}^{\text{diab}}(\mathbf{Q}) - \frac{1}{2} f_{ii,R}^{(ij)} \varepsilon_{ii}^{(ij)^2} + \frac{1}{2} \tilde{f}_{ii,R}^{(ij)} \varepsilon_{ii}^{(ij)^2} \qquad \textbf{Eq. 86}$$

The one-directional old quadratic curvature that we remove along the $\mathbf{R}_{ii}^{(ij)}$ direction, $f_{ii,R}^{(ij)}$, is defined as

$$f_{ii,R}^{(ij)} = \mathbf{R}_{ii}^{(ij)} . \mathbf{f}_{ii} . \mathbf{R}_{ii}^{(ij)} \qquad \textbf{Eq. 87}$$

where the dot symbol used in the scalar product (vector-matrix-vector contraction) means implicitly that the left vector is transposed (in other words, using matrix product, this would be expressed as $\mathbf{R}_{ii}^{(ij)\mathrm{T}}\mathbf{f}_{ii}\mathbf{R}_{ii}^{(ij)}$).

To define the one-directional new quadratic curvature, $\tilde{f}_{ii,R}^{(ij)}$, that we add along the $\mathbf{R}_{ii}^{(ij)}$ direction, let us consider a one-dimensional quadratic function along this direction (see Fig. 14). At the conical intersection geometry ($\mathbf{Q} = \mathbf{Q}_{ij} = \mathbf{Q}_{(\alpha\beta)\mathrm{X}}$), we want the new quadratic expansion to fulfill the following condition,

$$V_\alpha\left(\mathbf{Q}_{(\alpha\beta)X}\right) = H_{ii}^{\mathrm{diab}}\left(\mathbf{Q}_{(\alpha\beta)X}\right) = e_{ii} + \frac{1}{2}\tilde{f}_{ii,R}^{(ij)}(\mathbf{Q}_{(\alpha\beta)X} - \mathbf{Q}_{ii})^2 \qquad \textbf{Eq. 88}$$

Thus,

$$\tilde{f}_{ii,R}^{(ij)} = 2\frac{V_\alpha\left(\mathbf{Q}_{(\alpha\beta)X}\right) - e_{ii}}{(\mathbf{Q}_{(\alpha\beta)X} - \mathbf{Q}_{ii})^2} \qquad \textbf{Eq. 89}$$

We remind here that $V_\alpha\left(\mathbf{Q}_{(\alpha\beta)X}\right) = V_\beta\left(\mathbf{Q}_{(\alpha\beta)X}\right)$ and $\mathbf{Q}_{(\alpha\beta)X} = \mathbf{Q}_{ij}$ (where we suppose that $i \neq j$ and $\alpha \neq \beta$ but do not specify their values to keep the expressions general). To achieve the same condition for the other state and make sure that both quasidiabatic curves cross at the conical intersection, i.e. $H_{ii}^{\mathrm{diab}}\left(\mathbf{Q}_{(\alpha\beta)X}\right) = H_{jj}^{\mathrm{diab}}\left(\mathbf{Q}_{(\alpha\beta)X}\right)$, a similar procedure is used on the other side. We remind here that $H_{ij}^{\mathrm{diab}}\left(\mathbf{Q}_{(\alpha\beta)X}\right) = 0$ is already achieved by construction.

Hence, the original harmonic frequencies in the vicinity of the potential energy surface minima are modified according to the new quadratic curvatures defined in **Eq. 89**. Nevertheless, this new curvature may not be "compatible" with the remaining unmodified Hessian elements. By this, we mean that, once the quasidiabatic vibronic Hamiltonian gets diagonalized, the nature of the minima can be modified (going from a minimum to a transition state with a negative curvature) if the constraint on the conical intersection energy is too strong (i.e. large anharmonicity and/or large distance between the minimum and the conical intersection).

To illustrate this, let us take a hypothetical two-dimensional system, where the first dimension is the modified direction ($\mathbf{R}_{ii}^{(ij)}$). The Hessian in the original quadratic model (without curvature modification) at the original minimum reads

$$\begin{pmatrix} C_1 & C_2 \\ C_2 & C_3 \end{pmatrix}$$

where C_1, C_2, and C_3 have values such that the eigenvalues of the matrix are positive. C_1 is the curvature along the $\mathbf{R}_{ii}^{(ij)}$ direction from the minimum to the conical intersection. Then, if we apply the quadratic modification of the curvature as presented in this section, we will simply modify C_1 and the other parameters of the Hessian remain untouched. Therefore, the eigenvalues of this Hessian will change and could even become negative, which would then induce a change of nature of the point. This will happen if this change of curvature is too drastic (i.e. if C_1 after modification is too different from its original value; in other words if the intrinsic anharmonicity is too strong). To avoid this problem, one will need to modify also the cross term involving the $\mathbf{R}_{ii}^{(ij)}$ dimension (i.e. C_2) with respect to the modification of C_1.

This quadratic modification of the diagonal quasidiabatic potential energy surface is adapted to refine the potential in harmonic-like systems, such as aminobenzonitrile or 3-hydroxychromone (Chapter IV and III respectively). Therefore, to improve this first strategy in order to describe anharmonic systems, the idea is the following. We want to retain the harmonic frequencies of the diagonal quasidiabatic potential energy surface at the minimum while still having parameters to control the conical intersection energy. This is achieved by the following strategy using a Morse potential.

2. Morse Potential

Along the $\mathbf{R}_{ii}^{(ij)}$ direction we now remove the quadratic contribution to replace it with a Morse function. The Morse modified diagonal quasidiabatic potential energy surface reads,

$$H_{ii}^{\text{diab,Morse}}(\mathbf{Q}) = H_{ii}^{\text{diab}}(\mathbf{Q}) - \frac{1}{2} f_{ii,R}^{(ij)} \varepsilon_{ii}^{(ij)\,2} + \frac{1}{2} De_{ii}^{(ij)} \left(1 - \mathrm{e}^{\sqrt{\frac{f_{ii,R}^{(ij)}}{2De_{ii}^{(ij)}}} \varepsilon_{ii}^{(ij)}} \right)^2 , \qquad \textbf{Eq. 90}$$

where $De_{ii}^{(ij)}$ is the parameter that controls the energy of the asymptote (Fig. 15). It is optimized with the MINI program (developed by D. Lauvergnat) so as to constrain the conical intersection energy at its position.

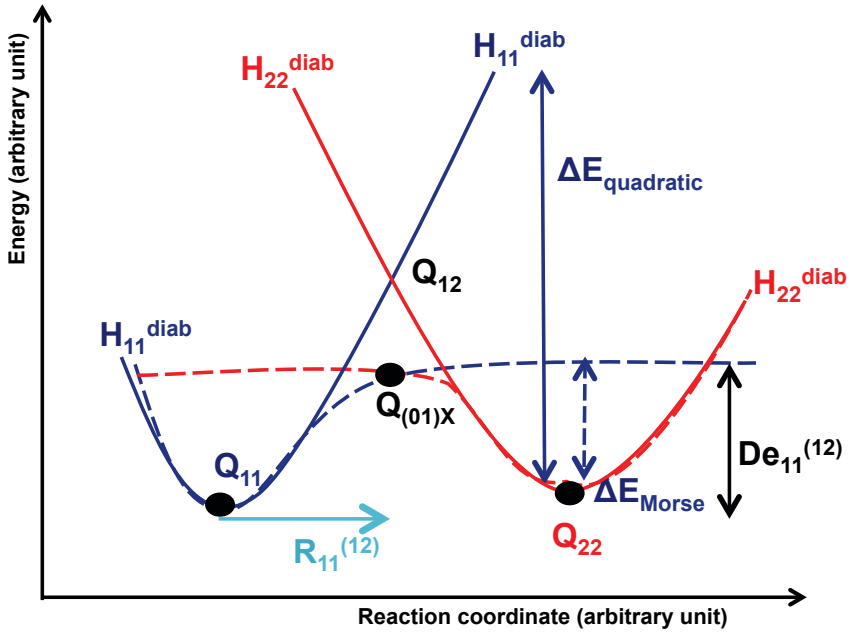

Fig. 15. Illustration of the Morse potential strategy. Plain lines: original quadratic diagonal quasidiabatic potential energy surfaces. Dashed lines: Morse diagonal quasidiabatic potential energy surfaces.

The main limitation of the Morse potential to describe coupled potential energy surfaces is the presence of the asymptote that can create non-physical additional crossings. If so,

when the energy gap becomes small, the off-diagonal terms start having a strong effect on the shape of the resulting adiabatic potential energy surfaces, which can even create non-physical minima (i.e. holes). As shown on Fig. 15, the difference in energy between the β and α adiabatic potential energies at the minima is lower with the Morse potential than in the quadratic potential. In addition, since the non-adiabatic coupling is proportional to $\frac{1}{V_\beta(\mathbf{Q})-V_\alpha(\mathbf{Q})}$ (**Eq. 68**), if the difference in energy between the two adiabatic states drops too much because of the asymptote, the non-adiabatic coupling will increase artificially, thus describing the wrong physics.

Therefore, to improve this second strategy, the idea is the following. Again, we want to retain the harmonic frequencies of the diagonal quasidiabatic potential energy surface while still having parameters that control the conical intersection energy. However, we want to avoid an asymptotic behavior. This is achieved by the following strategy using a switch potential.

3. Switch Potential

Along the $\mathbf{R}_{ii}^{(ij)}$ direction we now modify the quadratic curvature by modulating it with a switch function. It is based on a hyperbolic tangent function that allows a smooth transition between two curves (Fig. 17) and reads

$$F_{\text{switch}}\left(\varepsilon_{ii}^{(ij)}\right) = \frac{1+\tanh\left(C_2\left(\varepsilon_{ii}^{(ij)}-\varepsilon_{ii,0}^{(ij)}\right)\right)}{2}, \qquad \textbf{Eq. 91}$$

This function is centered around $\varepsilon_{ii,0}^{(ij)}$ and takes values between 0 and 1 asymptotically. According to the value of C_2, the value of this function can be considered as almost zero at $\varepsilon_{ii}^{(ij)} = 0$ and switches smoothly, most rapidly around $\varepsilon_{ii,0}^{(ij)}$, and reaches almost one at $2\varepsilon_{ii,0}^{(ij)}$.

Hence,

$$\varepsilon_{ii,0}^{(ij)} = \frac{\left\|\mathbf{Q}_{(\alpha\beta)X} - \mathbf{Q}_{ii}\right\|}{2}, \qquad \textbf{Eq. 92}$$

The C_2 parameters control the smoothing level of the function (how fast it changes from 0 to 1). The more it increases the closer the switch function is to a step distribution (Fig. 16). A too large value could thus create some unwanted discontinuity in the final adiabatic potential energy surfaces. Nevertheless, this parameter can be optimized by the user ("by hand") or automatically. Optimizing the value of C_2 by hand is, of course, time consuming but an automatic procedure could be tedious to implement and would involve a constraint that is not clearly defined. None of them correspond to the philosophy of our methodology (i.e. as little fitting as possible and avoiding the user to make choices for the values of the parameters). We thus fixed $C_2 = 1$, as it proved to be an adequate value in all the applications presented in this thesis work (note, however, that working with different values of C_2 is possible in the current implementation of the PAnDA program; its value is to be chosen by the user in the input file).

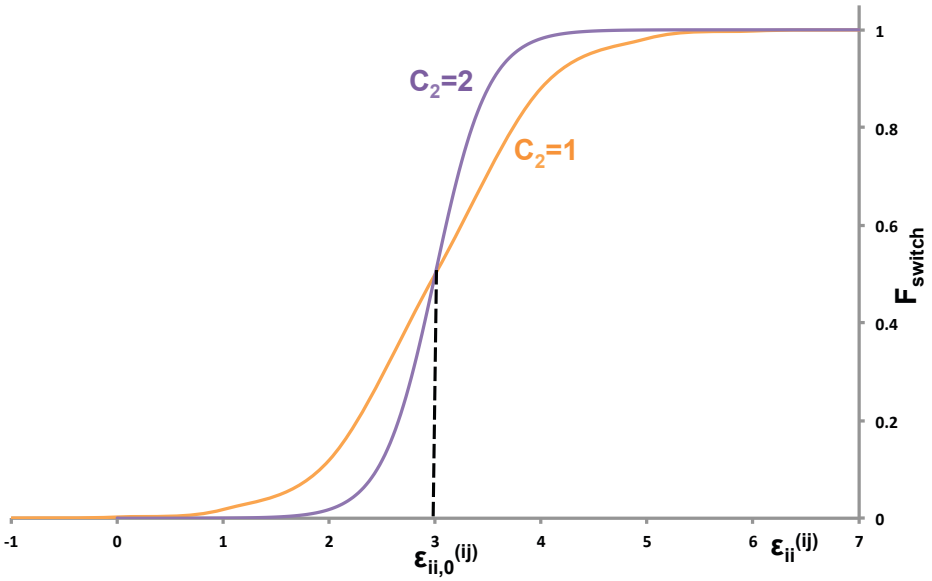

Fig. 16 Switch function of Eq. 91 centered around 3. Orange: C_2 = 1. Purple: C_2 = 2.

We use this switch function to vary smoothly from the actual quadratic curvature at the minimum of a diagonal quasidiabatic potential energy surface to a curvature that is able to constrain the energy to be equal to the ab-initio one at the conical intersection geometry ($2\varepsilon_{ii,0}^{(ij)}$) along the direction $\mathbf{R}_{ii}^{(ij)}$ linking both points, as shown in Fig. 17.

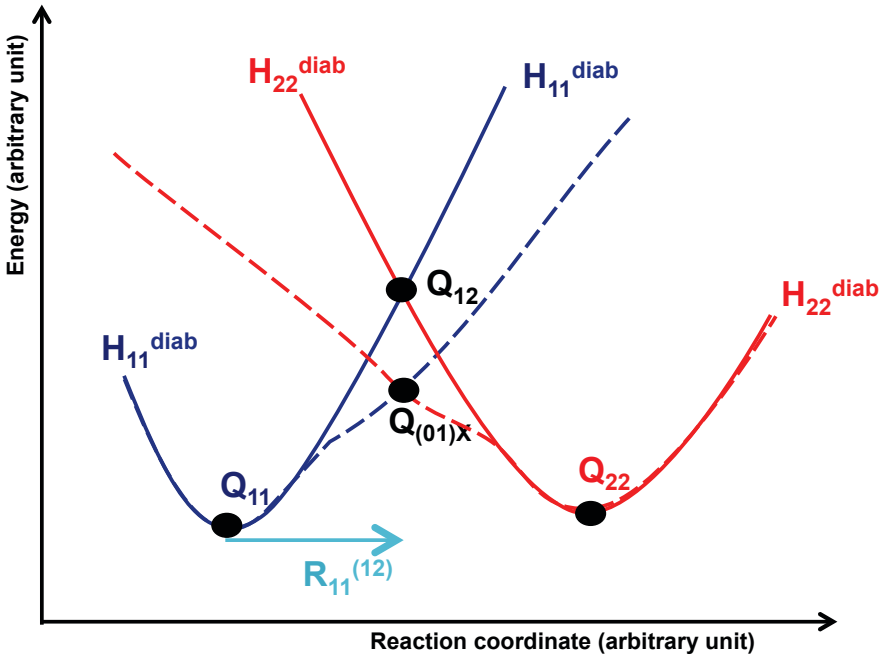

Fig. 17. Illustration of the switch potential strategy. Plain lines: original quadratic diagonal quasidiabatic potential energy surfaces. Dashed lines: switch diagonal quasidiabatic potential energy surfaces.

The switch modified diagonal quasidiabatic potential energy surface reads

$$H_{ii}^{\text{diab,Switch}}(\mathbf{Q}) = H_{ii}^{\text{diab}}(\mathbf{Q}) + \frac{1}{2}\breve{f}_{ii,R}^{(ij)}\left(F_{switch}\left(\varepsilon_{ii}^{(ij)}\right) - F_{switch}(0)\right)\varepsilon_{ii}^{(ij)\,2} \qquad \textbf{Eq. 93}$$

The $\breve{f}_{ii,R}^{(ij)}$ parameter is the new curvature that will constrain the conical intersection energy. It is defined with the same idea as for the quadratic modification expressed in **Eq. 89**,

$$\begin{aligned} V_{\alpha}\left(\mathbf{Q}_{(\alpha\beta)X}\right) &= H_{ii}^{\text{diab,Switch}}\left(\mathbf{Q}_{(\alpha\beta)X}\right) \\ &= H_{ii}^{\text{diab}}\left(\mathbf{Q}_{(\alpha\beta)X}\right) \\ &+ \frac{1}{2}\breve{f}_{ii,R}^{(ij)}\left(F_{switch}\left(2\varepsilon_{ii,0}^{(ij)}\right) - F_{switch}(0)\right)\left(2\varepsilon_{ii,0}^{(ij)}\right)^{2} \end{aligned} \qquad \textbf{Eq. 94}$$

Hence,

$$\check{f}_{ii,R}^{(ij)} = \frac{2\left(V_\alpha\left(\mathbf{Q}_{(\alpha\beta)X}\right) - H_{ii}^{\text{diab}}\left(\mathbf{Q}_{(\alpha\beta)X}\right)\right)}{\left(F_{switch}\left(2\varepsilon_{ii,0}^{(ij)}\right) - F_{switch}(0)\right)\left(2\varepsilon_{ii,0}^{(ij)}\right)^2} \quad \textbf{Eq. 95}$$

This switch contribution is a tool to control the energy (zero order) of the conical intersection ($\varepsilon_{ii}^{(ij)} = 2\varepsilon_{ii,0}^{(ij)}$) but it must not have an impact on the second derivative (curvature) of the diagonal quasidiabatic potential energy surface at the minimum ($\varepsilon_{ii}^{(ij)} = 0$). In other words, we want to keep our original harmonic frequencies. Hence, we chose the specific expression of the switch function (**Eq. 91**) because it was compatible with fulfilling the following condition,

$$\frac{\partial^2 H_{ii}^{\text{diab,Switch}}(\mathbf{Q}_{ii})}{\partial Q^M \partial Q^L} = \frac{\partial^2 H_{ii}^{\text{diab}}(\mathbf{Q}_{ii})}{\partial Q^M \partial Q^L} \quad \textbf{Eq. 96}$$

Let us differentiate our switch modified diagonal quasidiabatic potential energy surface of **Eq. 93** to prove that this condition is fulfilled,

$$\frac{\partial H_{ii}^{\text{diab,Switch}}(\mathbf{Q})}{\partial Q^M} \quad \textbf{Eq. 97}$$

$$= \frac{\partial H_{ii}^{\text{diab}}(\mathbf{Q})}{\partial Q^M} + \frac{1}{2}\check{f}_{ii,R}^{(ij)} \frac{\partial\left(F_{switch}\left(\varepsilon_{ii}^{(ij)}\right) - F_{switch}(0)\right)}{\partial Q^M} {\varepsilon_{ii}^{(ij)}}^2$$

$$+ \check{f}_{ii,R}^{(ij)}\left(F_{switch}\left(\varepsilon_{ii}^{(ij)}\right) - F_{switch}(0)\right)\varepsilon_{ii}^{(ij)} \frac{\partial \varepsilon_{ii}^{(ij)}}{\partial Q^M}$$

$$\frac{\partial^2 H_{ii}^{\text{diab,Switch}}(\mathbf{Q})}{\partial Q^M \partial Q^L}$$

$$= \frac{\partial^2 H_{ii}^{diab}(\mathbf{Q})}{\partial Q^M \partial Q^L} + \frac{1}{2}\check{f}_{ii,R}^{(ij)} \frac{\partial^2 \left(F_{switch}\left(\varepsilon_{ii}^{(ij)}\right) - F_{switch}(0)\right)}{\partial Q^M \partial Q^L} {\varepsilon_{ii}^{(ij)}}^2$$

$$+ \check{f}_{ii,R}^{(ij)} \frac{\partial \left(F_{switch}\left(\varepsilon_{ii}^{(ij)}\right) - F_{switch}(0)\right)}{\partial Q^L} \varepsilon_{ii}^{(ij)} \frac{\partial \varepsilon_{ii}^{(ij)}}{\partial Q^M}$$

$$+ \check{f}_{ii,R}^{(ij)} \frac{\partial \left(F_{switch}\left(\varepsilon_{ii}^{(ij)}\right) - F_{switch}(0)\right)}{\partial Q^M} \varepsilon_{ii}^{(ij)} \frac{\partial \varepsilon_{ii}^{(ij)}}{\partial Q^L}$$

$$+ \check{f}_{ii,R}^{(ij)} \left(F_{switch}\left(\varepsilon_{ii}^{(ij)}\right) - F_{switch}(0)\right) \frac{\partial \varepsilon_{ii}^{(ij)}}{\partial Q^M} \frac{\partial \varepsilon_{ii}^{(ij)}}{\partial Q^L}$$

$$+ \check{f}_{ii,R}^{(ij)} \left(F_{switch}\left(\varepsilon_{ii}^{(ij)}\right) - F_{switch}(0)\right) \varepsilon_{ii}^{(ij)} \frac{\partial^2 \varepsilon_{ii}^{(ij)}}{\partial Q^M \partial Q^L}$$

If we calculate the second derivative at the minimum, $\mathbf{Q} = \mathbf{Q}_{ii}$, we have $\varepsilon_{ii}^{(ij)} = 0$, such that all terms but the first one vanish, and **Eq. 96** is fulfilled.

However, there are some cases detailed in what follows, where this switch procedure must be adapted to describe more complicated adiabatic potential energy surfaces, such as in the two following situations.

(i) In **Fig. 18**, the conical intersection ($\mathbf{Q}_{(01)X}$) energy is lower than the one of the local minimum ($\mathbf{Q}_{(1)R}$) energy in S_1 (purple line). This situation was encountered in the aminobenzonitrile study (Chapter IV). If so, there is a risk that the switch procedure used to modify the diagonal quasidiabatic function makes it decrease after the conical intersection geometry, which unavoidably leads to the creation of a non-physical hole on the adiabatic potential energy surface: this is illustrated on Fig. 19 (blue plain line).

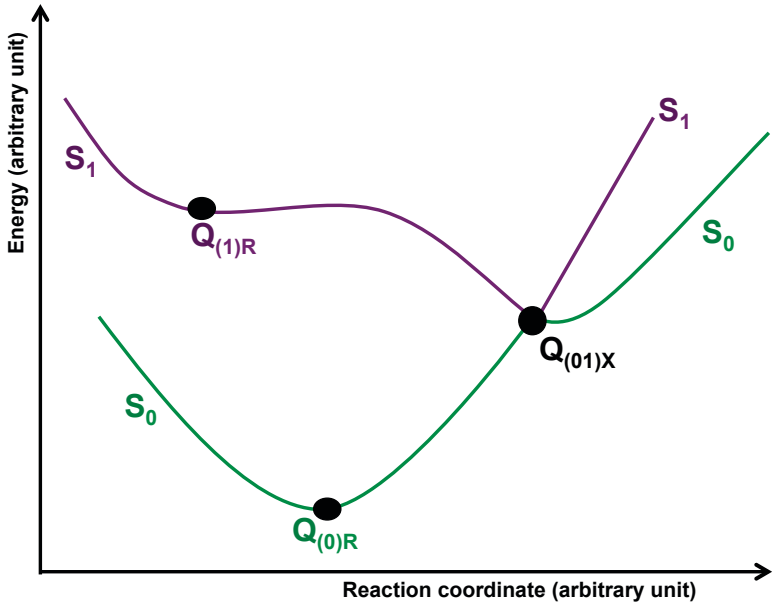

Fig. 18 Illustration of a situation where the conical intersection energy is lower than the one of the adiabatic minimum in S_1.

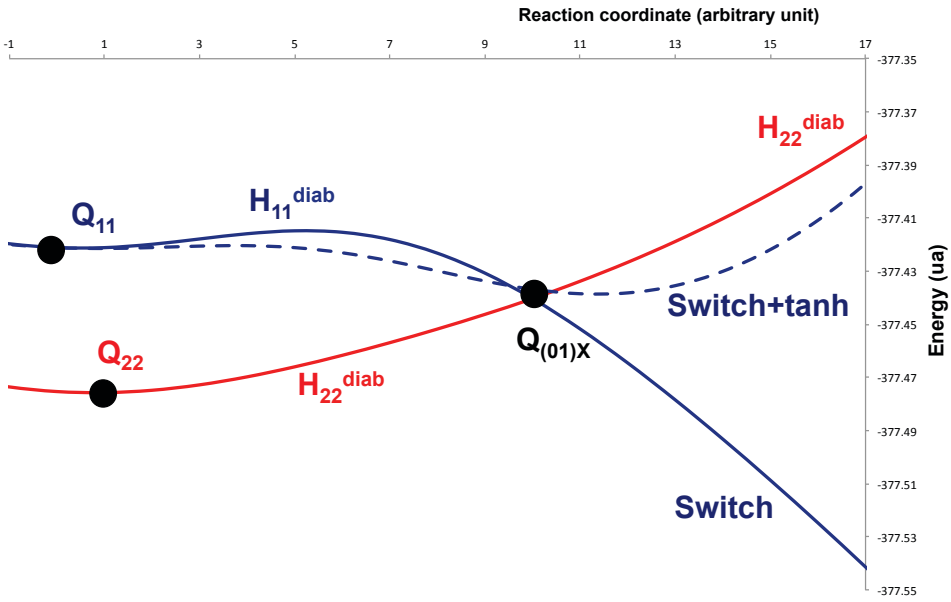

Fig. 19 Illustration of the switch+tanh strategy. Plain lines: original quadratic diagonal quasidiabatic potential energy surfaces. Dashed lines: switch+tanh diagonal quasidiabatic potential energy surface

To avoid this problem, one must replace the $\varepsilon_{ii}^{(ij)^2}$ term of **Eq. 93** by a function that increases faster, such as a squared hyperbolic tangent (blue dashed line in Fig. 19). Thus, in that situation the "switch+tanh modified" diagonal quasidiabatic potential energy surface reads

$$H_{ii}^{\text{diab,Switch}}(\mathbf{Q}) = H_{ii}^{\text{diab}}(\mathbf{Q}) + \frac{1}{2}\check{f}_{ii,R}^{(ij)}\left(F_{switch}\left(\varepsilon_{ii}^{(ij)}\right) - F_{switch}(0)\right)\left(\frac{\tanh\left(C_3\varepsilon_{ii}^{(ij)}\right)}{C_3}\right)^2 \quad \textbf{Eq. 98}$$

The C_3 parameter controls the gradient of the switch contribution. In other words, it controls how fast the diagonal quasidiabatic potential energy surface goes up in energy after the conical intersection geometry. We used $C_3 = 1$ in our application cases but this parameter can be defined by the user in the input of PAnDA.

The new curvature to constrain the conical intersection energy $\check{f}_{ii,R}^{(ij)}$ reads

$$\check{f}_{ii,R}^{(ij)} = \frac{2\left(V_\alpha\left(\mathbf{Q}_{(\alpha\beta)X}\right) - H_{ii}^{\text{diab}}\left(\mathbf{Q}_{(\alpha\beta)X}\right)\right)}{\left(F_{switch}\left(2\varepsilon_{ii,0}^{(ij)}\right) - F_{switch}(0)\right)\left(\frac{\tanh\left(2C_3\varepsilon_{ii,0}^{(ij)}\right)}{C_3}\right)^2} \quad \textbf{Eq. 99}$$

(ii) In Fig. 20, we can observe the existence of a pair of symmetric conical intersections. This situation was also encountered in the aminobenzonitrile study. Let us consider that we have a C_{2v} molecule (a planar molecule for example), where this symmetry is lowered to the C_s point group by a pyramidalization where a conical intersection occurs. The pyramidalization is a non-totally symmetric deformation, such that the "up and down" sides are equivalent. Hence, if the system has a conical intersection at an up-pyramidalized geometry it also has an equivalent conical intersection at the corresponding down-pyramidalized geometry (mirror image). Therefore, both directions must be modified in the exact same way (Fig. 20). This strategy was used to describe the pair of C_s S_1/S_2 conical intersections in the aminobenzonitrile system, see Chapter IV.

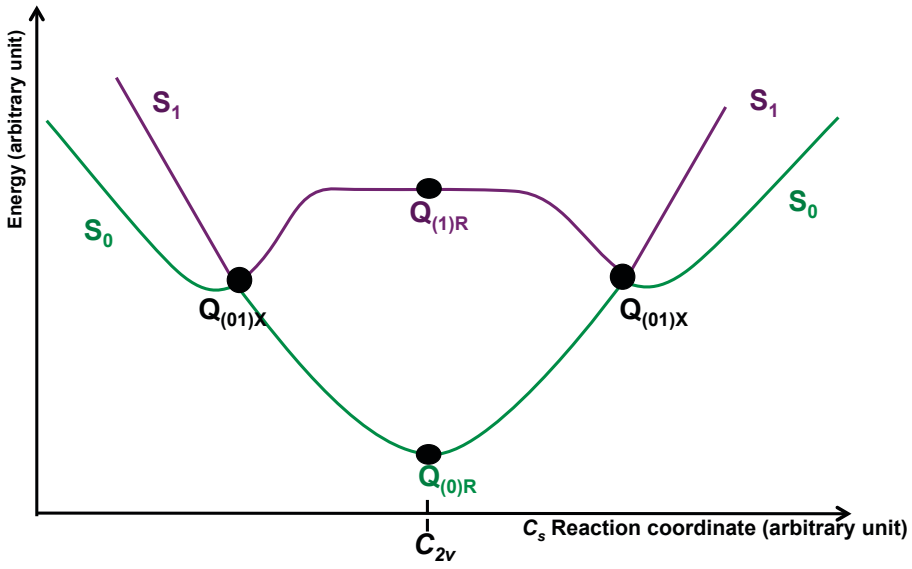

Fig. 20 Illustration of a situation where there is a pair of symmetric conical intersections.

The symmetric switch function (Fig. 21) reads

$$F_{\text{switch,symm}}\left(\varepsilon_{ii}^{(ij)}\right) = \frac{1+\tanh\left(C_2\left(\varepsilon_{ii}^{(ij)}-\varepsilon_{ii,0}^{(ij)}\right)\right)}{2} + \frac{1-\tanh\left(C_2\left(\varepsilon_{ii}^{(ij)}+\varepsilon_{ii,0}^{(ij)}\right)\right)}{2} \qquad \textbf{Eq. 100}$$

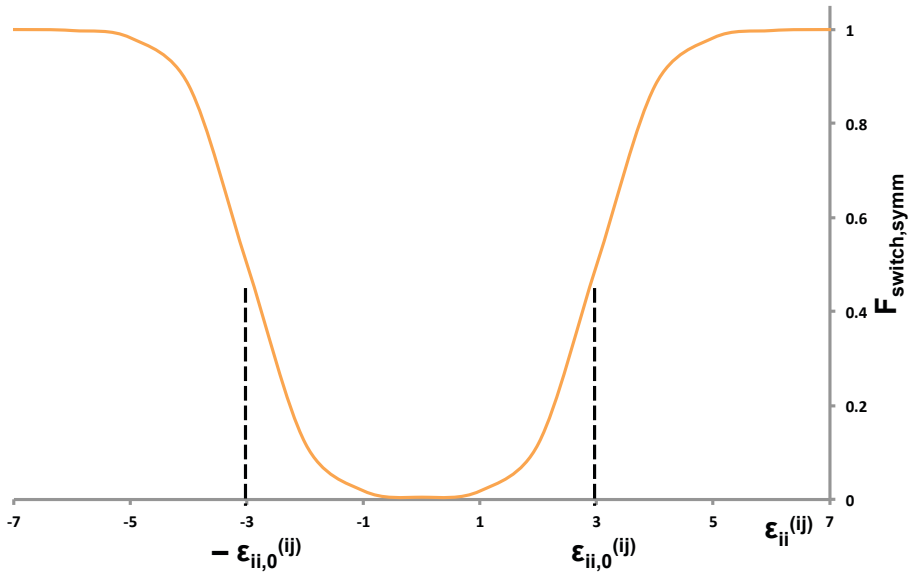

Fig. 21 Symmetric switch function of Eq. 100 centered around 3 and -3 with C_2=1.

Hence, the switch modified diagonal quasidiabatic potential energy surface and the new curvature to constrain the conical intersection energy $\check{f}_{ii,R}^{(ij)}$ read,

$$H_{ii}^{\text{diab,Switch,symm}}(\mathbf{Q}) = H_{ii}^{\text{diab}}(\mathbf{Q}) + \frac{1}{2}\check{f}_{ii,R}^{(ij)}\left(F_{switch,symm}\left(\varepsilon_{ii}^{(ij)}\right) - F_{switch,symm}(0)\right)\varepsilon_{ii}^{(ij)^2}, \quad \textbf{Eq. 101}$$

$$\check{f}_{ii,R}^{(ij)} = \frac{2\left(V_{\alpha}\left(\mathbf{Q}_{(\alpha\beta)X}\right) - H_{ii}^{\text{diab}}\left(\mathbf{Q}_{(\alpha\beta)X}\right)\right)}{\left(F_{switch,symm}\left(2\varepsilon_{ii,0}^{(ij)}\right) - F_{switch,symm}(0)\right)\left(2\varepsilon_{ii,0}^{(ij)}\right)^2} \quad \textbf{Eq. 102}$$

All these possible variants of switch functions are implemented within the PAnDA program and work routinely. However, the last case with the symmetric switch function can be more tedious in practice because it is sensitive to the symmetry of the original quadratic Hessian. One must "clean" it with respect to the higher symmetry point group (here C_{2v}) to make sure that the switch modification of the potential energy is numerically identical on both sides of the minimum. Otherwise, both conical intersections will not be described in the same way and one of them may become preferred, thus yielding a non-physical description of the dynamics of the system.

Nevertheless, the major default of this switch strategy is that it is not compatible with the "MCTDH format". In other words, the switch function applied along a specific direction is not separable into a sum of product of one-dimensional functions when using the original set of coordinates (because of the expression of the hyperbolic tangent). So, the strategy is to make a change of set of coordinates; an orthogonal transformation of the original set of coordinate is performed in order to associate a single coordinate to each $\mathbf{R}_{ii}^{(ij)}$ direction (in general, two directions are particularized: $\mathbf{R}_{11}^{(12)}$ and $\mathbf{R}_{22}^{(21)}$). The remaining linear combinations belong to the orthogonal complement. In that situation, the expressions of the quasidiabatic potential energies are now "MCTDH compatible" but the expression of the KEO in this new set of coordinate is no longer separable (as mentioned in the previous section). Thus, using a switch strategy requires the use of a numerical expression for the KEO (in our case, a

zero order approximation, i.e. a constant metric tensor). This transformation of coordinates is performed automatically with the Tnum program that reads the vectors $\mathbf{R}_{ii}^{(ij)}$ expressed in terms of the original coordinates.

We have presented the various strategies that we developed to extend the vibronic coupling Hamiltonian model to cases where anharmonicity can be an issue. They are implemented within the PAnDA program, which provides a quasidiabatic Hamiltonian matrix into the "MCTDH format" automatically once the required ab-initio calculations are made (i.e. geometries and Hessians at specific stationary points and geometry and branching space vectors of relevant conical intersections). Were used such models to run quantum dynamics with the ML-MCTDH method for two realistic application cases presented in Chapter III and IV.

Chapter III- HydroxyChromone Dyes

This Chapter is focus on the studied of the excited state proton transfer of hydroxychromone dyes (i.e. 3-hydroxychromone and 2-thionyl-3-hydroxychromone).
The study of and 2-thionyl-3-hydroxychromone was carried out in close collaboration with experimentalist the Dr. Thomas Gustavsson (CEA, France) and Prof. Rajan Das (Tata Institute of Fundamental Research, India) [on going research – paper in preparation].

We have performed a computational study of the photodynamics of 3-HC (quantum chemistry and quantum dynamics) in the gas phase and of 2T-3HC (quantum chemistry) in polar and non-polar solvents in order to suggest a rationalization of the experimental observations.

I- Introduction

Hydroxychromone dyes, much specifically 3-hydroxychromone (3-HC) (Fig. 22) and its derivatives, have attracted much interest over the last few years due to their dual fluorescence. The interplay between two emissions well separated on the frequency/wavelength domain can be modulated in a very distinct way, not only by chemical modification but also by changes in their surrounding environment. This extends dramatically the possibilities in the design of wavelength-ratiometric fluorescence sensors and probes [217–262].

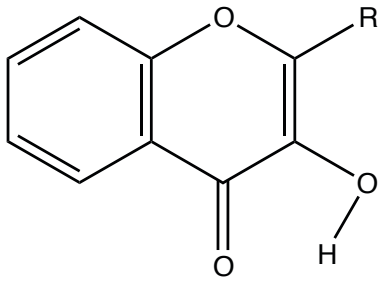

Fig. 22 Ground state Lewis structure of the 3-hydroxychromone dyes. Enol cis isomer. R = H: 3-HC.

Their remarkable spectral properties make 3-HC derivatives a useful family of fluorescent sensor of ions [247,248] and electric fields [262] in polymers [250], reverse micelles [251–253], lipid membranes [221,232,233,254–257], proteins [259], and DNA [233,246,260,261]. For example, one of the most promising 3-HC derivatives is 2-thienyl-3-hydroxychromone (2T-3HC) (Fig. 23), as modifying it with deoxyribose allows its incorporation into oligonucleotides. This makes it a possible sensor of the DNA microenvironment and DNA-protein interactions site-selectively [246,254,261,262].

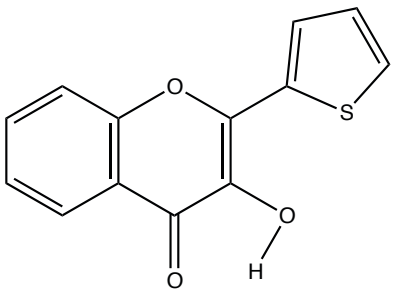

Fig. 23 Enol form of 2T-3HC.

Under the influence of UV light, 3-HC in its enol form (more stable ground-state isomer: cis, also called N is some references) undergoes an Excited State Proton Transfer (ESIPT) process in its first excited state to form the keto (tautomer) form, denoted T*, through a transition state where the transferred hydrogen is midway between both oxygen centers (Fig. 24) [263].

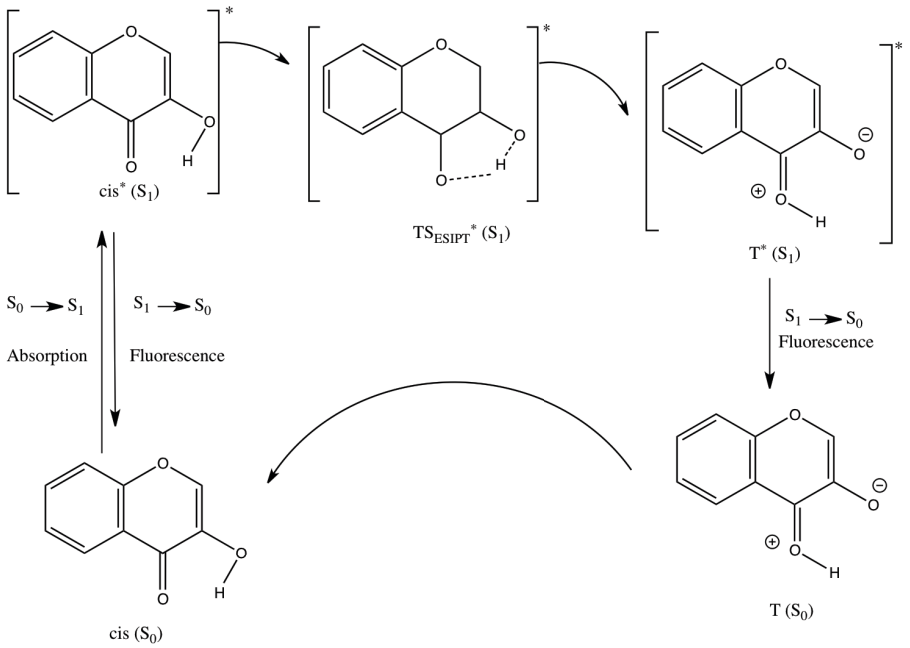

Fig. 24 Schematic representation of the ESIPT photoprocess cycle.

Both first excited state isomers (cis* and T*) have absorption bands and fluorescence bands well-separated. Their positions and intensities are very sensitive to chemical substitution, solvent polarity, but also to specific interactions such as hydrogen bonding with the surrounding medium (Fig. 25). This spectral sensitivity was significantly investigated from the experimental point of view in order to use it to monitor the physico-chemical properties of the microenvironment both from the positions and the relative intensities of their two emission bands [217–220,223–239,241–246].

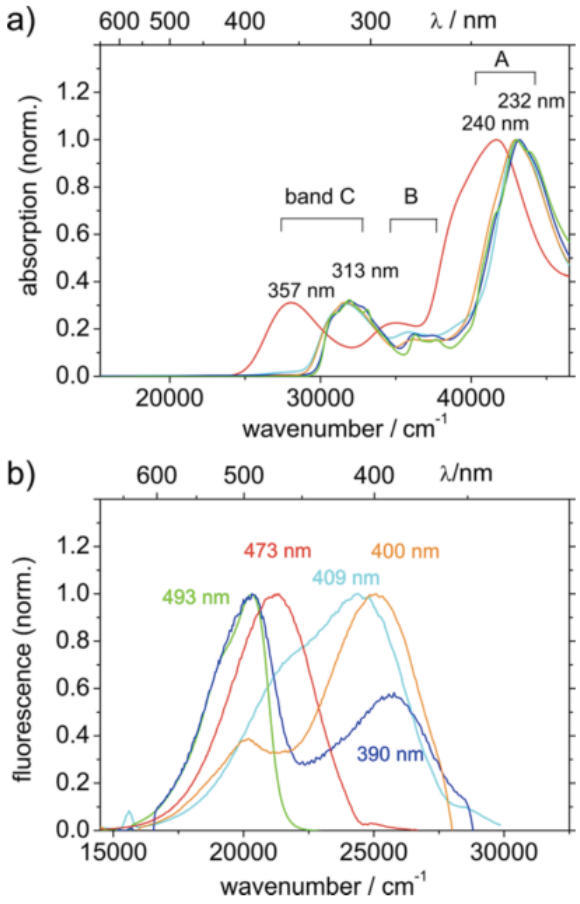

Fig. 25 (a) UV/Vis spectra of 3-HC dissolved in methylcyclohexane (green), acetonitrile (blue), ethanol (orange), and neat water at pH 7 (light blue) and pH 13 (red), with concentration varying from 5×10^{-5} to 5×10^{-4}mol.L^{-1}. (b) Static fluorescence spectra of 3-HC dissolved (4×10^{-4}mol.L^{-1}) in methylcyclohexane, acetonitrile, and ethanol as well as (5×10^{-5}mol.L^{-1}) in neat water at pH 7 and 13, color-coded as in (a) and with excitation wavelengths in the respective maxima of band C. The absorption and emission intensities have been normalized to their respective maxima. From Chevalier et al. (2013) [220].

A recent exhaustive experimental study of 3-HC into several solvents (polar, non-polar, and protic) by Chevalier et al. (2013) [220] has highlighted a unique behavior of the 3-HC molecule. The existence of two rate constants for the ESIPT process: a large one (femtosecond time scale) and a small one (picosecond time scale) irrespectively of the solvent nature. Into protic solvents, intermolecular solute-solvent interactions such as hydrogen bonds are present as well as anionic 3-HC molecules. Such interactions slow down the ESIPT process upon making the hydrogen less available for the proton transfer. However, they could not demonstrate the origin of the slow ESIPT process into aprotic polar and non-polar solvents. Nevertheless, they suggest that the trans* isomer (related to cis* on the first excited state along an out-of-plane motion of the hydrogen

torsion) could play the role of an intermediate during the ESIPT process, inducing a delay into the photoreaction, which could explain the slow ESIPT process for 3-HC (Fig. 26). One can notice that a trans* isomer of the tautomer form (T*) exists, but to reach this isomer, first the system needs to start the ESIPT process and in a second stage to activate the hydrogen torsion (out-of-plane motion). Therefore, one can expect that the –trans-T* isomer does not play any major role during the ESIPT process.

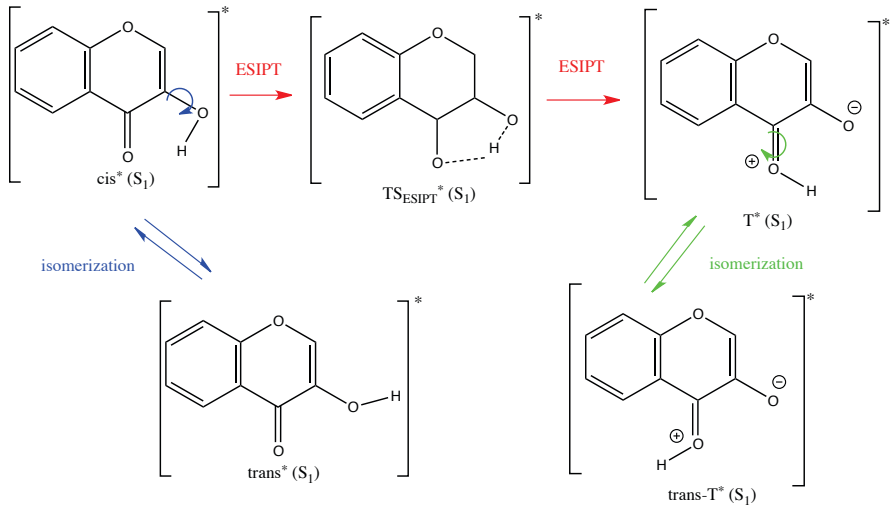

Fig. 26 Schematic representation of the geometries relevant for the ESIPT and cis-trans-isomerizations on the first excited state.

From a theoretical point of view very few studies were achieved; they were mostly focused on characterizing the protic solvent effects over spectral properties of some 3-HC derivatives to rationalize the large Stokes shift observed (defined as the difference between absorption and emission peak frequencies) [264] and to map the 3-HC direct ESIPT direction [263,265]. The latter authors optimized the ground state geometries of the cis and trans isomers. They showed that the cis isomer is the most stable species in the ground state and that it absorbs to the first excited state unlike the trans isomer. In addition, the Intrinsic Reaction Coordinate (IRC) of Ash et al. (2011) [263] on the first excited state highlights a barrierless ESIPT direction, which is consistent with the fast proton transfer process (femtosecond time scale). This result is a common feature of ESIPT processes [266–270]. Unfortunately, none of these theoretical studies investigated the role of the trans isomer on the first exited state and the physico-chemical effects behind the 3-HC ESIPT slow rate constants (picosecond time scale).

Part of this project has been conducted in close collaboration with experimentalists: Dr. Thomas Gustavsson (CEA, France) and Prof. Rajan Das (Tata Institute of Fundamental Research, India). They studied the time-fluorescence spectroscopy of 2T-3HC in several solvents. Their preliminary results show that the ESIPT process presents one fluorescence rate constant (picosecond time scale) in cyclohexane and two rate constants in polar solvents such as acetonitrile (unpublished results - paper in preparation). To the best of our knowledge, no theoretical work investigated this system, thus, we have studied the solvent polarity effect over the ESIPT process on its first excited state to rationalize experimental observations. 2T-3HC is a derivative of 3-HC where the substituent R = H is replaced by a thione fragment. Compared to the 3-HC original compound, 2T-3HC, due to its thione fragment, presents additional degrees of freedom, the most crucial one being the thione torsion (out-of-plane motion). Moreover, the thione fragment is not symmetric, thus, the isomers obtained through its torsion are not equivalent (Fig. 27). Hence, mapping the excited state potential energy surface for this system is expected to be more intricate than for the 3-HC original compound.

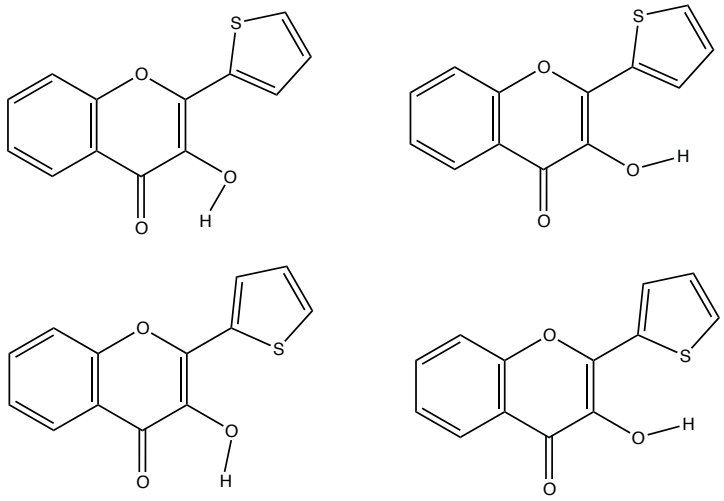

Fig. 27 Ground state structures of the four enol isomers of 2-thienyl-3-hydroxychromone.

3-HC is a prototype system for other derivatives because it is the basic unit of all flavonoid undergoing an ESIPT process and it is not perturbed by any substituent. Hence, we will first focus on understanding and characterizing the slow ESIPT process in 3-HC before studying the solvent polarity effect overt the ESIPT process in the 2T-3HC derivatives.

First, we mapped the first excited potential energy surface of 3-HC along several directions: in particular, the ESIPT direction and the hydrogen torsion (linking the cis to the trans isomers of the enol form). We showed that these two reaction coordinates occur to involve collective motions delocalized over the two rings and the CO bonds, as opposed to a simpler picture where only the transferred hydrogen would move around a rigid skeleton. We were able to optimize and characterize never-documented stationary points on this potential energy surface, which are connected to the cis-trans isomerization pathway and to an S_1/S_2 CoIn within the FC region. The existence of such a CoIn has never been discussed before and we suspect it to be, to some extent, the reason for the delay observed in the 3-HC ESIPT photoprocess upon trapping part of the system on the second excited state. The investigation of the potential energy surfaces landscapes provided the information required building a quasidiabatic model for the coupled potential energy surfaces. Then, we ran quantum dynamics calculations to demonstrate the non-negligible involvement of the CoIn and/or of the trans* isomer with respect to the ESIPT picosecond time scale rate constant.

We carried out a similar quantum chemistry study for 2T-3HC. However, in this case, we focused on understanding the solvent polarity effect over the potential energy surface landscape of the ground state and the first excited state. We highlighted the presence of two thione-rotamer channels that respond identically to the solvent polarity.

II- Computational Details

The level of theory used in this chapter for the electronic structure calculations is DFT for the ground state and TD-DFT for the excited states with the PBE0 functional [271] and an extended triple zeta basis set (i.e cc-pVTZ) implemented in the Gaussian09 package. The PBE0 functional was chosen because benchmark studies have shown that it produces excitation energies with an acceptable mean absolute error of 0.14 eV for some typical organic dyes [272,273]. In addition, it has already been used to study 3-HC derivatives [264], as it provides a good description of hydrogen bonding (necessary to describe the intermolecular hydrogen bonding between the two oxygen centers involved in the ESIPT process) [274]. Several studies compared the efficiency and

accuracy of TD-DFT with wave function methods (such as CASPT2 or CASSCF for example) over the description of the excited state involved in the ESIPT photoprocess [267–270]. They showed a gain of computational cost and a reliable description of the ESIPT energy profile.

Regarding the description of the CoIn, our level of theory may not be the most adequate [275]. Methods such as MCSCF, which include the static electron correlation required for an adequate description of a CoIn, are out of reach due to the large number of active electron in our system (19 electron for 3-HC). Nevertheless, the CoIn that we found happens to be between two excited electronic states, which are thus both calculated on the same footing, with the same method (TD-DFT). This situation is less problematic than cases where a CoIn occurs between the ground state and the first excited state, since, in that latter case, both electronic states are described at different levels (i.e. ground state: DFT and excited state: TD-DFT). This is known to often result in a poor description of the CoIn topography in its vicinity, which has been discussed in several papers in the literature [214–216,275] (this can be viewed as a generalization to TD-DFT of the Brillouin theorem for multiconfigurationnal wave functions: absence of interaction between a reference configuration and all related singly-excited configurations). In brief, the corresponding branching space is one-dimensional instead of two-dimensional because the electronic coupling is mistreated. Our situation is different, as both excited states under study are not necessarily related to each other through single excitations only. In any case, we have observed a normal behavior in the vicinity of the CoIn with a typical cusp and a two-dimensional branching space, as will be shown in this Chapter. Hence, we can be confident that our level of theory to describe the CoIn is adequate. Note that it was approximately located (i.e. not necessarily the minimum of the seam), as no CoIn optimization algorithm has been implemented yet in quantum chemistry packages for TD-DFT calculations. However, its direct accessibility from the Franck-Condon point is likely to make this point relevant.

Another point to make regarding our level of theory is about the solvent effect description for which we used the PCM model (see Chapter I). In these calculations, the absorption and emission energies are obtained taking into account the non-equilibrated solvent effect. In other words, for the absorption, the solvent is in its equilibrium state

for S_0 but not for S_1 and the other way around for the emission (a more extensive discussion about the solvent relaxation effect can be found in Chapter IV). As we are using an implicit description of the solvent (i.e. the PCM method), no explicit solute-solvent interaction such as hydrogen bonds is described, thus making the description of protic solvent effects unreliable. If one wants to investigate such solvent effects (intermolecular interactions), one needs to include explicit solvent molecule interactions, which have a significantly high computational cost [264], and possibly use non-straightforward methods such as QM/MM [276] or ONIOM [277] treatments, thus making this task even more tedious. Hence, we focused our study only on the effect of non-polar and polar solvents (mainly electrostatic interactions). In the following, we will not confront our results with experimental ones obtained into protic solvents.

III- 3-Hydroxychromone

The objective of our study is to rationalize the physical/chemical effects that explain why two rate constants are observed for the ESIPT process in 3-HC. The ground state and first excited state potential energy surfaces will be characterized to understand from a static point of view the connection between the critical points involved in the photoreactivity of this system. Our study has provided new stationary points in addition to the four already proposed in the literature (i.e cis, trans, TS_{ESIPT} and T) [263,264] as well as the discovery of a CoIn in the FC region. We suspect that this crossing between both excited states (S_1 and S_2) may play a significant role on the picosecond time scale (smaller rate constant) upon trapping the system to some extent. This hypothesis will be confirmed with non-adiabatic quantum dynamics calculations run on a model of coupled potential energy surfaces.

In what follows, when using “the hydrogen” with no further specification, we will always refer to the proton that is being transferred during the ESIPT process.

1. Potential Energy Surface Landscape

Within the usual FC picture, we consider that, after absorption of UV light, the system is promoted suddenly to the first excited electronic state. The nuclear wave packet that starts on the bright electronic state is considered as the vibrational ground state in S_0 (i.e. electronic ground state). It is centered on the FC geometry (i.e. the optimized geometry of the ground state). The width of this approximately Gaussian function along each internal coordinate is a measure of its delocalization. In our case, there is an initial FC force on the first excited state. Classically, this will lead the system to relax toward the first excited state cis minimum of the enol form, denoted cis* (Fig. 28) [263,264]. From a quantum point of view, the center of the wave packet will essentially follow the same initial relaxation direction but its widths will change as it propagates. This relaxation direction will be called the ESIPT direction, as it further leads to the excited tautomer (keto form), denoted T* (Fig. 28), as shown below. We now focus on a more detailed analysis of the shape of the potential energy surface along this ESIPT direction.

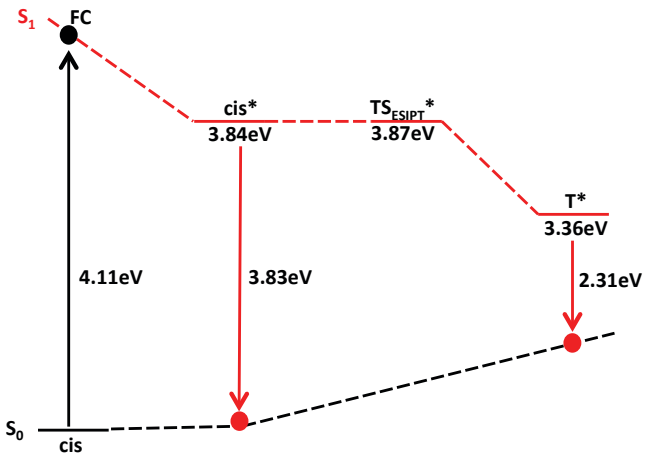

Fig. 28 Scheme of the ground state (black) and the first excited state (red) potential energy curves along the ESIPT direction. All energies are given in eV. Stationary points energies are given as differences with respect to the cis ground state energy. Vertical transition energies from cis (absorption) and from cis* and T* (fluorescence) are also indicated.

1-1 The ESIPT Direction

One can rationalize the geometry relaxation on the first excited state, from the FC point (i.e. vertical transition from the ground state global minimum, cis) to the cis* minimum, upon analyzing the bonding interactions within the singly-occupied orbitals involved in the first excited state (i.e. single electron excitations from the ground state) (see Fig. 29, Fig. 30 and Tab. 2).

As already mentioned, the first excited state differs from the ground state mainly by the excitation of a single electron between two orbitals: π (HOMO) to π* (LUMO) (ππ* electronic state). This implies a change in the bonding pattern of the electron distribution, hence a change in the geometry of the minimum. There are three possible types of local interactions between the orbitals of a bond: bonding, non-bonding, anti-bonding. If the local interaction in a bond goes, for example, from bonding (within the HOMO) to non-bonding or anti-bonding (within the LUMO), the bond length increases as it is destabilized, and the other way around if the local interaction goes from anti-bonding or non-bonding to bonding, etc. All the possible types of excitation combinations between the HOMO and LUMO orbitals with their effects on the bond lengths are displayed in Tab. 1. As will be discussed below, ambiguous cases will require some extra information.

Tab. 1 All possible changes of local bonding patterns from the HOMO to the LUMO orbitals and whether they stabilize or destabilize the corresponding bond. The respective evolution of the bond length ($||\mathbf{r}||$) is given.

LUMO / **HOMO**	**Non-Bonding**	**Bonding**	**Anti-Bonding**
Non-Bonding		Stabilization: $||\mathbf{r}||$ decreases	Destabilization: $||\mathbf{r}||$ increases
Bonding	Destabilization: $||\mathbf{r}||$ increases		Destabilization: $||\mathbf{r}||$ increases
Anti-Bonding	Stabilization: $||\mathbf{r}||$ decreases	Stabilization: $||\mathbf{r}||$ decreases	

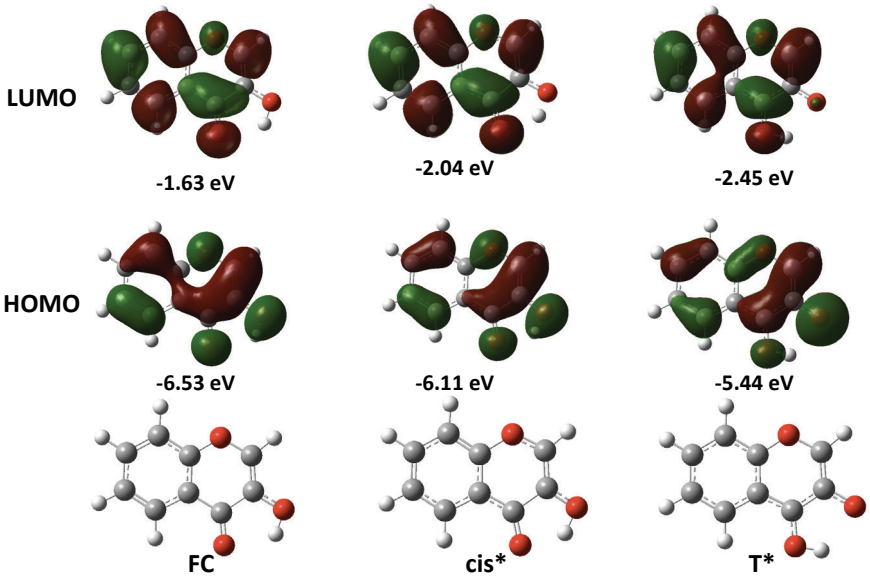

Fig. 29 HOMO and LUMO orbitals with their energies at the FC, cis*, and T* geometries.

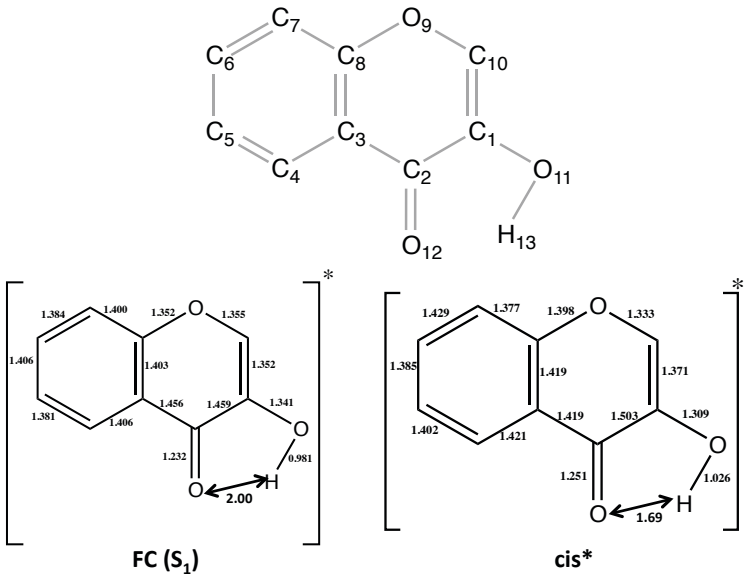

Fig. 30 Upper panel: atoms labels. Lower panel: FC and cis* bond lengths in angstrom.

Tab. 2 HOMO and LUMO local bonding patterns at the FC geometry. Δr is defined as the bond length difference between cis* and FC geometries ($\|\mathbf{r}_{\mathbf{cis}^*} - \mathbf{r}_{\mathbf{FC}}\|$)

Bond	HOMO interaction	LUMO interaction	Δr (Å)
C_1-C_2	Bonding	Non-bonding	0.044
C_2-C_3	Bonding	Bonding	−0.037
C_3-C_4	Anti-bonding	Anti-bonding	0.015
C_3-C_8	Bonding	Anti-bonding	0.016
C_4-C_5	Bonding	Anti-bonding	0.021
C_5-C_6	Anti-bonding	Bonding	−0.021
C_6-C_7	Bonding	Anti-bonding	0.045
C_7-C_8	Non-bonding	Bonding	−0.023
C_8-O_9	Non-bonding	Anti-bonding	0.046
O_9-C_{10}	Anti-bonding	Anti-bonding	−0.022
C_{10}-C_1	Bonding	Non-bonding	0.019
C_1-O_{11}	Anti-bonding	Non-bonding	−0.032
O_{11}-H_{13}	Bonding	Non-bonding	0.045
C_2-O_{12}	Anti-bonding	Anti-bonding	0.019

One can notice in **Tab. 2**, that the general rule to predict the geometry relaxation works in all cases where there is a change in the type of local interaction (e.g. bonding to anti-bonding). However, when the type of interaction for a bond is the same in the HOMO and LUMO, one could expect negligible geometrical change. This is not what we observed in our case: several bonds such as C_2-C_3, C_3-C_4, O_9-C_{10}, and C_2-O_{12} experience deformations. This can be understood upon considering a more subtle effect: the change of local density around the two atoms of the bond at the FC geometry (see **Fig. 31**). This does not necessarily induce a change of type of bonding interaction for a given bond. The quantity plotted on **Fig. 31** represents the electron density difference between the LUMO and HOMO orbitals. If the electron density increases on the two atoms of the bond, this means that the interaction type will be exalted once in the excited state. In other words, the molecular orbital becomes more bonding or more anti-bonding in the excited state for this bond. For example, the C_2-C_3 bond is bonding in the HOMO and LUMO. However, the local density on this bond increases in the first excited state. This

results in a stabilization of the bond (i.e. the bond length decreases), as its molecular orbital is more bonding in the first excited state. The C_2-C_3, C_3-C_4, O_9-C_{10} and C_2-O_{12} bond evolutions are displayed in **Tab. 3.**

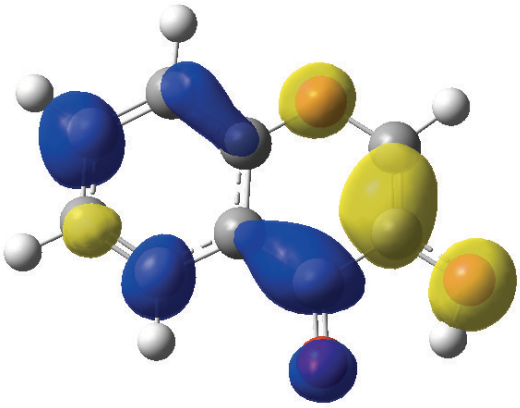

Fig. 31 Electron density difference between the densities of the LUMO and HOMO orbitals at the FC geometry. Blue: gain of electron density. Yellow: loss of electron density.

Tab. 3 Local density evolution for each bond between the HOMO and LUMO orbitals in Fig. 31. ₸Evolution of the interaction types from the ground state to the first excited state of the specific bond. °Corresponding evolution of the bond length ($||\mathbf{r}||$).

Bond	Local density	Bond type interaction₸	$\|\|r\|\|$ evolution°
C_2-C_3	Increases	More bonding	Stabilization: decreases
C_3-C_4	Increases on C_4	More anti-bonding	Destabilization: increases
O_9-C_{10}	Decreases on O_9	Less anti-bonding	Stabilization: decreases
C_2-O_{12}	Increases	More anti-bonding	Destabilization: increases

In addition, Fig. 31 highlights the Charge Transfer (CT) character of the first excited state with respect to the ground state at the FC geometry. One can notice that the electron density goes from the O_{11}-H region to the C=O_{12} bond (and to some extent to the benzene ring). This charge redistribution induces a change in the dipole moment direction of the first excited state with respect to the ground state (see Fig. 32). In the ground state, the dipole moment direction is due to the O-C polar bonds because oxygen atoms are more electronegative than carbon and hydrogen atoms. While on the first excited state at FC, as already mentioned, the electron density moves from the O_{11}-H

region to the C=O_{12} bond, which induces a separation of charge. This formally results in a negative charge on O_{12} and a positive charge on O_{11} on the corresponding Lewis structure (Fig. 32). One can notice that regarding the S_1 Lewis representation, we focus on rationalizing the O_{11}-H···O_{12} / O_{11}···H-O_{12} fragment, putting aside the electronic redistribution of the rest of the system. In addition, a single Lewis representation is not always enough to describe the electronic structure of excited states (this reflects their multiconfigurational character, more frequent than for typical closed-shell ground states). Hence, our Lewis interpretation is tentative and could be written in a different way, such as in Refs. [228,231,234,238,239,244,245,266,278]. One point of discussion about our Lewis representation is about the formal charge on O_{11} and O_{12}. At FC the CT character is characterized by the separation of charge induced by the electronic redistribution on the first excited state. However, the magnitudes of dipole moments of the first excited and ground electronic state are similar. This indicates a weak CT character with respect to the ground state in terms of magnitude. Hence, the formal charges in our Lewis representation could perhaps be replaced by radicals, with a different charge redistribution in the remaining of the molecule. In any case, the small change in the magnitude of the dipole moment is consistent with experimental observations regarding the absence of shift in the UV/vis absorption spectrum while increasing the solvent polarity (of aprotic solvent) indicating a weak CT character of 3-HC [220,226,234].

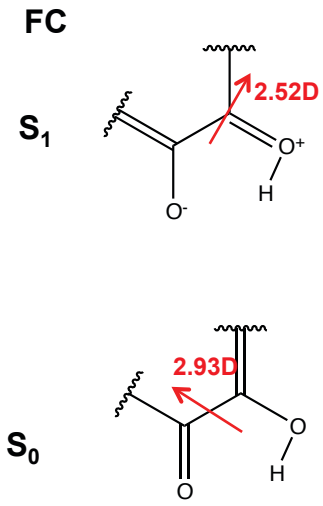

Fig. 32 Lewis representations and dipole moments (in Debye) of the FC geometry on S_0 and S_1.

As already explained, this change of nature of the electronic state induces a longer C=O_{12} bond and a shorter C-O_{11} bond at the cis* geometry, as well as a longer O_{11}-H bond and a shorter O_{12}-H distance (stronger H-bond). This is consistent with cis* being a precursor for a further ESIPT process. Simply, transferring the proton in the first excited state goes with removing the formal charges on both O_{11} and O_{12}. This emphasizes the idea that the driving force of an ESIPT process is based on the acidity of the proton donor (i.e. its ability to give the proton losing electron density) and the basicity of the proton acceptor (ability to accept the proton gaining electron density) [240,266,267,279–282].

This prediction is confirmed by the following observation: once the system relaxes from FC to the cis* minimum, it goes along the ESIPT direction to form the tautomer (T*) through an almost barrierless process (0.03 eV) (Fig. 28), which is consistent with an ultrafast ESIPT process on the femtosecond time scale (larger rate constant).

The absence of a barrier can be understood by analyzing the HOMO and LUMO orbitals at the cis* and T* geometries (Fig. 29). One can notice that they are very similar in terms of shape at both points, which means that there is no major electronic reorganization along the ESIPT coordinate. In other words, this direction does not influence much the electronic structure of the first excited state, which keeps its original diabatic character along this direction. Indeed, both the HOMO and LUMO stay essentially the same antisymmetric orbitals with respect to the molecular plane, i.e. out-of-plane orbitals (π and π* respectively), whereas the ESIPT coordinate essentially alters the in-plane σ system involved locally in the O_{11}-H···O_{12} / O_{11}···H-O_{12} fragment during the proton transfer.

The tautomer (T*) is a fluorescent minimum. In other words, at this geometry, the system relaxes from the first excited state to the ground state by emission of a photon. However, no tautomer minimum could be found on the ground state. Again, this can be rationalized in terms of frontier orbitals. The ground state is a closed-shell system (two electrons in the HOMO). Then, the total energy depends mainly on the HOMO energy [283], which is higher in the tautomer (S_0) than in the cis (S_0) geometry (Fig. 28 and Fig. 29). The absence of tautomer minimum on the ground state was observed in several other ESIPT systems such as salicylic acid for example [266,268–270].

Note that the evolution of the electronic structure of 3-HC during the ESIPT process on the first excited state has been interpreted by Alexander P. Demchenko et al. (2013) [266] in terms of Charge Transfer (CT) and Proton Transfer (PT) diabatic states (see Fig. 33). Our results show that the main configuration is essentially the same ππ* along the ESIPT coordinate. This is not necessarily in contradiction with the previous interpretation if the coupling, hence the mixing, between the CT and PT states is large at all points (strongly avoided crossing). If so, this merely is a difference of point of view with respect to the definition of the diabatic states. In addition, the dominant configuration is not the only one to be involved in the electronic state, which means that other configurations could be responsible of the CT/PT mixture. In any case, this description is interesting, as it explains the occurrence of a small barrier corresponding to a strongly avoided crossing.

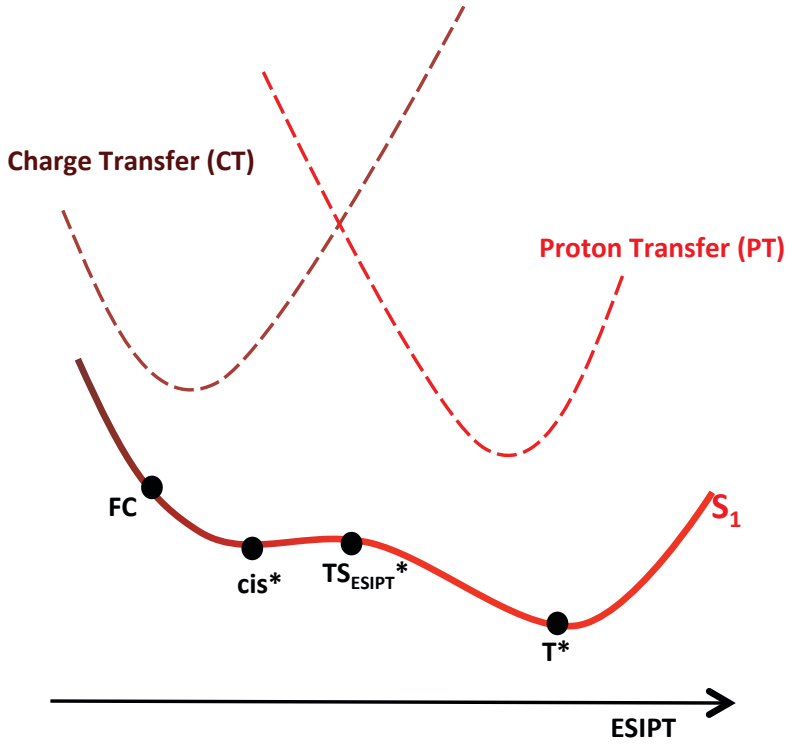

Fig. 33 Scheme of principle of the charge transfer ad porton transfer diabatic states (dashed lines) and S_1 adiabatic state (plain line) along the ESIPT coordinate.

Fig. 31 already suggests the existence of a CT character at the FC geometry upon strong charge redistribution after the excitation of the first excited state. Fig. 29 highlights the weak electronic reorganization of the π and π* molecular orbitals along the ESIPT

direction. This means that the CT character at FC and cis* (enol form) is strongly coupled with the PT character of the keto form (T*), i.e. the adiabatic ππ* electronic state is strongly shifted with respect to the diabatic CT and PT electronic states, leading to a barrierless ESIPT process and a weak CT character [266] (see Fig. 33). Those interpretations are compatible with the evolution of the dipole moment and our following Lewis representations depicted in Fig. 34. The dipole moments of FC and cis* are similar, the small difference in magnitude and direction is induced upon geometry relaxation; hence, one can conclude that cis* geometry is essentially related to the same CT diabatic electronic state as FC. At T*, the dipole moment is smaller than at cis* and in another direction. This is compatible with the fact that at T*, the proton get transferred to neutralize the charge separation. This explains that T* is the global minimum on the first excited state.

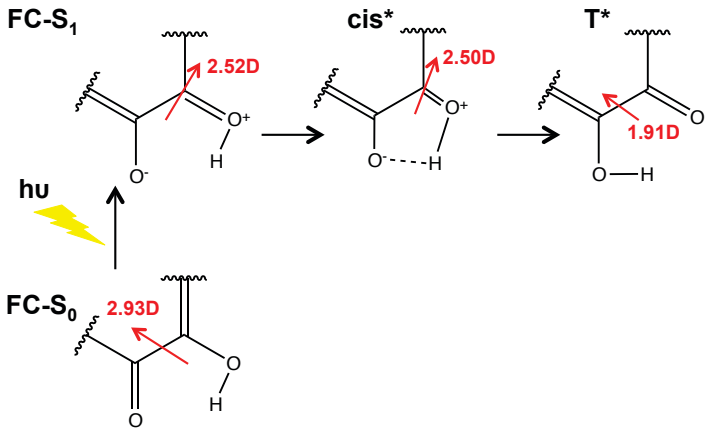

Fig. 34 Lewis representations and dipole moments (in Debye) at FC on S_0 and S_1, cis*, and T*.

At this point, we have shown that the barrierless potential along the ESIPT direction could explain the larger rate constant (femtosecond time scale) as characterized in other ESIPT systems [268–270]. However, nothing has been proposed yet to explain the smaller rate constant (picosecond time scale). Hence, we have investigated the potential energy surface along other directions. First, along an in-plane deformation coordinate (preserving the C_s symmetry) opposite to the ESIPT direction, we were able to locate a CoIn. In other words, the first two excited electronic states (i.e. S_1, S_2) cross along this direction, as discussed below. The existence of a such a CoIn in other ESIPT systems (i.e. malonaldehyde, *o*-hydroxybenzaldehyde, 7-hydroxy-1-indanone, and 2-(2'-

hydroxyphenyl)benzothiazole) was suggested by Aquino et al. (2005) [268] but never fully characterized.

1-2 Description of the S_1/S_2 Conical Intersection

The S_1/S_2 CoIn that we found is peaked: it connects two lower-energy stationary points on the first excited state: the cis* minimum and a never documented transition state, denoted TS_2* (Fig. 35). The geometry of the CoIn is similar to the FC point and its energy is only 0.13 eV higher. This makes it potentially accessible by the initial packet when accounting for its delocalized character in space and for the width of the energy distribution that reflects light absorption within a Franck-Condon picture. The extent to which the CoIn region is explored will be discussed based on results obtained from numerical simulations presented in the next section.

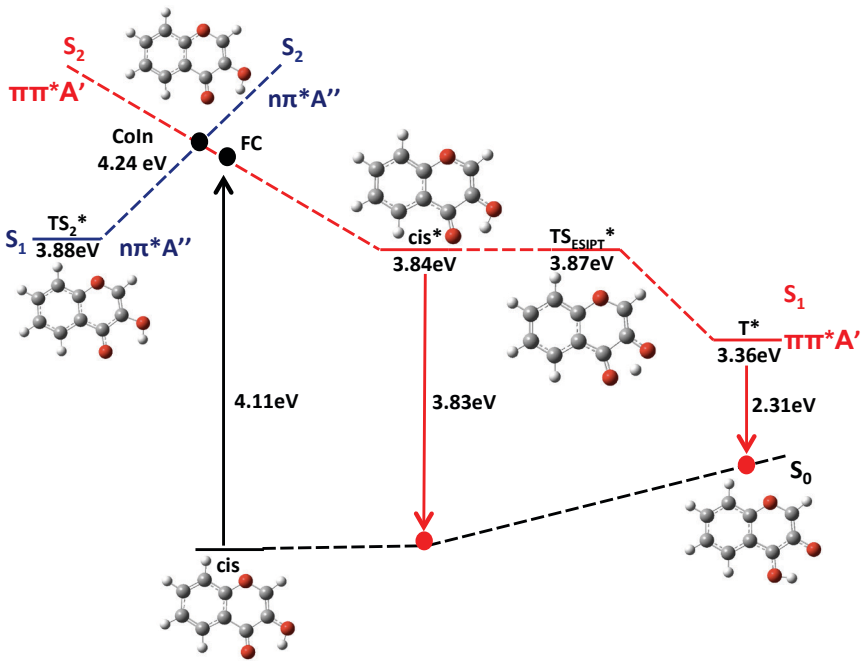

Fig. 35 Scheme of the diabatic and adiabatic potential energies along the ESIPT reaction coordinate. Blue: nπ* (A") Red: ππ* (A'). All energies are given in eV. Stationary points energies are given as differences with respect to the cis (S_0) energy.

Characterizing a CoIn requires to analyze the electronic structure involved in the electronic states that cross. Thus, we analyzed the dominant configurations in the

electronic structures of the first and second excited states at both stationary points (i.e. TS_2* and cis*) directly connected to the CoIn.

At the cis* geometry, the dominant configurations in the electronic wave functions of the first two excited states are similar to the ones at FC and mostly correspond to single excitations. The first excited state is ππ* and the second one is mainly characterized by a single excitation from the essentially non-bonding orbital localized on the oxygen of the C=O_{12} bond to the same π* orbital (LUMO). It will thus be referred to as an nπ* electronic state (Fig. 36). At the TS_2* geometry, the situation is the opposite: the nπ* electronic state is now the first excited state, while the second excited state is ππ* (Fig. 36).

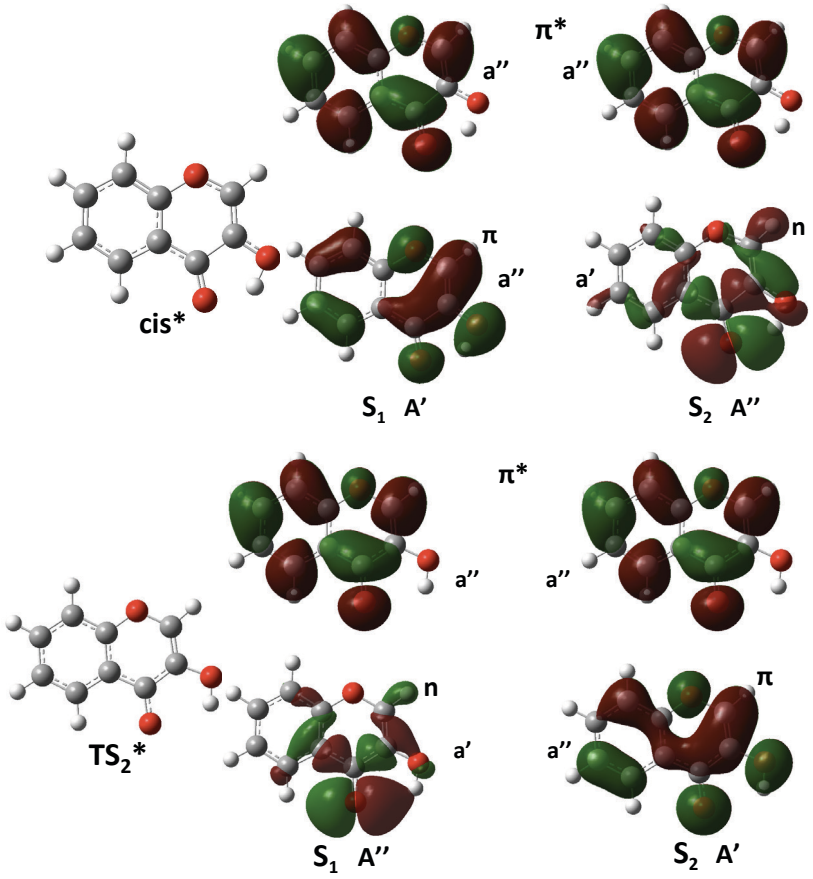

Fig. 36 Singly occupied orbitals at the cis* and TS_2* geometry for the first (S_1) and second (S_2) excited states. The symmetries of the orbitals and electronic states refer to the C_s point group.

Visual inspection of Fig. 36 shows that the n, π and π* orbitals at cis* and TS_2* are essentially the same. Hence, the CoIn in Fig. 35 can be rationalized, as illustrated and Fig.

37, in terms of a correlation diagram showing a crossing between the ππ* and nπ* configurations along a direction connecting the cis* and TS_2* geometries.

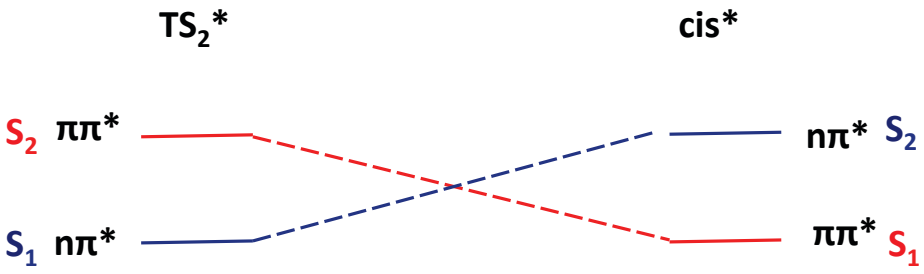

Fig. 37 Electronic state correlation diagram between TS_2* and cis* geometries.

As shown on Fig. 37, there is a crossing between S_1 and S_2 in terms of their dominant configurations nπ* and ππ*. This is confirmed in Tab. 4. Let us make a remark at this stage. Qualitative interpretations based on relative orbital energies are not always valid. For example, here, the orbitals of interest are n, π, and π*. One would have expected the first excited state to come mainly from a HOMO to LUMO excitation and the second excited state from a HOMO-1 to LUMO excitation and thus to observe a crossing of the HOMO and HOMO-1 orbitals but this is not the case. Indeed, this simplistic picture in terms of orbital energies does not account for electron correlation effects. For example, electronic repulsion may be too large to estimate the energy of the state simply upon adding the energies of the occupied orbitals (consider for instance the ground state configurations of the atoms in the d-block that do not follow the Klechkowski rule). In addition, a description based on a single-configuration picture is only an approximation. There is some influence of the other configurations in the state energies. Tab. 4 shows that the electronic structures (obtained at the TD-DFT level of calculation) of the first two excited states are mostly, but not fully, mono-configurational. The largest coefficient (dominant electronic configuration) is about 0.7 at all points for both states. However, the second coefficient is small but not negligible (about 0.1) and thus characterizes some electron correlation brought by the corresponding configurations into the electronic states.

Finally, it should be stressed that we are examining Kohn-Sham (DFT) orbitals. They can be interpreted in much the same way as Hartree-Fock orbitals in terms of their shape

[284] but the physical meaning of their energies and of their contributions to the total energy is unclear (especially for orbitals other than HOMO-LUMO) [285,286]. In our case, it proved not to be adequate to use Kohn-Sham orbital energies when building an orbital correlation diagram between the cis* and TS_2* geometries. However, the configuration correlation diagram displayed in Fig. 37 can be trusted as a faithful representation of the states and how they cross (Fig. 37).

Tab. 4 Summary of the first two excited state main electronic configurations named from their singly occupied orbitals and their coefficients (absolute values) obtained with the TD-DFT method.

	TS_2*	**FC**	**cis***
S_1	$n\pi^*$: 0.69	$\pi\pi^*$: 0.69	$\pi\pi^*$: 0.69
	$n\pi_3^*$: 0.10	$\pi_2\pi_2^*$: 0.10	< 0.1
S_2	$\pi\pi^*$: 0.68	$n\pi^*$: 0.69	$n\pi^*$: 0.69
	$\pi_2\pi_2^*$: 0.10	$n\pi_3^*$: 0.12	$n\pi_3^*$: 0.12

The CoIn is a crossing point between a $\pi\pi^*$ (A') and an $n\pi^*$ (A'') electronic state. Using the different symmetries of the electronic states will be helpful to characterize the CoIn branching space vectors. The symmetry of the dominant configuration, hence of the singly occupied orbitals, can be used to characterize the symmetry of the electronic state (the symmetry of the other configurations is, of course, the same than the main one due to vanishing interactions between configurations of different symmetries). As already mentioned, at the cis* geometry, the first excited state is $\pi\pi^*$. Within the C_s point group, both orbitals have a" symmetry, then the symmetry of the first excited state is $A" \otimes A" = A'$. The second excited state is of $n\pi^*$ type. The non-bonding orbital on the oxygen has a' symmetry and π^* is a". Then, the symmetry of the second excited state is $A' \otimes A" = A"$. At the TS_2* geometry, it is the other way around. The first excited state is A" ($n\pi^*$) and the second excited state is A' ($\pi\pi^*$) (see Fig. 35 and Fig. 36).

As the excited states have different symmetries (A' and A"), we are in a situation where the CoIn is said to be induced by symmetry and its branching space is well defined with respect to symmetry (this, because the gradients and derivative couplings are produced from adiabatic states that have well defined symmetries) (see Chapter I and II). The branching space vectors (i.e. gradient difference and derivative coupling) are displayed

in Fig. 38. Along the gradient difference ($\boldsymbol{x}^{0(23)1}$) direction, which is A', the C_s symmetry is conserved. This direction essentially connects the cis* and the TS_2* geometries via the FC point. It consists in an in-plane deformation mostly localized on the fragment undergoing the ESIPT process. The derivative coupling ($\boldsymbol{x}^{0(23)2}$) breaks the C_s symmetry of the molecular system and mixes both electronic states (i.e $A' \otimes A'' = A''$); it is an out-of-plane motion involving mainly the hydrogen torsion (as suggested by Aquino et al. (2005) [268]). Note that TD-DFT calculations do not produce analytic derivative couplings. The branching space was thus obtained with a numerical method based on the local shape of the double cone (see Appendix B) [73]. As already mentioned, using TD-DFT in the present situation, between two excited states, occurred not to suffer from the usual deficiencies of this method when applied to a crossing between the ground state and an excited state (for which the crossing is often ill-defined and the coupling vanishes). We checked that, as expected, both branching space vectors lifted degeneracy to first order correctly as illustrated in Fig. 39.

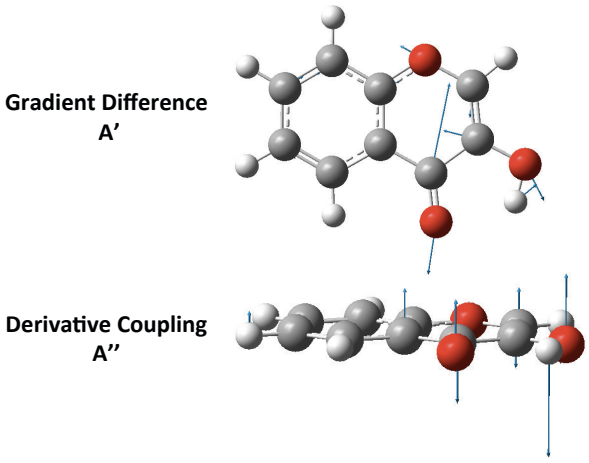

Fig. 38 Branching space vectors of the CoIn obtained with the numerical procedure. Upper panel: gradient difference, in-plane vectors. Lower panel: derivative coupling, out-of-plane vectors.

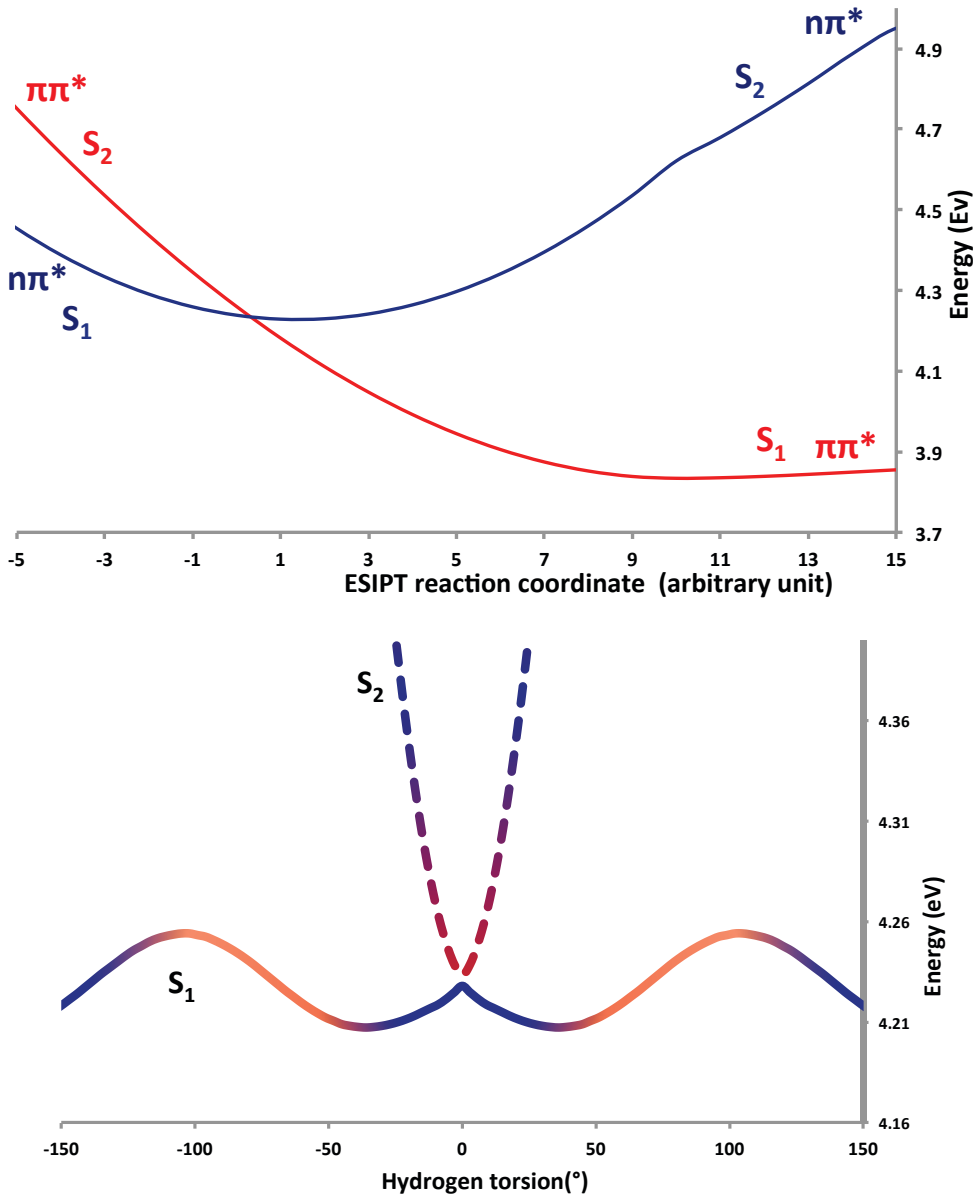

Fig. 39 Upper Panel: Scan along a C_s in-plane deformation equivalent to $x^{0(23)1}$ (GD) from the CoIn red: ππ* electronic state blue: nπ* electronic state. Lower panel: Scan along the hydrogen torsion from the CoIn; plain line: first excited state (S_1); dashed line: second excited state (S_2). Their colors are not uniform to show that the diabatic electronic states (ππ* and nπ*) mix along the derivative coupling direction ($x^{0(23)2}$-DC). Energies are given in eV as differences with respect to the global minimum energy on the ground state, i.e. cis (S_0).

Along the gradient difference (ESIPT direction), as already explained, the C_s symmetry is conserved. In other words, along the gradient difference, the ππ* and nπ* electronic states do not mix. Therefore, along C_s-conserved symmetry directions, the quasidiabatic electronic Hamiltonian is diagonal (no electronic coupling) leading to a particular case where the quasidiabatic electronic basis is identical to the adiabatic electronic basis except for the adiabatic state ordering that swap from on side to the other side of the

crossing: the lower-energy state, S_1, is identical to ππ* on the cis* side and to nπ* on the TS_2* side, and the reverse for S_2, as long as C_s symmetry is preserved (see Fig. 37).

The derivative coupling breaks the C_s symmetry and acts essentially along the out-of-plane hydrogen torsion motion. Tab. 5 displays the main configurations at the CoIn (H is 0° out of the molecular plane) and along the derivative coupling (H is ± 21° out of the molecular plane). This illustrates the mixing of the ππ* and nπ* electronic states (the quasidiabatic electronic Hamiltonian now is non-diagonal) as the adiabatic electronic states now show a relevant mixture of configurations while breaking the C_s symmetry.

Tab. 5 Summary of the first two excited state main electronic configurations named from their singly occupied orbitals and their coefficients (absolute values) at different points along the hydrogen torsion angle.

	0°	**21°**
S_1	ππ*: 0.68	nπ*: 0.62
		ππ*: 0.24
S_2	nπ*: 0.69	ππ*: 0.64
	ππ*: 0.12	nπ*: 0.23

In addition, one can notice the possible existence of two stationary points when H is ± 40° and 100° out of the plane of the molecule with respect to the CoIn. One should keep in mind that the potential energy surface along the hydrogen torsion depicted in Fig. 39 is a rigid scan. In such a case, the geometry parameters are kept constant (except for the scan-coordinate), hence, what seems to be stationary points on the scan are not optimized geometries. Therefore, one should expect the out-of-plane hydrogen torsion angle of the respective optimized geometries to be different from these approximate values.

Moreover, the symmetry of the derivative coupling (out-of-plane equivalent clockwise and anticlockwise motions) and its magnitude have as a consequence: the creation of two symmetric minima (denoted Min_+* and Min_-*) on both sides of the aforementioned TS_2* point. These three points define a flat region (barrier of 0.002 eV), with respect to the hydrogen torsion (transition vector deriving from the derivative coupling) where H is ±21.7° out of the molecular plane at the minima; this is an example of second-order

Jahn-Teller effect creating a negative curvature at the transition state (Fig. 40). Both minima around the transition state (i.e. Min_+* and Min_-*) correspond to the approximate constrained minima inferred from Fig. 39 where H was ±40° out of the molecular plane with respect to the CoIn. The occurrence of three minima around the crossing (cis*, Min_+*, and Min_-*) can be seen as a reminiscence of the prototypical threefold Jahn-Teller Mexican hat (e.g. in the benzene cation [287–291]) to a case with less symmetry.

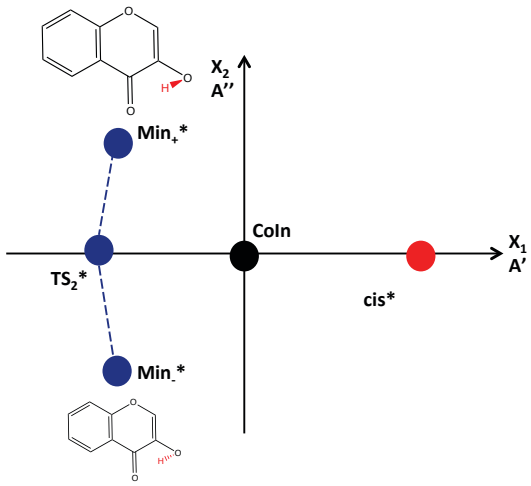

Fig. 40 Scheme of the stationary points around the CoIn in the branching space frame.

This CoIn has thus an impact on the shape of the first excited state potential energy surface. One can also expect it to have an influence over the photoreactivity of the molecule, as it is close to the FC region. Indeed, the electronic coupling within the FC region can momentarily trap part of the system on the second excited state before it decays back to the first excited state through the funnel in the second excited state (black circle on Fig. 41). In addition, its presence is the signature that the first excited state changes from ππ* on the cis* side to nπ* on the TS_2* side. So, even if there is not enough energy for a significant transfer to the second excited state, an adiabatic process involving a reaction path that "turns around" the CoIn would also result in some trapping in the S_1/nπ* state around TS_2*, thus on the wrong side with respect to the ESIPT process (blue circle on Fig. 41). Both mechanisms (respectively non-adiabatic and adiabatic) will potentially create a delay into the ESIPT rate constant and could be the origin of the picosecond time scale rate constant.

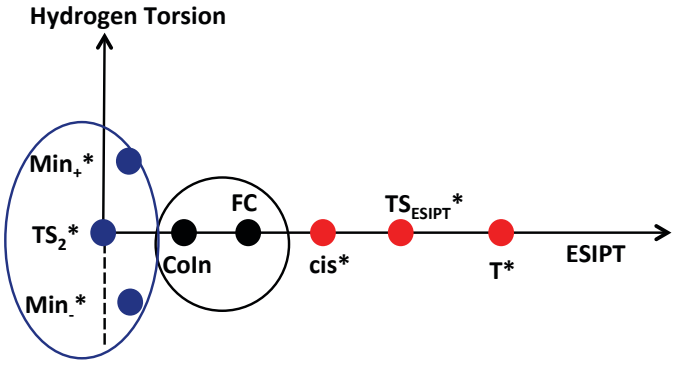

Fig. 41 Scheme of the relative positions of several stationary points along two dimensions: a global ESIPT reaction coordinate and the hydrogen torsion. Black circle: non-adiabatic trapping. Blue circle: diabatic trapping.

However, one of the hypotheses documented in previous studies to understand this low rate constant is the existence of a trans* minimum (i.e 180° out-of-plane torsion of the hydrogen) [220]. Hence, in the following part, we will focus on mapping the potential energy surface landscape around the cis* to trans* isomerization.

1-3 Study of the cis-trans Isomerization in the First Excited State.

The trans* minimum was found 0.19 eV below the FC point and 0.09 eV higher than cis*. From an energetic point of view, part of the system can access this region after photo-excitation, thus inducing a delay into the ESIPT process. So far, it is widely accepted that this trans* minimum comes from the hydrogen torsion of the cis* minimum through a single barrier [220,246,263]. In fact, we could not locate any transition state connecting directly the trans* and cis* minima. However, we did find a pair of never documented transition states between $Min_{\pm}$* and trans*, denoted TS_{τ}*, where the H torsion is ±109.43° (note that, as for $Min_{\pm}$*, there is a pair of such enantiomeric points, depending on whether TS_2* is connected to trans* either clockwise or anticlockwise). We thus propose that the isomerization minimum energy path from cis* to trans* corresponds to a two-step process that first involves a conversion from cis* to $Min_{\pm}$* (going through or around the CoIn) involving mostly in-plane skeletal deformations, followed by the hydrogen torsion connecting $Min_{\pm}$* to trans* (both clockwise and anticlockwise), as detailed below.

One can picture the relative positions of these stationary points (TS_2*, $Min_{\pm}$*, cis*, trans* and TS_{τ}*) on the first excited state along two dimensions as in Fig. 42. One must overcome a barrier of 0.09 eV to access the trans region from the TS_2* region (the flat double well including TS_2* and both $Min_{\pm}$*). This result is emphasized by the minimum energy paths that we determined on the first excited state along the hydrogen torsion both from the cis* minimum and TS_2* geometry as displayed in Fig. 43.

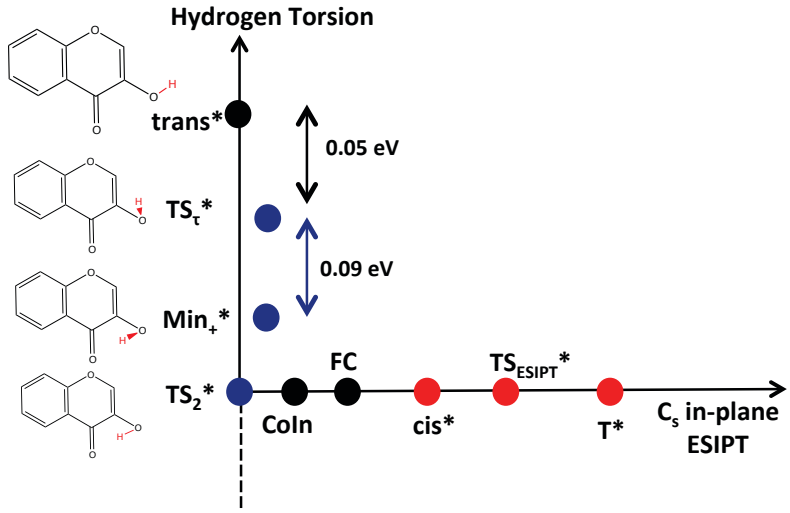

Fig. 42 Scheme of the relative positions of several stationary points along two dimensions: the ESIPT C_s in-plane coordinate and the hydrogen torsion (the corresponding energy barriers are indicated near the arrows). The periodicity of the potential energy along the hydrogen torsion is not shown on this figure for the sake of clarity.

The minimum energy path from TS_2* shows a direct pathway between the TS_2* region and the trans* minimum through TS_{τ}*. In contrast, the one from the cis* minimum shows an energy and geometry discontinuity around ±20° along the hydrogen torsion. In this minimum energy path, the system starts from a minimum (i.e. cis*) and in a first stage (Fig. 43 and Fig. 44) follows an ascending valley along the hydrogen torsion with almost no change in the other coordinates (Tab. 6). However, around ±20° of the hydrogen torsion (i.e. at the discontinuity), the system suddenly relaxes several C_s in-plane coordinates (i.e. C_1-C_2, C_2-O_{12}, O_{11}-O_{12}) (Fig. 44 stage2) and changes from the original valley to a lower valley, which happens to be the aforementioned minimum energy path going between the TS_2* region and the trans* minimum through TS_{τ}* (Fig. 44 stage3). This is proved by the C_s in-plane coordinates relaxation before and after the discontinuity displayed in Tab. 6. Before the discontinuity (i.e. B°) the bond lengths are

typical of the cis* minimum, while they become similar to these of the TS_2* point after the discontinuity (i.e. A°).

In other words, the cis*-trans* isomerization cannot be considered as a one-dimensional/one-step problem (i.e. hydrogen torsion and single barrier) but should be described rather with a two-dimensional/two-step mechanism: C_s in-plane deformation mixed with some hydrogen torsion that makes the system go trough or around the CoIn (first barrier) followed by almost pure hydrogen torsion (second barrier).

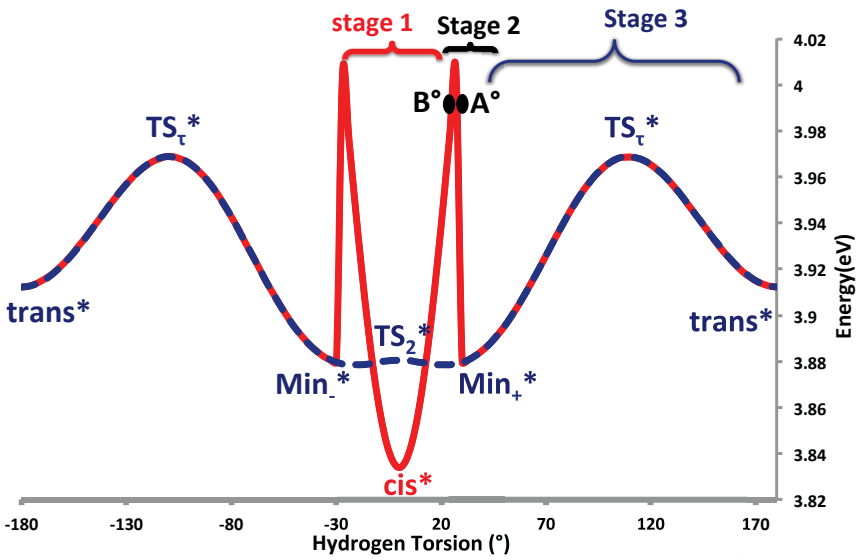

Fig. 43 Minimum energy paths along the hydrogen torsion (in degree °); red: from the cis* minimum; blue: from the TS_2* transition state. Energy difference in eV with respect to the enol global minimum in the ground state, i.e. cis (S_0) minimum. B°: Before the discontinuity; A°: after the discontinuity Tab. 6.

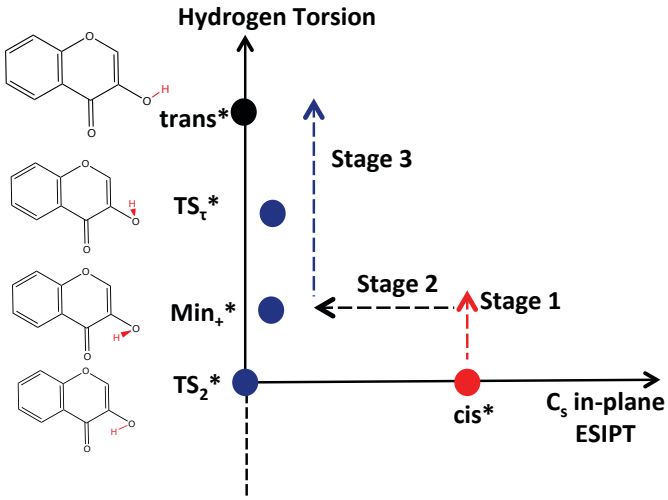

Fig. 44 Scheme of the relative positions of several stationary points along two dimensions: a global C_s in-plane coordinate and the hydrogen torsion. The three stages are related to the minimum energy paths. The periodicity of the potential energy along the hydrogen torsion is not shown on this figure for the sake of clarity.

Tab. 6 Bond lengths in angstrom (Å) of cis*, TS_2* and both "discontinuity points" along the minimum energy path from cis* to trans*: B° (before the discontinuity) and A° (after the discontinuity); see Fig. 43.

	C_1-C_2	C_2-O_{12}	O_{11}-O_{12}
cis*	1.503	1.251	2.483
B°	1.506	1.248	2.497
A°	1.425	1.314	2.80
TS_2*	1.422	1.320	2.797

Unfortunately, the minimum energy path from cis* to trans* does not give us much information about the surface landscape between cis* and $Min_{\pm}$* around the discontinuity. We suggest the existence of a pair of symmetric transition states on both sides of the CoIn and connecting cis* to $Min_{\pm}$* in much the same way as the prototypical threefold Mexican hat in the benzene cation [287–291] (illustrated in Fig. 45). In such systems, the electronic coupling induces the existence of three minima connected to each other by three transitions states on a loop around the CoIn, as illustrated in Fig. 45. Preliminary investigations of the potential energy surface in the suspected region seem to confirm this hypothesis. However, we have not been able to fully characterize this hypothetical transition state (TS 1 and TS 3 in Fig. 45) yet because of numerical

difficulties (or perhaps because there is a more complicated landscape involving some bifurcation). In any case, if there is such a pair of points (TS 1 and TS 3) between cis* and $Min_{\pm}$*, the minimum energy path that goes from cis* to trans* will still require, first, to follow a C_s in-plane deformation toward the TS_2* region (along with some hydrogen torsion contribution), which will lead to a pathway going around the CoIn; and then to turn fully along the hydrogen torsion direction.

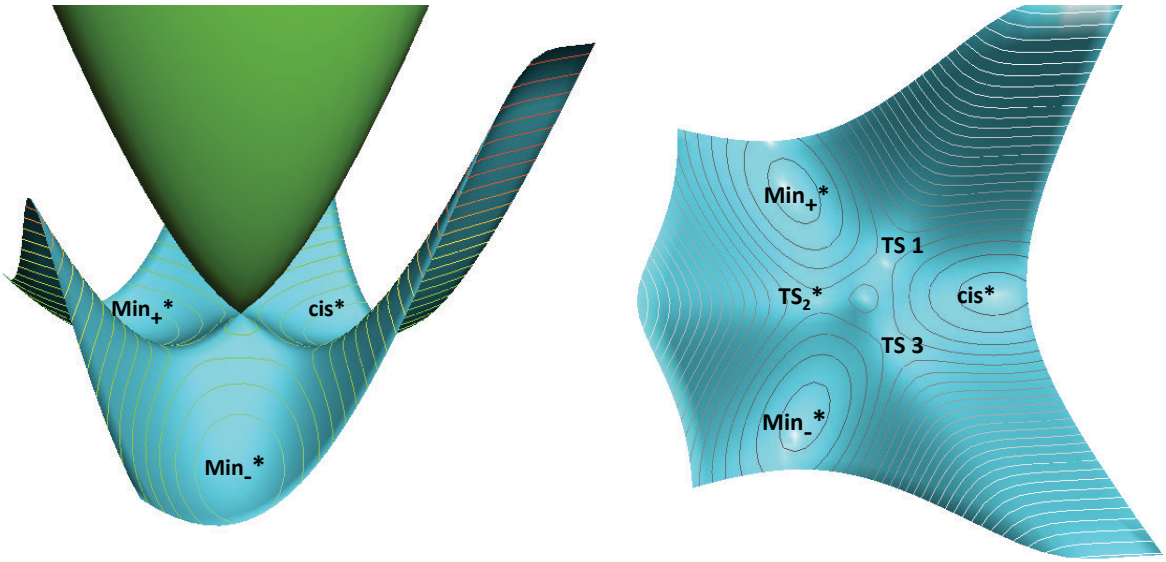

Fig. 45 Scheme of the Jahn-Teller prototypical three-fold Mexican hat in the benzene cation [287–291]**. The stationary points are named as for 3-HC (see main text) for the sake of clarity.**

Let us now focus on the nature of the first two excited states at the trans* minimum. Again, the first excited state is nπ* (A") and the second is ππ* (A') (**Fig. 46**). One can notice that the trans* minimum has the same electronic structure as TS_2*. In other words, from the TS_2* region the electronic structure does not change much in terms of dominant diabatic state along the hydrogen torsion. However, the second-order Jahn-Teller effect inducing the double well and the existence of the $Min_{\pm}$* minima reflects some mixture of the diabatic states (i.e. ππ* and nπ*) along the hydrogen torsion as a direct consequence of the electronic coupling around the CoIn. One can notice that we are in the same situation as in the previous section, i.e. Section1-2, while investigating the mixture of diabatic electronic states along the derivative coupling of the CoIn. This mixture of diabatic electronic states is highlighted in Tab. 7 that displays the main electronic configurations coefficients along the hydrogen torsion from TS_2* to trans*.

Tab. 7 Summary of the first two excited state main electronic configurations named from their singly occupied orbitals and their coefficients (absolute values), at different point along the hydrogen torsion coordinate.

	TS_2*	TS_τ*	trans*
S_1	nπ*: 0.69	nπ*: 0.64	nπ*: 0.69
	ππ*: 0.10	ππ*: 0.26	ππ*: 0.10
S_2	ππ*: 0.68	π π*: 0.60	ππ*: 0.67
	$\pi_2\pi_2$*: 0.10	nπ*: 0.24	nπ*: 0.11

In summary, the diabatic electronic states are not coupled at TS_2* for symmetry reasons (the electronic state are defined within the C_s point group at this point): the adiabatic states S_1 and S_2 correspond to nπ* and ππ*, respectively. Further along the path that goes to trans*, symmetry is lost and they start mixing significantly (for example around $Min_\pm$*). S_1 and S_2 finally decouple again at trans* for symmetry reasons (C_s symmetry is recovered at this point) where they correspond to nπ* and ππ*, respectively. As both states are similar in nature and occur with the same energy order at TS_2* and trans*, we can conclude that there is no avoided crossing between them along the isomerization pathway (i.e. there is no crossing between nπ* and ππ*).

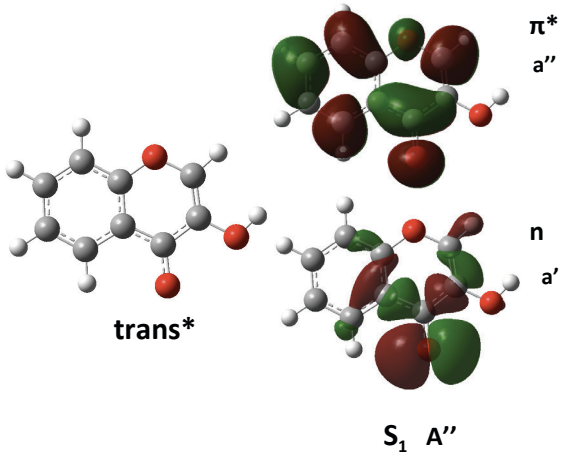

Fig. 46 Singly occupied orbitals at the trans* geometry for its first excited state.

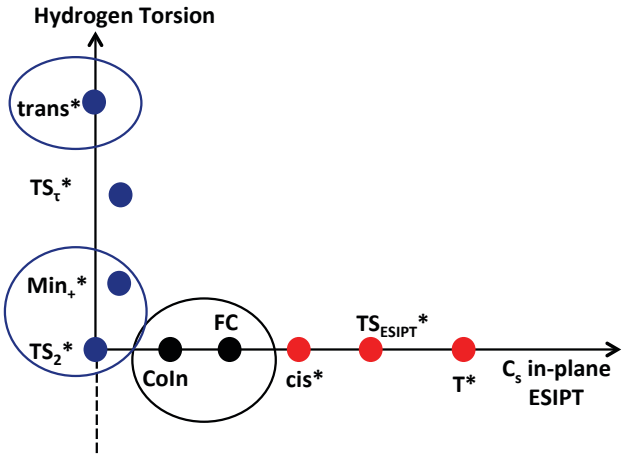

Fig. 47 Scheme of the potential energy surfaces along two dimensions: the hydrogen torsion and the ESIPT C_s in-plane coordinate. Circle: possible regions where parts of the system can be trapped into. The periodicity of the potential energy along the hydrogen torsion is not shown on this figure for the sake of clarity.

Fig. 47 summarizes in two dimensions (i.e. the ESIPT C_s in-plane deformation and the out-of-plane hydrogen torsion) the relative positions of all the critical points we located so far on the first excited state. As already explained, the FC transition occurs within the CoIn region. Thus, we expect some part of the system to follow directly the ESIPT direction with a rate constant on the femtosecond time scale. The other part of the system can be trapped momentarily in three different regions: on the second excited state because of the electronic coupling acting within the FC region (i.e. black circle in Fig. 47), in the TS_2* region through or around the CoIn and in the trans* region through several isomerization pathways (i.e. both blue circles in Fig. 47). To investigate the effect of the CoIn over the photoreactivity we have built a model of coupled potential energy surfaces and run quantum dynamics calculations, which are presented in the next section.

Before getting to the quantum dynamics section, let us make a short comment regarding the cis-trans isomerization of the tautomer form. This non-fluorescent trans minimum of the tautomer, denoted trans-T* was found 0.48 eV below the FC point and 0.31 eV higher than T* (see Fig. 48); hence, once the wave packet gets to FC, it has enough energy in principle to delocalize in the trans-T* region. However, the trans-T* minimum is not expected to be deep enough (i.e. 0.04 eV hydrogen torsion barrier) to trap the wave packet and induce a delay within the ESIPT process. Thus, this process will not be accounted for in the following coupled potential energy surfaces model (note, however,

that our simulations were run in full dimensionality). In addition, one should not expect any ESIPT process from trans* to trans-T* as the hydrogen is not ideally oriented for a direct transfer between both oxygen centers; as illustrated in Fig. 49, such a process would require first a trans*-cis* isomerization, then the ESIPT process would occur and be followed by a final T*- trans-T* isomerization. Moreover, this study focuses on the role of the CoIn within the ESIPT process. One of the outlooks of this project is a more thorough investigation including the cis-trans isomerization of the tautomer.

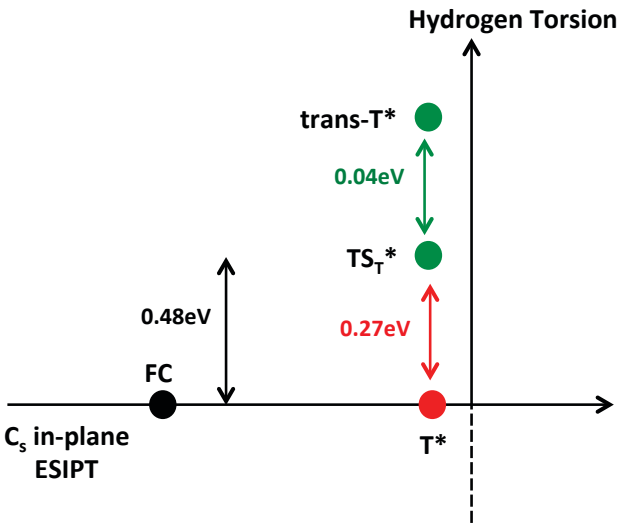

Fig. 48 Scheme of the potential energy surfaces along two dimensions: the hydrogen torsion and the ESIPT C_s in-plane coordinate. Arrow: hydrogen torsion barrier. Black: between FC and TS_T*. Red: between TS_T* and T. Green: between TS_T* and trans-T*. The hydrogen torsion angle of the cis-trans isomerization of the tautomer form is defined differently with respect to the enol form.

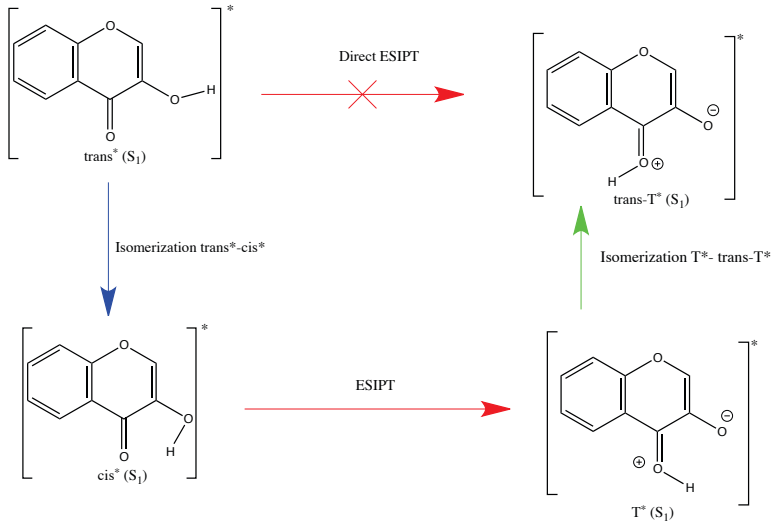

Fig. 49 Scheme of the various steps required to go from trans* to trans-T*.

2. Quantum Dynamics

2-1. Set of Coordinates

To describe the nuclear motion in 3-HC, we chose internal coordinates defined with a Z-matrix. This definition of the internal coordinates is different from the other application case studied in this thesis (aminobenzonitrile), where we used the polyspherical coordinate approach. In a set of coordinates defined with a Z-matrix, the first atom is fixed (A_1 in **Fig. 50**), the second atom is positioned with respect to the first with the distance between them (A_2), the third atom (if there is one) is positioned with a distance and a valence angle involving the fist two (A_3). If there are more than three atoms, each is positioned with three degrees of freedom involving three atoms among the previous ones (as A_4):

- a distance between two atoms: stretching (R_2,R_3,R_4);
- a valence angle between three atoms: local in-plane deformation (θ_3, θ_4);
- a dihedral angle between four atoms: local out-of-plane deformation, i.e. torsion (φ_4).

Z-matrix coordinates are similar to polyspherical coordinates (same types of degrees of freedom: distances, planar angles, and dihedral angles). The main difference concerns the definition of the intermediate frames related to the hierarchical description in terms of system subsystems, subsubsystems, etc. In some cases, Z-matrix coordinates fulfill the required conditions but not always (because there is no prescription about the group to which belong the three atoms used to define a new atom). Usually, Z-matrix coordinates are chosen as valence coordinates (fulfilling the natural connectivity of the molecule) but this is not compulsory. Dummy atoms can be used to define intermediate points and axes (often to deal with the indetermination of a dihedral angle when three atoms are aligned, but also potentially as a way to consider Jacobi vectors rather than valence vectors only). In our case, we used typical valence coordinates following the connectivity of the system except for the transferred H, as discussed below.

Atome						
A_1	**distance**	**Atome**				
A_2	R_2	A_1	**Angle de valence**	**Atome**		
A_3	R_3	A_1	θ_3	A_2	**Angle dièdre**	**Atome**
A_4	R_4	A_2	θ_4	A_1	φ_4	A_3

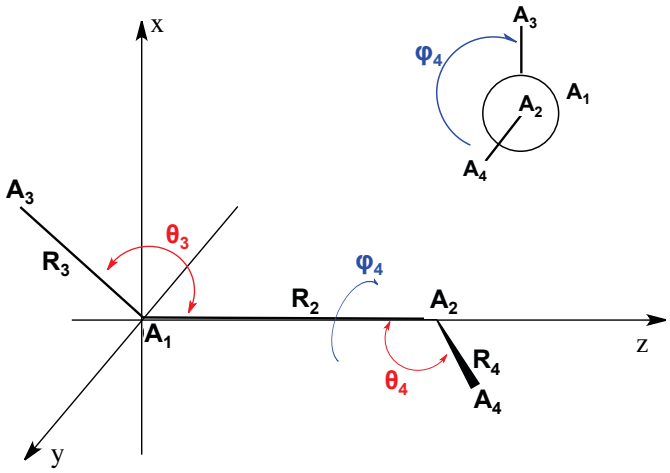

Fig. 50 Example of a set of six valence coordinates within a Z-matrix definition for a four atoms molecule (Table). Figure: geometrical definition of these coordinates within two framework point of view.

The ESIPT process induces a change of connectivity of the transferred H (typical of all chemical reactions where bonds are broken and formed), as illustrated in Fig. 34 where H_{13} goes from O_{11} in cis* to O_{12} is T*. For this reason, we defined the position of this atom with Cartesian coordinates (in the framework defined by the Z-matrix coordinates). This allows a more balanced description of the hydrogen motion (i.e. torsions and distances O-H-O) with respect to the two oxygen centers involved in the proton transfer. The full Z-matrix definition can be found in Appendix C and the following figure shows the Cartesian frame used for H_{13}.

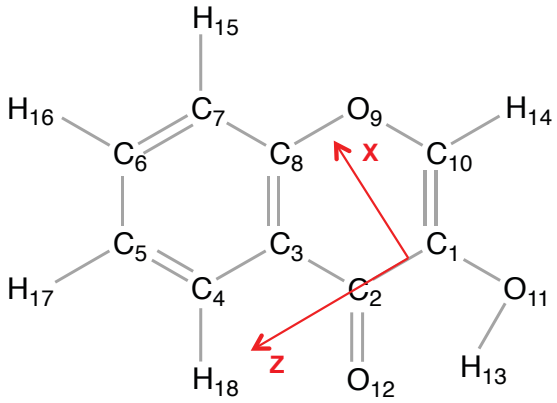

Fig. 51 Cartesian frame.

In the following, we present the model of coupled potential energy surfaces that we developed and used for quantum dynamics calculations to examine the role of the newly found CoIn. Note that the ESIPT process is almost barrierless such that vibrational motions with low frequencies are likely to play an important role during the dynamics. This is an example where using all nuclear coordinates could be crucial to describe vibrational energy redistribution adequately.

All parameters used to build the model were extracted from ab-initio calculations (TD-DFT/cc-pVTZ) at the four relevant geometries: $\mathbf{Q}_{\text{cis}}$, $\mathbf{Q}_{\text{cis}*}$, $\mathbf{Q}_{\text{TS}_2^*}$, and $\mathbf{Q}_{\text{CoIn}}$. The three stationary points were optimized as minima and TS. As no CoIn optimization algorithm at the TD-DFT level is currently available in the Gaussian package, we located the CoIn point as a crossing near the FC point. The corresponding BS vectors (in particular, the derivative coupling that is not available at the TD-DFT level) were calculated with a numerical method (see Appendix B).

2-2. Coupled Potential Energy Surfaces Model

2-2-1 General Overview

We represented the coupled potential energy surfaces with a vibronic-coupling Hamiltonian model, developed during this thesis and addressed in Chapter II, based on three quasidiabatic states. It consists in a real symmetric matrix $\mathbf{H}^{\text{diab}}(\mathbf{Q})$ made of three diagonal potential energy functions: $H_{11}^{\text{diab}}(\mathbf{Q})$, $H_{22}^{\text{diab}}(\mathbf{Q})$ and $H_{33}^{\text{diab}}(\mathbf{Q})$, and three off-

diagonal electronic couplings, $H_{12}^{\mathrm{diab}}(\mathbf{Q})$, $H_{13}^{\mathrm{diab}}(\mathbf{Q})$ and $H_{23}^{\mathrm{diab}}(\mathbf{Q})$, where $\mathbf{Q}$ denotes the set of nuclear Z-matrix coordinates detailed in the previous section (48-dimensional vectors). In the FC region the three quasidiabatic states (dashed line in Fig. 52) coincide with the relevant adiabatic states (plain line in Fig. 52): state 1 (S_0/GS), state 2 ($S_1/\pi\pi^*$), and state 3 ($S_2/n\pi^*$).

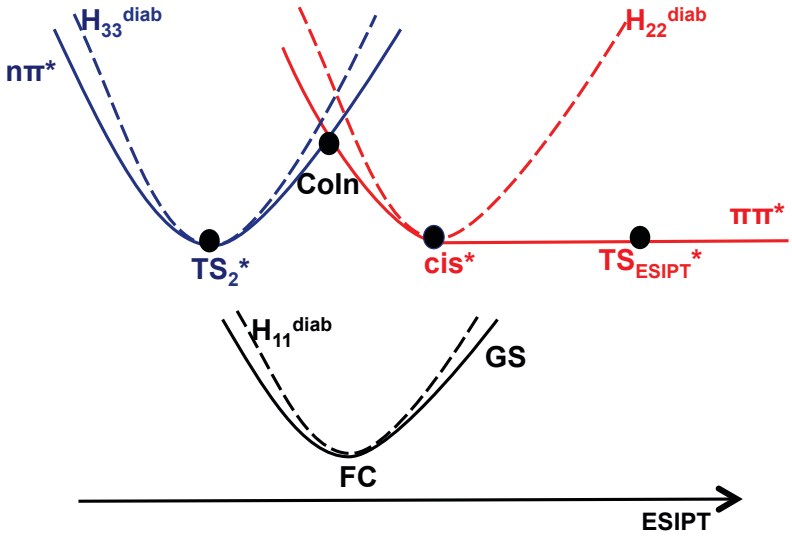

Fig. 52 Schematic representation of the quasidiabatic quadratic expansions around each minimum (dashed lines) and the corresponding adiabatic ab-initio surfaces (plain lines).

Each diagonal entry, $H_{ii}^{\mathrm{diab}}(\mathbf{Q})$ is expanded quadratically around a reference geometry, $\mathbf{Q}_{ii}$, among the relevant stationary points: $\mathbf{Q}_{\mathrm{GS}} = \mathbf{Q}_{\mathrm{cis}}$, $\mathbf{Q}_{\pi\pi^*} = \mathbf{Q}_{\mathrm{cis}^*}$, and $\mathbf{Q}_{n\pi^*} = \mathbf{Q}_{\mathrm{TS}_2^*}$ as depicted in Fig. 52.

The non-adiabatic coupling terms between the ground state and the two excited states can be neglected, due to the absence of relevant CoIn between the ground state and the excited states. As a consequence, $H_{11}^{\mathrm{diab}}(\mathbf{Q})$ is chosen such that it corresponds to the ground state potential energy surface (to second order around the GS minimum), and the electronic couplings $H_{12}^{\mathrm{diab}}(\mathbf{Q})$ and $H_{13}^{\mathrm{diab}}(\mathbf{Q})$ are set to zero.

The quasidiabatic vibronic-coupling Hamiltonian matrix reads as,

$$H^{\mathrm{diab}}(\mathbf{Q}) = \begin{pmatrix} H_{11}^{\mathrm{diab}}(\mathbf{Q}) & 0 & 0 \\ 0 & H_{22}^{\mathrm{diab}}(\mathbf{Q}) & H_{23}^{\mathrm{diab}}(\mathbf{Q}) \\ 0 & H_{23}^{\mathrm{diab}}(\mathbf{Q}) & H_{33}^{\mathrm{diab}}(\mathbf{Q}) \end{pmatrix} \qquad \textbf{Eq. 103}$$

The remaining coupling, $H_{23}^{\mathrm{diab}}(\mathbf{Q})$, is expanded linearly around the S_2/S_1 CoIn geometry (i.e. $\mathbf{Q}_{\mathrm{CoIn}}$). Its parameters are obtained using the two vectors of the branching space that were generated numerically in a previous stage. The cis* minimum is used as a reference point for setting the value of the arbitrary mixing angle between both degenerate states so as to satisfy $H_{23}^{\mathrm{diab}}(\mathbf{Q}_{\mathrm{cis}^*})=0$. As the quasidiabatic electronic coupling is zero at this point, coincidence is enforced between the adiabatic minimum obtained from the model and the quasidiabatic minimum chosen for the model. As the latter was chosen as the ab-initio cis* minimum, they all coincide by construction. Hence, with this choice of reference point (i.e. cis* and not TS_2*) we ensure an adequate qualitative description of the investigated regions (i.e. FC region and ESIPT process direction). One needs to keep in mind that in this study we focus on investigating the effect of the non-adiabatic couplings within the FC region on the reactivity of the system. In other words, we want to know if such non-adiabatic couplings are strong enough to trap part of the wave packet on the second excited state and induce a slower ESIPT process. The TS_2* transition state was not chosen as the reference point because a fine description of the dynamics in this region is not relevant to our study in a first stage. Thus, the condition $H_{23}^{\mathrm{diab}}\left(\mathbf{Q}_{\mathrm{TS}_2^*}\right)=0$ is not necessarily ensured. Nevertheless, we make the reasonable approximation that the quasidiabatic electronic couplings are not strong enough at the TS_2* transition state to shift its geometry significantly from the quasidiabatic representation to the adiabatic representation.

The quasidiabatic curvatures of the diagonal entries, $H_{ii}^{\mathrm{diab}}(\mathbf{Q})$, were obtained from the ab-initio ones through a second-order Jahn-Teller procedure. In the TS_2* region, as seen on Fig. 53, the quasidiabatic force constant along the H torsion is positive by construction (i.e. $H_{33}^{\mathrm{diab}}(\mathbf{Q})$ is quadratic and always positive). The second-order Jahn-Teller effect (due to the non-adiabatic coupling between the first and the second excited states) is strong enough at this point in our model to make the corresponding adiabatic

force constant negative and thus induce, as expected, a double well in the surface of the first excited state, characterized by the presence of both $Min_{\pm}$* minima on each side of TS_2*. Indeed, as seen on Fig. 53, in constrast with $H_{33}^{\mathrm{diab}}(\mathbf{Q})$, the adiabatic curvature on S_1 is negative around the origin. Note that the ab-initio difference in energy between TS_2* and $Min_{\pm}$* is very small (around 0.002 eV), which explains why the S_1 profile along the hydrogen torsion seems so flat.

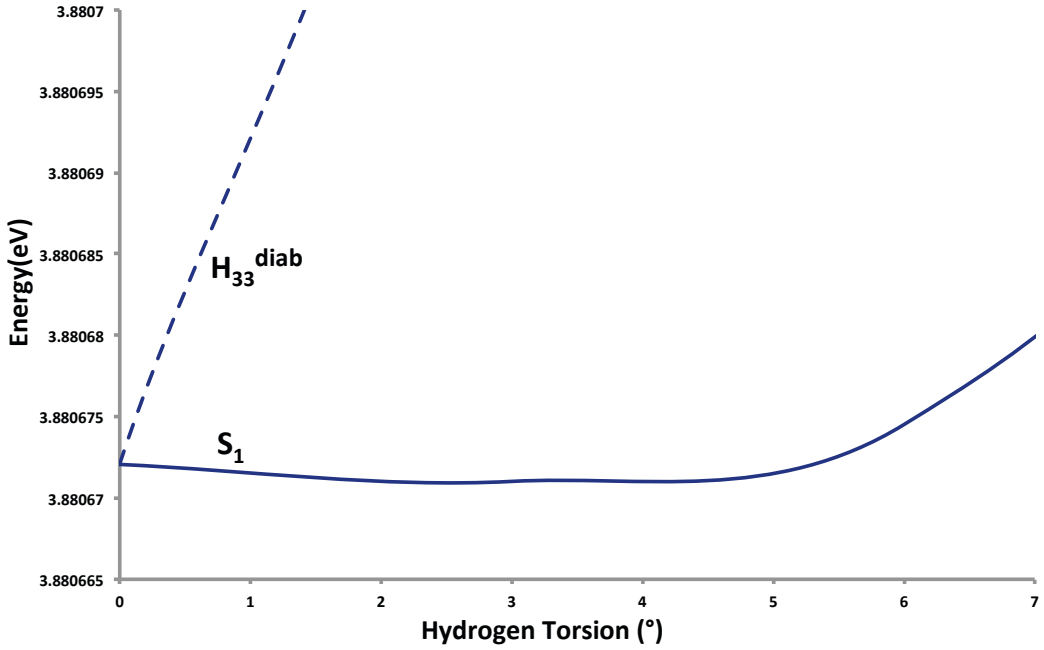

Fig. 53 Scan along the hydrogen torsion from TS_2* (ab-initio geometry) using the vibronic–coupling Hamiltonian model. Plain line: adiabatic potential – S_1; dashed line: diabatic potential – H_{33}. Energies are given in eV with respect to the global minimum energy on the ground state, i.e. cis (S_0).

Furthermore, the curvature of the quasidiabatic $H_{22}^{\mathrm{diab}}(\mathbf{Q})$ function along the almost barrierless TS_{ESIPT}* direction (i.e. $\mathbf{Q}_{cis^*} - \mathbf{Q}_{TS^*_{ESIPT}}$) was adjusted according to the switch function modification procedure that we developed and which is presented in Chapter II. It allows the cis* minimum harmonic frequencies to be conserved while ensuring that we describe adequately the strong anharmonicity along the ESIPT coordinate until the transition state (TS_{ESIPT}*). Up to now, one can notice that we never mentioned the involvement of the tautomer (T*) minimum into our coupled potential energy surfaces model. This is because we are not focusing on understanding and investigating the full proton transfer dynamics, which would require a much more advanced model. However, if the ESIPT direction is not adequately described from cis* to TS_{ESIPT}*, the wave packet

will be trapped artificially within the FC region due to its impossibility to spread along the reaction coordinate. That would thus falsify our results and interpretations. Tom summarize, we believe that our model ensures an adequate description of the first stages of the ESIPT process (i.e. from the absorption at FC to the transition state TS_{ESIPT}*). We could have added a complex absorbing potential along the ESIPT direction (a practical tool used in quantum dynamics calculations to describe dissociative processes [31]). However, this was not mandatory here, as we focused on the early stages of the dynamics (< 100 fs), where the wave packet stays mainly localized within the FC-cis* region.

Another technical point that is investigated in the following regards the validity of our model for describing the isomerization pathway from TS_2* to trans* along the hydrogen torsion.

2-2-2 Isomerization TS_2-trans**

The H torsion is a symmetric (i.e. up or down) and periodic motion that should, in principle, involve periodic functions rather than quadratic expansions in the expressions of the potential energy functions. Nevertheless, using this type of functions will complicate the formalism on which our model is based, as we should then adapt the mathematical relationships among all derivatives. In particular, implementing expressions of the quasidiabatic electronic couplings with periodic functions along this torsion coordinate would require a fitting procedure of their parameters; in addition the presence of a second-order Jahn-Teller effect at TS_2* adds a difficulty that could be tedious to recast in terms of periodic functions rather than a second-order expansion. However, if the wave packet does not have time to overcome the hydrogen torsion barrier to go from the TS_2* region to the trans* minimum (i.e. 0.09 eV) — in other words, if the wave packet does not spread significantly along the hydrogen torsion direction to form the trans* species — then an adequate periodic description of this motion and the description of the trans* region in our model will not be mandatory.

In order to check this hypothesis, we ran a one-dimensional quantum dynamics simulation along the hydrogen torsion. To this end, we built a one-dimensional potential

energy surface (for the first excited state) along the hydrogen-torsion coordinate (dihedral angle denoted β) using a periodic function (i.e. cosine function, **Eq. 104**). The corresponding parameters were optimized for the function to go trough the relevant stationary points along the hydrogen-torsion (i.e. TS_2*, $Min_{\pm}$*, TS_{τ}*, and trans*). Note that $Min_{\pm}$* and TS_{τ}* are not displaced only along the hydrogen torsion from TS_2*, as seen on Fig. 47; however, this is a good approximation (99% and 98% overlaps between the normalized directions of the actual displacements and the hydrogen torsion coordinate). The obtained one-dimensional potential energy surface along the hydrogen torsion is depicted on Fig. 54; one can notice a slight shift between the ab-initio and the one-dimensional model at the relevant stationary points, which is expected to be too small to have a relevant impact on the wave packet behavior (no more than about 10^{-3} eV in terms of energy).

$$E_{1D}(\beta) = 3.7429519 * 10^{-3} - 2.3153736 * 10^{-3} * \cos(\beta) - 1.6050716 * 10^{-3} * \cos(2\beta) + 1.2737786 * 10^{-3} * \cos(3\beta) \qquad \textbf{Eq. 104}$$

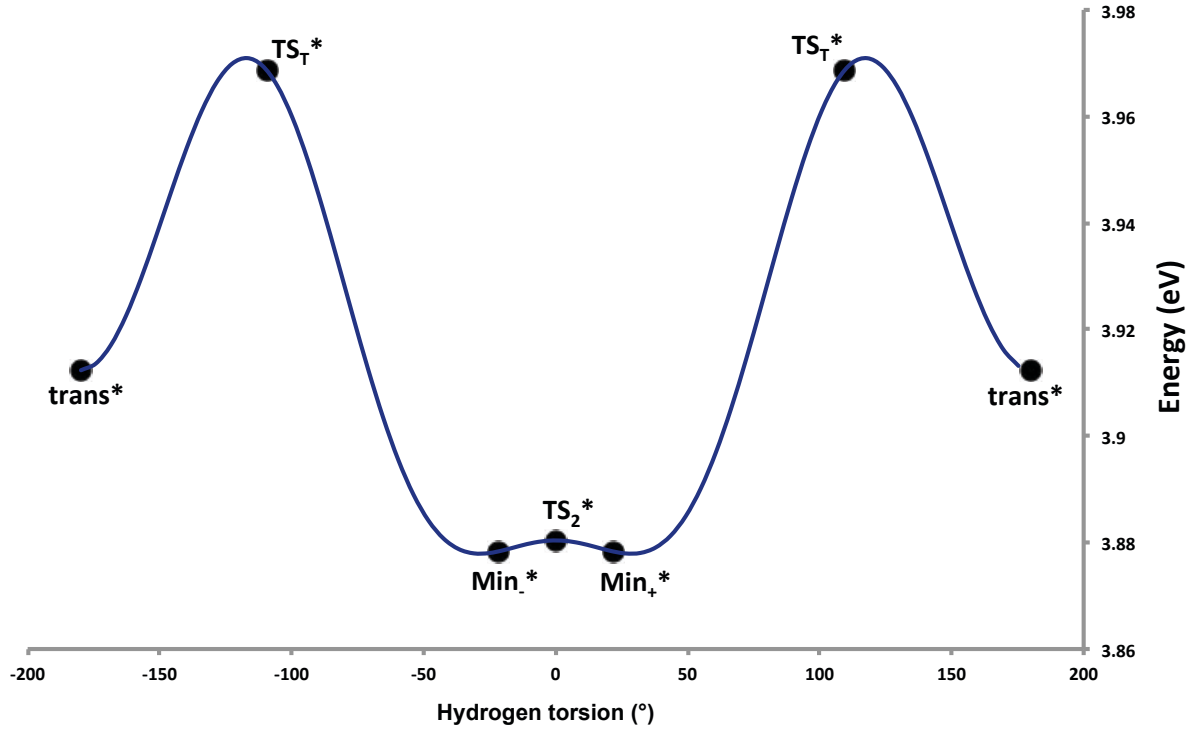

Fig. 54 One-dimensional potential energy surface along the hydrogen torsion coordinate (β).

The following one-dimensional wave packet propagation starting at TS_2* (Fig. 55) were achieved using the ElVibRot program developed at the Laboratoire de Chimie Physique, Orsay, France by David Lauvergnat.

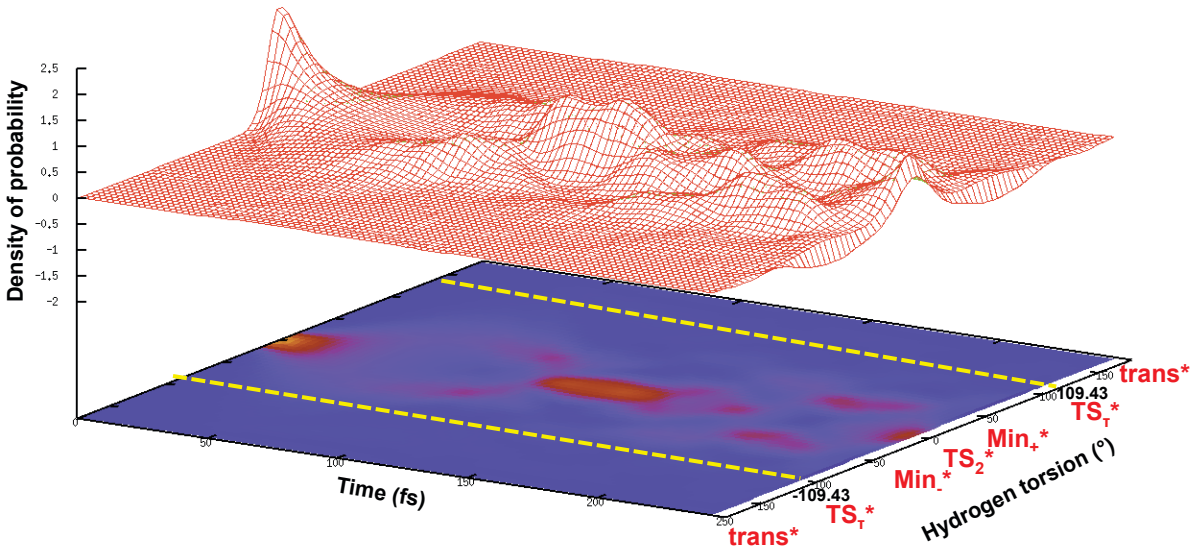

Fig. 55 One-dimensional wave packet propagation along the hydrogen torsion coordinate over time (wave packet isodensity contour plot).

Fig. 55 shows the time evolution of the density of probability along the hydrogen torsion during 250 fs. Initially (i.e. t = 0 fs) the wave packet is center in TS_2*, and it oscillate in time along the hydrogen torsion ("breathing" of the packet). One can notice that the density of probability stays very close to zero within the trans* region. In other words, the wave packet does not overcome the 0.09 eV torsion barrier to delocalize along the TS_2*-trans* isomerization pathway.

In conclusion, as the wave packet stays localized within the TS_2* region, it will thus not spread significantly along the hydrogen-torsion, at least during 250 fs. This justifies why it is not necessary in a first stage to have an adequate description of the entire hydrogen torsion motion (i.e. using periodic functions). The TS_2* region (from 0° to 20°) is thus the most relevant part of the hydrogen-torsion pathway and a quadratic expansion is sufficiently accurate within the relevant time scale for the dynamics under study.

In summary, in our coupled potential energy surfaces model:

- The full ESIPT process is not described (no description of the T* basin).
- The ESIPT direction is described using a switch function modification strategy.
- Our methodology to diabatize the ab-initio Hessian provides an automatic description of the $Min_{\pm}$* minima induced by a second-order Jahn-Teller effect.
- There is no requirement to use a periodic function to describe the full hydrogen torsion, as the system does not overcome the torsion barrier within a relevant time scale.
- We focus on investigating the role of the non-adiabatic electronic coupling induced by the CoIn within the FC region.

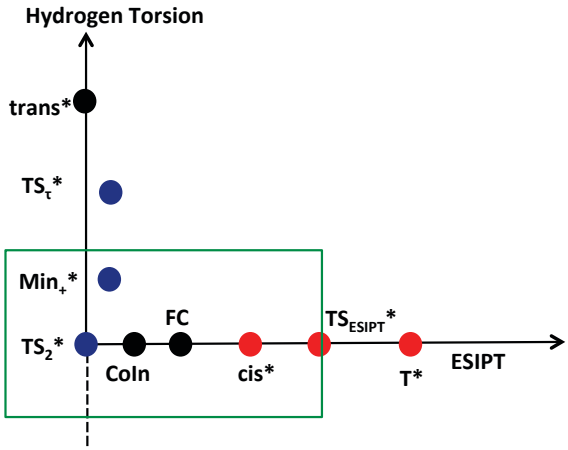

Fig. 56 Scheme of the potential energy surface of the first-excited state along two dimensions: the hydrogen torsion and the ESIPT coordinate. Green box: region of interest. The periodicity of the potential energy along the hydrogen torsion is not shown on this figure for the sake of clarity.

The green box in Fig. 68 illustrates the region of interest for our coupled potential energy surfaces model. In the following, we address the comparison between the coupled potential energy surfaces obtained by our methodology and the ab-initio data.

2-2-3 Comparison of Our Model with Ab-initio Data

Fig. 59 shows the agreement between the ab-initio energies (dashed lines) and the ones of our vibronic coupling Hamilonian model (plain lines) along the ESIPT direction and along the hydrogen torsion direction. One can notice that the CoIn position in our model is slightly shifted with respect to the ab-initio CoIn position (i.e. the maximal deviation

for the C_1-C_2, C_6-C_7, C_8-O_9, O_{11}-H_{13} bonds, highlighted in green, is around 0.004 Å and 0.5 ° for the O_{12}-C_2-C_1 valence angle denote θ; These coordinates are displayed in Fig. 57); but the strong anharmonicity on the first excited state along the ESIPT direction until TS_{ESIPT}* is reproduced perfectly with respect to the ab-initio data.

There was no direct curvature modification along the CoIn direction (i.e. $\mathbf{Q}_{cis^*} - \mathbf{Q}_{CoIn}$), but, as already mentioned, we added a curvature modification along the ESIPT direction (i.e. $\mathbf{Q}_{cis^*} - \mathbf{Q}_{TS^*_{ESIPT}}$). As both directions are not orthogonal, there is an indirect effect along the CoIn direction, which explains the shift of this point. This highlights one of the limitations of our model: the inability to modify simultaneously curvatures along similar directions.

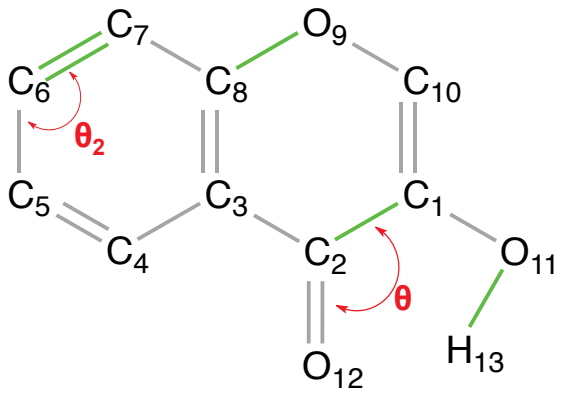

Fig. 57 3-HC molecule.

Nonetheless, on the one hand, as observed on the ABN application case (Chapter IV), a slight shift of the CoIn position does not have a significant impact on the qualitative behavior of the quasidiabatic populations. On the other hand, this shift in the CoIn region induces a larger gradient at FC with our model than in the ab-initio data. Hence, in our dynamics calculations one should expect the wave packet to leave faster the FC region than in the experimental situation. Therefore, this gradient effect should be visible while comparing the model and experimental UV absorption spectrum, as discussed in the following section.

Up to now, we did not discuss the ~0.3-0.5 eV shift of the second excited state between our model and the ab-initio data along the ESIPT direction when $x > 10$ (from the cis*

point toward TS_{ESIPT}*). However, this region is not relevant for our study, as we do not expect the wave packet to have enough energy to delocalize significantly along this region in the second excited state (i.e. between 0.44-0.9 eV higher than FC). One should keep in mind that if the second excited state is populated, this will occur through the S_1/S_2 peaked CoIn, thus, it will be populated through the bottom of the CoIn whereas the CoIn gradients are driving the system back to the first excited state. This idea is depicted in Fig. 58.

Let us now focus on the description of the energy landscape along the hydrogen torsion (a large component of the derivative coupling). The periodicity of the hydrogen motion along this specific direction is not reproduced here, as the expressions of our potential energy surfaces do not take into account the periodicity with respect to the torsion angle (details are provided in the previous section). On the first excited state, we observe an apparent minimum around ± 36° in the cut along the hydrogen torsion angle from the CoIn in the ab-initio data, whereas in our model this apparent minimum is around ± 18°. Note that this double-well-type shape around the crossing point occurs in the adiabatic surfaces but not in the diabatic ones and is thus due to the effect of the off-diagonal diabatic coupling term. By construction, our model uses the derivative coupling calculated at the CoIn as the gradient of this off-diagonal term. It is thus correct, at least to first-order. However, the curvatures of the diagonal diabatic entries along such directions are determined from ab-initio data calculated at the minima. There is thus no direct control of their influence on the shape of the adiabatic energies obtained after diagonalization, which is the explanation for the discrepancy observed between the model and the ab-initio energy profiles. This is a limitation of our procedure that cannot reproduce the adiabatic curvatures perfectly at all points but rather preferentially around the minima while the derivative coupling will be correct around the conical intersection. In any case, the global shape around the conical intersection is quite well reproduced, as our model displays a pair of apparent minima on S_1 for relatively small values of the hydrogen torsion angles, as expected. One should keep in mind that this type of model is not meant to calculate highly accurate data such as an IR spectrum or a quantum yield, but rather to appreciate the role of the dark state (crossing the bright state) during the ESIPT process. This study must be seen as a first step in the

construction of a more sophisticated model that should be used to describe the ESIPT process more quantitatively.

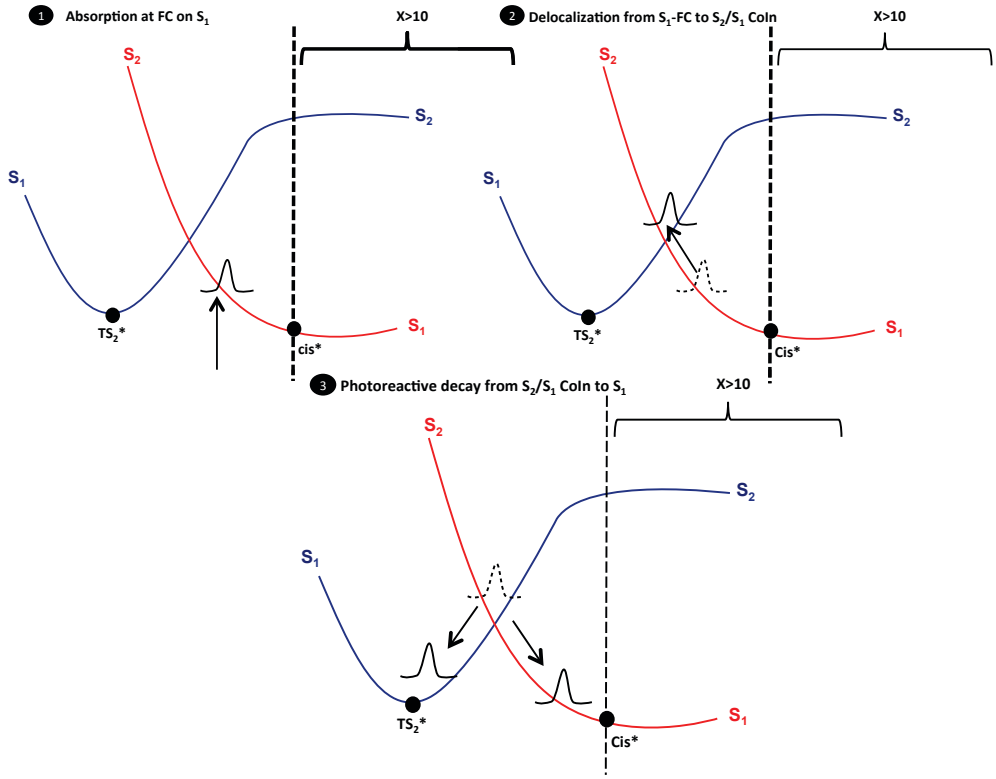

Fig. 58 Simplified picture of the earlier stage of the ESIPT process just after absorption on the first excited state. 1: absorption at FC on the first excited state. 2: delocalization of the wave packet from the FC region on the first excited state to the S_2/S_1 CoIn region. 3: formation of TS_2* and cis* from the S_2 to S_1 non-radiative decay. Note that we will show later on that the initial wavepacket is actually quite delocalized around the conical intersection.

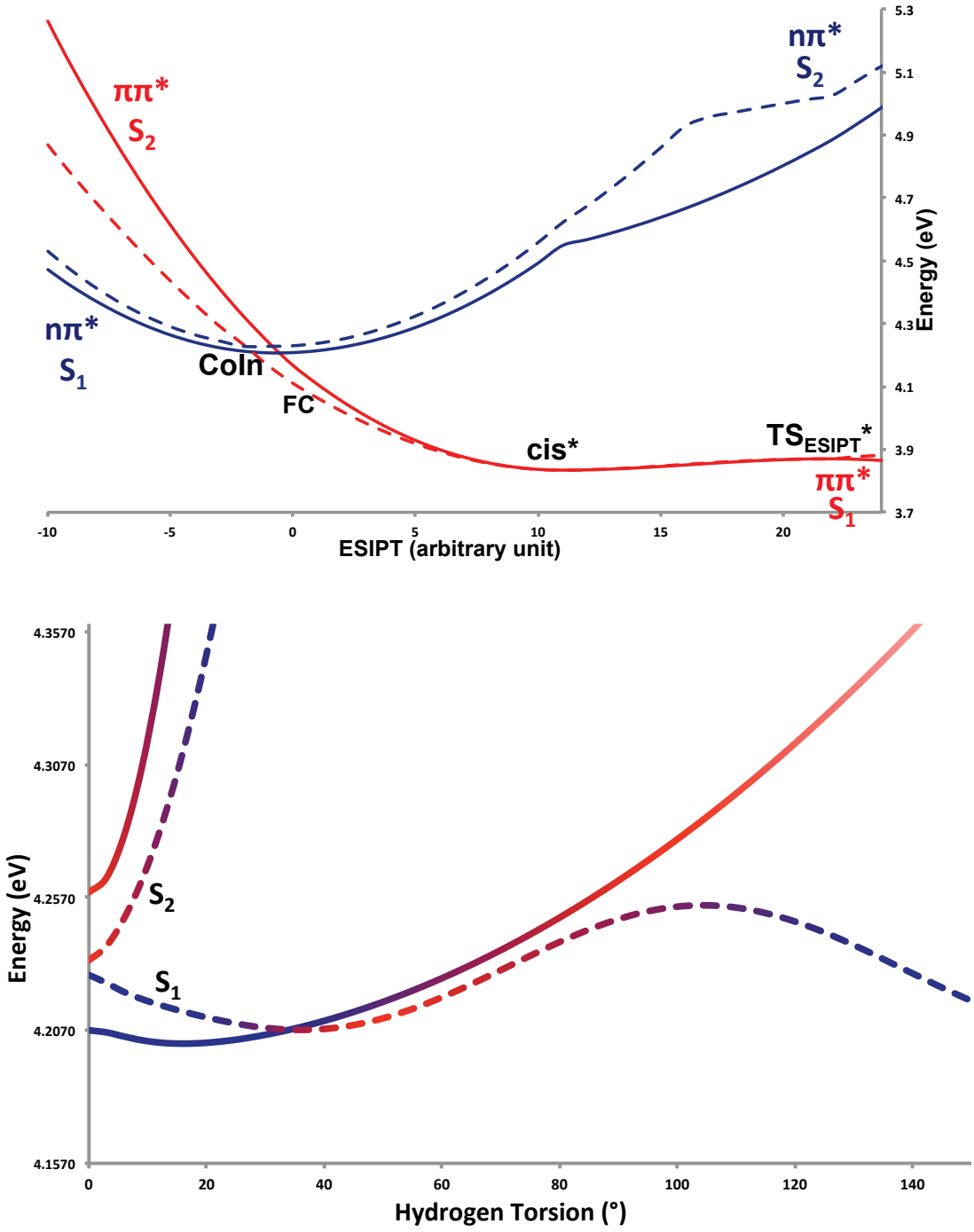

Fig. 59 Upper Panel: ESIPT direction along a linear interpolation from FC (x = 0) to TS_{ESIPT}* (x = 20) through cis* (x = 10) (equivalent to $x^{0(23)1}$ (GD)). Energies are given in eV with respect to the ground-state minimum. Dashed line: ab-initio; plain line: vibronic-coupling Hamiltonian model. Red: ππ* electronic state; blue: nπ* electronic state. Lower panel: Scan along the hydrogen torsion from the CoIn (ab-initio geometry); plain line: vibronic –coupling Hamiltonian model; dashed line: ab-initio. Their colors are not uniform to show that the diabatic electronic states (ππ* and nπ*) mix along the derivative coupling direction ($x^{0(23)2}$-DC). Energies are given in eV with respect to the global minimum energy on the ground state, i.e. cis (S_0).

We ran quantum dynamics on this coupled potential energy surfaces model and obtained the corresponding UV absorption spectrum and the evolution of the quasidiabatic populations over time, which are presented in the following to investigate the role of the non-adiabatic coupling induced by the CoIn within the FC region.

2-3. UV Absorption Spectrum

The UV absorption spectrum was calculated as the Fourier transform of the autocorrelation function of the wave packet propagated on the previously detailed coupled potential energy surfaces model (Fig. 60) [31]. Comparing the calculated and experimental UV absorption spectrum gives a measure of the quality of our model through its ability to describe the FC region correctly.

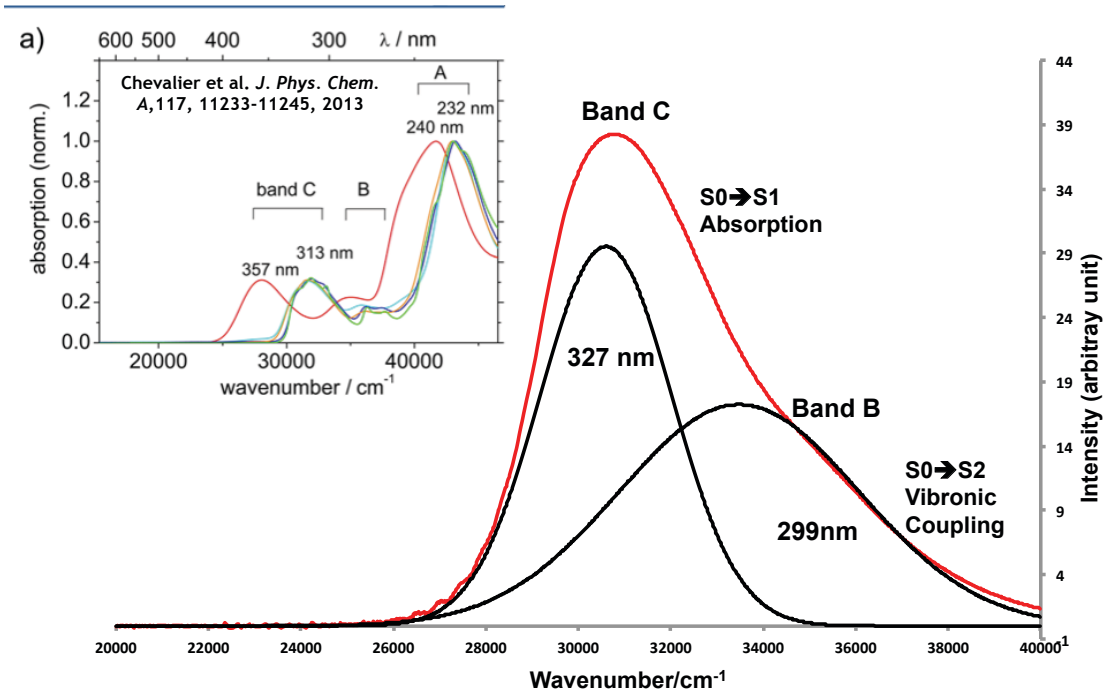

Fig. 60 Calculated UV absorption spectrum (main panel). a) Experimental spectrum from [220] **UV/Vis spectra of 3-HC dissolved in methylcyclohexane (MCH) (green), acetonitrile (CAN) (blue), EtOH (orange), and neat water at pH 7 (light blue) and pH 13 (red), with concentration varying from 5×10^{-3} to 5×10^{-4} M.**

Fig. 60 depicts our calculated spectrum and the experimental one (the one of interest is represented with the green line, as it was obtained in cyclohexane, a non-polar solvent). The experimental interpretation of the UV absorption spectrum assigns Band C to the

first excited state absorption and Band A to the third excited state absorption [220]. This is consistent with our computational results, as shown on

Tab. 8 that displays the oscillator strengths at FC between the ground state and the first three excited states. Only the first and third excited states absorb a photon within the FC region (i.e. no-zero oscillator strength between the ground state and the specific excited state). Note that our spectrum does not reproduce Band A by construction, as we did not include the description of the third excited state within our model (it is not a relevant excited state to study the first excited state ESIPT process).

Tab. 8 Oscillator strengths calculated at the TD-DFT/cc-pVTZ level of theory for the first three excited electronic states.

Excited electronic state	Oscillator strength at FC
S_1	0.0868
S_2	0.0000
S_3	0.0028

In addition, Band B is not explained from experimental data neither with ab-initio data such as oscillator strengths (the second excited state does not absorb at FC). This band has not been observed among the UV absorption spectrum of other 3-HC dyes such as 3-hydroxyflavone (3-HF). Nevertheless, the large band we observe in our calculated spectrum can be decomposed in terms of two Gaussian contributions centered at 327 nm (~3.79 eV) and 299 nm (~4.15 eV). The first peak (327 nm) is the most intense, which reflects an allowed absorption transition between the ground state and this excited state (non-zero oscillator strength); moreover, from its position at 327 nm, one can safely associate this peak to Band C (experimental position: 330 nm), the S_0 to S_1 absorption transition. The spectral shift of 3 nm (~0.03 eV) between our calculated and the experimental bands is small and corresponds to the accuracy limits of the level of theory used to generate the ab-initio data that we based our model on. The second peak (299 nm) is, thus, associated to Band B (experimental position: 278 nm). It is to be interpreted as induced by the vibronic couplings that occur in the CoIn region embedded in the FC region (as observed in other systems such as pyrazine [292,293]). Its position is more shifted with respect to the experimental spectrum (21 nm shift, ~0.3eV) than for

Band C. This band is induced by vibronic couplings, which have a large effect around CoIn points. We thus expect it to be sensitive to the position of the CoIn point in our model. One should remember that in our model the CoIn position is slightly shifted with respect to the ab-initio data and we already mentioned that could have a relevant impact on the UV spectrum but not on the global behavior of the quasidiabatic populations.

To check if the spectral position of Band B is really sensitive to the CoIn position, we ran quantum dynamics calculation on a coupled potential energy surfaces model where we adjusted the CoIn position upon a quadratic modification of the curvature along the $\mathbf{Q_{cis^*}} - \mathbf{Q_{CoIn}}$ direction (Chapter II) (see Fig. 61). One should note that we no longer describe the energies of the first and second excited states along the ESIPT direction adequately, as both modifications are not compatible with each other. However, this is not the purpose of this new model, which is to check the effect of the CoIn position over the UV absorption spectrum. In other words, the relevant region under discussion now is around FC.

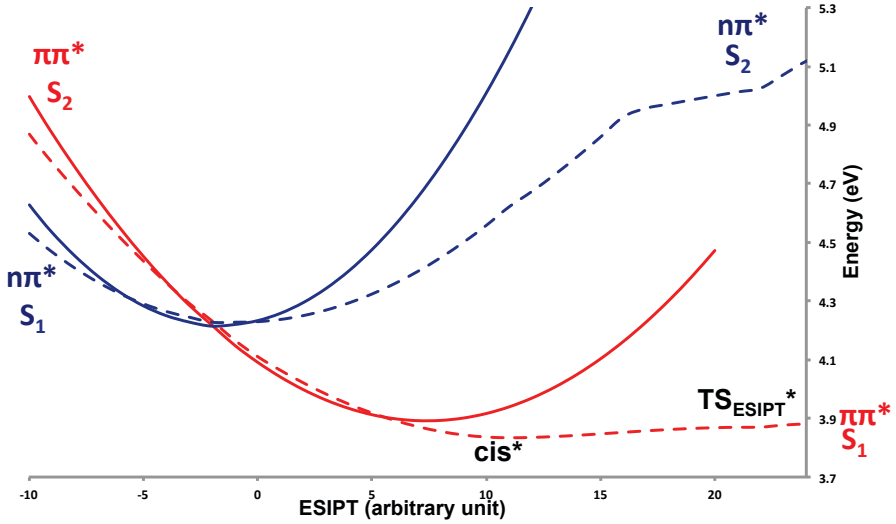

Fig. 61 ESIPT direction along a linear interpolation from FC (x = 0) to TS_{ESIPT}* (x = 20) through cis* (x = 10). Energies are given in eV with respect to the ground-state minimum. Dashed line: ab-initio; plain line: vibronic-coupling Hamiltonian model.

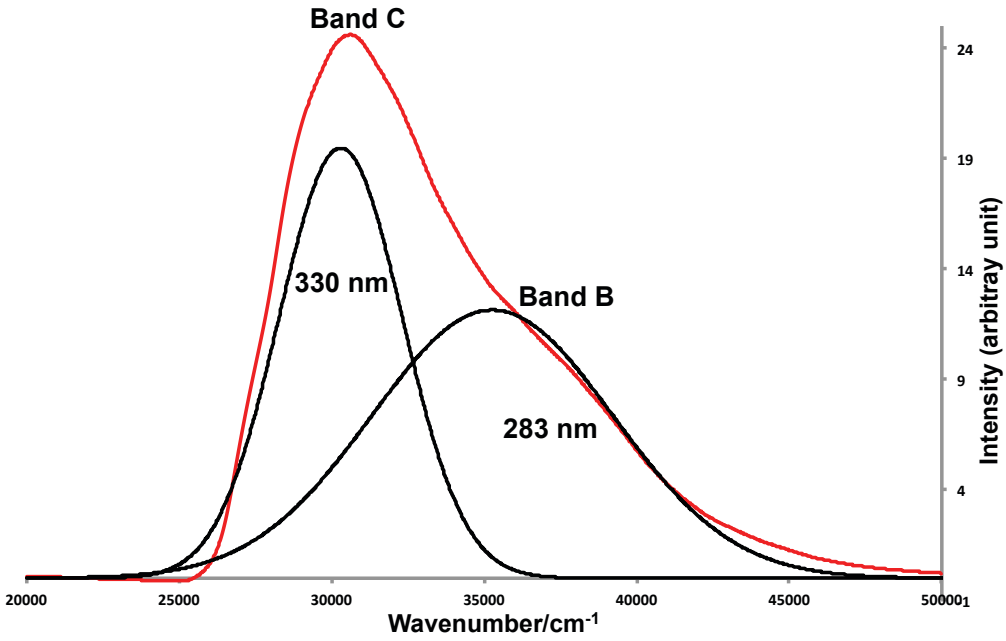

Fig. 62 Calculated UV absorption spectrum using a coupled potential energy surfaces model where only the CoIn position was adjusted.

Fig. 62 shows the UV spectrum obtained with the new model depicted on Fig. 61, where the CoIn position was adjusted. One can notice on this spectrum that we still have two peaks. They are in the latter case more separated than in the previous spectrum depicted in Fig. 60. The position of Band C remains globally untouched (330 nm) while the position of band B is now at 283 nm (16 nm shift with respect to the model where the CoIn is not at the exact ab-initio position), which is closer to the experimental position.

In summary, Band B (intensity-borrowing vibronic coupling band) is quite sensitive to the CoIn position, which is probably due to its proximity to the FC region, as this affects the non-adiabatic coupling and the magnitude of the gradient around this region.

A this point, let us make some technical comments regarding the shift of the peak positions of our calculated spectra with respect to the experimental data.

First, one should keep in mind that our vibronic coupling Hamiltonian is based on gas phase ab-initio data, while the experiments were carried out in solvents. A non-polar solvent is not expected to change the potential energy surface landscape drastically, but higher-order intermolecular interactions (involving polarizability, etc.) can affect the excited states differently according to their respective dipole moments. In addition, this

shift can be induced by two other possibilities: as already mentioned, the level of calculation used to obtain the ab-initio data may not be accurate enough and the initial wave packet may not be fully converged. Regarding the quantum chemistry level of theory, we used the TD-DFT method with the cc-pVTZ basis set. Wave function methods of CASPT2 type would be more adequate than TD-DFT for treating non-adiabatic process. Unfortunately, they are too much time consuming for such a large system (18 molecular orbitals are to be included within the active space to describe the CoIn region). Regarding the quantum dynamics calculations, we used a development version of the ML-MCTDH method of the MCTDH Heidelberg package. One of the limitations of the current implementation is the necessity to dramatically increase the number of SPF basis functions to converge the initial nuclear wave function. This is a very expensive process in terms of computation time (see Tab. 9 for an example), which compels the user to make, most of the time, a compromise between computation time and convergence accuracy of the nuclear wave function. Here, we increased the number of SPF basis functions to converge the zero point energy within 10^{-1} – 10^{-2} eV (i.e. the order of magnitude for the error expected from accurate ab-initio vertical transitions energies). Technical details regarding the quantum dynamics calculations (SPF, ML-tree, etc..) can be found in Appendix C.

Tab. 9 Example of computation times for a 20 fs relaxation on 3-HC ground state. *Number of SPFs per mode and per layer within the ML-tree in Appendix C. (same ML-tree for both relaxations). Harmonic zero point energy: 3.64 eV

SPFs*	Time (days)	Energy (eV)
6	5	3.665
12	31	3.654

Another point to highlight is the necessity for some systems to include the effect of vibronic couplings when calculating UV absorption spectra (by the use of quantum chemistry or quantum dynamics calculations). Fig. 63 depicts the UV absorption spectrum obtained using the Gaussian09 package, which is mostly based on the ab-initio oscillator strength. As expected, this approach does not describe the shoulder of the UV absorption spectrum induced by vibronic couplings effects (Band B), since the oscillator strength between the ground state and the second excited state at FC is zero (only one

band at 301nm-Band C). In contrast, quantum dynamics calculations, such as ours, are able to account for vibronic couplings effects (if, of course, they are based on a vibronic coupling Hamiltonian model). Calculating a correct spectrum can be achieved from relatively short wave packet propagation but an accurate description of the FC region is mandatory (this contrasts with studies focused on reactive processes where large-amplitude motions must be considered, which implies to invest time for building more sophisticated potential energy models). Finally, let us note there are static methods that account for vibronic couplings effects upon introducing them as perturbations [294].

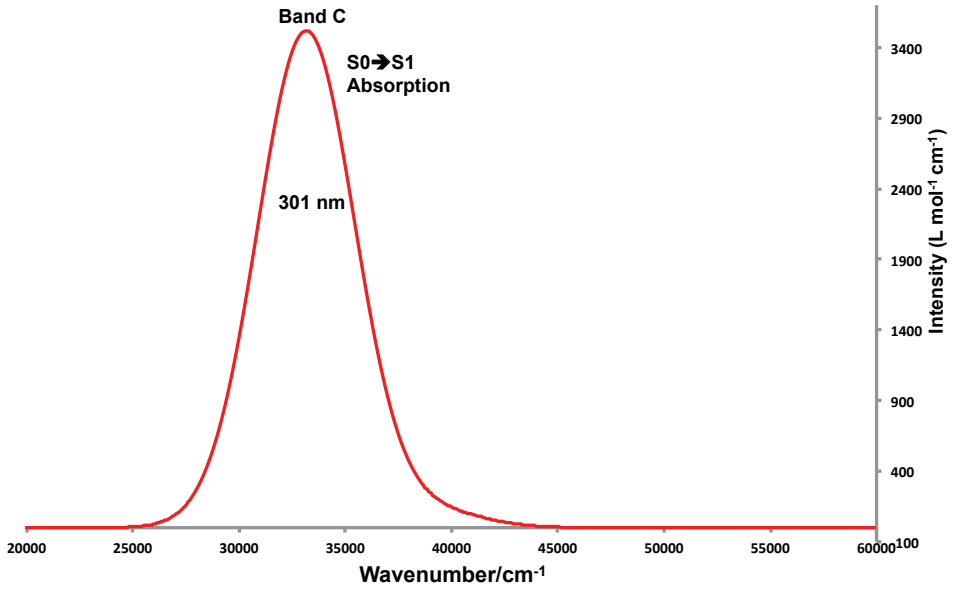

Fig. 63 Calculated UV absorption spectrum with the procedure implemented in the Gaussian09 package (PBE0/cc-pVTZ level of theory).

To conclude, our coupled potential energy surfaces model (curvature modification to adjust the energy profile along the ESIPT direction, as depicted in Fig. 59) describes adequately the experimental UV absorption spectrum with respect to the global shapes and positions of the bands (note that the intensities of the calculated spectrum are comparable to the experimental ones only up to an arbitrary scaling factor). Hence, we considerer that we reproduce adequately for the purpose of our study the FC and CoIn regions (the regions of main interest here).

In the following section, we use these quantum dynamics calculations to analyze the system evolution during the early stage of the ESIPT process (< 50 fs).

2-4. Photoreactivity

To investigate the ESIPT process over time, in particular the effects of the non-adiabatic couplings within the FC region, we used quantum dynamics calculations with the first quasidiabatic potential energy surfaces described above (based on TD-DFT/cc-pVTZ gas phase data and with the curvature modification procedure based on a switch function along the ESIPT direction).

As already mentioned, technical details about the quantum dynamics calculations presented in the following are given in Appendix C (SPF, ML-tree, primitive basis).

Let us make a technical remark about the set of coordinates before analyzing the evolution of the quasidiabatic populations. In the previous section we modified our coupled potential energy surfaces with the use of a switch function that is not "MCTDH compatible" (see Chapter II for an explanation). Therefore, to fulfill the "MCTDH format", and then run quantum dynamics calculations with this method, one must perform linear combinations of coordinates to distinguish the ESIPT direction as a single coordinate. Furthermore, to decrease the computation time and the number of SPF basis functions, we considered the remaining 47 coordinates as normal mode coordinates obtained from the Hessian matrix (projected out of the ESIPT direction) expressed in terms of the linear combinations of the original Z-matrix coordinates at the FC geometry, see Fig. 64. As already explained, the ESIPT coordinate remains untouched.

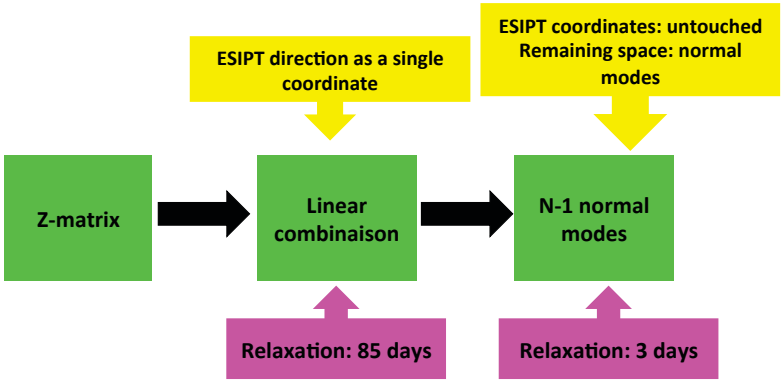

Fig. 64 Summary of the different sets of coordinates used. The relaxation times are based on relaxation of 3-HC in its ground state during 10 fs. The set of coordinates is different; hence, the ML-tree is different. Therefore, the number of SPF basis functions (36 per mode and per layer) is not meaningful here.

The choice of normal mode coordinates is justified as they diagonalize the projected Hessian at a specific geometry (here FC). Hence, this choice reduces the number of terms that need to be calculated to generate the initial wave packet. However, one should keep in mind that normal mode coordinates are different from one stationary point to another. This means that the normal modes at FC do not diagonalize the cis* or TS_2* Hessians. In other words, this new set of coordinates implies a reduced number of terms in the ground state Hessian only. This choice was motivated by the need to decrease the computation time required to generate the initial wave packet.

Fig. 67 depicts the evolution of the quasidiabatic populations over time (50 fs). The red line is the quasidiabatic population of ππ*, the state corresponding to the second quasidiabatic potential energy surface ($H_{22}^{\mathrm{diab}}(\mathbf{Q})$), which correlates to the ESIPT side on the lower adiabatic surface. The blue line is the quasidiabatic population that is transferred from the second to the third quasidiabatic state nπ* (corresponding to $H_{33}^{\mathrm{diab}}(\mathbf{Q})$), which correlates with the TS_2* side on the lower adiabatic surface. The frontier between both sides is characterized by the CoIn point (see Fig. 66).

Adiabatic populations are not available with the current implementation of ML-MCTDH. They would tell us how much of the system stays on the lower surface or gets trapped into the higher adiabatic state. Quasidiabatic populations are a good estimate of the branching between the ESIPT and the TS_2* sides only if the contribution from the higher adiabatic state stays small. This probably is a valid hypothesis, as we can expect that only the lower adiabatic state will be populated significantly after a certain time, but there is no numerical proof to support this.

In addition, it should be noted that the quasidiabatic population is a global result obtained upon integration over the full space of nuclear coordinates; hence, there is no possibility to know where exactly the wave packet is located on the quasidiabatic potential energy surfaces. The quasidiabatic population dynamics on ππ* ($H_{22}^{\mathrm{diab}}(\mathbf{Q})$) shown on Fig. 67 does not tell us if the population is around the ESIPT TS (already transferring the proton) or whether it is still trapped in the CoIn region, as pointed out in Fig. 65. A finer analysis of the dynamics of the system on $H_{22}^{\mathrm{diab}}(\mathbf{Q})$ would require step distributions to be added along a specific coordinate around specific regions (see

Chapter IV on ABN for an example of this type of analysis). This analysis is currently ongoing and will not be presented in this thesis.

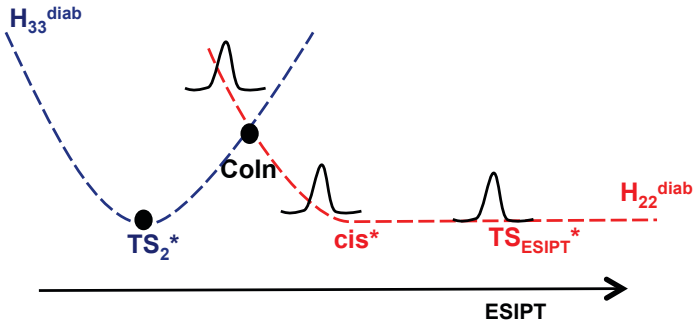

Fig. 65 Scheme to represent the possible positions of the wave packet on the second quasidiabatic potential energy surface.

We focused on the dynamics only during the first 50 fs and did not extend our investigation over a longer period of time to study the entire proton transfer process (i.e. until T*). This is due to our potential energy surface model: as already mentioned, along the ESIPT coordinate we have a flat potential energy profile that has about the same energy as TS_{ESIPT}* and we did not use any complex absorbing potential on the right-hand side of the grid. Thus, the wave packet can bounce against the border of the grid along this direction (stage 2 Fig. 66) and then come back to the FC region (stage 3), leading to a non-physical new transfer of population through the S_2/S_1 CoIn (stage 4), as pictured in Fig. 66.

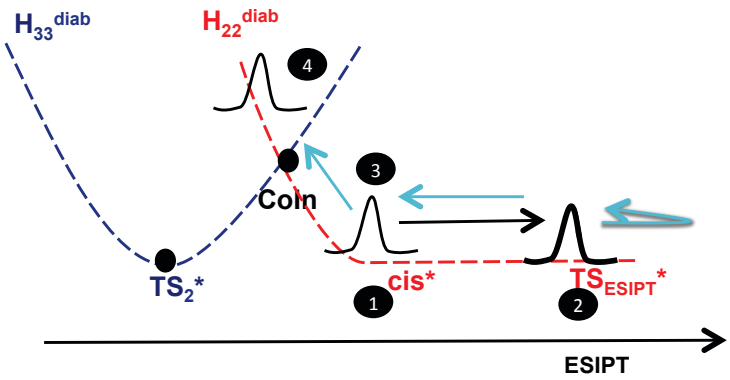

Fig. 66 Scheme to represent the wave packet bouncing on the border of the grid on the right hand side.

The evolution of the quasidiabatic populations (Fig. 67) shows that from an early stage (< 5 fs) a non-negligible amount of the system (at least ~27%) is trapped on the third quasidiabatic potential energy surface. As a first approximation, this means that less than ~73% of the quasidiabatic population follows directly the ESIPT direction on an ultrafast time scale (with a rate constant on the femtosecond time scale). The remaining part of the system (~27% first, then 10% around 50 fs) is momentarily trapped on the unreactive side, which induces a delay and might be the reason for the second rate constant on the picosecond time scale.

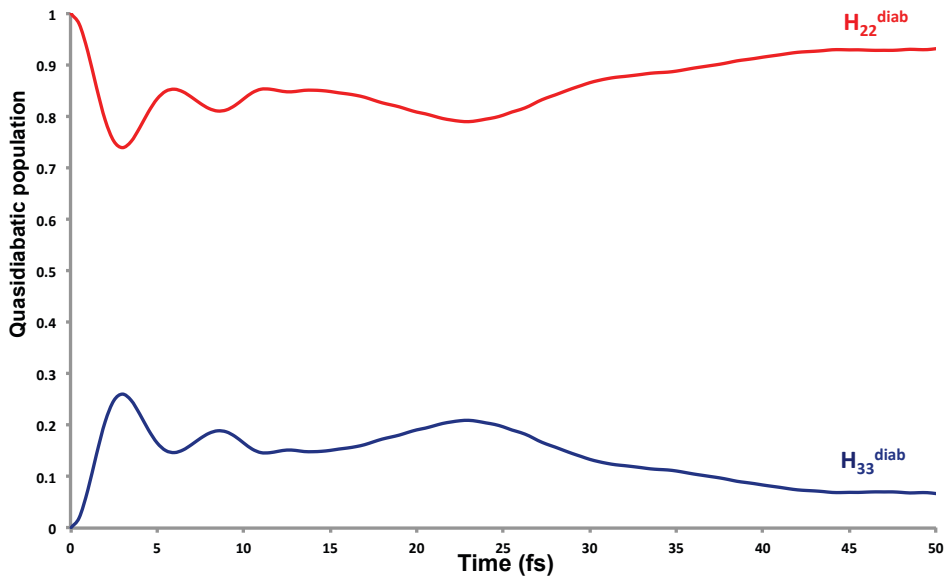

Fig. 67 Evolution of the quasidiabatic populations as functions of time in the gas phase. Red: ππ* state; blue: nπ* state. Coupled potential energy surfaces based on PBE0/cc-pVTZ data.

Our quantum dynamics results show a non-negligible transfer of population from the reactive ππ* state (ESIPT side) to the unreactive state nπ* (TS_2* side). This is a quasidiabatic picture. In terms of adiabatic states, this shows that the presence of the CoIn within the FC region has a significant impact on the photoreactivity, either adiabatically (the system can go to the other side and stay on the lower surface by turning around the conical intersection) or non-adiabatically (by transferring some population to the higher adiabatic state). In any case, this appears to be one of the key points to understand the origin of two different rate constants for the ESIPT process (femtosecond and picosecond time scales). To be able to have a more thorough analysis of the ESIPT rate constants, one should go further, for example upon including step

distributions to investigate the dynamics of the system on ππ* ($H_{22}^{\mathrm{diab}}(\mathbf{Q})$). Adding a complex absorbing potential would also help by making possible to increase the duration of the wave packet propagation.

As a final remark, let us stress that the absorption spectrum presented above had already shown that the dark nπ* state was significantly coupled to the bright ππ* state. This is consistent with our investigation of the photoreactivity where the nπ* state is able to trap some of the system, thus inducing a delay in the ESIPT process occurring on the ππ* state.

IV- 2-Thionyl-3-Hydroxychromone

The 2-Thionyl-3-Hydroxychromone (2T-3HC) study was carried out in collaboration with experimentalists: Dr Thomas Gustavsson (CEA, France) and Prof. Rajan Das (Tata Institute of Fundamental Research, India). They studied the time-fluorescence spectroscopy of 2T-3HC in several solvents. Their preliminary results show that the ESIPT process presents one fluorescence rate constant (picosecond time scale) in cyclohexane and two rate constants in polar solvents such as acetonitrile (unpublished results - paper in preparation).

As several other 3-hydroxychromone dyes, 2T-3HC presents three important reaction coordinates. One corresponds to the ESIPT process already explained in the 3-HC study. The other two are out-of-plane coordinates describing the hydrogen torsion (leading to the trans isomer) and the thione (α) torsion (Fig. 68). They give access to multiple cis and tautomer conformers (Fig. 69). These various conformers may contribute to some extent to the experimental observables (i.e. absorption spectrum, fluorescence rate decay, fluorescence bands, etc…) and on the ESIPT rate constant, which is addressed in this section. In particular, the role of the different conformers and the effect of the solvent polarity during the photoreactivity are investigated. We used cyclohexane (CyHxn) as a non-polar solvent and acetonitrile (MeCN) as a polar solvent within the

PCM description (Chapter I). For more details regarding the solvent description, see the previous section, i.e. Section II-.

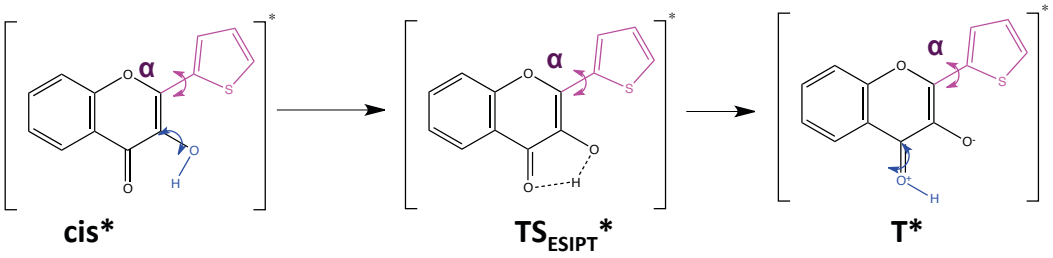

Fig. 68 Lewis representations of the stationary points along the ESIPT coordinate. Purple: thione fragment torsion. Blue: hydrogen torsion. The dihedral angles associated with the hydrogen torsion are defined differently in the enol (i.e. cis) or the keto (i.e. T) forms due to a change of connectivity between them (this has already been pointed out in the 3-HC study).

1. Ground State Potential Energy Surface

As explained previously, there are two extra degrees of freedom to be considered in 2T-3HC in addition to the ESIPT coordinate studied in 3-HC. The torsion angle of the thione fragment will be denoted α (see Fig. 68). These lead to four enol ("cis") conformers, displayed in Fig. 69: the first two have the hydrogen torsion angle at 0° and α = 0 or 180° (i.e. cis or cis(α)), and the last two have the hydrogen torsion angle at 180° and α = 0 or 180° (i.e. trans or trans(α)). The same is true for the keto (tautomer) minima that are now four (i.e. T, T(α), trans-T, trans-T(α); see Fig. 69).

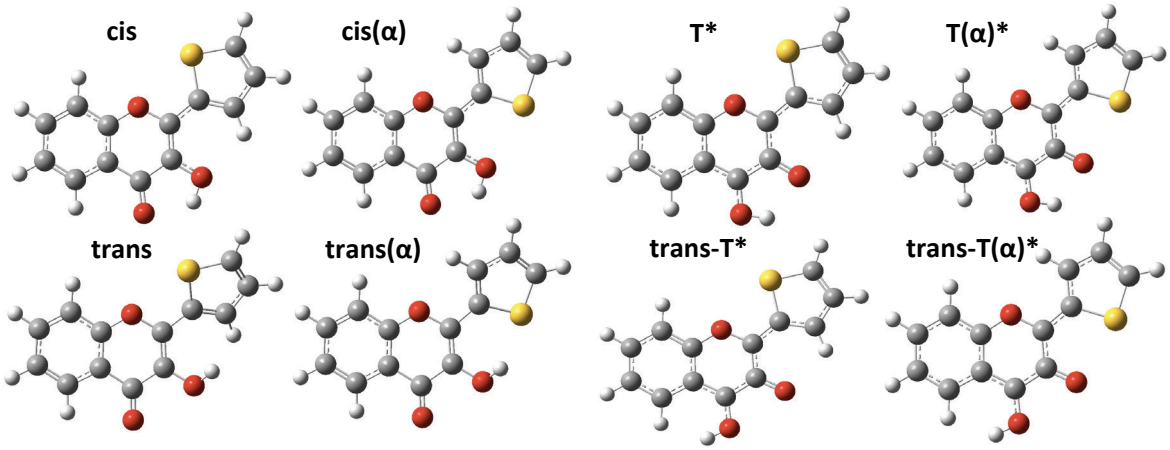

Fig. 69 Enol rotamer optimized minima on the ground state (left panel) and keto rotamer optimized minima on the first excited state (right panel). All the displayed geometries were obtained into cyclohexane solvent. The tautomer rotamers do not exist as minima on the ground state.

However, all these enol conformers (rotamers) do not have the same ground state energies (cis and cis(α) are more stable than trans and trans(α), Tab. 10), thus, their populations are not equivalent. With a Boltzmann distribution, one can estimate the populations of the minima:

$$\frac{N_i}{N} = \frac{g_i e^{-E_i/k_B T}}{\sum_j g_j e^{-E_j/k_B T}} \qquad \textbf{Eq. 105}$$

where N_i is the population of the ith quantum state among a total population N and g_i represents the degeneracy of that state. As cis and cis(α) have the same energy, they are considered as one quantum state with a degeneracy of two; the same goes for trans and trans(α) into acetonitrile (Tab. 10). k_B is the Boltzmann constant and T is the temperature. In our case, we consider room temperature: 298.15 K. In that situation, only cis and cis(α) are populated (i.e. 0.99 of the population) and both minima absorb on the first excited state with the same oscillator strength and a similar vertical transition energy (Tab. 10). Moreover, this result is independent of the solvent polarity.

Tab. 10 Enol conformer energies, vertical transition energies and oscillator strengths from the ground to the first excited state. *Relative energies with respect to the global minimum cis in the ground state. All the energies are given in eV.

	Cyclohexane			Acetonitrile		
	S_0 E*	**E(FC)**	f^{S_1}	**S_0 E***	**E(FC)**	f^{S_1}
cis	0	3.50	0.4378	0	3.52	0.4515
cis(α)	0	3.52	0.4311	0	3.54	0.4463
trans	0.41			0.32		
trans(α)	0.45			0.32		

Hence, at room temperature, we can expect that the absorption spectrum will always present a single absorption band with, possibly, a shoulder related to the cis and cis(α) minima (small difference between their vertical transition energies) but no significant shift due to solvent polarity (results are similar for both solvents). In the following, we investigate the solvent effect on the first excited state and its consequence over the ESIPT process and emission properties.

2. First Excited State Potential Energy Surface

2T-3HC has an electronic structure equivalent to 3-HC. Again, the first and the second excited states are respectively ππ* (A" symmetry) and nπ* (A' symmetry) at both FC and FC(α) geometries (Fig. 70). The thione torsion does not influence the electronic structure, as seen on Fig. 70, the bounding patterns for the n, π and π* orbitals do not change between FC and FC(α) geometries. In addition, in our case, the solvent polarity does not influence the excited states electronic structures either, hence, only molecular orbitals computed into the cyclohexane solvent are displayed in Fig. 70.

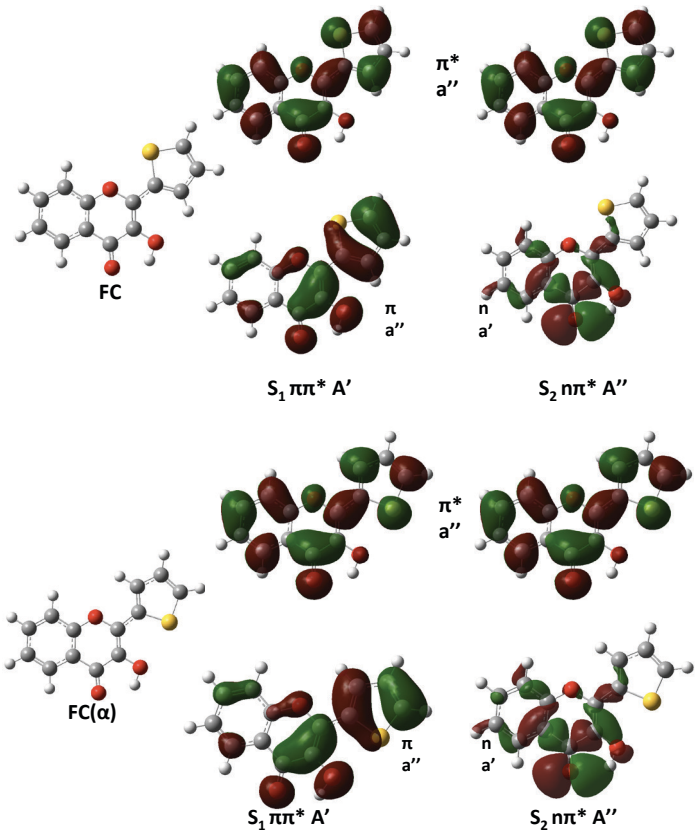

Fig. 70 Singly occupied n, π and π* orbitals for the first excited state (S_1) and the second excited state (S_2) at FC and FC(α) geometries into cyclohexane. The symmetry of the orbitals and electronic states are given for C_s point group symmetry.

The first two excited states of 2T-3HC (i.e. ππ* and nπ*) are similar to the ones of 3-HC. Hence, one can expect the presence and the non-negligible role of a CoIn close to the FC region as in 3-HC, which will be elucidated in the following.

2-1. S_1/S_2 Conical Intersection Characterization

As can be expected, there are two equivalent CoIns (CoIn and CoIn(α)) between the first and the second excited states similar to the ones in 3-HC (Fig. 71).

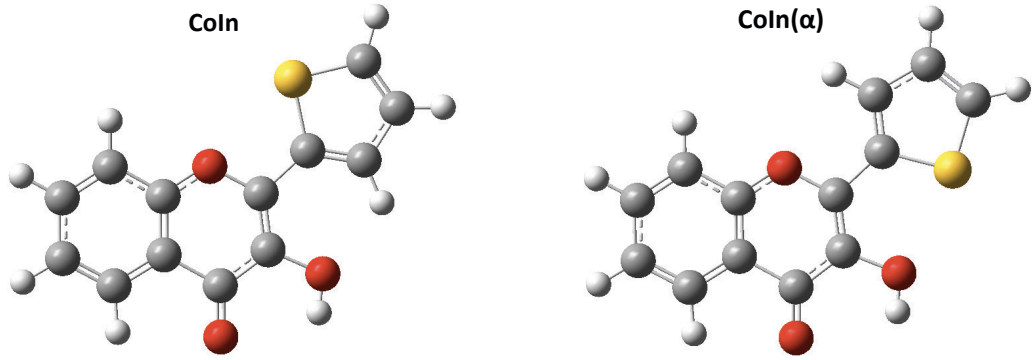

Fig. 71 CoIn and CoIn(α) geometries obtained in cyclohexane. There is no noticeable difference in acetonitrile.

However, their topography changes from peaked in 3-HC to sloped in 2T-3HC (Fig. 72). The TS_2* and TS_2(α)* transition states are now on the second excited state and not on the first one as in 3-HC (Fig. 72). This change of CoIn topography between 3-HC and 2T-3HC is due to the gain of electron delocalization in π orbitals induced by the thione fragment. This can be rationalized quite simply in terms of Hückel theory (Fig. 72). To highlight this idea, we used the free program called HuLiS developed by Nicolas Goudard et al. from the University of Aix-Marseille [295–297], which calculates the energy of any π system with the Hückel method. The corresponding energies of the π and π* orbitals in 3-HC and 2T-3HC are displayed in Fig. 72. One can see that the enhanced delocalization reduces the energy gap between the π and π* orbitals [295–297], which in turn stabilizes the energy of the ππ* electronic state. The stabilization of π* induces a stabilization of the nπ* electronic state as well. However, as the n orbital is not altered, the stabilization of the nπ electronic state is lower than that of the ππ* electronic state. As a consequence, this induces a swap in energy between the first two excited electronic states at the TS_2* geometry in 2T-3HC.

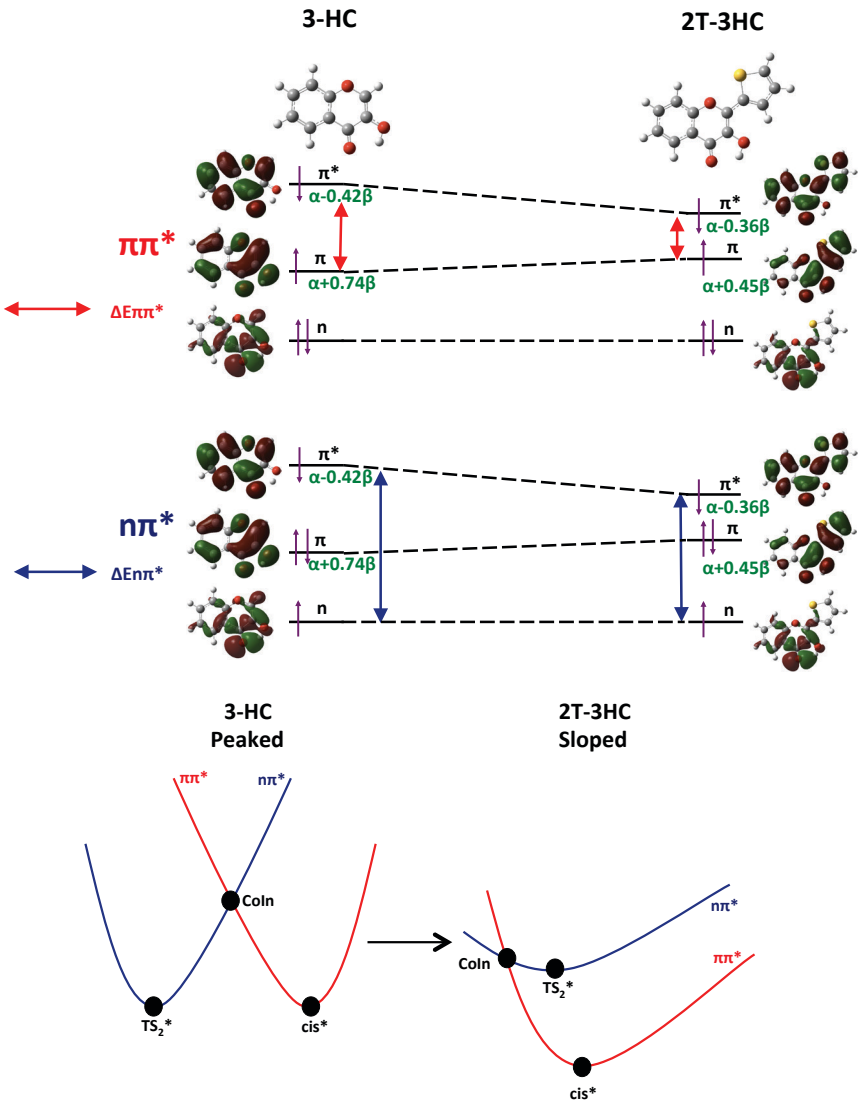

Fig. 72 Upper panel: orbital "correlation diagram" between 3-HC and 2T-3HC and corresponding dominant configurations of the first two excited electronic states. The orbitals energies were obtained with the HuLiS program [295–297] **at the FC geometry only to illustrate the stabilization principle. Red arrow: energy gap between the π and π* orbitals. Blue arrow: energy gap between n and π*. Lower panel: scheme illustrating the change from a peaked (3-HC) to a sloped CoIn (2T-3HC).**

Tab. 11 Energies of the optimized TS_2* and $TS_2(\alpha)$* on the second excited state, of CoIn and CoIn(α), and energy differences between CoIn (CoIn(α)) and FC (FC(α)) within cyclohexane and acetonitrile. Energies are all in eV. The critical point energies are given with respect to the global ground state minimum (cis).

	Cyclohexane	Acetonitrile
$E(S_2)$ TS_2*	3.77	3.94
E CoIn	4.74	4.97
ΔE(CoIn-FC)	1.24	1.45
$E(S_2)$ $TS_2(\alpha)$*	3.25	3.93
E CoIn(α)	4.75	4.88
ΔE(CoIn(α)-FC(α))	1.26	1.36

From their energies, one cannot expect the CoIns in 2T-3HC to play a significant role in the photo-induced process because they are not accessible from FC (more than 1 eV higher) (**Tab. 11**), as opposed to 3-HC. Hence, we will not focus on this region for the rest of this study, but, instead, we will concentrate on the description of the solvent effect over the shape of the first excited state potential energy surface along the ESIPT direction.

2-2. ESIPT Direction

As for the 3-HC study, let us first focus on the geometry relaxation from the FC region after absorption from the cis and cis(α) ground state minima to the first excited state.

To analyze the geometry relaxation on the first excited state from the FC (or FC(α)) geometry to the cis* (or cis(α)*) minimum, one can conduct the same HOMO/LUMO analysis as for 3-HC (Fig. 73 and **Tab. 12**). As said previously, the molecular orbitals do not change in nature between FC and FC(α) geometries. Therefore, this analysis is detailed only for the FC/cis* relaxation (the same holds in the FC(α)/cis(α)* case). As shown on Fig. 73, conclusions are not affected by the solvent polarity. Indeed, as already mentioned, it does not influence the electronic structure, even if it induces a slight shift of the cis*(and cis(α)) equilibrium geometries on the first excited state (the variation of bond lengths is enhanced by the solvent polarity).

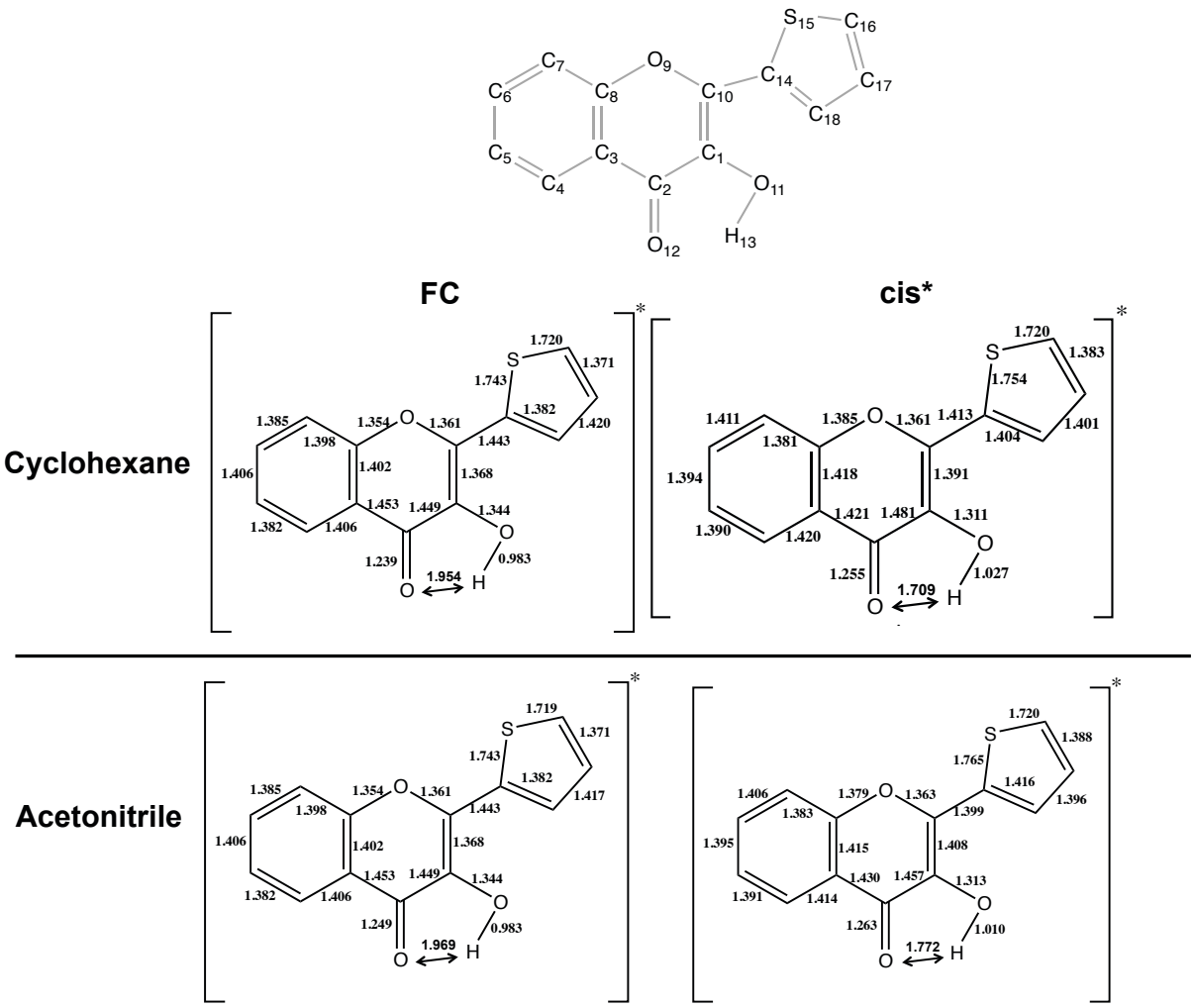

Fig. 73 Upper panel: atom labels. Lower panel: FC (on S_1) and cis* bond lengths in Angstrom in cyclohexane and acetonitrile.

Tab. 12 Nature of the π and π* molecular orbitals at the FC geometry. Δr is defined as the bond length difference between the cis* and FC geometries ($\|r_{cis*} - r_{FC}\|$).

Bond	π interaction	π* interaction	Δr_{CyHxn} (Å)	Δr_{MeCn} (Å)
C_1-C_2	Bonding	Bonding	0.032	0.008
C_2-C_3	Non-bonding	Bonding	−0.032	−0.023
C_3-C_4	Non-bonding	Anti-bonding	0.014	0.008
C_3-C_8	Non-bonding	Anti-bonding	0.016	0.013
C_4-C_5	Non-bonding	Anti-bonding	0.008	0.009
C_5-C_6	Anti-bonding	Bonding	−0.012	−0.011
C_6-C_7	Bonding	Anti-bonding	0.026	0.021
C_7-C_8	Non-bonding	Bonding	−0.017	−0.015
C_8-O_9	Non-bonding	Anti-bonding	0.031	0.025
O_9-C_{10}	Anti-bonding	Anti-bonding	0	0.002
C_{10}-C_1	Bonding	Anti-bonding	0.023	0.040
C_1-O_{11}	Anti-bonding	Non-bonding	−0.033	−0.031
O_{11}-H_{13}	Bonding	Non-bonding	0.044	0.027
C_2-O_{12}	Anti-bonding	Anti-bonding	0.016	0.014
C_{10}-C_{14}	Anti-bonding	Bonding	−0.030	−0.044
C_{14}-S_{15}	Non-bonding	Anti-bonding	0.011	0.022
S_{15}-C_{16}	Non-bonding	Anti-bonding	0	0.001
C_{16}-C_{17}	Bonding	Non-bonding	0.012	0.017
C_{17}-C_{18}	Anti-bonding	Non-bonding	−0.019	−0.021
C_{18}-C_{14}	Bonding	Anti-bonding	0.022	0.034

As seen on **Tab. 12,** C_1-C_2 and C_2-O_{12} should not experience much deformation, contrarily to S_{15}-C_{16} that should increase. As for 3-HC, Fig. 74 shows the electron density difference between the π* and π orbitals at the FC geometry. Regarding the C_1-C_2 and C_2-O_{12} bonds, it is trivial to understand their evolution. The C_1-C_2 interaction is bonding within the π and π* orbitals. Within the π* orbital the local density on C_1 decreases (yellow). Hence, this interaction becomes less bonding within the π* orbital. This induces a destabilization, thus, an increase of the C_1-C_2 bond length. The same idea goes for the C_2-O_{12} bond. The local density increases (blue) on this bond within the π* orbital. Hence, the corresponding interaction becomes more anti-bonding. This induces a

destabilization, thus, an increase of the C_2-O_{12} bond length. The S_{15}-C_{16} bond length evolution is less trivial to understand. The orbitals go from non-bonding to anti-bonding, thus, rather than staying identical, the bond length should increase. However, Fig. 74 shows a gain of density on S_{15} and a loss of density on C_{16}, which must compensate each other. Therefore, the anti-bonding orbital becomes so much less anti-bonding that it is practically a non-bonding interaction, explaining the lack of change in the S_{15}-C_{16} bond length.

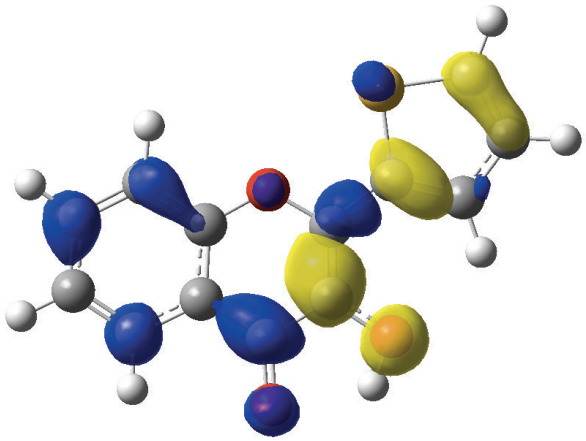

Fig. 74 Electron density difference between the density of the π* and π orbitals at the FC geometry in cyclohexane. Blue: gain of density. Yellow: loss of density.

In addition, as for 3-HC, Fig. 74 highlights the charge transfer (CT) character of the first excited state with respect to the ground state at the FC geometry. One can notice that the electron density goes from the O_{11}-H region (and thione ring) to the C=O_{12} bond (and to some extent to the benzene ring).

As already explained, this change in the nature of the electronic state induces a longer C=O_{12} bond and a shorter C-O_{11} bond at the cis*(cis(α)*) geometry, as well as a longer O_{11}-H bond and a shorter O_{12}-H distance (stronger H-bond). This is consistent with cis*(cis(α)*) being a precursor for a further ESIPT process. Simply, transferring the proton in the first excited state goes with removing the formal charges on both O_{11} and O_{12}. This emphasizes the idea that the driving force of an ESIPT process is based on the acidity of the proton donor (i.e. its ability to give the proton / losing electron density) and the basicity of the proton acceptor (ability to accept the proton / gaining electron density) [240,266,267,279–282].

This analysis shows that initial relaxation from the FC region is expected to yield the cis*(cis*(α)) minimum. From there, the system can further explore multiple directions: direct ESIPT process, hydrogen out-of-plane motion (torsion) or thione fragment out-of-plane motion (i.e. α torsion). Nevertheless, in both solvents, the energies (see Tab. 13) of the TSs related to the cis – trans isomerization of the enol forms (cis* and cis(α)) (i.e. TS_H* and TS_H(α)*, where H is ±90° out of the molecular plane) are higher than the FC energy (~ 3.5 eV). Hence, the hydrogen torsion (from the enol form) is not expected to be involved in the first stage of the ESIPT process.

In addition, Fig. 75 shows that, the α (thione) torsion barrier between cis* and cis(α)* (TS(α)*, where the thione fragment is ±90° out of the molecular plane) is 0.3 or 0.4 eV higher than the FC point (in purple), according to the nature of the solvent. Again, the solvent polarity does not have much influence on this. In both cases, the height of this barrier suggests that two independent ESIPT pathways coexist (with no significant transfer between them): the α = 0° channel and the α = 180° channel, to form two tautomers, denoted T* and T(α)*.

Now, there is also an α torsion barrier between T* and T(α)*. The energy of TS-T(α)* (where the thione fragment is ±90° out of the molecular plane) is close to the FC energy in cyclohexane and 0.06 eV lower in acetonitrile. We could thus expect some significant transfer between both channels in this region, as the barrier is now accessible. However, the system will go through the enol forms (cis* and cis(α)*) as it proceeds along the ESIPT pathways,. As these are fluorescent species, one can expect the system to spend enough time around these minima to redistribute its energy. If so, there may be not enough energy left along the relevant degrees of freedom once it arrives around T* or T(α)* to overcome the TS-T(α)* barrier between them (0.67 or 0.73 eV, depending on the solvent).

The same idea can be applied to the ~ 0.4 - 0.5 eV hydrogen torsion barrier from the tautomer forms. These TSs are denoted TS_H-T* and TS_H-T(α)* and are slightly higher than TS_{ESIPT}* and TS_{ESIPT}(α)*, see Tab. 13. Therefore, we expect the out-of-plane motion not to be relevant for the study of the ESIPT process on the first excited state.

Regarding the thione fragment torsion motion between TS_{ESIPT}* and $TS_{ESIPT}(\alpha)$*, the presence of a transition state or of a second-order saddle point is not to be discarded but we have not found any such point yet.

Tab. 13 Energies of the TSs along the hydrogen torsion from the enol form in cyclohexane and acetonitrile. Energies are given with respect to their respective global minima on the ground state.

	Cyclohexane				**Acetonitrile**			
	TS_H*	**$TS_H(\alpha)$***	**TS_H-T***	**$TS_{H\text{-}T}(\alpha)$***	**TS_H***	**$TS_H(\alpha)$***	**TS_H-T***	**$TS_{H\text{-}T}(\alpha)$***
E (eV)	4.11	3.79	3.38	3.37	3.81	3.81	3.18	3.15

Fig. 75 highlights that, still independently of the solvent polarity, both enol forms (cis* and cis(α)*) and tautomer forms (T* and T(α)*) have the same vertical transition energies from the excited state to the ground state (emission energies — blue and green arrows). Hence, experimentally, the system should present a single absorption band but a dual florescence (one emission peak from the enol forms and another one from the tautomer forms). In addition, the emission energies of the enol and tautomer forms are slightly shifted (~ 0.05 eV) when increasing the solvent polarity. Our calculations are thus consistent with the preliminary experimental results (not published yet) gathered in Tab. 14: one single absorption band and a dual fluorescence that is slightly shifted when increasing the solvent polarity. Regarding the position of the bands, one can notice that our calculations reproduce adequately the absorption and the emission related to the enol forms (cis*) but the emission of the tautomer forms (T*) is shifted by about 0.1 - 0.2 eV with respect to the experimental values. Note that this difference lies within the range of error on excitation energies of organic dyes benchmarked for the PBE0 functional [272,273]. We thus trust our results to describe adequately the UV/vis spectral behaviour of 2T-3HC first excited states.

Tab. 14 Experimental absorption and emission of the enol form (cis*) and the tautomer form (T*) in cyclohexane and acetonitrile.

	Cyclohexane	Acetonitrile
$E_{absorption}$	3.49 eV	3.51 eV
$E_{emission}$ cis*	3.09 eV	3.00 eV
$E_{emission}$ T*	2.27 eV	2.29 eV

Although our results describe adequately the steady-state experimental studies (absorption and emission transitions), they cannot explain the reactivity of the 2T-3HC ESIPT photoprocess because they show no influence of the solvent polarity on the ESIPT barrier (Fig. 75) whereas experiments show a single ultrafast ESIPT rate constant in non-polar solvents and two rate constants when increasing the solvent polarity.

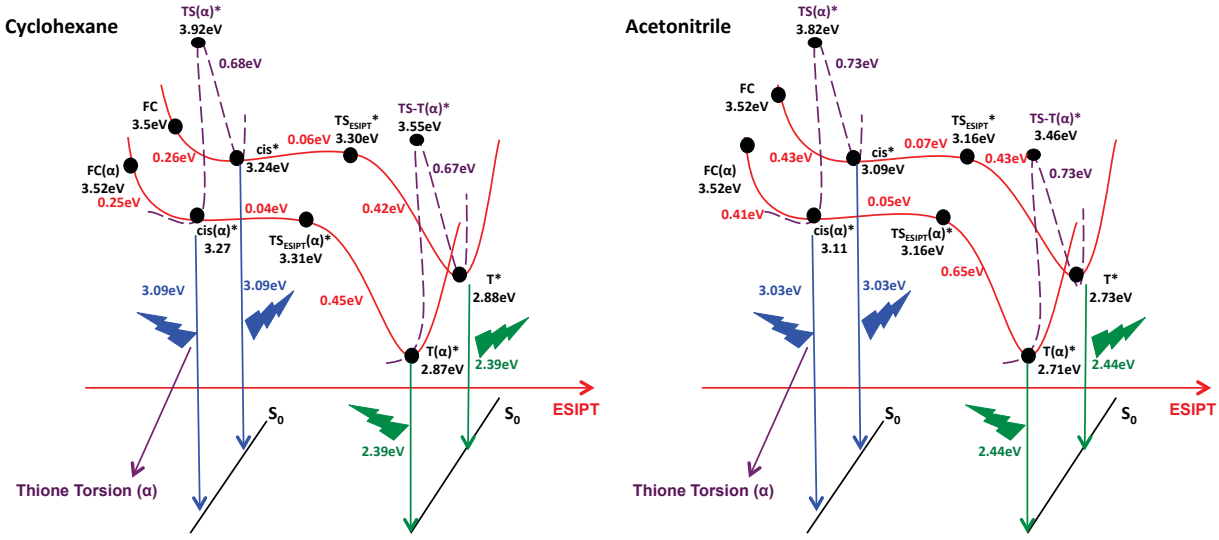

Fig. 75 Scheme of the first excited state (ππ*) along two dimensions: the ESIPT C_s in-plane coordinate (red) and the thione fragment out-of-plane motion (purple). Left: in cyclohexane. Right: in acetonitrile. The optimized stationary point energies are given with respect to the global minimum on S_0 (for each solvent). The geometries were optimized considering the solvent in its equilibrium state in the PCM model. Energy differences between stationary points along the ESIPT direction are in red. The thione fragment torsion barrier is indicated in purple. Emission energies are in blue and green for the enol and tautomer form, respectively (this choice of color corresponds to the experimental color observed during the fluorescence of 2T-3HC).

One of the limitations of our calculations regards the approach used to describe the solvent. A mistreatment of its effect could be the reason of the discrepancy with respect to some of the experimental observations. Modeling solvent effects in non-adiabatic phenomena has an additional difficulty given the different time scales of the various processes undergone by the solute, and the finite relaxation time required by the solvent to equilibrate with the changing geometry or electronic distribution of the solute.

In this study we chose to consider the ESIPT process slower than the solvent relaxation (i.e. solvent equilibrated for the first excited state). However, if there is an important CT character of the electronic state during the ESIPT process (i.e. S_1 electronic state composed of two strongly coupled CT and PT diabatic states, as mentioned for 3-HC and illustrated in Fig. 33), one can expect some impact of the solvent relaxation over the ESIPT dynamics, as discussed by Demchenko et al. on other 3-HC derivatives [266]**.** In other words, the solvent relaxation and subsequent processes that take place on the excited state, such as internal conversion for example, can proceed on the same time scale [298,299]. To the best of our knowledge, this latter situation is impossible to compute with the PCM method currently available [144–146].

Therefore, to account for a different situation than the one presented in this thesis, in a first place, we should considerer the other extreme case that can be adequately addressed computationally: when the solvent is equilibrated for the ground state (study currently on going). This would mean that the ESIPT process is considered faster than the solvent relaxation. For example, this methodology is used to compute adequate excitation energies because the vertical transition can be considered as an instantaneous process.

Also, to explain the experimental observations, one could suggest an alternative ESIPT process involving the sulfur center of the thione fragment, such as illustrated on Fig. 76. It could be in competition with the ESIPT process discussed in this thesis. However, we could not find any T_{SH}* species corresponding to this hypothetical process on the first excited state neither in a non-polar or a polar solvent. In addition, for this new ESIPT process to occur, the system would have to delocalize first along the H-torsion

coordinate to form the trans(α)* species, whereas it is not-reachable from FC as already mentioned at the beginning of this Section, see Tab. 13.

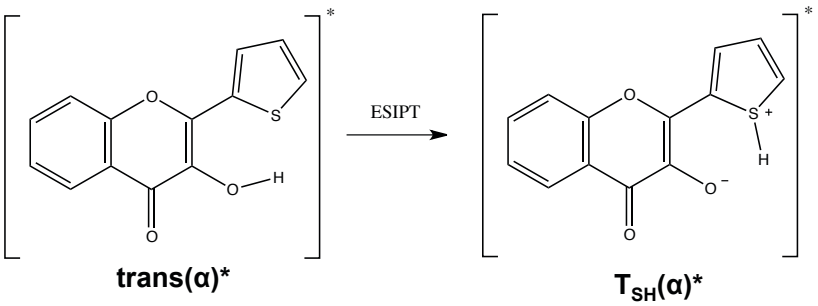

Fig. 76 Hypothetical alternative ESIPT process.

Let us now turn to the method used in our calculations. The most serious deficiency of TD-DFT is arguably the underestimation of charge-transfer excitation energies, which require the use of a non-local exchange correction [300–302]. Therefore, as we suggested the existence of a CT character coupled to a PT one, our level of calculation may not be adapted to describe the whole potential energy landscape. This could be another explanation of why the ESIPT barriers in 2T-3HC are not affected by the polarity of the solvent in our calculations. However, the CT character that we suggest is expected to be weak (strong coupling with the PT, as already mentioned for 3-HC) and occurring over a short range (donor and acceptor fragments close to each other: mainly localized around the O_{12}—H_{13}—O_{11} fragment, as illustrated in Fig. 31 and in Fig. 74). In addition, as already pointed out, our calculations reproduce adequately the excitation energies with respect to the preliminary experimental results and PBE0 has been benchmarked as a good candidate to describe ESIPT processes in 3-HC derivatives. Therefore, we are confident that PBE0 is capable of describing the potential energy surfaces of 2T-3HC. However, as a study based on molecular orbitals only is not enough to make definitive conclusions regarding the nature of the diabatic states (CT, PT) that compose S_1, we suggest completing our study with a valence-bond description that would bring new insights.

As a final remark, we believe that, in this situation, treating the dynamics of the solvent relaxation is a key point to describe adequately the effect of the solvent over the photodynamics.

V- Conclusion and Outlooks

We have performed a computational study of the photodynamics of 3-HC in the gas phase and of 2T-3HC in polar and non-polar solvents in order to suggest a rationalization of the experimental observations: 3-HC presents two ESIPT rates constant [220] as well as 2T-3HC in a polar solvent (a single ESIPT rate constant for 2T-3HC in a non-polar solvent). The study of 2T-3HC is part of a collaborative project with the experimentalists Dr. Thomas Gustavsson (CEA, France) and Prof. Rajan Das (Tata Institute of Fundamental Research, India) [on going research – paper in preparation].

We have carried out TD-DFT calculations to describe the topography of the potential energy surface of the first excited state involved in the photoprocess. A new CoIn was characterized between the ππ* and the nπ* electronic states with a totally planar geometry (C_s symmetry), along a direction approximately parallel to the relaxation coordinate from the Franck Condon point to enol minimum (i.e. cis*).

In 3-HC this peaked CoIn is in the FC region and the system is expected to go through (or close by around) this crossing to further achieve cis-trans isomerization of the enol form. This opens a new channel for an ultrafast population of the nπ* state upon internal conversion. Using full-dimensional models of coupled potential energy surfaces developed during this Thesis work, first based on TD-DFT energies and geometries, we have run quantum dynamics simulations with the multilayer version of the multiconfiguration time-dependent Hartree (ML-MCTDH) method [200]. Our quantum dynamics calculations clearly indicate that the nπ* quasidiabatic electronic state is populated right after photoexcitation, thus showing that the non-adiabatic coupling within the FC region is crucial to understand the ESIPT dynamics. This feature is expected to be even more efficient in polar solvents than in the gas phase due to different stabilizations of the electronic states according to their dipole moments. This results in making cis-trans isomerization of the enol form more accessible (ongoing study that requires a better description of the H torsion within the potential energy surfaces model). Such computational results are consistent with the recent experimental observations of Chevalier et al. [220], where the possible involvement of the trans species is mentioned. These results suggest that the ESIPT process, which is a planar

motion, is in competition with the cis - trans isomerization of the enol form (out-of-plane motion).

In contrast, in 2T-3HC this CoIn is sloped and not reachable from FC; in other words, it is expected to be too high in energy to have a relevant impact on the photoprocess. In addition, our calculations in polar and non-polar solvents could describe the spectral behavior adequately but not the reactivity (we suspect that the effect of the solvent on the barrier requires a more sophisticated approach). Therefore, the quantum chemistry study of 2T-3HC should be extended, possibly with a valence-bond analysis of the nature of the first excited state to get more details about its CT/PT characters [303]. In addition, to make totally sure that the method we used is adequate, one may try to run RASSCF calculations (CASSCF with a reduced rather than complete active space). Then, if the CT character is significant in the first excited state, this study may have to be completed with a more adapted method such as RASSCF [304,305] or using TD-DFT with a non-local exchange correction [300–302]. In addition, one should study the effect of the solvent polarity with the PCM model when the solvent is equilibrated for the ground state and not for the excited state (the ESIPT process will then be considered faster than the solvent relaxation). The key point is to determine if there is an important deformation of the potential energy landscape while considering different dynamics for the solvent relaxation. If so, one should thus use a more advanced model of the solvent dynamics, for example a QM/MM method with an explicit description of the solvent (hence, explicit solvent relaxation dynamics), such as the strategy developed by Prof. B. Mennuci et al. [306–309]. Another possible strategy to follow before using a more complex representation of the solvent dynamics would be to run dynamics calculations in order to check if the hydrogen and the thione fragment torsions really are irrelevant motions during the dynamics of the photoprocess. To accomplish this task, one should not use our model as it is because it should be improved with the implementation of periodic functions to describe both torsions correctly. However, on-the-fly dynamics such as DD-vMCG [31,310] or ab-initio molecular dynamics [311–313] may give first insights.

Chapter IV- Aminobenzonitrile intramolecular charge transfer

This Chapter is focus on the studied of the ultrafast intramolecular charge transfer process of aminobenzonitrile.

It was carried out in close collaboration with the group of Dr. Mar Reguero from the Universitat Rovira i Vigili in Tarragona, Spain. This group is specialized in CASPT2 calculations on excited states. Pedro J. Castro, as part of his PhD thesis, achieved all the CASPT2 and some of the CASSCF and PCM quantum chemistry calculations on ABN.

The specificity of the present thesis was first to understand the static landscape of the excited states involve in the photoprocess by the used of quantum chemistry calculations and, then, build a quasidiabatic Hamiltonian model and run quantum dynamics calculations.

I- Introduction and Context

Intramolecular Charge Transfer (ICT) in electron donor–acceptor molecules is a process of high interest that has given place to a strong debate over the last decades. A large amount of experimental and theoretical studies have been devoted to this kind of systems, often focused on the aminobenzonitrile family, and particularly on the parent system, 4-aminobenzonitrile (ABN) (R=H, Fig. 77), and on its N-dimethyl derivative, DMABN (R=CH_3, Fig. 1); see [314] for an extensive review. The small size and simple architecture of ABN and DMABN have made them prototype systems for studying photoinduced ICT phenomena.

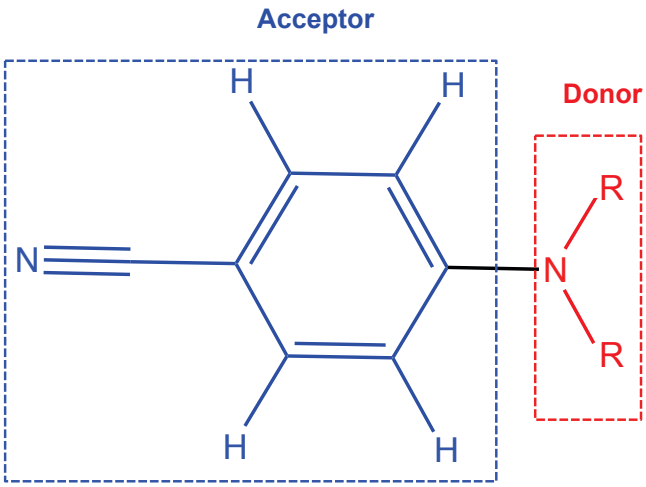

Fig. 77 Donor and acceptor parts of the aminobenzonitrile family. R=H:ABN, R=CH_3:DMABN.

They are particularly interesting because, despite their similarity, their luminescent patterns are quite different: while ABN only shows a single (normal) fluorescence band in any environment, DMABN exhibits normal fluorescence in non polar solvents, but dual fluorescence in polar ones [314–318] (Fig. 78). This indicates that the different photochemical behaviors are not due to different characters of the electronic states, but to changes induced by the polar environment. This dual fluorescence sensitivity to the environment makes ABN derivatives good candidates as fluorescent probes, chemical sensors, molecular switches or electrooptical switches [228,319–323].

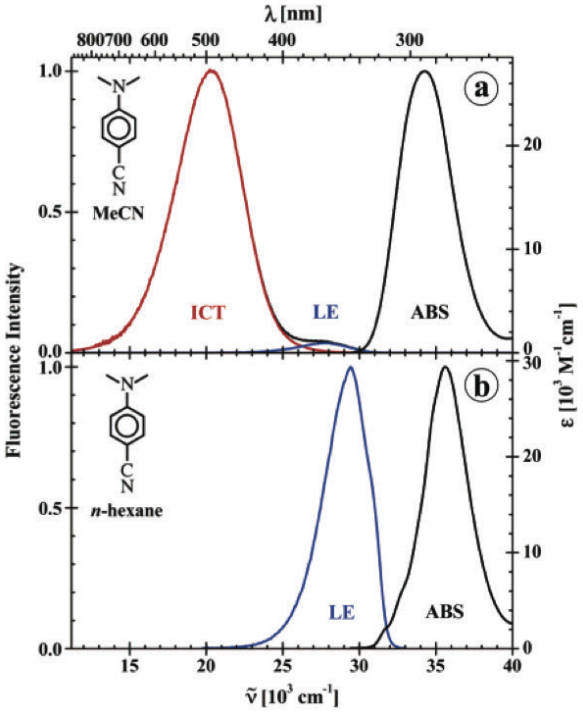

Fig. 78 Fluorescence (LE and ICT) and absorption (ABS) spectra of 4-(dimethylamino)-benzonitrile (DMABN) in (a) acetonitrile (MeCN) and (b) in n-hexane at 25°C. Excitation wavelength: λ_{exc}= 267 nm (from Ref. [317]**).**

In spite of the large amount of time and effort invested in their study, there is still a very lively controversy involving these systems [314]. It is well-established that the normal band is originated from a Locally Excited (LE) electronic state, while the anomalous band is due to a Charge Transfer (CT) electronic state of high dipole moment that is stabilized in polar solvent environments. In other words, the intensity and mean frequency of the charge transfer state emission has been found to depend strongly on the polarity of the solvent [314,315,318,324–328].

The exact structures of the species responsible of the anomalous band and the mechanism that populates them are, though, still not clarified questions due to contradictory arguments, based on both experimental observations and theoretical calculations, which support different models and hypotheses [314,316–318,324,329–345].

Mainly, three models are in the lead of the controversy regarding the structure of the luminescent charge transfer species: the Planar ICT model (PICT) with the amino group lying in the benzene plane [328,335,336,346] (Fig. 79), the Twisted one (TICT) (Fig. 79), which involves some charge separation in the charge transfer state resulting from a

complete decoupling between the amino (donor, see Fig. 77) and benzonitrile (acceptor, see Fig. 77) moieties by twisting the amino group into a perpendicular position [324,347,348], and the partially twisted or pretwisted one (pTICT) [340] (Fig. 79), where the benzene and amino groups are only partially rotated (twisting angle <90°), so the decoupling between both moieties is not complete. It seems sufficiently proved that the PICT and TICT species do in fact correspond to two minimum-energy points of the potential energy surface (PES) of the excited charge transfer state both in ABN and DMABN, but their role in the fluorescence spectra is less clear. A fourth model, the rehybridized ICT (RICT) [339] (Fig. 79) is characterized by the rehybridization from sp to sp^2 of the cyano-carbon atom. The RICT species corresponds to the minimum energy structure of the so-called πσ* state, where the excitation is localized on the triple bond of the cyano group. It is nowadays discarded as a luminescent species [338] but there are still debates on the involvement of the πσ* state in the mechanism of the intramolecular charge transfer process [341,342,349]. Among the arguments against the RICT model: the calculated ν(CN) frequency in the infrared spectra is quite different from the experimentally observed one, in Ref. [329].

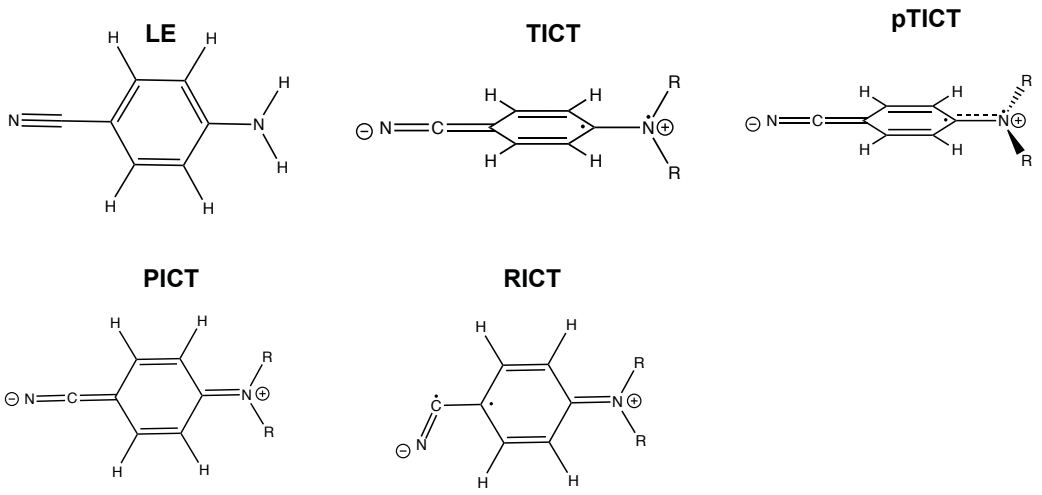

Fig. 79 Structures of the excited state minima of the aminobenzonitrile family. R=H: ABN, R=CH_3: DMABN.

Support for the TICT model was mainly derived from an interpretation of the photophysical behavior of model compounds in which rotation of the amino group was hindered, or in which a large twisting angle of the amino group was already present in the electronic ground state [314]. However, recent experiments have shown that efficient ICT can be observed in similar molecules forced to be planar: namely, 1-tert-

butyl-6-cyano-1,2,3,4-tetrahydroquinoline (NTC6) and fluorazene [350] (Fig. 80). This suggests that the formation of a TICT structure may not be required for excited state charge transfer in aminobenzonitriles. Furthermore, some authors suggest that the TICT species is in fact dark (i.e. does not emit) and that the pTICT species is thus the one that could be responsible for the anomalous fluorescence band [340]. Nevertheless, the theoretical study of several ABN family molecules by Jödicke et al. [351] highlights the fact that the excited states behave very differently along the torsion coordinates depending on ortho substitution by methyl groups on the benzene moiety.

More recently, to explain the observed rise and decay times of fluorescence of ABN derivatives measured by time-resolved transient absorption spectra, some authors suggested the involvement of the πσ* state in the mechanism of population of the ICT luminescent species [352]. Subsequent experiments reinforced this idea [349,353], but later experimental [342,343] and theoretical [341] studies suggested a different interpretation of the experimental observations, so the involvement of the πσ* state in the charge transfer mechanism is now doubtful. Therefore, if one wants to clarify the luminescent charge transfer species controversy, a thorough analysis of the energy landscapes of the first and second excited electronic states of the various ABN-type molecules is mandatory. The subtle interplay between the nature of the electronic states and molecular structures could explain why there is so much contradictory evidences supporting either TICT, PICT, or pTICT models, and a quantum dynamics study is required to give new relevant information. Nevertheless, in the present thesis we will not concentrate on elucidate this PICT/TICT controversy but rather focus on understanding the early stage of the ICT process and internal conversion between the LE and CT states, which we believe may also give some new insight into the PICT/TICT controversy.

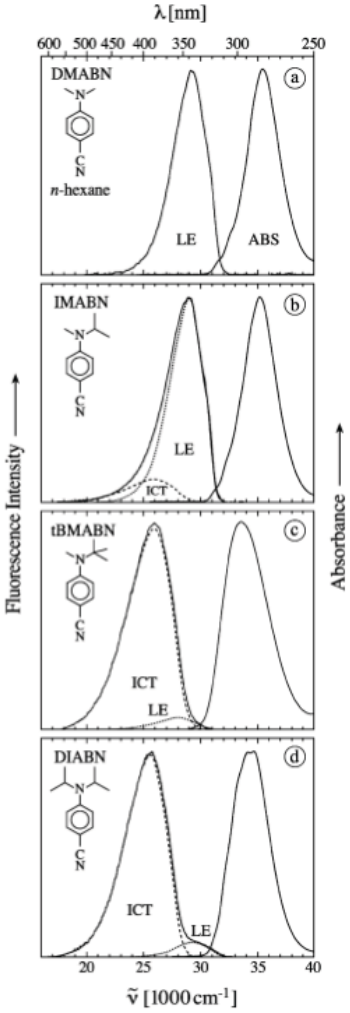

Fig. 80 Fluorescence (LE and ICT) and absorption (ABS) spectra in n-hexane at 25°C of (a) 4-(dimethylamino)benzonitrile (DMABN), (b) 4-(isopropylmethylamino)-benzonitrile (IMABN), (c) 4-(tert-butylmethylamino)benzonitrile (tBMABN), and (d) 4-(diisopropylamino)benzonitrile (DIABN). The fluorescence spectrum of DMABN consists of a single LE emission, whereas IMABN, tBMABN, and DIABN are dual fluorescent (LE and CT). Excitations were made in the maxima of the absorption spectra. From Ref. [350].

We will now focus on the ICT mechanism. It is well-established that the initial excitation populates first the second excited electronic state of charge transfer character, i.e., S_2-CT [354]. The subsequent sequence of steps along the LE or CT potential energy surfaces until the luminescent species are populated is still under discussion. Robb et al. in 2005 proposed the following mechanism [354]. After excitation to the second excited electronic state, the system relaxes to the S_2-PICT minimum. Along the ring-bending coordinate the system follows a barrierless pathway to the optimized S_1/S_2 CoIn denoted CoIn-C_s. Because of the extended conical intersection seam, ultrafast nonradiative decay from S_2 to S_1 can take place at various torsion angles of the amino

group leading either to the S_1-LE or the S_1-TICT geometries (see Fig. 81). Experimental works suggest initial population of the LE state and later equilibration with a charge transfer state [317].

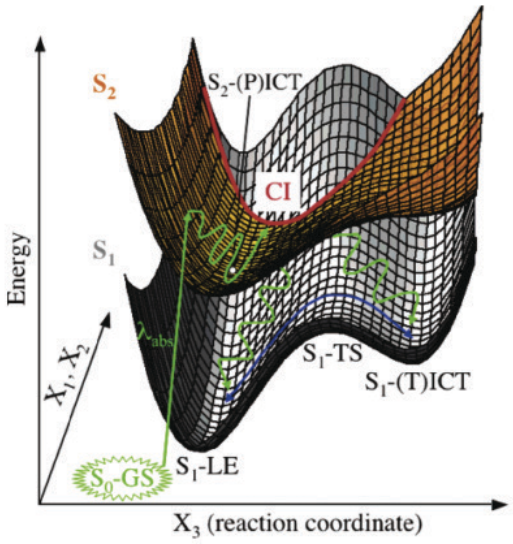

Fig. 81 Schematic representation of the conical intersection between S_1 and S_2 in a space that includes one of the two branching space coordinates (X_1,X_2) and the reaction coordinate (mainly the amino group torsion), and the energy. The green curve shows the non-adiabatic pathway. The blue curve shows the adiabatic pathway. From Ref. [354].

Park et al. have published a recent paper reporting a study of highly Time-Resolved Fluorescence Spectra (TRFS) over the whole emission region of DMABN in acetonitrile [343]. The accurate measurements of this study give information about the dynamics of the ICT process free from the interferences of the solvent reorganization and vibrational relaxation dynamics that occur on the same time scale. The experimental techniques used in that work also give access to an analysis of the ultrafast events that occur within the first few femtoseconds. From their observations it is concluded that, after photoexcitation to the second excited electronic state, both the CT and LE states are populated in less than 30 fs for geometries that are still quasiplanar. A similar ultrafast interval conversion was also proposed in a previous work by McCamant et al [344,355]. This early internal-conversion process is the main focus of the present Chapter. Subsequent processes from the initial LE and ICT species leading to the formation of the ICT specie(s) responsible of the anomalous fluorescence band have been studied recently by our Spanish collaborators [316].

Computational studies carried out on ABN and DMABN have shown that the topography of the potential energy surfaces of the low-lying states of both systems are similar, but small energetic changes induce a different interplay between the LE and CT species that leads to different luminescent patterns [316,354]. The initial steps of the photochemistry, though, are expected to be analogous in both systems, so the experimental conclusions derived by Park et al. [343] for DMABN, must hold in a qualitative way also for ABN.

In this collaborative project, we have performed a computational study (quantum chemistry and quantum dynamics) on ABN in the gas phase and acetonitrile in order to corroborate or discard the hypothesis of Park et al. [343] and provide further information about the ultrafast process that populates the LE state almost immediately after the initial photoexcitation.

We have carried out a preliminary CASSCF(12,11)/cc-pVDZ study to describe the topography of both coupled potential energy surfaces involved in the initial steps of the process using the Gaussian 09 package. In this way we have established the paths and regions of the surfaces that determine the mechanism of the ultrafast process under study (< 30fs) and highlighted a new photoreactive pathway in agreement with the experimental results of Park et al. [343]. The energies in these regions have then been recalculated at the CASPT2 level with the Molcas 7 package to include the effect of dynamic correlation in the calculations. To treat the conical intersection region with the CASPT2 method, one must apply the second order perturbation correction to (quasi)degenerate electronic states. To this end, the Multi-State Complete Active Space Second Order Perturbation Theory (MS-CASPT2) approach was used. It builds an effective Hamiltonian between the perturbed electronic states and then diagonalizes the resulting matrix in order to obtain the resulting perturbed electronic states treated on the same footing.

The solvent effect was included implicitly within the PCM model (Chapter I). We developed full-dimensional models of coupled potential energy surfaces, first based on CASSCF energies and geometries and further refined to match CASPT2 data, both in the gas phase and in acetonitrile, and used them to run quantum dynamics simulations with

the multilayer version of the multiconfiguration time-dependent Hartree (ML-MCTDH) method [200].

II- Quantum Chemistry

To determine the paths and regions involved into the early stage of the ultrafast intramolecular charge transfer, we analyzed in a first stage the nature of the electronic states within the FC region and determined the relevant stationary points. In a second stage, we characterized several CoIns. The solvent effect on the photoprocess was investigated in a third stage.

1. Franck-Condon Region

First, CASSCF/CASPT2 calculations in the gas phase show that light absorption occurs from a double-well region in the ground-state potential energy surface. The two equivalent minima, denoted FC-C_s, have a wagged geometry belonging to C_s point-group symmetry. Both points are connected through a planar C_{2v} transition state (TS), for which the transition vector corresponds mainly to the pyramidalization of the amino group (see Fig. 82). This planar transition state, named FC-C_{2V}, has a small energy barrier of 0.06eV at the CASPT2 level (see **Tab. 15** for CASSCF/CASPT2 energies of the critical points in the gas phase). The objective of this study is not to consider possible tunneling in the ground state but what occurs in the excited states. We will thus consider this FC-C_{2V} TS as an effective average FC point.

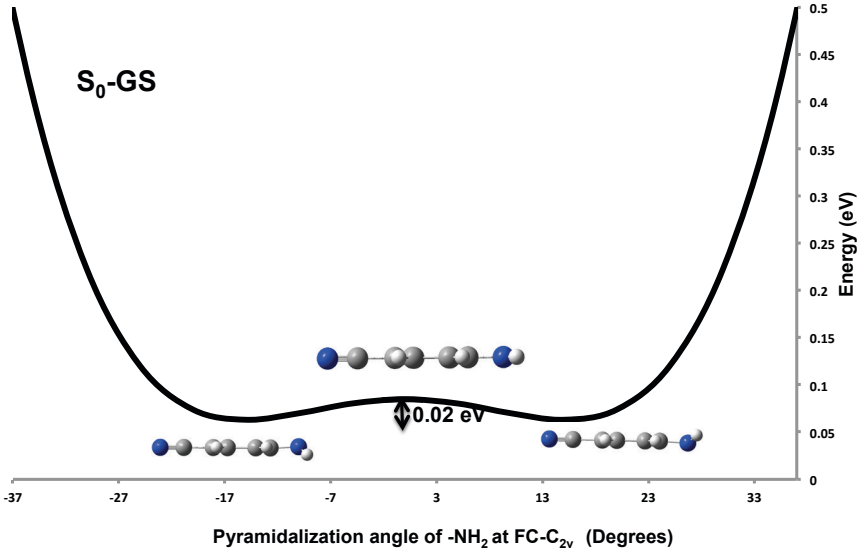

Fig. 82 SA4-CASSCF/cc-pVDZ scan for the ground state along the -NH_2 pyramidalization coordinate, from FC-C_{2v}. Energies in eV are given with respect to the FC-C_s global minimum at the SA4-CASSCF/cc-pVDZ level of theory (note that CASSCF energies are different from the values given in Tab. 15 because SA4 was used here rather than SA2).

Tab. 15 Energies in eV and oscillator strengths calculated at the CASSCF(12,11)/cc-pVDZ and CASPT2/cc-pVDZ levels of theory for various critical points of ABN on the first three electronic states, in the gas phase. * Energies calculated using SA2-CASSCF(12,11)/cc-pVDZ. Energies calculated using MS2-CASPT2/cc-pVDZ.**

		GS	LE	CT
FC-C_s	E_{CASSCF}	0.00	4.79	6.54
	E_{CASPT2}	0.00	4.67	5.44
	f	/	0.01	0.43
FC-C_{2v}	E_{CASSCF}	0.08	4.83	6.38
	E_{CASPT2}	0.06	4.64	5.38
	f	/	0.01	0.49
LE-C_s	E_{CASSCF}	0.20	4.59	6.40
	E_{CASPT2}	0.10	4.42	5.31
	f	/	0.01	0.39
LE-C_{2v}	E_{CASSCF}	0.27	4.64	6.28
	E_{CASPT2}	0.16	4.39	5.27
PICT	E_{CASSCF}	0.44	4.89	6.11
	E_{CASPT2}	0.26	4.59	5.15
	f	/	0.02	0.66
CoIn-C_s	E_{CASSCF}*	/	5.62	5.62
	E_{CASPT2}**	/	5.03	5.00
CoIn-C_{2v}	E_{CASSCF}*	/	6.71	6.71
	E_{CASPT2}**	/	5.62	5.61

As aforementioned, the first and the second excited electronic states in the Franck-Condon (FC) region correspond to the LE and CT states, respectively. Their electronic characters are determined by their orbital populations, which we represent with the density difference of the S_1 or S_2 excited states with respect to the ground state (at FC), as shown in Fig. 83. The first excited state shows an excitation of the electronic density delocalized over the whole molecule, mainly on the benzene ring (LE). One can notice that the electronic density in the excited state is less bonding and tends to relocalize the π system on the carbon atoms of the ring. On the cyano and amino fragments, the change in the electronic density shows that out-of-plane orbitals are depopulated to the profit of

in-plane orbitals. The second excited state shows a motion of the electronic density from the donor fragment (amino group) to the acceptor fragment (the rest of the molecule). This latter electronic behavior creates a separation of charge, the so-called intramolecular charge transfer, as illustrated by the large value of the dipole moment of S_2-CT: 11.30 [11.51] D, while it is only 5.02 [5.30] D for S_1-LE (CASPT2 [CASSCF] values, in agreement with already published dipole moment in Ref. [316]).

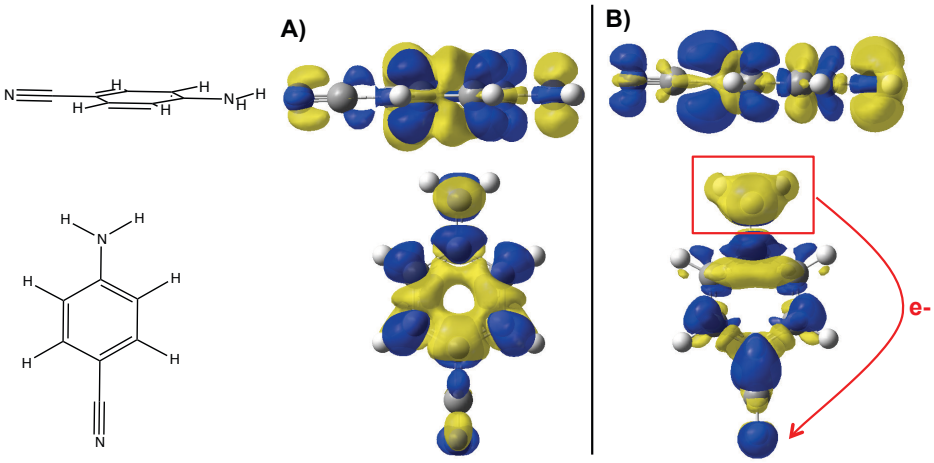

Fig. 83 Electron density difference between the total electron density of: A) the first excited state, B) the second excited state, with respect to the ground state at the FC geometry. Blue: gain of electronic density. Yellow: loss of electronic density.

The S_1-LE potential energy surface also has a double-well shape. The corresponding TS (LE-C_{2v}) is 0.03eV (CASPT2; 0.01eV, CASSCF) higher than the LE wagged minima, which are 4.42 eV (dipole: 5.11 [5.40] D) above the ground-state ones (see Fig. 84).

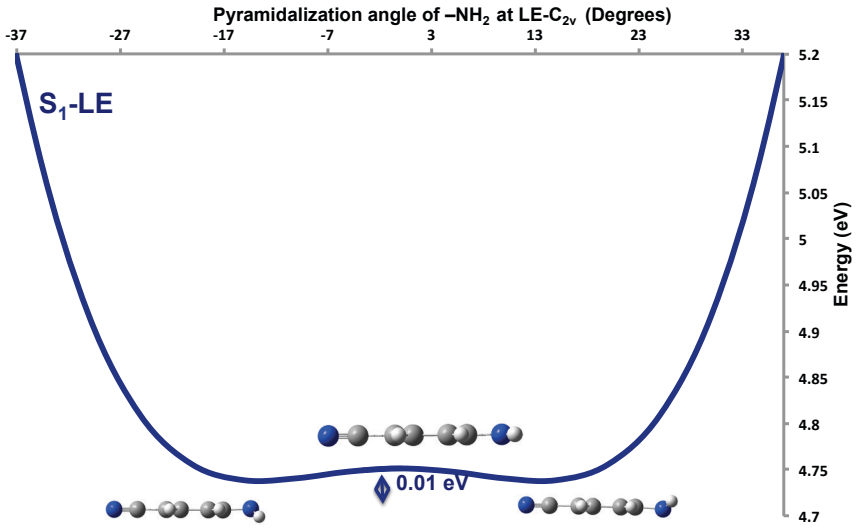

Fig. 84 SA4-CASSCF/cc-pVDZ scans for the LE excited state along the -NH_2 pyramidalization coordinate, from LE-C_{2v}. Energies in eV given with respect to the FC-C_s global minimum at the SA4-CASSCF/cc-pVDZ level of theory (note that CASSCF energies are different from the values given in Tab. 15 because SA4 was used here rather than SA2).

The S_2-CT potential energy surface shows a flat single well with a planar C_{2v} minimum denoted PICT, 5.15 eV (dipole: 11.71 [11.91] D) above the ground state FC-C_s minima (see Fig. 85).

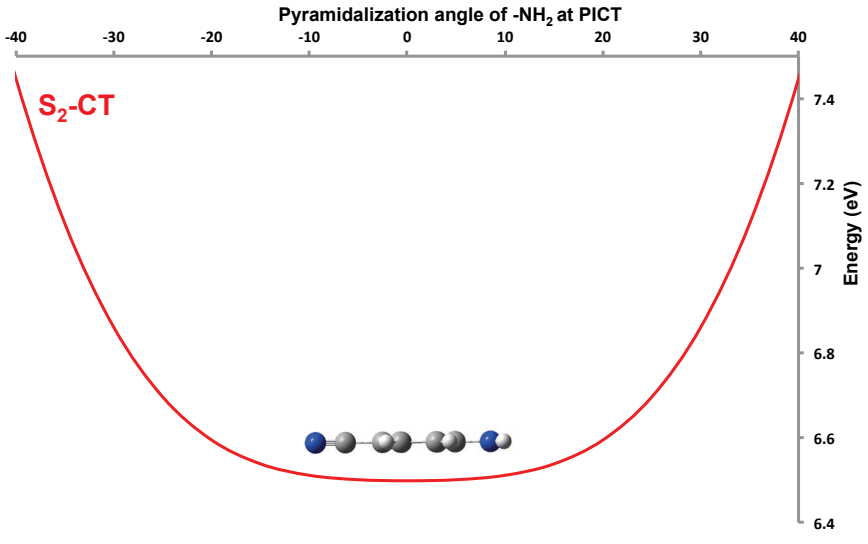

Fig. 85 SA4-CASSCF/cc-pVDZ scans for the CT state along the -NH_2 pyramidalization coordinate, from PICT. Energies in eV given with respect to the FC-C_s global minimum at the SA4-CASSCF/cc-pVDZ level of theory (note that CASSCF energies are different from the values given in Tab. 15 because SA4 was used here rather than SA2).

The large oscillator strength found for the excitation to S_2-CT from the FC-C_{2v} transition state, as well as from the FC-C_s wagged minima (i.e. f = 0.4-0.5 at the CASPT2 level; see **Tab. 15**), indicates that S_2 is the most optically active one. The corresponding excitation energies (4.67 and 5.44 eV in the gas phase for LE and CT respectively; $\Delta E(S_1\text{-}S_2)$ = 0.77 eV) are in reasonable agreement with experimental results (4.72 eV for the maximum of the absorption band and $\Delta E(S_1\text{-}S_2)$ = 0.59 eV in *n*-hexadecane) [356]. As seen on Fig. 86, which depicts the S_2- FC-C_s forces obtained at the CASSCF level, the initial relaxation on the S_2-CT state is governed mainly by an in-plane quinoidal coordinate with contributions from the out-of-plane motion of the amino group and leads directly to the region of the PICT species (0.29 eV below the excitation energy).

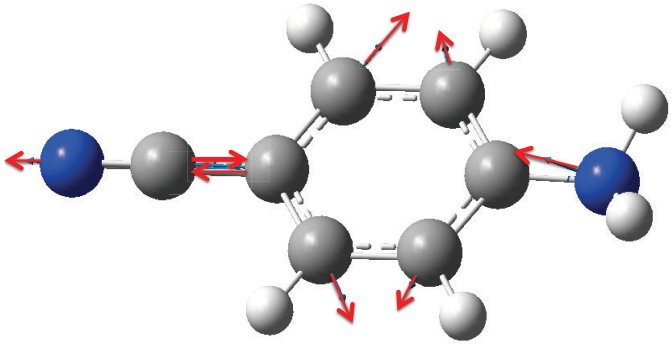

Fig. 86 Force at the S_2-FC-C_s point.

2. Conical Intersection Seam

In collaboration with the group of Dr. Mar Reguero, a new conical intersection was found between the S_2-CT state and the S_1-LE one for a totally planar geometry (C_{2v} symmetry), along a direction approximately parallel to the relaxation coordinate from the Franck Condon point to S_2-CT PICT minimum. This opens a new channel for an ultrafast population of the S_1-LE state upon internal conversion, which could discard the need for out-of-plane motions or the involvement of the $\pi\sigma^*$ state in the charge transfer process, at least during its early stages (~10fs).

Has already mentioned, Robb et al. [345,354] have reported a minimum-energy conical intersection (CoIn) point between the S_1-LE and S_2-CT states, of non-planar C_s geometry

denoted CoIn-C_s with a bent ring and a slightly wagged amino group. There are two equivalent and symmetric CoIn-Cs: one with the bent ring "up" and the other one with a bent ring "down" (see Fig. 87). Its branching space vectors are mostly made of skeletal deformations of the phenyl ring coupled with the C-N stretch of the amino group as depicted in Fig. 88 (CASSCF level).

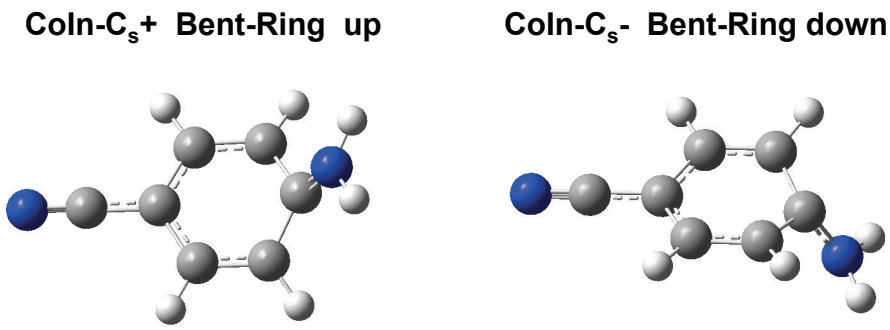

Fig. 87 Optimized geometry at the CASSCF/cc-pVDZ level of theory of the pair of S_2/S_1 CoIns denoted CoIn-C_s+ and CoIn-C_s-.

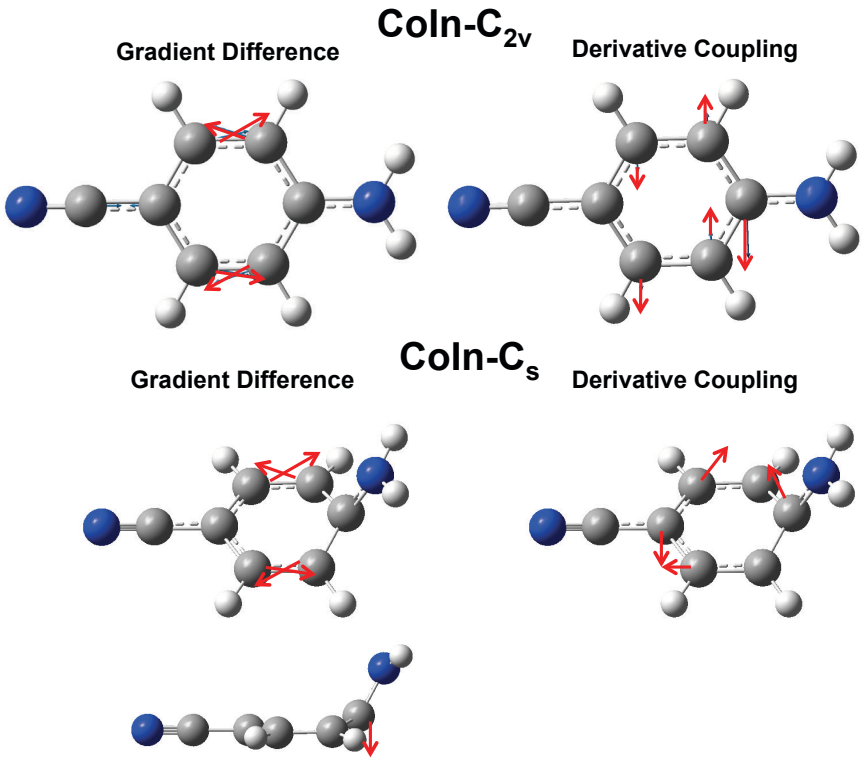

Fig. 88 Gradient differences and derivative couplings at both CoIns calculated at the CASSCF level.

In our recent paper [357], we reported a new CoIn belonging to C_{2v} point-group symmetry with a planar geometry, denoted CoIn-C_{2v}. This point has been optimized at

the CASSCF level, but its position and energy slightly shift when recalculating the energy profiles at the CASPT2 level. The relocated crossing point is 0.16 eV above the energy of the S_2-CT state at the FC-C_s geometry, 0.46 eV above the PICT minimum, and ~0.60 eV above the CoIn-C_s point (see **Tab. 15** –CASPT2 level and Fig. 89).

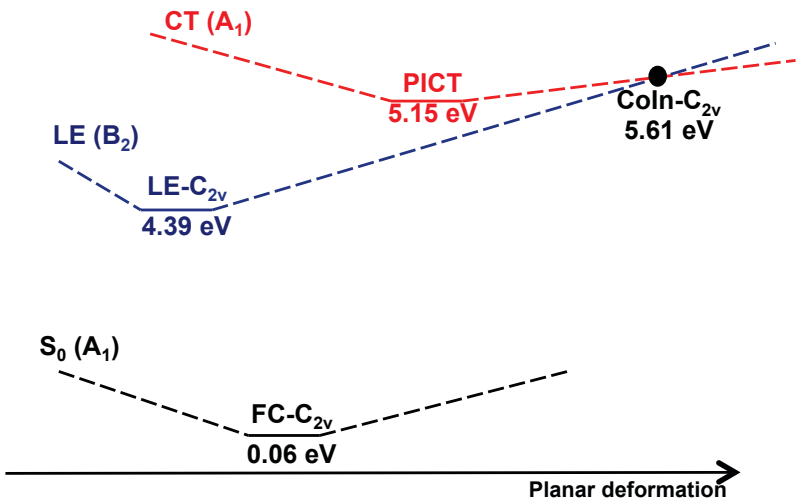

Fig. 89 Energies of the critical points of C_{2v} symmetry at the CASSCF(12,11)//CASPT2/cc-pVDZ level of theory. The irreducible representation of each state is indicated within parentheses.

The initial relaxation that leads from FC-C_{2V} on S_2-CT to the PICT minimum (the force at the FC-C_{2v} point is a quinoidal deformation, see Fig. 90) further leads to CoIn-C_{2v} (72% overlap between the gradient at S_2-FC-C_{2V} and the direction from FC to CoIn-C_{2V}). In addition, the gradient difference of this CoIn conserves the C_{2v} symmetry (Fig. 88).

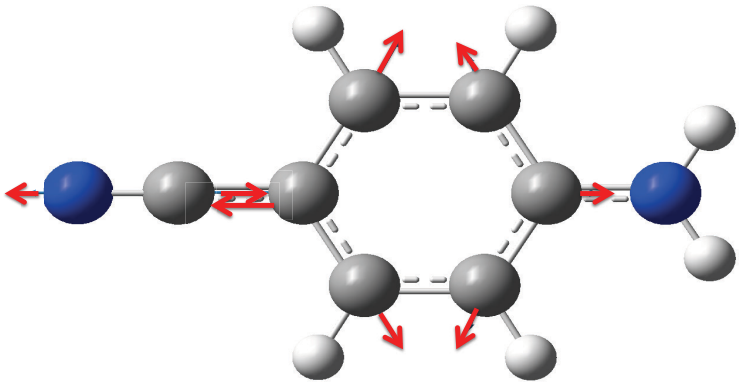

Fig. 90 Force at the S_2-FC-C_{2v} point.

This indicates that access to this CoIn is favored due to the momentum acquired by the nuclei during the initial relaxation. This new CoIn is thus easily accessible according to both energetic and geometric criteria, and deactivation through this point is expected to be ultrafast.

The CoIn-C_s point (optimized at the CASSCF level and also relocated at the CASPT2 level) is ~ 0.60 eV lower than the CoIn-C_{2v} point. In collaboration with our Spanish colleagues, a continuous seam of conical intersection joining these two points and decreasing monotonically was characterized along a relaxed-interpolated coordinate (optimizing conical intersections for fixed values of the bending angle defined by the out-of-plane motion of the carbon atom bonded to the amino group) [357]. This was calculated at the CASSCF level only because such optimizations are not available at the CASPT2 level. However, we can safely assume that the landscape does not change qualitatively when dynamic correlation is included, as proved by the existence of both CoIn-C_{2v} and CoIn-C_s relocated points at the CASPT2 level. See Fig. 91, for a schematic representation of the seam in three dimensions.

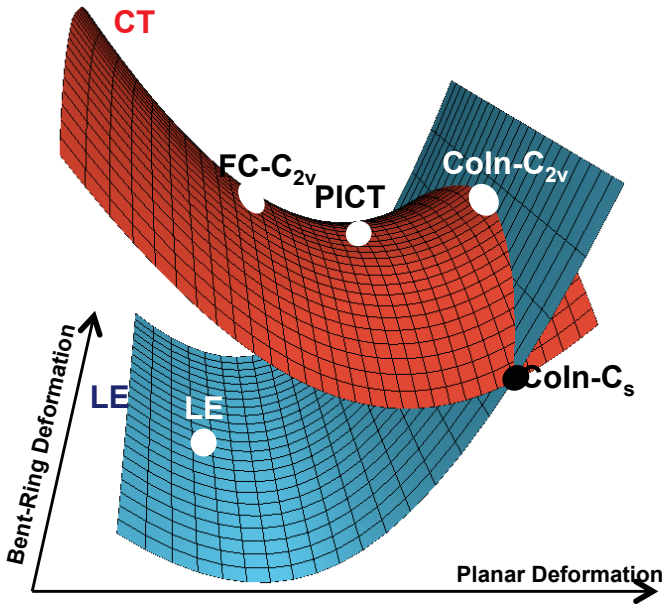

Fig. 91 Scheme of the conical intersection seam along the planar and bent-ring deformation.

The S_1-LE and S_2-CT states have B_2 and A_1 symmetry within the C_{2v} point group, respectively (using Mulliken's convention where the *x*-axis is perpendicular to the molecular plane, as depicted in Fig. 92).

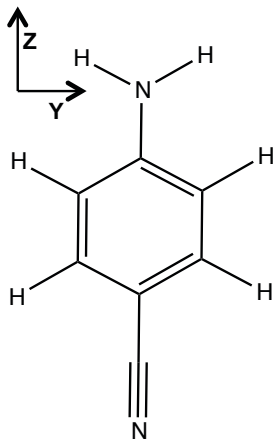

Fig. 92 Cartesian frame used in this study (Mulliken's convention).

The bending deformation that lowers the symmetry to C_s is B_1 (out of plane), such that S_1-LE and S_2-CT become A" and A', respectively, with no further coupling. The derivative coupling is a B_2 /A" ($B_2 \otimes A_1 = B_2/A'' \otimes A' = A''$) Kekulé-like motion all over the seam (see Fig. 88). Internal conversion can thus take place at any point along the seam and implies activation of motions that break the left/right symmetry of the molecule.

However, the topographies of both crossings are different: CoIn-C_{2v} is sloped, whereas CoIn-C_s is peaked (see Fig. 93). These characteristics have been determined from the profiles of the potential energy surfaces of the LE and CT states calculated between the geometries of the critical points optimized at the CASSCF level displayed in Fig. 93. Including electron dynamic correlation (CASPT2 calculations) induces an energy shift all along each surface that is not constant but quite smooth for both, i.e. 0.3-0.5 eV for the LE and 1.1-1.2 eV for the CT states. This results in a relative stabilization of the CT state of about 0.7–0.8 eV with respect to the LE state. Consequently, the critical points at the CASPT2 level are not located at the same geometries as at the CASSCF level. The shape of the surfaces is quite similar at both levels, as shown in Fig. 93. In addition, CASPT2 calculations show that the CoIn-C_{2v} region is even more accessible from the FC region compared to CASSCF calculations. In any case, the different topographies of both CoIn-C_s

(i.e. peaked) and CoIn-C_{2v} (i.e. sloped) crossings and the fact that the CoIn-C_s geometry is farther from the FC region than the CoIn-C_{2v} one, are expected to make the bent deactivation pathway (through CoIn-C_s) occur later than the planar one (through CoIn-C_{2v}) and more in favor of populating the LE minimum.

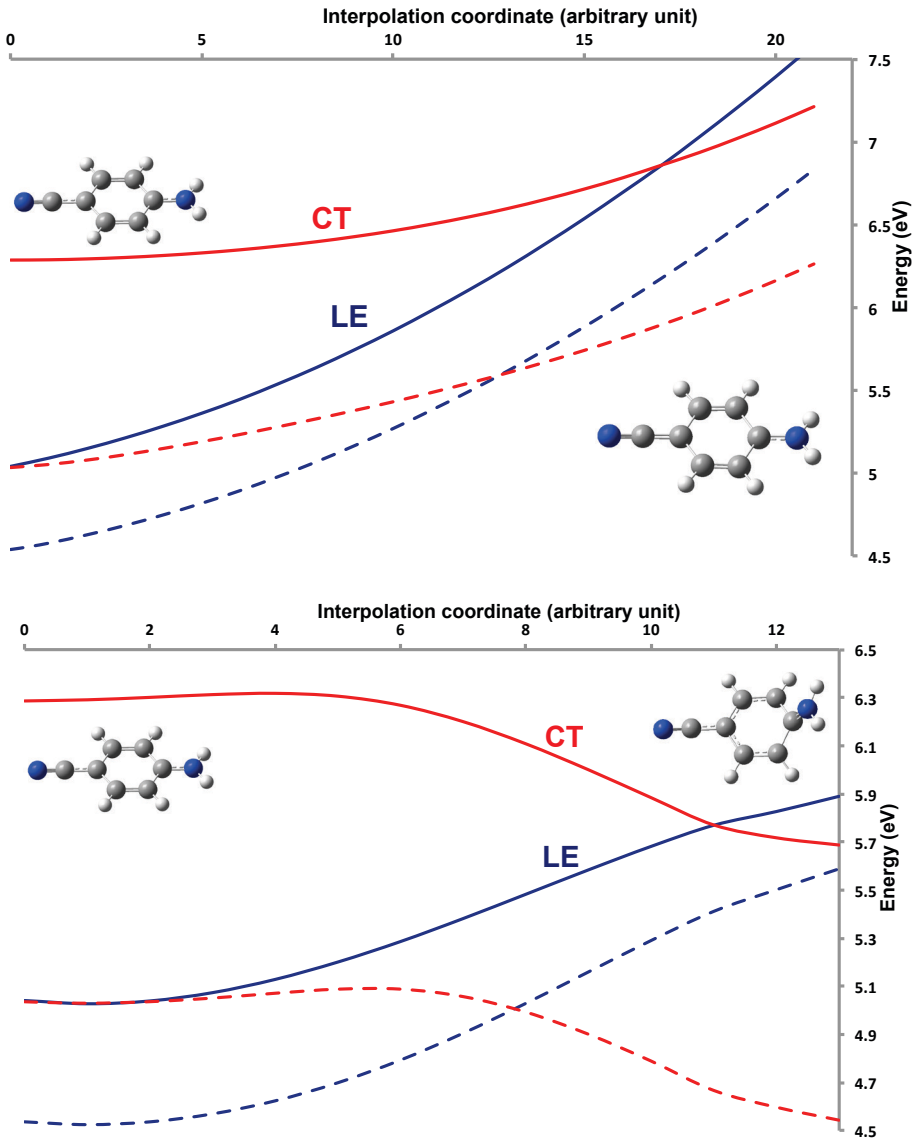

Fig. 93 SA2-CASSCF (plain line) CASSPT2 (dashed line) energy profiles of the CT (red) and LE (blue) states along the PICT to CoIn-C_{2v} interpolation (upper panel) and the PICT to CoIn-C_s interpolation (lower panel). Energies are given in eV with respect to their respective global ground state minima FC-C_s in SA2-CASSCF and CASPT2.

Describing experimental conditions more accurately requires the solvent environment to be taken into account. In the following we investigate the solvent effect on the planar

deactivation pathway. The corresponding study for the bending deactivation pathway through CoIn-C_s is currently ongoing.

3. Investigation of the Solvent Effect on the Planar Deactivation Pathway

We modeled the acetonitrile solvent using the polarizable continuum model (PCM) approach, chapter I. Modeling solvent effects in non-adiabatic phenomena has an additional difficulty given the different time scales of the various processes undergone by the solute, and the finite relaxation time required by the solvent to equilibrate with the changing geometry or electronic distribution of the solute.

Furthermore, the relaxation and subsequent processes that take place on the excited state, such as internal conversion for example, can proceed in the same time scale than the solvent relaxation [298,299]. To the best of our knowledge, this latter situation is impossible to compute with the PCM method implemented into quantum chemistry packages such as Gaussian or Molcas.

Therefore, to account for different situations, we will considerer the two extreme cases that can be adequately addressed computationally:

- The solvent is equilibrated for the ground state. It means that we will considerer that our process (ICT) is faster than the solvent relaxation (Fig. 94). For example, this methodology is used to compute adequate excitation energies because the vertical transition can be considered as an instantaneous process.
- The solvent is equilibrated for the excited state, in our case the charge transfer state S_2-CT, as it is the excited electronic state where the process under study occurs during the first few femtoseconds (Fig. 94). In that situation the process under study (ICT) is considered slower than the solvent relaxation.

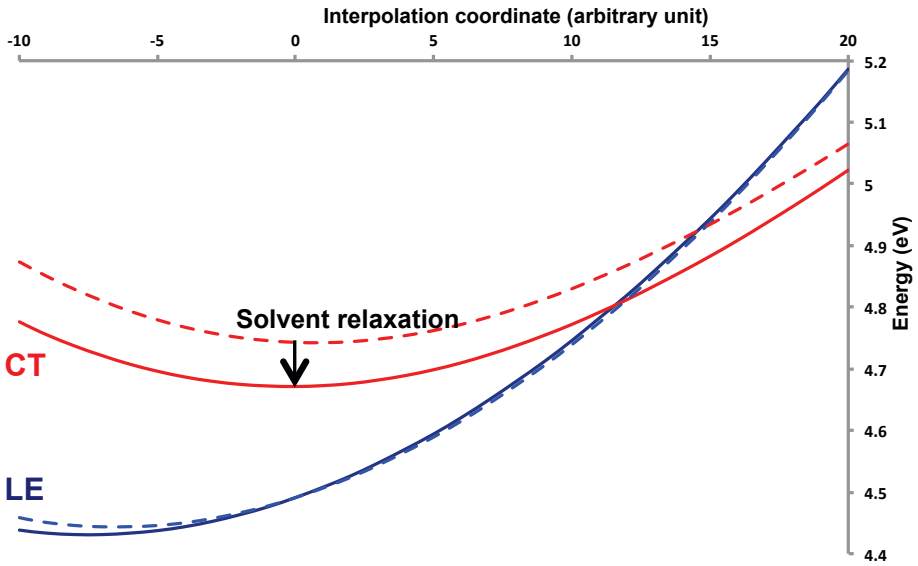

Fig. 94 SA2-CASSCF/CASPT2 energy profiles of the CT (red) and LE (blue) states along the PICT to CoIn-C_{2v} interpolation in a polar solvent. Plain line: solvent equilibrated for the CT state. Dashed line: solvent equilibrated for the ground state. Energy differences are given with respect to the ground-state minimum.

The profiles of the interpolation from PICT to CoIn-C_{2v} recalculated at the CASPT2 levels using both models expressed above are depicted in Fig. 94. They show that the global shapes of the surfaces are not changed by the solvent relaxation dynamics (i.e. solvent equilibrated for the ground state or for the charge transfer excited state), although the charge transfer state is stabilized within a polar environment preferentially due to its larger dipole moment.

Optimizing a CoIn within the PCM approach is not an available technique at the moment. We thus identified a shifted crossing point by recomputing the energies in the presence of acetonitrile along a linear interpolation pathway from the PICT point to the CoIn-C_{2v} point obtained in the gas phase (see Fig. 95 for a comparison gas phase against solvent). Our results show that when the solvent is equilibrated for the CT state, the latter is stabilized with respect to the LE state by about 0.3 eV (around the PICT minimum) and when it is equilibrated for the ground state, the CT state is stabilized by about 0.15 eV with respect to the LE state. This effect is not strong enough to invert the energies and the PICT minimum still belongs to the second excited electronic state. In addition, the energy of the CoIn-C_{2v} point with respect to the FC point is lower than in the gas phase (see Tab. 16 for CASPT2 energies of critical points within acetonitrile for different state equilibrium). This general features are independent of the equilibration of the solvent

(i.e. equilibrated for the ground state or for the charge transfer electronic state). The point to emphasize is that when we consider our process to be faster than the solvent relaxation (i.e. solvent equilibrated for the ground state), the CT state is less stabilized than the situation where we consider the solvent relaxation to be faster than the internal conversion of the system (i.e. solvent equilibrated for the CT state) (see Fig. 94). Therefore, the CoIn-C_{2v} is more accessible (around 0.15 eV lower) in the latter situation.

Tab. 16 Energies in eV calculated at the CASPT2/cc-pVDZ level of theory for various critical points of ABN in acetonitrile. E_{CT} is the energy when the solvent is equilibrated for the CT electronic state. E_{S0} is the energy when the solvent is equilibrated for the ground state * Energies calculated using MS2-CASPT2/cc-pVDZ

	FC-C_s	**FC-C_{2v}**	**LE-C_s**	**LE-C_{2v}**	**PICT**		**CoIn-C_{2v}**	
	E	E	E	E	E_{CT}	E_{S0}	E_{CT} *	E_{S0}*
GS	0.00	0.04	0.08	0.12	0.18	0.18	0.38	0.38
LE	4.69	4.59	4.42	4.34	4.53	4.53	4.79	4.94
CT	5.24	5.11	5.07	4.97	4.89	4.74	4.77	4.93

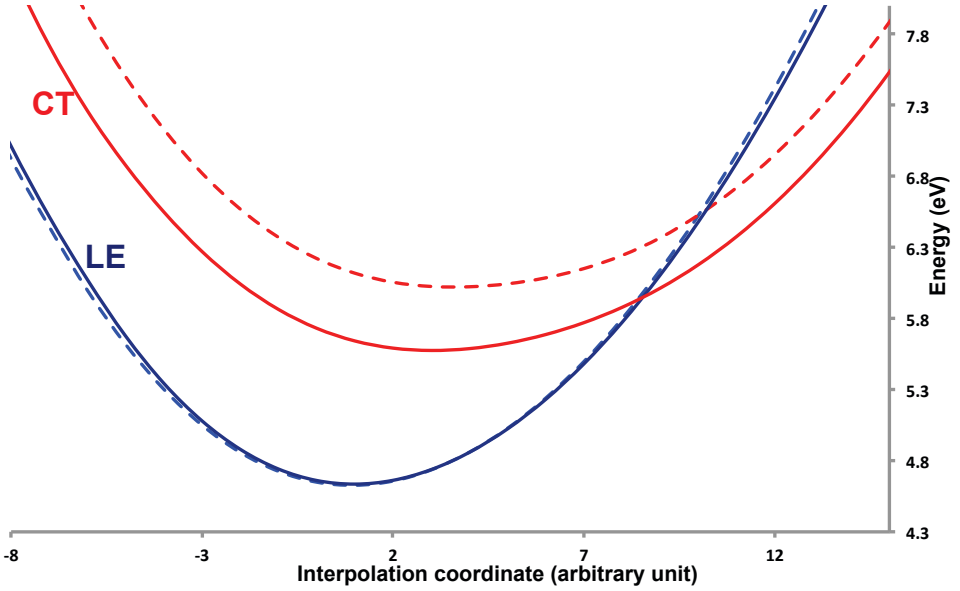

Fig. 95 SA2-CASSCF energy profiles of the CT (red) and LE (blue) states along the PICT (x=0) to CoIn-C_{2v} interpolation in the gas phase (plain line) and polar solvent-acetonitrile (dashed line). The solvent is equilibrated for the CT state (if the solvent were equilibrated for the ground-state the energy of the CT state would be less shifted down). Energy differences are given with respect to the ground-state minimum.

In summary, the CoIn-C_{2v} point appears closer to the PICT minimum when the effect of the solvent is considered (0.8-0.9 eV lower in acetonitrile than in the gas phase), and even more in the situation where the solvent is equilibrated with respect to the CT state. In other words, the planar deactivation channel should be more accessible in the solvent than in the gas phase. Furthermore, the case where the process is slower than the solvent relaxation should be the most efficient one (see **Tab. 15** and Tab. 16). However, the efficiency of the deactivation pathway does not necessary imply the adequate description of the physics of the solvent effect. A realistic description of the solvent effect on the CT electronic state might be a middle case between both extreme situations considered here.

Quantum dynamics calculations were run to confirm our various hypotheses about the deactivation mechanism and the effect of the solvent. Results are presented in the next Section.

III- Quantum Dynamics

Quantum dynamics calculations were run in full dimensionality (39 internal degrees of freedom) with the multilayer version [200] of MCTDH (ML-MCTDH) of the Heidelberg package [181] (see Chapter I). [200]. The electronic Hamiltonian matrix was expressed using a vibronic coupling Hamiltonian model [20] that we developed (Chapter II) whereby quasidiabatic potential energy surfaces and coupling terms are expressed as quadratic expansions along the nuclear coordinates. Time-resolved electronic populations were calculated over 100 fs for coupled potential energy surfaces based on both CASSCF and CASPT2 data. Technical details regarding the quantum dynamics calculations (SPF, ML-tree, etc..) can be found in Appendix D.

1. Set of Coordinates

The set of polyspherical coordinates [155,160,358] (see Chapter I) was chosen in a way that it could describe what was determined to be as the main motions involved in the process, display in Fig. 96:

1) Quinoidal stretching (motion along the CoIn-C_{2v} direction)
2) Symmetric stretching of the allyl-like fragment on the amino side
3) Envelope ring-puckering on the amino side (involved into the bending motion of the CoIn-C_s)
4) Pyramidalisation of the C-atom attached to the amino side (involved into the bending motion of the CoIn-C_s)
5) Torsion and pyramidalization (wagged) of the amino group

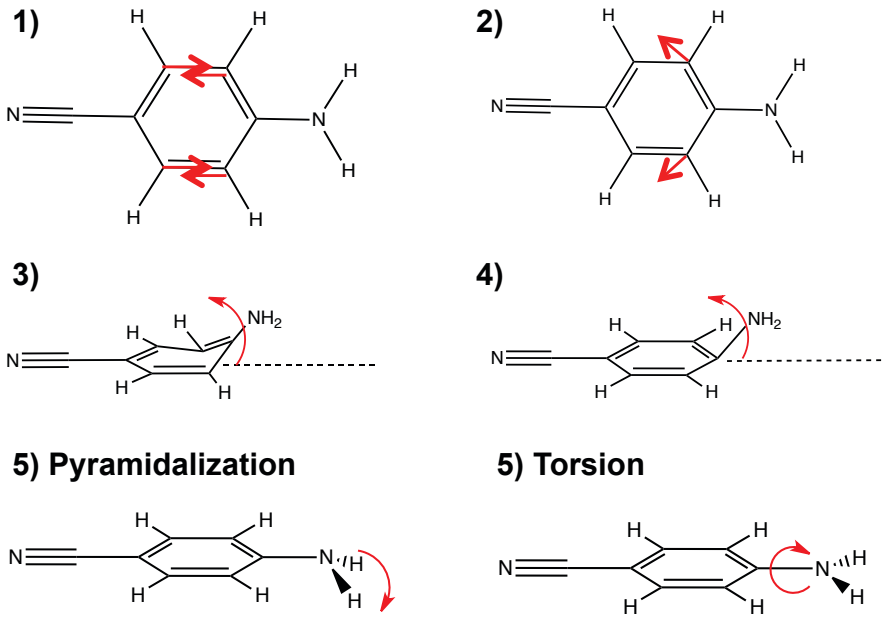

Fig. 96 Main motions involved in the process.

Furthermore, they were selected to correspond to the Z-matrix coordinates used for the quantum chemistry calculations. Therefore, the polyspherical vectors mainly link atoms along chemical bonds (valence vectors) except for the ring (see Fig. 97). The vectors of the ring ($\boldsymbol{R}_1^{(1)}, \boldsymbol{R}_1^{(1,1)}, \boldsymbol{R}_2^{(1,1)}, \boldsymbol{R}_1^{(2,1)}, \boldsymbol{R}_2^{(2,1)}$) enable to define its main deformations in a symmetrical way (quinoidal stretching, envelope ring-puckering, …).

Then, those vectors were regrouped (see Fig. 97) into two subsystems ($S_{1,1}$ and $S_{2,1}$) and a sub-subsystem ($S_{1,2,1}$). These enable the use of polyspherical parameterization angles, which correspond to the Z-matrix ones (used to perform quantum chemistry calculations with an equivalent set of coordinates) and also to avoid the numerical singularities that occur when a vector is almost parallel to a *z*-BF axis (as mentioned in Chapter I).

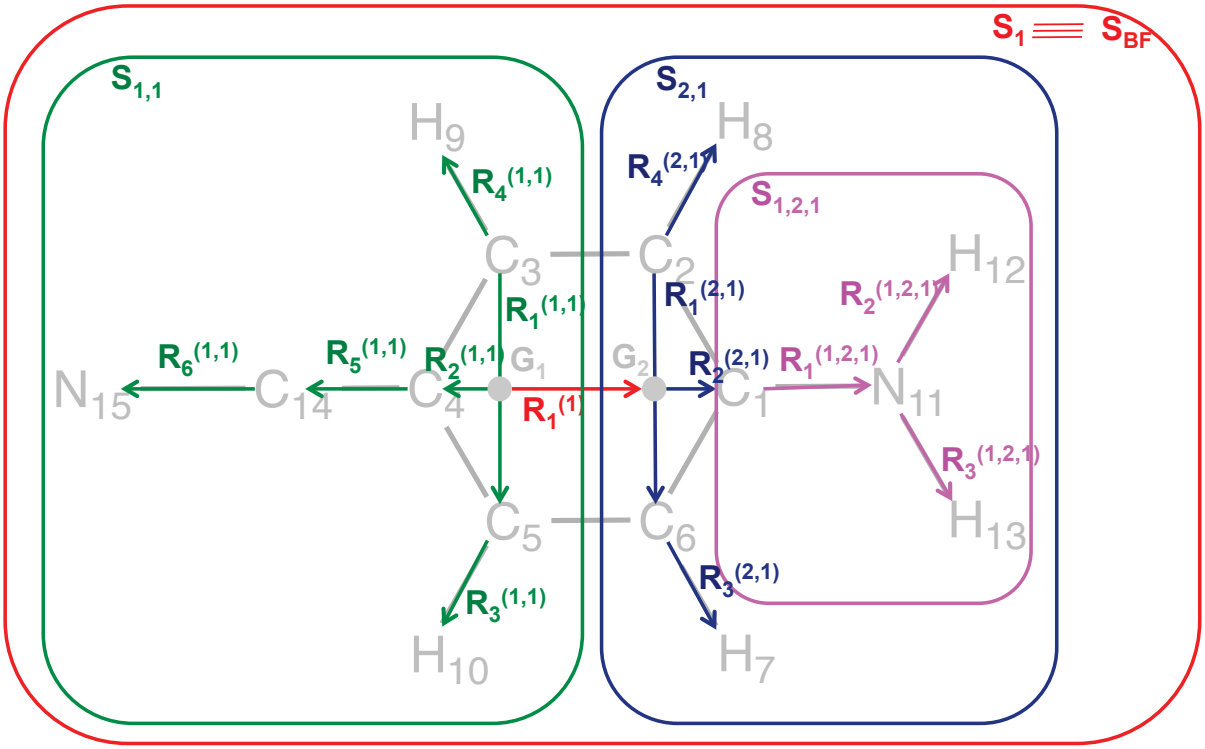

Fig. 97 The set of polyspherical coordinates used in the vibronic model and to perform the dynamics.

The relevant coordinates to describe the main motions are displayed in Tab. 17.

Tab. 17 The most relevant polyspherical coordinates to describe the intramolecular charge transfer process.

Motions	Polyspherical Coordinates
Quinoidal stretching	$R_1^{(1)}$
Symmetric stretching of the allyl-like fragment on the amino side	$R_2^{(2,1)}$
Envelope ring-puckering on the amino side	$\gamma^{(2,1)}$
Pyramidalisation of the C-atom attached to the amino group	$\alpha^{(1,2,1)}$
Torsion and pyramidalisation of the amino group	$\gamma^{(2,1)}$ and $\varphi_3^{(1,2,1)}$

One must notice that $\mathbf{R}_2^{(1,2,1)}$ is used to define the subsubsystem $S_{1,2,1}$ whereas $\mathbf{R}_3^{(1,2,1)}$ is defined within this subsubsystem. This leads to an asymmetrical definition of both H-atoms motions (H_{12} and H_{13}) on the amino group, such that the wagged motion cannot be described in a symmetrical way. In that situation one should used another set of coordinates where the H-atoms of the amino group are equivalently defined with respect to the same Jacobi vector as shown on Fig. 98.

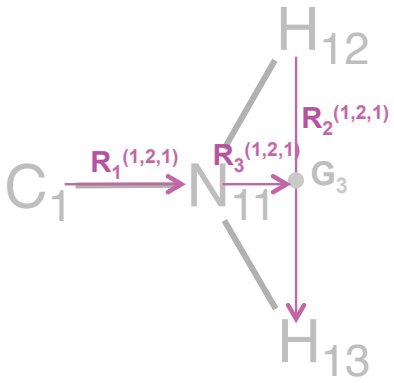

Fig. 98 Alternative set of polyspherical coordinate for the S_{121} subsubsystem.

During this study, we mainly focused on understanding the early stages of the ICT process on the second excited electronic state. As seen previously in the quantum chemistry part, most of our geometries will be considered within the C_{2v} point group. This removes the wagging of the amino group wagging from the list of relevant coordinates. Therefore, the first set of coordinates that we chose should be adequate for our purpose, but the aforementioned limitation must be kept in mind.

In the following, we present the model of coupled potential energy surfaces that we developed to examine the role of the newly-found planar deactivation channel upon running quantum dynamics calculations. First, the efficiency of the planar deactivation channel and the solvent effect is investigated. This is followed by a discussion about the competition between the planar and bent-ring motion deactivation pathways.

All parameters of the model were extracted from ab-initio calculations (CASSCF(12,11)/cc-pVDZ and CASPT2) at the four relevant geometries: $\mathbf{Q_{GS}}$, $\mathbf{Q_{LE}}$, $\mathbf{Q_{PICT}}$, $\mathbf{Q_{CoIn-C_{2V}}}$, and $\mathbf{Q_{CoIn-C_s}}$ (a two-state-average CASSCF was used at the CoIn only; the minima are from single-state CASSCF calculations). The solvent (acetonitrile) effect was taken into account with the PCM (polarizable continuum model; see Chapter I).

2. Planar Deactivation Pathway Model

2-1. In the Gas Phase

We represented the potential energy surfaces and non-adiabatic couplings with a vibronic-coupling Hamiltonian model, developed during this thesis and expressed in Chapter II, based on three quasidiabatic states. It consists in a real symmetric matrix $\mathbf{H}^{\mathrm{diab}}(\mathbf{Q})$ made of three diagonal potential energy functions: $H_{11}^{\mathrm{diab}}(\mathbf{Q}), H_{22}^{\mathrm{diab}}(\mathbf{Q})$ and $H_{33}^{\mathrm{diab}}(\mathbf{Q})$, and three off-diagonal electronic couplings, $H_{12}^{\mathrm{diab}}(\mathbf{Q}), H_{13}^{\mathrm{diab}}(\mathbf{Q})$ and $H_{23}^{\mathrm{diab}}(\mathbf{Q})$, where $\mathbf{Q}$ denotes the set of nuclear polyspherical coordinates detailed in the previous section (39-dimensional vector). In the FC region the three quasidiabatic states coincide with the relevant adiabatic states: state 1 (S_0/GS), state 2 (S_1/LE), and state 3 (S_2/CT) (see Fig. 91 and Fig. 52).

The quasidiabatic vibronic-coupling Hamiltonian reads as

$$H^{\mathrm{diab}}(\mathbf{Q}) = \begin{pmatrix} H_{11}^{\mathrm{diab}}(\mathbf{Q}) & 0 & 0 \\ 0 & H_{22}^{\mathrm{diab}}(\mathbf{Q}) & H_{23}^{\mathrm{diab}}(\mathbf{Q}) \\ 0 & H_{23}^{\mathrm{diab}}(\mathbf{Q}) & H_{33}^{\mathrm{diab}}(\mathbf{Q}) \end{pmatrix} \qquad \textbf{Eq. 106}$$

Each diagonal entry, $H_{ii}^{diab}(\mathbf{Q})$ is expanded quadratically around a reference geometry, $\mathbf{Q_{ii}}$, corresponding to the relevant C_{2v} stationary points: $\mathbf{Q_{GS}} = \mathbf{Q_{11}}, \mathbf{Q_{LE}} = \mathbf{Q_{22}}$, and $\mathbf{Q_{PICT}} = \mathbf{Q_{33}}$ as in Fig. 52.

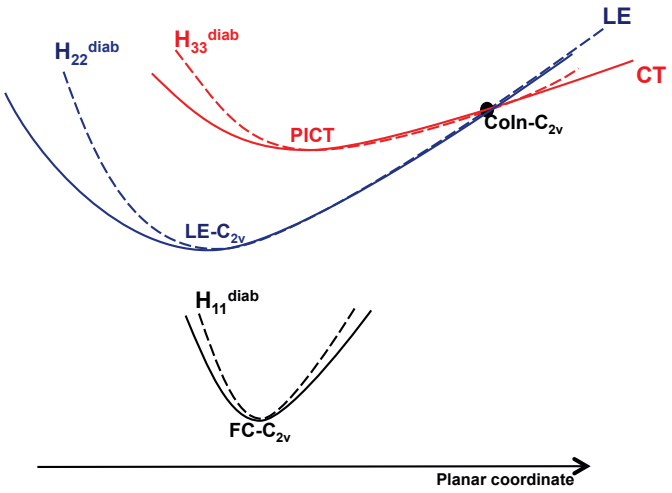

Fig. 99 Schematic representation of the quasidiabatic quadratic expansions around each minimum (dashed line) based on ab-initio data (adiabatic, plain line).

The off-diagonal coupling terms between the ground state and the other two states can be neglected, due to the large energy difference between the ground state and the excited states for all relevant geometries considered here (in particular from FC to the S_2/S_1 CoIn). In other words, $H_{11}^{\mathrm{diab}}(\mathbf{Q})$ corresponds to the ground state potential energy surface, and the electronic couplings $H_{12}^{\mathrm{diab}}(\mathbf{Q})$ and $H_{13}^{\mathrm{diab}}(\mathbf{Q})$ are set to zero.

The remaining coupling, $H_{23}^{\mathrm{diab}}(\mathbf{Q})$, is expanded linearly around the S_2/S_1 CoIn-C_{2v} geometry (i.e. $\mathbf{Q_{CoIn-C_{2v}}}$). The parameters of this electronic coupling are obtained using the two vectors of the branching space and the PICT minimum is used as a reference point for setting the value of the arbitrary mixing angle between both degenerate states so as to satisfy $H_{23}^{\mathrm{diab}}(\mathbf{Q_{PICT}})$=0, which ensures that the quasidiabatic electronic coupling does not shift the adiabatic PICT minimum on the potential energy surfaces with the respect to the quasidiabatic minimum. $\mathbf{Q_{PICT}}$ is thus chosen as the minimum optimized with ab-initio calculations. The LE minimum could have been chosen as an alternative reference point; however, we are going to analyze the dynamics on the second excited state through the PICT minimum. Therefore, the most important part of the surface that

we must describe adequately is the second excited state from FC to the CoIn as well as the CoIn topography (i.e. the branching space). In our model, the LE minimum is not the reference point for setting the value of the arbitrary mixing angle between both degenerate states, thus, the previous constraint $H_{23}^{\mathrm{diab}}(\mathbf{Q_{LE}})$=0 is not necessarily ensured. However, we make the reasonable approximation that the quasidiabatic electronic couplings are not strong enough at the LE minimum to shift the geometry significantly. This consideration holds for two-state crossing cases such as in ABN or 3-HC (Chapter II).

The curvatures of the diagonal entries, $H_{ii}^{\mathrm{diab}}(\mathbf{Q})$, were obtained through a second-order Jahn-Teller procedure. However, for both excited states, the curvatures along the directions leading from the minima to the planar CoIn (i.e. $\mathbf{Q_{LE}} - \mathbf{Q_{CoIn-C_{2V}}}$ and $\mathbf{Q_{PICT}} - \mathbf{Q_{CoIn-C_{2V}}}$) were adjusted according to the quadratic modification procedure developed in Chapter II (whereby harmonic frequencies are modified) to ensure that the two quasidiabatic potential energy surfaces $H_{22}^{\mathrm{diab}}(\mathbf{Q})$ and $H_{33}^{\mathrm{diab}}(\mathbf{Q})$ cross exactly at the ab-initio geometry and energy of the CoIn-C_{2V} (i.e. $\mathbf{Q_{CoIn-C_{2V}}}$).

Fig. 59 shows the agreement between the ab-initio energies and the ones of the vibronic coupling Hamiltonian model along the $\mathbf{Q_{PICT}} - \mathbf{Q_{CoIn-C_{2V}}}$ direction when using CASSCF data. The upper panel is the first quadratic curvature model and the lower panel is this model improved with the quadratic modification of the curvature to correct the CoIn position. One can notice on these figures that the quadratic curvature modification is a small alteration. In that situation, the CoIn energy and position is refined by about 0.2 eV from the first quadratic model (i.e. without the quadratic modification of the curvature).

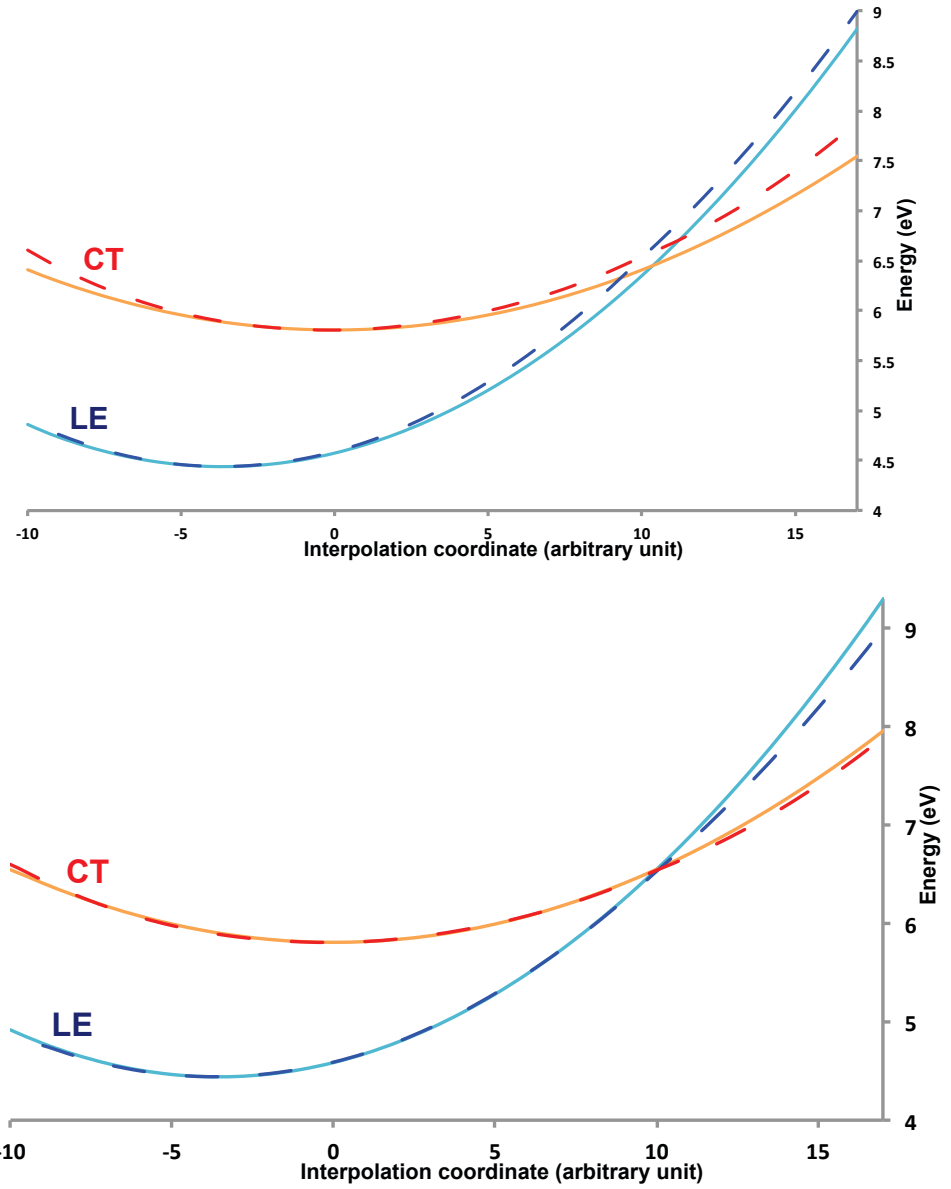

Fig. 100 planar pathway along a linear interpolation from PICT (x = 0) to CoIn-C_{2v} (x = 10), in the gas phase. Energies are given in eV with respect to the ground-state minimum. Dashed line: ab-initio; plain line: vibronic-coupling Hamiltonian model (Upper panel: quadratic model, lower panel: the model with quadratic curvature modification). Ab-initio level of theory: CASSCF(12,11)/cc-pVDZ with variable state-average weights (single-state calculations on each state at x = 0; 0.5:0.5 weights on S_1/S_2 at x = 10; linear interpolation in between).

These models of potential energies and couplings were used to run quantum dynamics simulations. The time evolution of the quasidiabatic populations in both cases (i.e. quadratic and quadratic with modified curvature) can be considered as almost identical (the difference between both calculated quasidiabatic populations is about 0.1%). Such a difference is not relevant enough to be detected graphically, hence, only the time evolution of the quasidiabatic populations for the model with the modified curvature is

depicted in Fig. 67. The modification we used to correct the curvature in our quasidiabatic potential energy surfaces is small enough that it has a negligible impact on the evolution of the populations. In other words, the exact position of the CoIn is relevant to some extent but a small shift in position or energy will not change the physical behavior by much. In photochemistry, if one wants to investigate the global evolution of populations to rationalize a mechanism, an extremely accurate potential energy surface model is not mandatory, as opposed to those required for spectroscopy studies for example.

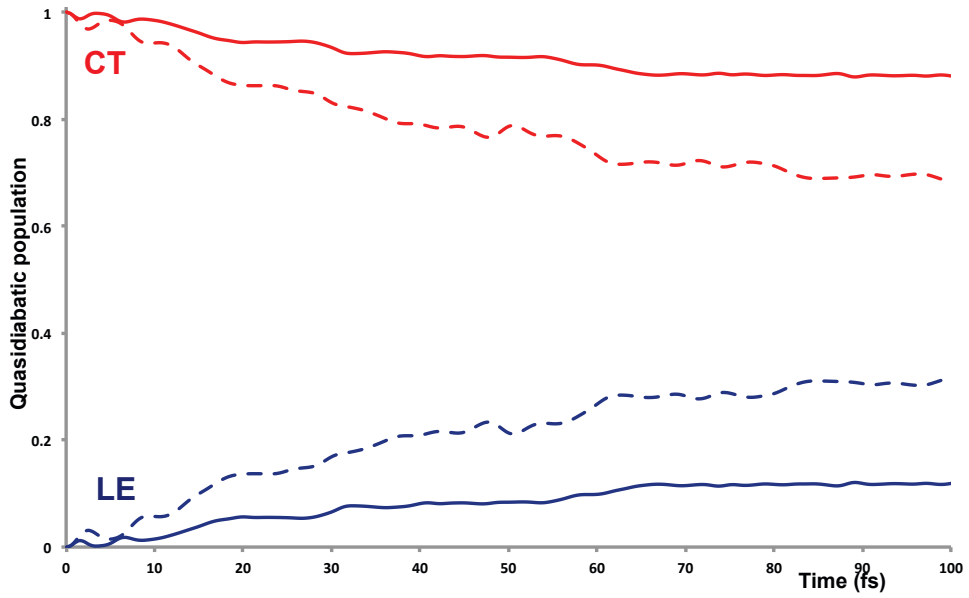

Fig. 101 Evolution of the quasidiabatic populations as functions of time in the gas phase. Red: CT state; blue: LE state. Plain line: coupled potential energy surfaces based on CASSCF data (Plain line) and on CASPT2 data (dashed line).

A more accurate model of coupled potential energy surfaces based on CASPT2 data was obtained by shifting the geometries and energies to the relevant relocated points (all minima and crossings). Again, and with the same methodology, the quadratic curvature was slightly adjusted along the LE/PICT- CoIn-C_{2v} directions (Fig. 102).

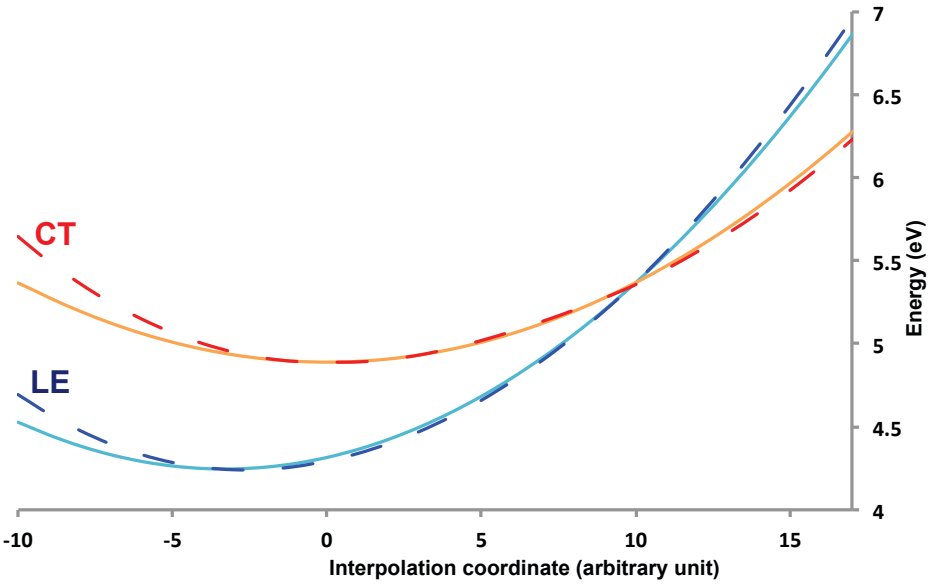

Fig. 102 Planar pathway along a linear interpolation from PICT (x = 0) to CoIn-C_{2v} (x = 10), in the gas phase. Energies are given in eV with respect to the ground-state minimum. Dashed line: ab-initio; plain line: vibronic-coupling Hamiltonian model ab-initio level of theory: CASSCF(12,11)/CASPT2/cc-pVDZ with variable state-average weights (single-state calculations on each state at x = 0; 0.5:0.5 weights on S_1/S_2 at x = 10; linear interpolation in between).

The evolution of the quasidiabatic population transferred from the CT state to the LE state through the CoIn-C_{2v} region is depicted in Fig. 102. It shows that internal conversion starts immediately. Including electron dynamic correlation (CASPT2 data) only amplifies the conclusions that could be drawn from a less accurate description based on CASSCF data, which is what we were expecting as CoIn-C_{2v} is closer to FC with CASPT2 data (see Fig. 93). Already at 10 fs, a significant part of the wave packet starts to be delocalized over the CoIn-C_{2v} region where we start to observe some transfer of population between the first two excited electronic states. A significant ultrafast radiationless decay from PICT to LE (transfer of population) within the planar channel is observed: at 100 fs, 30% of the population has already been transferred in the gas phase.

We expect such conclusions to be reinforced in a polar solvent, as the CoIn-C_{2v} is closer to FC than in the gas phase due to the stabilization of the CT electronic states (0.8-0.9 eV at the CASPT2 level) with respect to the LE electronic state. To validate this hypothesis, the same study was carried out while accounting for the solvent effect.

2-2. In a Polar Solvent

The methodology to generate the coupled potential energy surfaces taking into account the solvent effect is the same as the one exposed in the previous section. The only difference is that we shifted the energies of the critical points (i.e. ground state minimum, LE and PICT minima, and CoIn-C_{2V}) with respect to the solvent effect that we rationalized previously in the quantum chemistry section.

Fig. 103 shows the agreement between the ab-initio energies and those of the vibronic-coupling Hamiltonian model (with a quadratic modification to fit the energy and geometry of the CoIn with respect to the ab-initio data) that we developed to account for the different solvent relaxation time scales (i.e. faster or slower than the ICT process) along the direction from PICT to CoIn-C_{2v} when using CASPT2 data. The LE state is slightly shifted in our model with respect to the ab-initio data (maximum shift of 0.07 eV). One needs to keep in minds that in our model the curvatures are calculated at the CASSCF level without inclusion of the solvent effect, thus inducing a shift between the potential energy surfaces model and the ab-initio data in acetonitrile at the CASPT2 level. However, our present study is focused on understanding the early stages of the ultrafast process. In other words, we mainly focus our study on the dynamics from FC to the CoIn, i.e. the ICT dynamics on S_2.

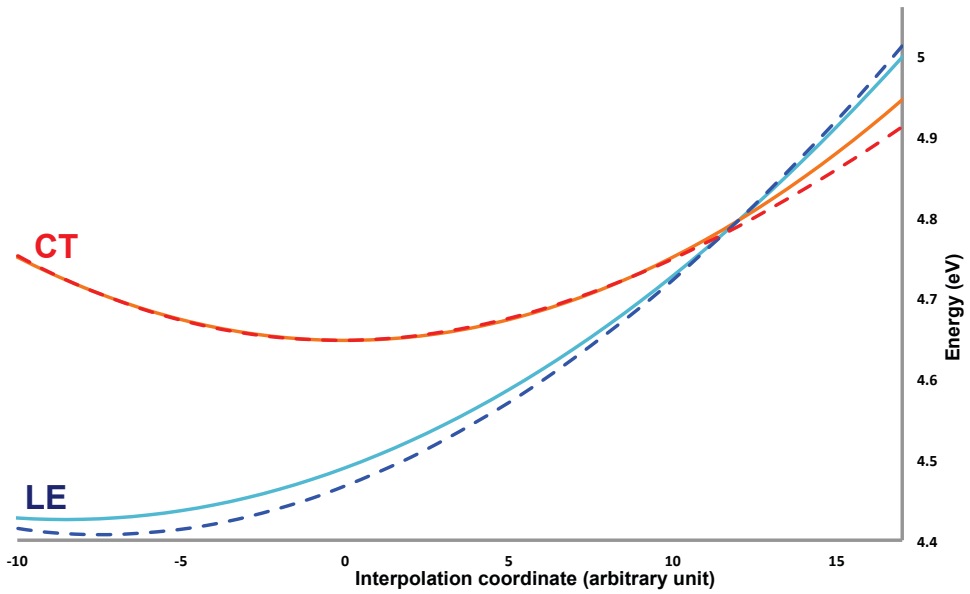

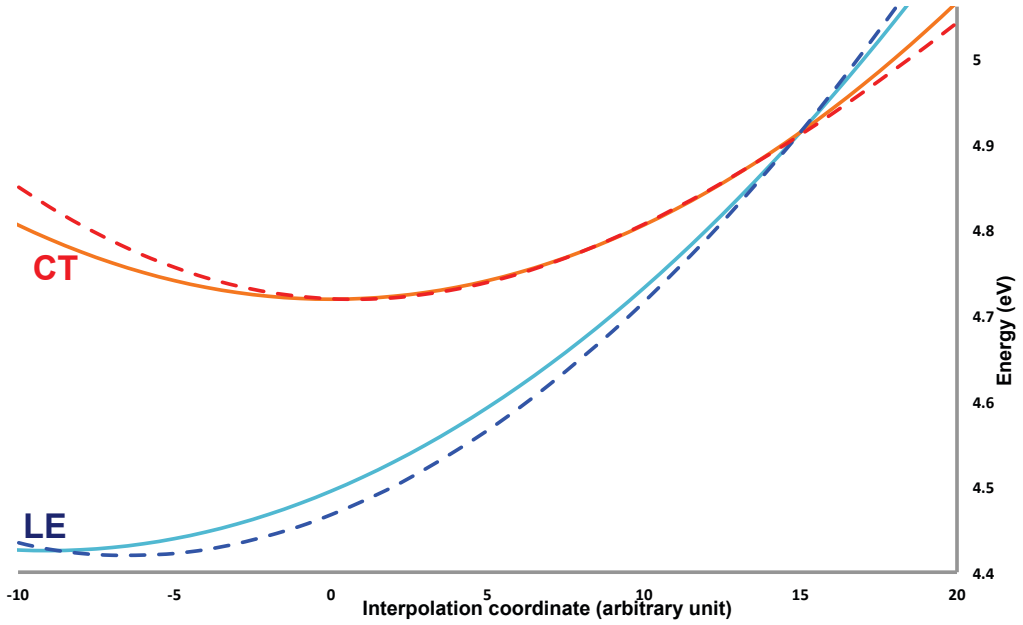

Fig. 103 Planar pathway along a linear interpolation from PICT (x = 0) to CoIn-C_{2v} (x = 10), in a polar solvent (upper panel: solvent equilibrated for the CT state; Lower panel: solvent equilibrated for the GS). Energies are given in eV with respect to the ground-state minimum. Dashed line: ab-initio; plain line: vibronic-coupling Hamiltonian model Ab-initio level of theory: CASSCF(12,11)/CASPT2/cc-pVDZ with variable 0.5:0.5 state-average weights.

The corresponding evolutions of quasidiabatic populations are depicted in Fig. 104. They highlight our previous hypothesis regarding the efficiency of the pathway depending on the solvent relaxation time scale (i.e. faster or slower than the ICT process). If the solvent relaxation is slower than the ICT process, as said previously, the solvent is at its equilibrium state for the CT electronic state. In that situation, the CT electronic state is more stabilized by the solvent polarity than if the solvent relaxation is faster than the ICT process (i.e. solvent equilibrated for the GS) (Fig. 103). This induces the CoIn-C_{2v} to be closer to FC in the first situation than in the latter one (about ~0.15 eV). Hence, as expected, the CoIn-C_{2v} gets crossed (inversion of the quasidiabatic populations in Fig. 104) ~8 fs earlier when the solvent relaxation is slower than the ICT process (solvent equilibrated for the CT electronic state). However, the dynamics of the relaxation does not influence the qualitative behavior of the system, the evolutions of the quasidiabatic populations in both situations are similar with respect to their ~8 fs shift in time and the final ratio of population transferred is identical (at 100 fs 80% of the population has been transferred).

Therefore, we can conclude that in this situation the dynamics of the solvent relaxation is not a key point to describe the solvent effect over the photodynamics as it does not have much influence on the behavior of the populations. The adequate description of the solvent is likely to correspond to a situation between both cases that we addressed in this thesis where the CoIn-C_{2v} gradually shifts down in energy during the dynamics. However, these types of models are very involved and require a different description of the solvent depending on the nuclear coordinates and on time.

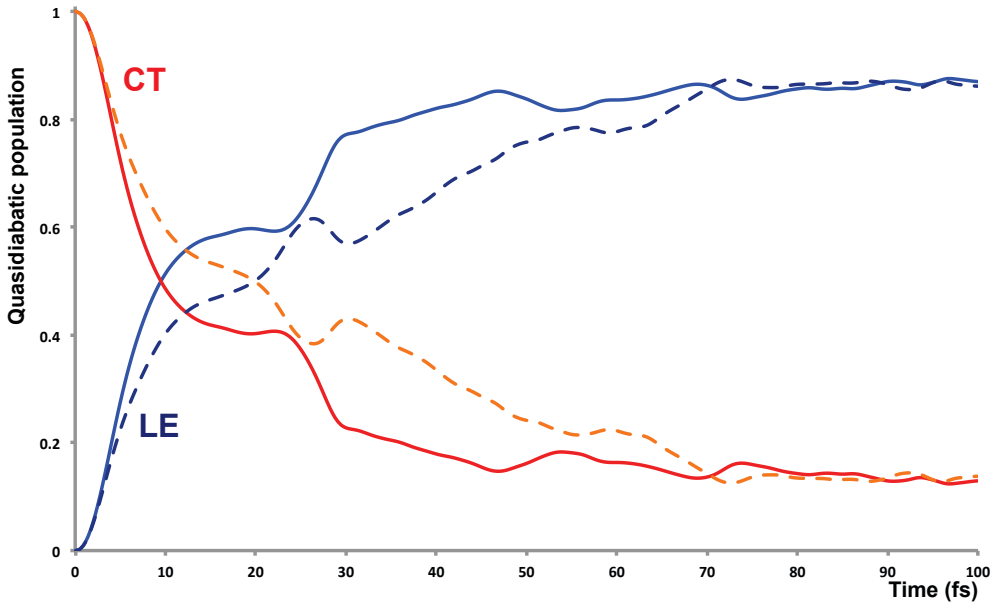

Fig. 104 Evolution of the quasidiabatic populations as functions of time in a polar solvent. Red/orange: CT state; blue: LE state. Plain line: solvent relaxation slower than the ICT (solvent equilibrated for the CT). Dashed line: solvent relaxation faster than the ICT (solvent equilibrated for the GS). Coupled potential energy surfaces based on CASPT2/PCM data.

In addition, as expected, the transfer of population along the planar pathway is more efficient in a polar solvent than in the gas phase, i.e. at 100 fs, an extra 50% of population has been transferred in a polar solvent compared to the gas phase (Fig. 67 and Fig. 104). One can conclude that the effect of the solvent polarity has a significant impact over the transfer of population through the CoIn-C_{2v} upon an important stabilization of the CT electronic state with respect to the LE electronic state (from 0.2 to 0.8 eV). However, as already mentioned, the dynamics of the solvent relaxation does not have such a relevant effect on the physics of the system.

3. Bent Deactivation Pathway Model

In order to investigate more deeply the planar deactivation channel (around the CoIn-C_{2v} point) and how it may compete with a mechanism involving the ring bending motion (involved in forming the non-planar C_s CoIn, denoted CoIn-C_s, that was reported in previous studies [345,354]) we ran additional quantum dynamics calculations with coupled potential energy surfaces that describe simultaneously both types of CoIns. In the following, a more complete model of potential energy surfaces is thus proposed, describing adequately both the planar and bent channels at the CASSCF level in the gas phase.

3.1. Coupled Potential Energy Surfaces Model

The quadratic vibronic-coupling Hamiltonian model with modified curvature used in the previous section was built to study the planar deactivation pathway with a correct description of the CoIn-C_{2v} point. However, the energy of the CoIn-C_s point is 5.6 eV, which is 0.6 eV higher than the ab-initio energy (energies given at the CASPT2 level). Hence, the corresponding bending motion is not described adequately regarding the photodynamics of the system. To adjust our model, we further added a modification of the curvature along the bending direction to fit the CoIn-C_s ab-initio energy and geometry. The quasidiabatic electronic coupling defined in the previous section remains untouched, which is a valid approximation. Indeed, as already pointed out, the derivative coupling at the CoIn-C_{2v}/C_s points is a B_2/A" Kekulé-like motion that breaks the left/right symmetry of the molecule, and which does not change much all over the seam (see Fig. 88). Further improving the model would require the derivative coupling (here, the gradient of the quasidiabatic electronic coupling) to depend explicitly on the point on the seam.

As previously said, accessing the bent CoIn (CoIn-C_s) requires to break the C_{2v} symmetry of the molecule with a non-totally symmetric bending motion of the amino group. In other words, there is a pair of equivalent bent CoIns (i.e. CoIn-C_s+ and CoIn-C_s-) where the amino group is bent either up or down with respect to the molecular plane.

Therefore, to modify the curvature, it is mandatory to use a function that will act symmetrically with respect to the amino bending direction. As seen on Fig. 105, to reach both CoIn-C_s points from either of the two C_{2v} minima (S_2-PICT or S_1-LE) the system must relax along two main deformations: a planar deformation and the amino bending motion (up or down). From a technical point of view, the bending direction cannot be defined directly by interpolating between one of the quasidiabatic electronic state minima and one of the CoIn-C_s points. If one modifies the curvature along such a direction, the other equivalent CoIn-C_s point will not be described adequately. Therefore, the modification of the curvature to fit the energy and geometries of both CoIn-C_s points together must be achieved along a pure bending direction (i.e. a non-totally symmetric coordinate for which both sides are mirror images of each other). This approach is easy to implement in our situation, as the CoIn-C_s points are mainly displaced along the bending direction with respect to the central CoIn-C_{2v} point or the two C_{2v} minima (99% overlap between the bending direction and the normalized displacements from either of the C_{2v} points to the CoIn-C_s point).

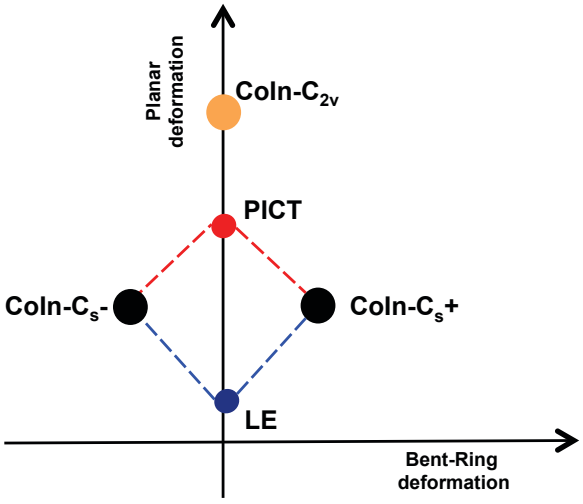

Fig. 105 Schematic representation of the CoIn-C_s+, CoIn-C_s-, CoIn-C_{2v} relative positions with respect to the LE and PICT minima along the bent-ring and planar deformations.

The bending motion breaks the C_{2v} symmetry into C_s, which results in the CoIn-C_s points to be 0.62 eV lower than the CoIn-C_{2v} point. In addition, the potential energy surface shows significant anharmonicity along this direction (see Fig. 91 and Fig. 93). Hence, to account for this difficulty, we modified the original vibronic-coupling Hamiltonian

curvature along the bending direction using a symmetrical switch function (detailed in Chapter II).

The main difficulty in the description of this deformation is to build a model of coupled potential energy surfaces that is totally symmetric along this specific direction and will give exactly the same numerical values of the energies at both CoIn-C_s geometries (i.e. CoIn-C_s+ and CoIn-C_s-). To this end, one must "clean" the ab-initio Hessians with respect to symmetry before using them in our vibronic-coupling Hamiltonian model, meaning that a "cleaned" Hessian at a C_{2v} geometry must be block-diagonal (in a set of symmetrized coordinates) with respect to the irreducible representations of the C_{2v} point group of symmetry, as represented on Fig. 106. This new set of symmetrized coordinates is obtained upon defining specific linear combinations of the original set of polyspherical coordinates, such that they now belong to the irreducible representations of C_{2v} (the corresponding symmetrized coordinates are displayed in Appendix D). We transformed all relevant data (Hessians, geometries, and branching space vectors) to this new set of coordinates with the Tnum program [165].

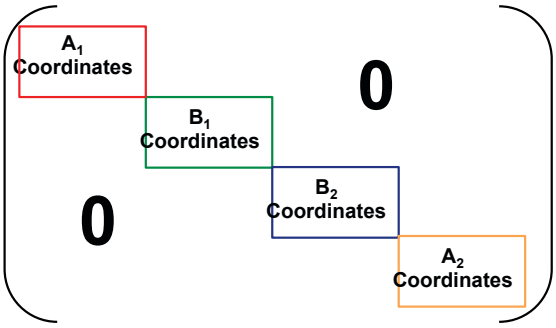

Fig. 106 Representation of a block diagonal Hessian matrix according to C_{2v} symmetry.

The following figure (Fig. 107) shows a comparison between the ab-initio energies (in the gas phase at the CASSCF level) and the ones of our final vibronic-coupling Hamiltonian along the amino group bending direction.

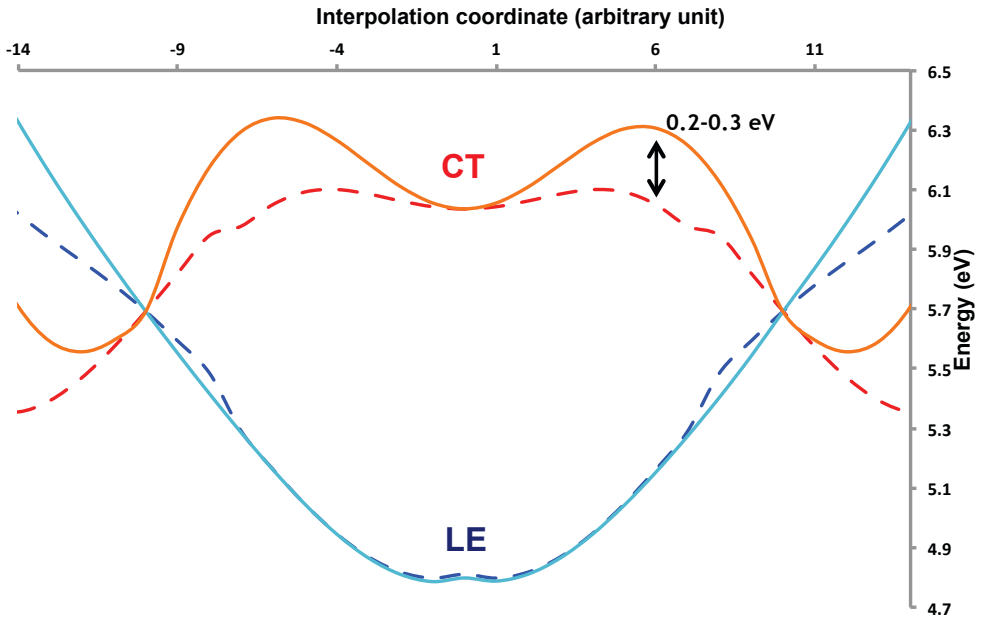

Fig. 107 Bent-ring pathway along a linear interpolation from PICT (x = 0) to CoIn-C_s+ (x = 10) and CoIn-C_s- (x = −10), in the gas phase. Energies are given in eV with respect to the ground-state minimum. Dashed line: ab-initio; plain line: vibronic-coupling Hamiltonian model. Ab-initio level of theory: CASSCF(12,11)/cc-pVDZ with variable state-average weights (single-state calculations on each state at x = 0; 0.5:0.5 weights on S_1/S_2 at x = ±10; linear interpolation in between).

In a first place, one can notice that the ab-initio interpolation is not totally smooth. This is due to a jump in the stage average weights. For most points along this interpolation, we used smoothly varying state average weights (to describe minima as accurately as possible and conical intersections with equal weights, i.e. from single state on each state at x = 0 to 0.5:0.5 on S_1/S_2 at x = ±10). However, at x = ±7, the 0.35:0.35 weights on S_1/S_2 happened not to converge and 0.4:0.4 weights were used instead (note that such intermediate data points are presented here only for comparison but were not used as such for generating our model, based on data at x = 0 and x = ±10 only).

As seen on Fig. 107, the barrier along the bending direction is 0.2-0.3 eV higher in our model than in the ab-initio data at the CASSCF level (0.16 eV barrier). This is a limitation of the curvature modification procedure. Fortunately, the model barrier occurs to have about the same height as the ab-initio data at the CASPT2 level (0.25 eV barrier). As seen above in the quantum chemistry section, including dynamic electron correlation results in a smooth stabilization of the CT electronic state with respect to the LE state and, consequently, in CoIns being closer to the FC region (without noticeable impact on the

geometries of the minima). Moreover, the corresponding quantum dynamics calculations show that, as expected, the transfer of population is enhanced while using a coupled potential energy surface model based on CASPT2 data. In any case, we can safely assume that for the bending direction we described fortuitously but fortunately potential energy surfaces at the CASPT2 level using CASSCF data.

One needs to keep in mind that our quasidiabatic potential energy surfaces are functions of all the internal nuclear dimensions (i.e. 39 dimensions for ABN). The improved model (with respect to the bending motion) corresponds thus to a more accurate description than the original model designed to describe the planar pathway. We can now consider two specific deactivation channels: the planar and bent pathways (in the full 39-dimensional space) depicted schematically in two dimensions in the following figure (Fig. 108). Subsequent quantum dynamics calculations are presented below.

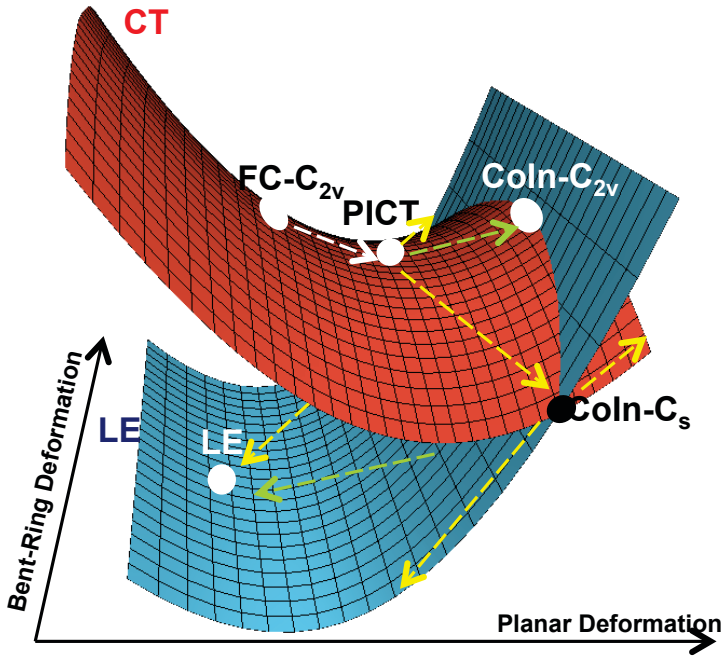

Fig. 108 Schematic representation of the conical intersection seam along the planar and bent-ring deformations. The arrows represent the possible deactivation pathways for the system. Yellow: through CoIn-C_s (peaked). Green: through CoIn-C_{2v} (sloped).

A technical remark should now be made about the set of coordinates used in the following dynamics. Up to now, we changed our polyspherical coordinates for symmetrized coordinates. Nevertheless, the curvature modification we presented here

was based on switch functions that are not "MCTDH compatible" (not separable as sums of products of low-dimensional functions). Therefore, to get a separable form for the quasidiabatic energy surfaces, we used linear combinations of coordinates whereby the bending and planar directions are treated as two explicit and linearly independent coordinates.

3.2. Quantum Dynamics

Fig. 109 shows a comparison of the evolution of the quasidiabatic populations obtained with the original model (plain line) and with the improved model (dashed line) both in the gas phase and using CASSCF data. In the first case, we describe adequately the planar deactivation channel only (the CoIn-C_s points cannot be reached by construction). In the second case, we treat both situations on the same footing. As can be observed, both types of populations behave similarly. However, this result is global and does not discriminate the relative efficiencies and roles of the different CoIns (i.e. CoIn-C_s and CoIn-C_{2v}) with respect to the deactivation process. A more detailed analysis is required, as shown below.

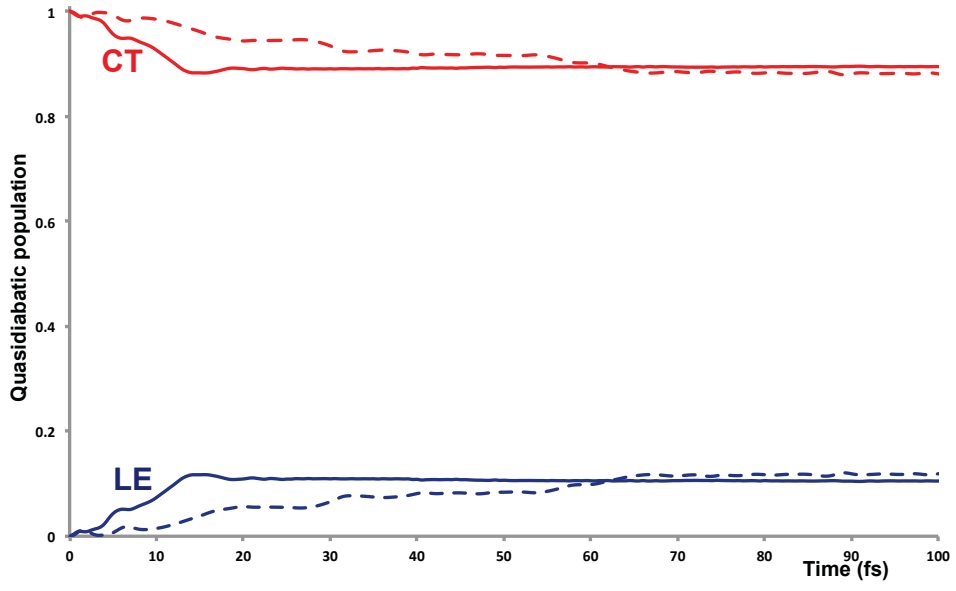

Fig. 109 Time evolution of the quasidiabatic populations of the LE and CT electronic states in the gas phase. Coupled potential energy surfaces based on CASSCF data. Plain line: model describing both bent and planar deactivation pathways. Dashed line: model describing the planar deactivation pathway.

As already mentioned, in these calculations we used a set of coordinates that are defined as linear combinations of the original set of polyspherical coordinates. This linear combination procedure was made in such a way that the PICT minimum and each CoIn (i.e. CoIn-C_{2v} and Coin-C_s) belong to a plane spanned by two coordinates: the planar relaxation and the bent-ring deformation (see Fig. 105 and Fig. 108). Although calculations were performed in the full 39-dimensional space, we will focus our analysis of the dynamics results within the frame of these two reaction coordinates.

First, in this two-dimensional frame (see Fig. 105), we can localize each relevant stationary point on the S_2-CT electronic state and define two regions for analyzing separately both types of CoIns: regions A and B in **Fig. 110**. These are implemented in practice as auxiliary operators in the ML-MCTDH operator file in the form of step distributions along the bent-ring coordinate, centered on each CoIn, and of half width the distance between CoIn-C_{2v} and CoIn-C_s along the bent-ring coordinate. This defines two borders, midway between both types of CoIns: region B is the union of both separate regions outside the borders and region A is inside the borders, as displayed in **Fig. 110**. This will give us information about how the wave packet spreads on the coupled potential energy surface over time along this coordinate. The partial populations obtained inside the regions defined by the step distributions will be called local quasidiabatic populations (for each specific CoIn region) and will be discussed later in this section.

Let us, in a first place, analyze the delocalization of the initial wave packet at FC (t = 0 fs). At the initial time, the wave packet is already delocalized symmetrically around the FC point along the bent-ring coordinate, with a typical width that basically corresponds to the size of region A (the partial norm of the wave packet is equal to one when integrated over region A only). This suggests that, even if the transfer of population is efficient within CoIn-C_s regions (region B), the system will first tend to transfer population around the planar CoIn region (region A) before further spreading.

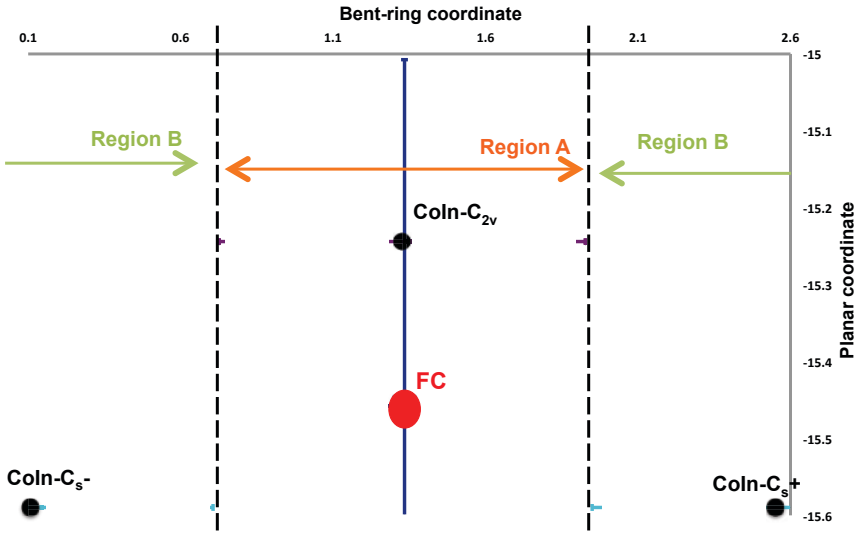

Fig. 110 Position of the CoIns and the FC point within the planar and bent-ring coordinate frame. Dashed line define the two regions used to analyze the wave packet delocalization.

To go further, we analyzed the transfer of local quasidiabatic populations in the various CoIn regions (A and B) to investigate in more details the relative efficiencies of the different regions for transferring population between both electronic states. The evolution of the local quasidiabatic populations within the different CoIn regions (**Fig. 111**) shows two sequences. The first sequence is < 20 fs when the transfer of population occurs in the vicinity of CoIn-C_{2v}. This is proved by the local quasidiabatic population in region A being very similar to the total quasidiabatic population evolution displayed on **Fig. 109** (the population transfer increases around both CoIn regions but is still negligible in region B compared to region A). After 20 fs, the local quasidiabatic population within the bent-ring CoIn region (region B) becomes significant and evolves as a mirror image of the local quasidiabatic population within the planar CoIn region (region A). One can notice that at the same time the global quasidiabatic populations no longer evolve (plain line). This indicates that the width of the wave packet has now increased enough for both regions to be populated and that it oscillates in time ("breathing" of the wave packet). To summarize, the non-adiabatic transfer of population occurs before 20 fs almost exclusively along the planar deactivation channel. Once the respective populations of LE and CT have stabilized, the system keeps spreading in an oscillatory manner along the bending motion (Fig. 112).

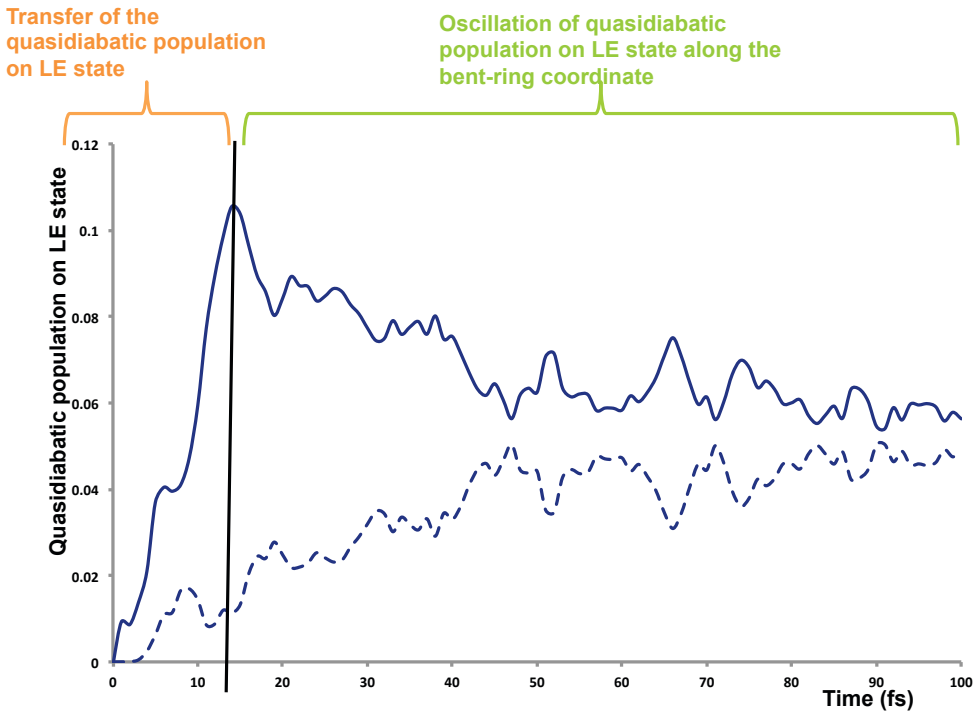

Fig. 111 Time evolution of the local quasidiabatic populations transferred to the LE state in the gas phase. Coupled potential energy surfaces based on CASSCF data. Plain line: local population transfer trough region A (around CoIn-C_{2v}); Dashed line: local population transfer trough region B (around both CoIn-C_s+ and CoIn-C_s-). The black line highlights the two different sequences.

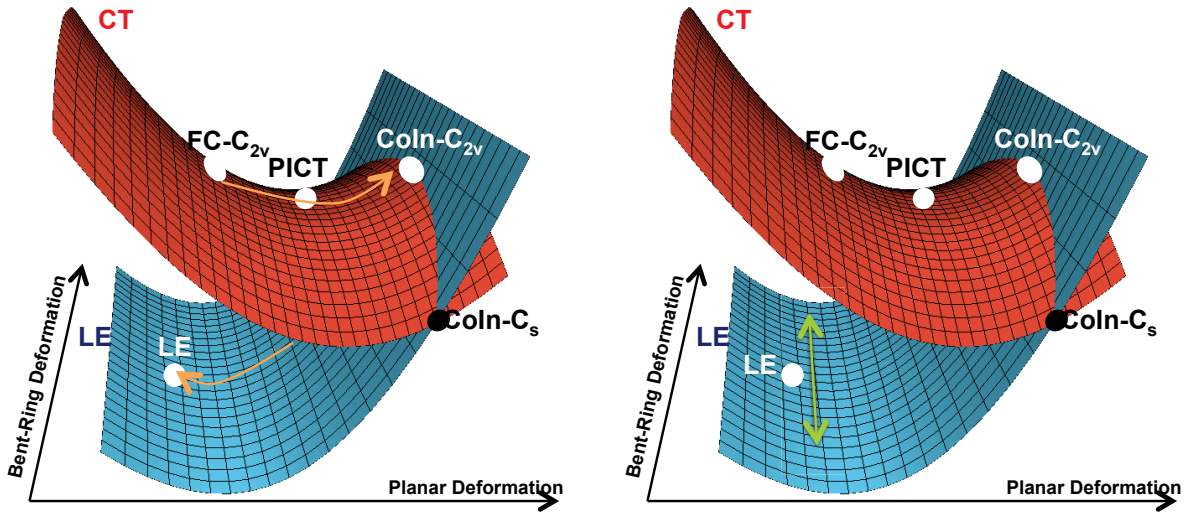

Fig. 112 Scheme of the conical intersection seam along the planar and bent-ring deformations. Left panel: typical pathway of the wave packet on the CT state when population is transferred to the LE state; Right panel: "breathing" of the wave packet transferred to the LE state.

This calculation in the gas phase indicates that the PICT species is populated right after photoexcitation where it radiationlessly decays to the LE species very early through a

newly-found, planar CoIn. This radiationless decay happens with a minimal contribution (almost none) of the bending motion. This feature is expected to be even more efficient in a polar solvent owing to the quantum dynamics results that we obtained when investigating the solvent effect on the planar deactivation pathways model.

IV- Conclusion and Outlooks

In this study, we have performed a computational study on ABN in the gas phase and acetonitrile in order to corroborate or discard the hypothesis of Park et al. [343] and provide further information about the ultrafast process that populates the LE state almost immediately after the initial photoexcitation.

This work is part of a collaborative project with the group of Dr. Mar Reguero and Pedro J. Castro from the Universitat Rovira i Vigili in Tarragona, Spain, for most of the quantum chemistry calculations. We have carried out a CASSCF(12,11)//CASPT2 study to describe the topography of both coupled potential energy surfaces involved in the initial steps of the process. A new conical intersection was characterized between the S_2-CT and the S_1-LE electronic states with a totally planar geometry (C_{2v} symmetry), along a direction approximately parallel to the relaxation coordinate from the Franck Condon point to the S_2-CT minimum (i.e. PICT). This opens a new channel for an ultrafast population of the LE state upon internal conversion. Using full-dimensional models of coupled potential energy surfaces developed during this Thesis work, first based on CASSCF energies and geometries and further refined to match CASPT2 data, both in the gas phase and in acetonitrile, we have run quantum dynamics simulations with the multilayer version of the multiconfiguration time-dependent Hartree (ML-MCTDH) method [200]. Our quantum dynamics calculations clearly indicate that the PICT species is populated right after photoexcitation where it radiationlessly decays to the LE species very early through this newly-found, planar CoIn thus showing that the bending motion is not crucial for the radiationless process. This feature is expected to be even more efficient in polar solvents than in the gas phase due to the strong stabilization of the CT state, which results in making the CoIns closer to the FC region. Such computational results are consistent with the recent experimental observations of Park et al. [31] on

the parent system DMABN where the first deactivation step is attributed to quasiplanar motions inducing ultrafast internal conversion and direct formations of LE in less than 30 fs.

These results suggest that the new planar deactivation channel discards the need for out-of-plane motions or the involvement of the πσ* state in the charge transfer process, at least during its early stages.

However to be more conclusive we need to improve some aspects of the present potential energy surfaces model:

- Regarding the bending deactivation pathway, we must be able to adjust the new curvature parameters (denoted $\check{f}_{ii,R}^{(ij)}$ when using a switch function, see Chapter II), to improve the barrier obtained in our coupled potential energy surfaces model with respect to the ab-initio data. In other words, we need to modify the harmonic curvature as in a quadratic curvature modification strategy but without modifying the nature of the stationary points (minima or transition states).
- One will need to run the same quantum dynamics calculations with the coupled potential energy surfaces model that adequately describe the planar and bending deactivation channels based on ab-initio data calculated at the CASPT2 level and in a polar solvent. This will corroborate or not our expectations regarding the role played by the planar CoIn on the photoreactivity in the gas phase and in the presence of a polar solvent. This will possibly discard the necessity of out-of-plane motions to transfer population from the second to the first excited electronic states. This task is currently in progress.
- The involvement of the πσ* state in the charge transfer process could be considered upon improving the treatment of the in-plane bending motion of the cyano fragment. A switch function should be adequate to achieve that purpose.

From a more general point of view one can raise the question about the level of description of the solvent. In this study, we ran quantum dynamics calculations on potential energy surfaces that describe the solvent relaxation in two extreme cases: the solvent relaxation is slower than the ICT process (the solvent is equilibrated for the CT electronic state) or the solvent relaxation is faster than the ICT process (the solvent is

equilibrated for the GS). We showed that in our situation the solvent relaxation dynamics does not influence the physics of the system, as the qualitative behavior of the population over time is conserved. The adequate description of the solvent must be a situation between both extreme cases that we addressed in this thesis, where the CoIn-C_{2v} gradually shifts down in energy during the dynamics. However, these types of model are very involved and require a different description of the solvent depending on the nuclear coordinates and on time. In addition, as expected, the transfer of population along the planar pathway is more efficient in a polar solvent than in the gas phase. One can conclude that the effect of the solvent polarity as a significant impact over the transfer of population through the CoIn-C_{2v} due to a large stabilization of the CT electronic state with respect to the LE electronic state.

In addition, the description of the amino bent-ring motion is a mix of at least two CT states (PICT — CT and CT'), which is the reason of the shoulder/barrier of the potential energy surface along the CoIn-Cs direction, as in Fig. 113. The nature of CT' is still an open question and participate to the debate of the existence and role of the TICT/pTICT species.

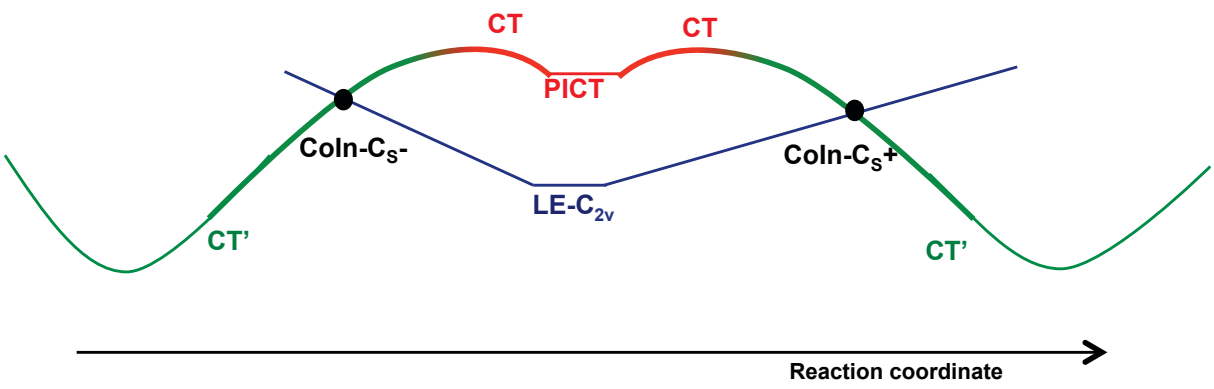

Fig. 113 Scheme of the CT mixed along the reaction coordinate mainly along the amino bent-ring motion.

In that situation, one could use a different Hamiltonian model. Instead of having three quasidiabatic electronic states to describe three adiabatic electronic states, one could account for four quasidiabatic electronic states to describe three adiabatic electronic states, as in Fig. 114. The shoulder could be adjusted upon:

- Fitting the quasidiabatic electronic coupling parameters on ab-initio data as done by L. Joubert-Doriol et al. [359] and B. Lasorne et al. [360,361] but only along the relevant directions (i.e. minima to CoIns).
- Finding the CoIn between both CT electronic states and determining the quasidiabatic electronic coupling parameters analytically as developed in this thesis. However, this is a tedious task (difficulty to localized high-energy CoIns with CASPT2 level of calculations). Furthermore, a thoughtful study about the nature of CT' is require, which seams to be one of the most important and difficult question to answer regarding this system [314].
- In addition, such as in benzopyran [359], one quasidiabatic electronic state crosses with two others and this creates electronic coupling singularities that we do not know how to correct yet.

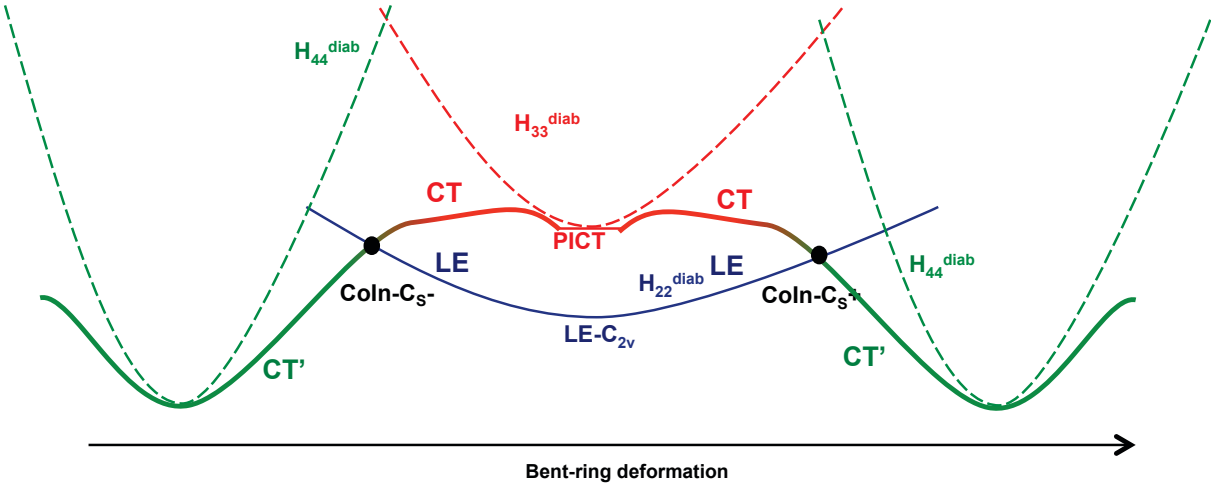

Fig. 114 Schematic representation of the quasidiabatic quadratic expansion around each minimum (dashed line) to represent the ab-initio data (adiabatic-plain line). Strategy using four diabatic states to represent three adiabatic states strategy.

Conclusion Générale et Perspectives

A l'occasion de cette thèse nous avons mis en place une méthodologie systématique pour générer des surfaces d'énergie potentielle couplées sous forme de modèles d'hamiltoniens vibroniques. Celle-ci a été appliquée à l'étude de la réactivité de processus photo-induits à l'aide de simulations utilisant une approche de dynamique quantique en cours de développement appelée ML-MCTDH spécifiquement dédiée au traitement des systèmes de grande taille.

L'originalité de ce travail de thèse a été de mettre en place une méthodologie permettant l'obtention automatique des paramètres du modèle (base diabatique) à l'aide de relations analytiques explicites impliquant directement les données obtenues par les calculs de chimie quantique (représentation adiabatique). Cette stratégie permet ainsi de s'affranchir de certaines limitations des modèles d'hamiltoniens vibroniques, notamment concernant la dimensionnalité du problème. En effet, ce dernier point peut s'avérer l'étape limitante dans les procédures plus habituelles d'ajustement non linéaire de paramètres (*fits*). Au contraire, notre méthodologie n'est pas limitée par le nombre de degrés de liberté du système et peut ainsi être appliquée à l'étude de la réactivité par dynamique quantique de systèmes considérés comme étant de grande taille (i.e. plus d'une dizaine de degrés de liberté). Ceci nous a mené à développer le code PAnDA qui permet de générer automatiquement les surfaces d'énergies potentielles couplées dans un format adapté à la méthode de dynamique quantique que nous avons utilisée (i.e. ML-MCTDH).

D'un point de vue technique, nos modèles s'inspirent des modèles d'hamiltoniens vibroniques développés par Köppel et al. [20,110–112] dans lesquels les surfaces d'énergie potentielle en représentation diabatique sont en général exprimées comme des formes quadratiques (deuxième ordre). Cependant, en l'état, de tels modèles sont limités à la description de processus (quasi)harmoniques. Pour le traitement de cas moins harmoniques, nous avons étendu cette description et mis en place différentes stratégies pour modifier le modèle diabatique quadratique initial en introduisant une

certaine part d'anharmonicité. Comme il est visible dans les chapitres d'applications (Chapter III et IV), les modèles ont été élaborés dans l'optique d'être facilement adaptables à la description de différents types de paysages énergétiques, plus ou moins complexes. Ils ont donc ainsi permis la production dans un temps "raisonnable" d'une étude prenant en compte toutes les dimensions du système et les effets quantiques des noyaux sur la photo-reactivité du processus non-adiabatique en question. Ces stratégies sont présentées formellement dans les Chapitres I et II, et appliquées à l'étude de deux processus photo-induits: le transfert de charge dans l'aminobenzonitrile et le transfert de proton du 3-hydroxychromone.

L'étude du transfert de charge dans l'aminobenzonitrile à été réalisée en collaboration avec le groupe du Dr. Mar Reguero et Pedro J. Castro (Universitat Rovira i Vigili, Tarragona, Espagne) qui ont réalisé une partie des calculs de chimie quantique. Lors de cette étude, nous avons mis en place un modèle qui a permis la description d'une "couture" (*seam*) connectant deux types différents d'intersections coniques entre les deux mêmes états électroniques. D'un point de vue dynamique, ce type de modèle nous a permis de comparer l'efficacité des deux types de chemins photo-réactionnels. Ceci nous a mené à l'une des conclusions majeures de ce chapitre vis-à-vis de la chimie du système: le chemin réactionnel majoritairement responsable du transfert de population non-radiatif entre les deux premiers états excités n'est pas le chemin de plus basse énergie. La dynamique (i.e. description du mouvement des noyaux) est donc un outil essentiel à la compréhension de la réactivité des processus photo-induits.

Nous avons également étudié l'effet du solvant sur le processus en question. Rappelons ici que l'état qui absorbe à FC est un état à transfert de charge ; il va donc être stabilisé en présence d'un solvant polaire, ce qui va induire une plus grande accessibilité (énergies plus basses) des intersections coniques au cours de la photo-réaction. Nous avons pu observer que dans les limites de notre description (solvant implicite décrit avec la méthode PCM), la présence du solvant accentuait les résultats obtenus en phase gaz mais que cependant la stabilisation de l'état à transfert de charge n'était pas assez importante pour modifier la réactivité d'un point de vue qualitatif : l'intersection conique n'a pas changé de nature et la topographie des surfaces d'énergie potentielle est restée globalement la même (et ce, que le solvant soit relaxé ou non sur l'état excité).

L'étude du transfert de proton photo-induit du 3-hydroxychromone nous a demandé une analyse préliminaire de chimie quantique, ce qui nous a permis de mettre en évidence pour la première fois l'existence d'une intersection conique dans la région de FC mais aussi de rationaliser le processus d'isomérisation cis-trans qui s'avère plus complexe que ce que la littérature pouvait sous-entendre. La question posée lors de cette étude concernait l'observation expérimentale de deux temps de réaction pour le transfert de proton. Nous avons pu rationalisé ceci à l'aide de calculs de dynamique quantique. Nous avons pu montrer que la présence d'une intersection conique dans la région de FC avait un impact non négligeable sur la réactivité car les couplages non-adiabatiques entre S_1 et S_2 y sont non négligeables. Ceci va donc induire un retard d'une partie du système qui va partiellement se délocaliser le long de l'isomérisation cis-trans. En d'autres termes, nos calculs ont montré qu'effectivement l'isomérisation cis-trans était un chemin en compétition avec le transfert de proton comme le supposait la littérature. En revanche, ce mécanisme, plus complexe que prévu, implique plus d'états électroniques que ce qui pouvait être attendu.

Cependant, le modèle d'hamiltonien électronique utilisé pour obtenir ces résultats ne décrit pas l'isomérisation cis-trans dans sa totalité. En effet, le mouvement associé à cette isomérisation (torsion de l'hydrogène) n'est, à l'heure actuelle, pas décrit dans notre modèle comme un mouvement périodique mais comme un mouvement lié. Cette étape nécessite d'adapter les expressions analytiques des paramètres du modèle diabatique, ce qui est actuellement un travail en cours.

Comme nous venons de le souligner, ces modèles nécessitent encore un certain nombre de développements qui s'orientent principalement vers : comme déjà suggéré, l'implémentation de fonctions périodiques et la possibilité de décrire plusieurs intersections coniques entre des états électroniques différents (la difficulté concerne l'impossibilité de séparer simplement l'hamiltonien électronique diabatique comme une série de problèmes à deux états indépendants). Ce point permettrait de pouvoir augmenter le nombre d'état diabatiques pour décrire un même état adiabatique (Cf. *Conclusion and Outlooks* Chapitre IV sur l'aminobenzonitrile) et ainsi de développer une nouvelle stratégie de description de l'anharmonicité. Ceci pourrait également assurer une meilleure description locale des intersections coniques et de leurs espaces de

branchement (*branching spaces*) et donnerait, en tout état de cause, plus de flexibilité dans la description des surfaces d'énergie potentielle couplées ayant des topographies complexes.

Une des perspectives à long terme sur le développement de ce type de méthodologie serait de pouvoir la combiner avec d'autres méthodes pour continuer à aller vers le traitement de systèmes de plus grande taille et plus complexes (i.e. en interaction forte avec un environnement intra et/ou intermoléculaire). On peut ainsi concevoir une stratégie hiérarchisée avec une description précise du système et une modélisation plus approchée de la dynamique cet environnement et de ses effets sur le système (par des méthodes de dynamique quantique utilisant des modes effectifs ou par des méthodes de dynamique plus approximatives dans le traitement quantique des noyaux du type DD-vMCG ou « ab initio multiple spawning »).

Appendix A- Acronyms

2T-3HC: 2-Thienyl-3-HydroxyChromone

3-HC: 3-HydroxyChromone

ABN: AminoBenzoNitrile

BF: Body-Fixed

BS: Branching Space

CASSCF: Complete Active Space Self-Consistent Field

CI: Configuration Interaction

CoIn: Conical Intersection

CT: Charge Transfer

CyHxn: CycloHexane

DC: Derivative Coupling

DD-vMCG: Direct Dynamics variational MultiConfigurational Gaussian

DFT: Density Functional Theory

DMABN: Dimethyl-AminoBenzoNitrile

ESIPT: Excited State Proton Transfer

FC: Franck Condon

GD: Gradient Difference

GGA: Generalized Gradient Approximation

GS: Ground State

ICT: Intramolecular Charge Transfer

IRC: Intrinsic Reaction Coordinate

IVR: Intramolecular Vibrational Redistribution

KEO: Kinetic Energy Operator

LDA: Local Density Approximation

LE: Locally Excited

LF: Laboratory-Fixed

LVC: Linear Vibronic Coupling

MCSCF: MultiConfigurational Self-Consistent Field

MCTDH: MultiConfigurational Time-Dependent Hartree

MeCN: acetonitrile

Min: Minimum

ML-MCTDH: Multilayer MultiConfigurational Time-Dependent Hartree

MS-CASPT2: MultiState Complete Active Space Second Order Perturbation Theory

NAC: Non-Adiabatic Coupling

PCM: Polarizable Continuum Model

PCS: Potential Coupling Surfaces

PES: Potential Energy Surface

PICT: Planar Intramolecular Charge Transfer

pTICT: preTwisted Intramolecular Charge Transfer

PT: Proton Transfer

QVC: Quadratic Vibronic Coupling

RASSCF: Reduced Active Space Self-Consistent Field

RICT: Rehybridized Intramolecular Charge Transfer

SA: State Average

SPF: Single Particle Function

TD-DFT: Time-Dependent Density Functional Theory

TDH: Time-Dependent Hartree

TDSCF: Time-Dependent Self-Consistent Field

TICT: Twisted Intramolecular Charge Transfer

TRFS: Time-Resolved Fluorescence Spectrum

TS: Transition State

VCH: Vibronic Coupling Hamiltonian

Appendix B- Procedure for Generating Numerically the Branching Space Vectors of a Conical Intersection

We tested this approach on 3-HC (see Chapter III). Additional benchmarking tests have been carried out by Benjamin Gonon (PhD student co-supervised by Fabien Gatti in Montpellier and Stéphane Guérin in Dijon). A paper is in preparation.

Analytic-derivative techniques [362] have been key for progress in quantum-chemistry methods. However, not all types of derivatives or non-adiabatic couplings have been implemented yet.

A procedure proposed by Köppel and Schubert in Ref. [363] for a two-dimensional case is generalized to determine the branching-space vectors from a normal-mode analysis of the square energy difference around a conical intersection. This approach can prove vital in two types of situations: when analytic derivatives are not available at all or when the analytic gradients are available but not the derivative couplings.

The definitions of the branching-space vectors and related quantities have been given in Chapter I. If $\boldsymbol{\mathcal{R}_0}$ is the locus of a conical intersection between S_1 and S_0, although $\Delta V(\boldsymbol{\mathcal{R}})$ is not well-behaved around $\boldsymbol{\mathcal{R}_0}$, $\Delta V^2(\boldsymbol{\mathcal{R}})$ is differentiable and satisfies

$$\Delta V^2(\boldsymbol{\mathcal{R}_0}) = 0, \qquad \textbf{Eq. 107}$$

$$\frac{\partial \Delta V^2(\boldsymbol{\mathcal{R}_0})}{\partial \mathcal{R}^I} = 0,$$

$$\frac{\partial^2 \Delta V^2(\boldsymbol{\mathcal{R}_0})}{\partial \mathcal{R}^I \, \partial \mathcal{R}^L} = 2\left(\boldsymbol{x}_I^{\theta_{01}(01)1}\boldsymbol{x}_L^{\theta_{01}(01)1} + \boldsymbol{x}_I^{\theta_{01}(01)2}\boldsymbol{x}_L^{\theta_{01}(01)2}\right)$$
$$= 2\left(\boldsymbol{x}_I^{0(01)1}\boldsymbol{x}_L^{0(01)1} + \boldsymbol{x}_I^{0(01)2}\boldsymbol{x}_L^{0(01)2}\right).$$

This properties hold at any point of the crossing seam, not only at the minimum-energy conical intersection. Remarkably, the second derivative is invariant through the arbitrary mixing angle θ_{01}, which reflects again the fact that the branching-space vectors are defined up to an arbitrary rotation.

The branching-space vectors are involved as first-order terms in the expansion of $\Delta V(\boldsymbol{\mathcal{R}})$ from $\boldsymbol{\mathcal{R}_0}$, hence as second-order terms in that of $\Delta V^2(\boldsymbol{\mathcal{R}})$. Higher-order terms will thus appear only in higher derivatives.

For notation simplicity, we introduce the following notations

$$\begin{aligned} \kappa_I &= \boldsymbol{x}_I^{0(01)1}, \\ \lambda_I &= \boldsymbol{x}_I^{0(01)2}. \end{aligned} \qquad \textbf{Eq. 108}$$

$$\begin{aligned} \tilde{\kappa}_I &= \boldsymbol{x}_I^{\theta_{01}(01)1} = \cos 2\theta_{01}\, \kappa_I - \sin 2\theta_{01}\, \lambda_I, \\ \tilde{\lambda}_I &= \boldsymbol{x}_I^{\theta_{01}(01)2} = \sin 2\theta_{01}\, \kappa_I + \cos 2\theta_{01}\, \lambda_I. \end{aligned} \qquad \textbf{Eq. 109}$$

The Hessian matrix of the square energy difference at $\boldsymbol{\mathcal{R}_0}$, $\mathbf{F} = \left[\frac{\partial^2 \Delta V^2(\boldsymbol{\mathcal{R}_0})}{\partial \mathcal{R}^I \partial \mathcal{R}^L}\right]$, reads (for any θ_{01}),

$$F_{IL} = 2\left(\tilde{\kappa}_I \tilde{\kappa}_L + \tilde{\lambda}_I \tilde{\lambda}_L\right). \qquad \textbf{Eq. 110}$$

Thus, for any vector $\mathbf{v}$, we get

$$\sum_L F_{IL} v_L = 2\left(\sum_L \tilde{\kappa}_L v_L\right)\tilde{\kappa}_I + 2\left(\sum_L \tilde{\lambda}_L v_L\right)\tilde{\lambda}_I. \qquad \textbf{Eq. 111}$$

Now, if the angle θ_{01} is chosen such that $\left(\tilde{\boldsymbol{\kappa}}, \tilde{\boldsymbol{\lambda}}\right)$ are made orthogonal,

$$\sum_L \tilde{\kappa}_L \tilde{\lambda}_L = 0, \qquad \textbf{Eq. 112}$$

the vectors $\tilde{\boldsymbol{\kappa}}$ and $\tilde{\boldsymbol{\lambda}}$ happen to be two eigenvectors of $\mathbf{F}$ with non-vanishing eigenvalues,

$$\sum_L F_{IL}\tilde{\kappa}_L = 2\sum_L \left(\tilde{\kappa}_I\tilde{\kappa}_L + \tilde{\lambda}_I\tilde{\lambda}_L\right)\tilde{\kappa}_L = \left(2\sum_L \tilde{\kappa}_L^2\right)\tilde{\kappa}_I, \qquad \textbf{Eq. 113}$$

$$\sum_L F_{IL}\tilde{\lambda}_L = 2\sum_L \left(\tilde{\kappa}_I\tilde{\kappa}_L + \tilde{\lambda}_I\tilde{\lambda}_L\right)\tilde{\lambda}_L = \left(2\sum_L \tilde{\lambda}_L^2\right)\tilde{\lambda}_I.$$

There always exists a value of θ_{01} that can be used to make $\left(\tilde{\boldsymbol{\kappa}}, \tilde{\boldsymbol{\lambda}}\right)$ orthogonal (it is obtained upon diagonalizing the overlap matrix between the original $(\boldsymbol{\kappa}, \boldsymbol{\lambda})$, see [363]). This thus proves that diagonalizing $\mathbf{F}$ in practice produces a pair of orthogonal branching-space vectors, the eigenvalues of which are twice their square lengths. The remaining eigenvectors correspond to almost-zero eigenvalues.

As can be noticed, this problem is formally similar to a normal mode analysis where $\boldsymbol{\mathcal{R}}$ are mass-weighted Cartesian coordinates. However, non-mass-weighted Cartesian coordinates are equally valid for our purpose and only result in different orthonormality relationships among vector components. In contrast, curvilinear coordinates would involve explicit use of the metric tensor and a generalized eigenproblem (see, e.g., Ref. [364]).

Appendix C- 3-Hydroxychromone Dyes

Definition of the Z-matrix

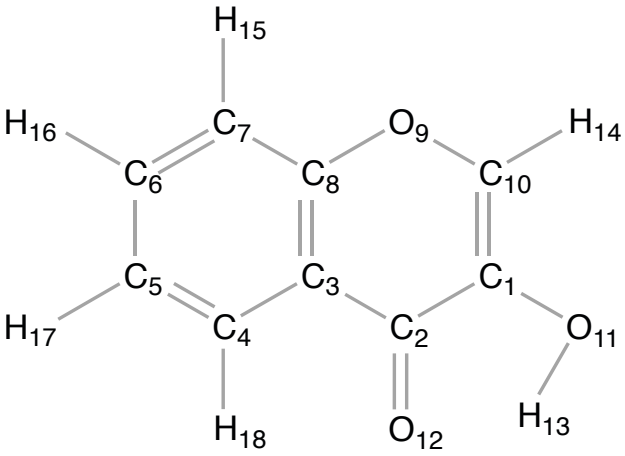

Atome						
C_1	**Distance**	**Atome**				
C_2	R_1	C_1	**Valence angle**	**Atome**		
C_3	R_2	C_2	θ_1	C_1	**Dihedral angle**	**Atome**
C_4	R_3	C_3	θ_2	C_2	φ_1	C_1
C_5	R_4	C_4	θ_3	C_3	φ_2	C_2
C_6	R_5	C_5	θ_4	C_4	φ_3	C_3
C_7	R_6	C_6	θ_5	C_5	φ_4	C_4
C_8	R_7	C_7	θ_6	C_6	φ_5	C_5
O_9	R_8	C_8	θ_7	C_7	φ_6	C_6
C_{10}	R_9	O_9	θ_8	C_8	φ_7	C_7
O_{11}	R_{10}	C_1	θ_9	C_2	φ_8	C_3
O_{12}	R_{11}	C_2	θ_{10}	C_1	φ_9	O_{11}
H_{13}	R_{12}	O_{11}	θ_{11}	C_1	φ_{10}	C_2
H_{14}	R_{13}	C_{10}	θ_{12}	O_9	φ_{11}	C_8

H_{15}	R_{14}	C_7	θ_{13}	C_6	φ_{12}	C_5
H_{16}	R_{15}	C_6	θ_{14}	C_7	φ_{13}	C_8
H_{17}	R_{16}	C_5	θ_{15}	C_6	φ_{14}	C_7
H_{18}	R_{17}	C_4	θ_{16}	C_5	φ_{15}	C_6

Quantum Dynamics

Relaxation: 20fs

ZPE: 3.665337 eV

KEO: numerical; zero-order Taylor expansion

Primitive basis: Harmonic Oscillator with 40 primitive basis functions per coordinates.

ML-Tree in the "ML-MCTDH" format :

Label of the layer > number of SPFs for Qi

One must keep in mind that the coordinates used during the dynamics calculations are linear combination of curvilinear coordinates, and do not have physical meaning anymore.

0> 3 3

 # Electronic

1> [el]

 # vibrations

1> 6 6

2> 6 6

3> 6 6

4> [Q_1 Q_{48}]

4> [Q_2 Q_3]

3> [Q_4 Q_{40}]

2> 6 6

3> 6 6

4> 6 6 6

5> [Q_5 Q_7]

5> 6 6

6> [Q_{15} Q_{19}]

6> [Q_{16} Q_{19}]

5> 6 6

6> [Q_{18} Q_{34}]

6> [Q_{10} Q_{14}]

4> 6 6 6

5> 6 6

6> [Q_{11} Q_{13}]

6> [Q_{12} Q_{16}]

5> 6 6

6> [Q_{17} Q_{18}]

6> [Q_{20} Q_{25}]

5> 6 6

6> [Q_{21} Q_{26}]

6> [Q_{22} Q_{24}]

3> 6 6

4> 6 6 6

5> 6 6

6> [Q_{23} Q_{27}]

6> [Q_{28} Q_{33}]

5> 6 6

6> [Q_{29} Q_{31}]

6> [Q_{30} Q_{35}]

5> 6 6

6> [Q_{32} Q_{37}]

6> [Q_{36} Q_{39}]

4> 6 6

5> 6 6

6> [Q_{38} Q_{41}]

6> [Q_{42} Q_{47}]

5> 6 6

6> [Q_{43} Q_{44}]

6> [Q_{45} Q_{46}]

Appendix D- Aminobenzonitrile

Symmetric Coordinates

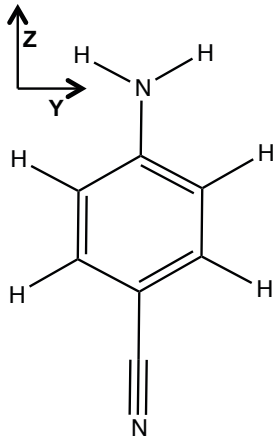

Cartesian frame used in this study (Mulliken's convention).

Small variations of the original set of polyspherical coordinates with respect to a flat C_{2v} reference geometry, $\Delta\mathbf{Q} = \mathbf{Q} - \mathbf{Q}_0$ can be symmetrized as follows:

$\boldsymbol{A_1}\ [\boldsymbol{C_{2v}} \Rightarrow\ \boldsymbol{C_{2v}}]$	$\boldsymbol{A_2}\ [\boldsymbol{C_{2v}} \Rightarrow\ \boldsymbol{C_2}]$	$\boldsymbol{B_1}\ [\boldsymbol{C_{2v}} \Rightarrow\ \boldsymbol{C_s^{\perp}}]$	$\boldsymbol{B_2}\ [\boldsymbol{C_{2v}} \Rightarrow\ \boldsymbol{C_s^{\parallel}}]$
ΔR_1^1	$\frac{\Delta\varphi_4^{11} - \Delta\varphi_3^{11}}{2}$	$\frac{\Delta\varphi_4^{11} + \Delta\varphi_3^{11}}{2}$	$\frac{\Delta R_4^{11} - \Delta R_3^{11}}{2}$
ΔR_1^{11}	$\frac{\Delta\varphi_4^{21} - \Delta\varphi_3^{21}}{2}$	$\Delta\varphi_5^{11}$	$\frac{\Delta R_4^{21} - \Delta R_3^{21}}{2}$
ΔR_2^{11}	$\Delta\gamma^{121} + \frac{\Delta\varphi_3^{121}}{2}$	$\Delta\varphi_6^{11}$	$\frac{\Delta R_3^{121} - \Delta R_2^{121}}{2}$
$\frac{\Delta R_4^{11} + \Delta R_3^{11}}{2}$	$\Delta\alpha^{21}$	$\frac{\Delta\varphi_4^{21} + \Delta\varphi_3^{21}}{2}$	$\Delta\theta_2^{11}$
ΔR_5^{11}		$\Delta\varphi_3^{121}$	$\frac{\Delta\theta_4^{11} + \Delta\theta_3^{11}}{2}$
ΔR_6^{11}		$\Delta\alpha^{121}$	$\Delta\theta_5^{11}$
ΔR_1^{21}		$\Delta\gamma^{11}$	$\Delta\theta_6^{11}$
ΔR_2^{21}		$\Delta\gamma^{21}$	$\Delta\theta_2^{21}$

$\frac{\Delta R_4^{21} + \Delta R_3^{21}}{2}$		$\frac{\Delta\theta_4^{21} + \Delta\theta_3^{21}}{2}$
ΔR_1^{121}		$\frac{\Delta\theta_3^{121} - \Delta\theta_2^{121}}{2}$
$\frac{\Delta R_3^{121} + \Delta R_2^{121}}{2}$		$\Delta\beta^{11}$
$\frac{\Delta\theta_4^{11} - \Delta\theta_3^{11}}{2}$		$\Delta\beta^{21}$
$\frac{\Delta\theta_4^{21} - \Delta\theta_3^{21}}{2}$		$\Delta\beta^{121}$
$\frac{\Delta\theta_3^{121} + \Delta\theta_2^{121}}{2}$		

In this, we used the convention where (zy) is the molecular plane (||) and (zx) is the perpendicular plane (⊥). A_2 deformations are torsions, B_2 deformations are in-plane left-right-breaking motions, and B_1 deformations are out-of-plane up-down-breaking motions.

Planar Deactivation Pathway Model

Relaxation: 10 fs

ZPE: 3.153966 eV

KEO: analytic

Primitive basis: Harmonic Oscillator with 40 basis functions per coordinates except for the following in plane-angles that are expanded in a sinus basis with 80 basis functions per coordinates: $\beta^{1,1}, \theta_2^{1,1}, \theta_5^{1,1}, \theta_6^{1,1}, \beta^{2,1}, \theta_2^{2,1}, \beta^{1,2,1}, \theta_2^{1,2,1}, \theta_4^{2,1}, \theta_3^{2,1}, \theta_4^{1,1}, \theta_3^{1,1}, \theta_3^{1,2,1}$

ML-Tree in the "ML-MCTDH" format :

Label of the layer > number of SPFs for Qi

0> 3 3

 # Electronic

1> [el]

 # vibrations

1> 6 6 6

2> $[R_1^1]$

2> 6 6 6 6

3> $[R_1^{1,1}\ \beta^{1,1}]$

3> 6 6

4> 6 6

5> $[R_2^{1,1}\ \theta_2^{1,1}]$

5> $[\gamma^{1,1}]$

4> 6 6

5> 6 6

6> $[R_5^{1,1}\ \theta_5^{1,1}]$

6> $[\varphi_5^{1,1}]$

5> 6 6

6> $[R_6^{1,1}\ \ \theta_6^{1,1}]$

6> $[\varphi_6^{1,1}]$

3> 6 6

4> $[R_3^{1,1}\quad \theta_3^{1,1}]$

4> $[\varphi_3^{1,1}]$

3> 6 6

4> $[R_4^{1,1}\quad \theta_4^{1,1}]$

4> $[\varphi_4^{1,1}]$

2> 6 6 6 6

3> 6 6

4> $[R_1^{2,1}\ \beta^{2,1}]$

4> $[\alpha^{2,1}]$

3> 6 6

4> 6 6

5> $[R_2^{2,1}\ \theta_2^{2,1}]$

5> $[\gamma^{2,1}]$

4> 6 6

5> 6 6

6> $[R_1^{1,2,1}\ \beta^{1,2,1}]$

6> $[\alpha^{1,2,1}]$

5> 6 6

6> 6 6

7> $[R_2^{1,2,1}\ \theta_2^{1,2,1}]$

7> $[\gamma^{1,2,1}]$

6> 6 6

7> $[R_3^{1,2,1}\ \theta_3^{1,2,1}]$

7> $[\varphi_3^{1,2,1}]$

3> 6 6

4> $[R_3^{2,1}\ \theta_3^{2,1}]$

4> $[\varphi_3^{2,1}]$

3> 6 6

4> $[R_4^{2,1}\ \theta_4^{'2,1}]$

4> $[\varphi_4^{2,1}]$

Bent Deactivation Pathway Model

Relaxation: 20 fs

ZPE: 2.580435 eV

KEO: numeric (zero order Taylor expansion)

Primitive basis: Harmonic Oscillator with 40 basis functions per coordinates.

ML-Tree in the "ML-MCTDH" format :

Label of the layer > number of SPFs for Qi

One must keep in mind that the coordinates used during the dynamics calculations are linear combination of curvilinear coordinates, and do not have physical meaning anymore.

0> 3 3

 # Electronic

1> [el]

 # vibrations

1> 6 6 6 6

2> 6 6

3> [Q_2 Q_3]

3> 6 6 6

4> 6 6

5> [Q_4 Q_5]

5> [Q_6 Q_7]

4> 6 6

5> [Q_8 Q_9]

5> [Q_{10} Q_{11}]

4> 6 6

5> [Q_{12} Q_{13}]

5> [Q_{14} Q_{15}]

2> 6 6

3> [Q_{16} Q_{17}]

3> [Q_{18} Q_{19}]

2> 6 6 6 6

3> [Q_{20}]

3> 6 6

4> [Q_{21} Q_{22}]

4> [Q_{23} Q_{24}]

3> 6 6

4> [Q_{25} Q_{26}]

4> [Q_{27} Q_{28}]

3> 6 6

4> [Q_{29} Q_{30}]

4> [Q_{31} Q_{32}]

2> 6 6

3> [Q_1]

> 6 6 6 6

4> [Q_{33}]

4> [Q_{34} Q_{35}]

4> [Q_{36} Q_{37}]

4> [Q_{38} Q_{39}]

Appendix E- Résumé en Français

Introduction Générale

Le développement de la technologie laser au cours des dernières décennies a permis la génération de pulses ultracourts de l'ordre de la picoseconde et de la femtoseconde [1] (et même récemment de l'ordre de l'attoseconde [2–4]). Ceci a mené à la conception de nombreuses méthodes expérimentales de spectroscopie ultrarapide [5–7]. En d'autres termes, nous sommes désormais capable de sonder le mouvement des systèmes moléculaires en temps réel et de le contrôler (influencer la réactivité avec un pulse laser optimisé pour atteindre une cible prédéterminée) [8–16]; ce domaine de recherche est appelé femtochimie (pour les réactions considérés comme ultrarapides de l'ordre de la femtoseconde). Ahmed Zewail fut le pionnier de l'utilisation de pulses laser ultracourts pour étudier la dynamique femtoseconde d'états de transition. Il reçut le prix Nobel de Chimie en 1999 pour ses travaux dans le domaine de la spectroscopie ultrarapide [1,17].

L'étude de processus ultrarapides en photochimie a permis l'émergence de nouvelles technologies dans des domaines très hétéroclites tels que : l'élaboration de nouveaux protocoles de synthèse en chimie moléculaire (e.g. réaction de Diels-Alder photoinduite, photopolymerisation), l'obtention de nouveaux matériaux avec des propriétés optiques particulières (e.g. photochromisme, optique non-linéaire), des méthodes d'analyse en biochimie (e.g. marqueurs fluorescents, des traitements médicaux (e.g. photothérapie). L'intérêt et l'utilisation des processus photoinduits dans certains des domaines mentionnés précédemment sont décrits en détail dans les introductions des deux chapitres d'applications portant sur le transfert de proton dans l'état excité du 3-hydroxychromone et le transfert de charge intramoléculaire photoinduit dans l'aminobenzonitrile (respectivement Chapitres III et IV). Il est donc capital de pouvoir traiter ce type de réactivité chimique d'un point de vue théorique et ainsi apporter une complémentarité aux expérimentateurs afin de pouvoir déterminer avec précision les mécanismes de ces réactions et, à terme, de les contrôler et/ou d'optimiser les propriétés physicochimiques des systèmes photosensibles (e.g. absorption, émission,

rapports de branchement réactif(s)/produit(s)) dans l'optique de développements technologiques [18,19].

La photochimie possède des propriétés mécanistiques tous être explicitées avec des outils standard de chimie quantique et une dynamique reposant sur les lois de la mécanique classique telle que la dynamique moléculaire par exemple. Une réaction photochimique étant une réaction induite par l'absorption d'un photon par le système moléculaire, la réaction va donc se produire en partie ou en totalité sur un ou plusieurs états électroniques excités; on va donc devoir utiliser des méthodes de chimie quantique qui ne sont pas limitées à l'état électronique fondamental (les méthodes utilisées lors de ce travail de thèse pour traiter la structure électronique des systèmes étudiés sont explicitées dans le Chapitre I).

De plus, il existe des géométries particulières où certains états électroniques sont proches en énergie, voire dégénérés (i.e. intersections coniques). Dans les régions proches de ces géométries particulières, l'approximation de Born-Oppenheimer n'est plus valide. Le système chimique est dans un régime de dynamique appelé non-adiabatique (la dynamique des noyaux et des électrons se couple dans ces régions, Cf. Chapitre I). Il est donc nécessaire de traiter le mouvement des noyaux comme évoluant sur plusieurs surfaces d'énergies potentielles couplées entre elles. Ces couplages non-adiabatiques permettent des transferts de population non-radiatifs (sans émission de photon) entre états électroniques de même spin (conversion interne). Ceci suggère que l'état électronique excité après absorption (état initial du point de vue Franck-Condon) n'est pas nécessairement l'état électronique final de la réaction. Ces transferts de population non-radiatifs sont plus efficaces dans les régions ou les états électroniques sont quasi-dégénérés, c'est-à-dire, lorsque le système s'approche d'une région d'intersection conique. Ce point particulier de dégénérescence entres états électroniques joue donc un rôle central dans les processus ultrarapides photoinduits [20–22].

Lors d'une étude de ce type de processus, l'intersection conique est un point qui se doit donc d'être caractérisé et qui peut être vu qualitativement comme le pendant pour la photochimie non-adiabatique d'un état de transition pour les processus thermiques.

Cependant ne connaitre que la position et l'énergie de l'intersection conique n'est pas toujours suffisant pour comprendre et déterminer le mécanisme de la réaction. Le système peut être soumis à plusieurs chemins réactionnels en compétition. A la différence de la réactivité thermique, en photochimie non-adiabatique, il ne suit pas nécessairement le chemin de plus basse énergie. Lors de l'étude d'un processus photochimique ultrarapide, on peut être amené à devoir considérer le système comme pouvant se délocaliser le long de plusieurs chemins réactionnels couplés (ceci est observé et discuté dans les chapitres d'applications étudiées lors de ce travail de thèse Chapitres III et IV). Ceci montre la nécessité d'étudier ce type de réactivité avec des outils de dynamique adaptés.

Ceci est moins crucial pour les processus photochimiques dit adiabatiques, qui sont des processus photoinduits ayant lieu sur un seul état électronique excité considéré comme isolé (séparation importante en énergie par rapport aux autres états électroniques). On peut voir ce type de photoreactivité comme étant similaire aux processus thermiques où le système ne serait pas à l'équilibre dans sont état initial. De plus, comme l'approximation de Born-Oppenheimer reste valide pour ce type de processus, il est plus simple de ce point de vue de décrire leur dynamique car l'intégralité de la réactivité se passe sur la même surface d'énergie potentielle. Il est courant dans ce cas d'utiliser des méthodes de type dynamique moléculaire ab initio (les noyaux sont traités comme des particules classiques évoluant sur un potentiel calculé par une méthode de chimie quantique). Cependant, lors de ces travaux de thèse nous nous sommes principalement concentrés sur l'étude de processus photochimiques non-adiabatiques.

Le développement de méthodes de dynamique adaptées aux processus non-adiabatiques dans des systèmes moléculaires est en plein essor. Différentes approches, quantiques, semi-classiques (ou hybrides) coexistent. Nous allons évoquer certaines d'entre elles dans ce qui suit.

Dans le cas d'une méthode dite semi-classique telle que le « surface hopping » [23], la dynamique du système est décrite par une trajectoire classique. L'énergie potentielle et la force sont calculées « on-the-fly » (au vol). L'efficacité du processus non-radiatif (donc non-adiabatique) est obtenue par la probabilité pour le système de « sauter » d'un état

électronique à un autres en fonction de la vitesse de la trajectoire, de la différence d'énergie entre les deux états et de leur couplage. Cette méthode ne permet pas de rendre compte de la délocalisation quantique du mouvement des noyaux que l'on devrait en toute rigueur représenter par ce que l'on appelle un paquet d'ondes nucléaire (fonction d'onde nucléaire dépendante du temps). Ceci caractérise la capacité du système à avoir une probabilité de présence différente et non nulle pour plusieurs géométries en même temps. Ainsi, les différentes trajectoires calculées ne sont pas couplées (elles évoluent indépendamment les unes des autres). Or, le système se délocalise avec une certaine « cohérence », c'est à dire que les trajectoires ne devraient pas être indépendantes les unes des autres d'un point de vue quantique. Cependant, une approche statistique basée sur un grand nombre de trajectoires est utilisée en échantillonnant les conditions initiales du système pour au moins « mimer » l'état vibrationnel initial dans l'état électronique fondamental (et son énergie de point zéro).

La cohérence quantique peut être vu comme une « force » qui va influencer la délocalisation du paquet d'ondes et ses interférences, ce qui peut être crucial quand, par exemple, il passe à travers la même intersection conique plusieurs fois dans un laps de temps ultracourt. Récemment, des expériences ont suggéré l'existence et l'implication de cohérence quantique pendant un temps long (de l'ordre de la picoseconde) dans des processus biologiques [24,25]. Il est donc préférable de pouvoir représenter le caractère quantique du mouvement des noyaux par un paquet d'ondes.

L'« ab initio multiple spawning » [26,27] s'affranchit du coté classique et statistique de la méthode de « surface hopping » en représentant le paquet d'ondes nucléaire par un ensemble de gaussiennes couplées quantiquement (et dont le nombre augmente quand une intersection conique est rencontrée) mais qui suivent des trajectoires classiques. La description du paquet d'ondes dans cette dernière méthode est donc plus correcte et plus représentative. On peut la considérer comme un ensemble de trajectoires classiques couplées quantiquement. La référence suivante dresse une comparaison entre la méthode « surface hopping » et l'« ab initio multiple spawning » [28].

La méthode DD-vMCG (Direct Dynamics variational MultiConfigurational Gaussian) [29,30] peut être vue d'une certaine façon comme une extension de l'« ab initio multiple

spawning », de part le fait que le paquet d'ondes est aussi décrit comme une collection de gaussiennes couplées quantiquement (dont le nombre et les largeurs sont fixés dans les conditions initiales et ne changent pas au cours du temps dans la plupart des applications) mais qui vont maintenant évoluer en suivant des « trajectoires quantiques » (c'est-à-dire que la position et l'impulsion moyennes des gaussiennes sont obtenues par résolution variationelle de l'équation de Schrödinger dépendante du temps [31]). Ceci permet donc d'avoir besoin de moins de gaussiennes pour converger le paquet d'ondes que dans la méthode précédente (i.e. l'« ab-initio multiple spawning »). Cette méthode prometteuse de dynamique que je considère à mon sens comme étant une dynamique semi-quantique est à l'heure actuelle en plein développement. Ce qui la rend encore limitée dans la taille des systèmes est essentiellement dû à des raisons techniques comme par exemple la nécessité de calculer des dérivées secondes au centre de chaque gaussienne et à chaque pas de la dynamique.

Les méthodes de dynamique quantique sur grille ont pour philosophie de décomposer le paquet d'ondes nucléaire sur une grille de points représentant l'espace des coordonnées nucléaires. Ceci impose de représenter préalablement les surfaces d'énergie potentielle sous forme analytique, à l'inverse des trois méthodes précédemment évoquées ou ce calcul est réalisé « on-the-fly » le long de chaque trajectoire. Le mouvement des noyaux est obtenu par résolution de l'équation de Schrödinger dépendante du temps. Il n'y a donc pas d'approximation dans le traitement de la nature quantique des noyaux (tout comme dans la méthode DD-vMCG). Par ceci, nous entendons que ce type de méthode est en principe exact à convergence pour un hamiltonien donné.

Cependant, ces types de dynamiques sont difficiles à mettre en œuvre pour des systèmes moléculaires de grande taille (nombreux degrés de liberté nucléaires). De par le fait qu'elles coutent cher en termes de temps de calcul (pouvant atteindre plusieurs mois pour converger le paquet d'ondes nucléaire initial) mais aussi car il faut dans un premier temps générer les surfaces d'énergie potentielle et les couplages électroniques sous forme de fonctions analytiques. De plus, comme nous pourrons le voir au cours de cette thèse (Cf. Chapitre I), selon la méthode de dynamique quantique choisie, il peut y avoir des contraintes sur la forme mathématique des fonctions qui composent la représentation matricielle de l'hamiltonien électronique. Ceci peut s'avérer limitant car,

comme déjà mentionné, en photochimie la réactivité implique souvent des paysages énergétiques complexes possédant de nombreux points stationnaires (minima, états de transition, intersections coniques) et ce pour plusieurs états électroniques. A ceci s'ajoute la description des couplages non-adiabatiques qui comme on le montrera n'est pas un problème trivial dans un système multidimensionnel. Toutes ces difficultés font que la représentation des hamiltoniens électroniques en photochimie est une tâche difficile (plus précisément l'obtention des paramètres définissant les fonctions du modèle à partir de données ab initio) et devient bien souvent l'étape limitante dans la description quantique de la dynamique de ce type de systèmes.

C'est pourquoi de nombreuses méthodologies sont encore à l'heure actuelle en cours de développement pour palier à ces difficultés. La première stratégie la plus intuitive est de réduire le nombre de degrés de liberté du système en déterminant les modes les plus importants pour décrire le chemin réactionnel (appelés en général modes actifs dans la littérature) [32–40]. Cependant, ces modèles ne prennent pas en compte la dissipation de l'énergie contenue dans ces modes actifs vers le reste des modes, dit inactifs. Par construction la dissipation vibrationnelle (relaxation vibrationnelle intramoléculaire) n'est pas décrite correctement. Cependant, ces méthodes se justifient en partie de part le fait que dans les processus ultrarapides (ordre de la femtoseconde), le système n'a pas le temps de redistribuer totalement son énergie [41,42]. Ce type de modèles trouve donc sa place dans la description des systèmes où il y a vraiment possibilité de faire une distinction franche entre les coordonnées dites actives et inactives (donc le couplage entre ces deux groupes de coordonnées se doit d'être faible par construction). Cependant, il est judicieux de garder en tête que le passage du paquet d'ondes nucléaire d'une surface d'énergie potentielle à une autre à travers une intersection conique est gouverné par deux directions particulières qui induisent le transfert de population électronique. Il est donc nécessaire qu'elles soient bien décrites par les modes actifs. Or, puisque la dissipation vibrationnelle du système est sous-estimée, l'énergie contenue dans les modes actifs est surestimée. On va donc augmenter artificiellement la probabilité de transfert de population, ce qui va donc mal décrire la réactivité du système (le transfert de population se fera plus rapidement et plus efficacement) [43]. Dans les cas ou il est nécessaire de prendre en compte cette dissipation vibrationnelle, il a été montré que l'on pouvait hiérarchiser les différentes coordonnées pour décrire la

dissipation dans une région d'intersection conique à l'aide de groupes de trois coordonnées bien spécifiques appelées modes effectifs et dont l'importance décroît de groupe en groupe [44–47].

La méthodologie développée lors des travaux présentés dans cette thèse est différente. Nous avons voulu traiter toutes les dimensions du système au même niveau, c'est à dire sans avoir à les hiérarchiser ou les séparer en groupes de coordonnées. Les paramètres de nos modèles sont obtenus analytiquement, nous permettant d'éviter des procédures de « fit » (parfois non-linéaires) qui sont difficiles à mettre en œuvre pour décrire des systèmes photochimiques de grande taille et impliquant des déformations géométriques de grande amplitude. De plus, ce choix à été motivé par la possibilité d'utiliser une nouvelle méthode de dynamique quantique capable de traiter les systèmes chimiques de grande taille (plus d'une dizaine d'atomes) ; cette méthode, en cours de développement à Heidelberg, est appelée ML-MCTDH (Multilayer MultiConfigurational Time-Dependent Hartree).

Le premier chapitre propose une brève description du formalisme non-adiabatique et des intersections coniques ainsi que des méthodes de chimie quantique et de dynamique quantique utilisées lors de ces travaux. Le deuxième chapitre présente la méthodologie mise en place pour obtenir la représentation matricielle de l'hamiltonien électronique (surfaces d'énergie potentielle et couplages électroniques). Les deux derniers chapitres exposent les applications étudiées et sur lesquelles nous avons appliqué notre méthodologie : le chapitre trois concerne le transfert de proton dans l'état excité du 3-hydroxychromone et le quatrième chapitre porte quant à lui sur le transfert de charge intramoléculaire photoinduit dans l'aminobenzonitrile.

Chapitre I- Formalisme et Méthode

Ce Chapitre a pour but d'exposer les principes formels nécessaires à la compréhension des travaux exposés dans cette thèse ainsi que les méthodes utilisées dans la production de résultats numériques.

1- Formalisme

La fonction d'onde qui est solution de l'équation de Schrödinger moléculaire dépend des degrés de liberté des électrons et des noyaux :

$$i\hbar \frac{\partial}{\partial t} \left|\Psi^{\mathrm{mol}}(t, \boldsymbol{\mathcal{R}})\right\rangle = \widehat{H}^{\mathrm{mol}} \left|\Psi^{\mathrm{mol}}(t, \boldsymbol{\mathcal{R}})\right\rangle \qquad \textbf{Eq. 114}$$

La dépendance vis-à-vis des coordonnées électroniques est ici sous-entendue (notation en « kets » ; à l'inverse, elle est explicite vis-à-vis des coordonnées nucléaires, $\boldsymbol{\mathcal{R}}$. Dans la plupart des situations, le temps typique et l'énergie associés aux particules légères (les électrons) et les particules lourdes (les noyaux) diffèrent de plusieurs ordres de grandeur. La résolution du problème moléculaire peut donc être divisée en deux étapes : la première étape résout l'équation de Schrödinger indépendante du temps pour les électrons à noyaux fixes pour un état électronique α donné (ceci passe par des calculs de chimie quantique),

$$\widehat{H}^{\mathrm{elec}}(\boldsymbol{\mathcal{R}})|\Psi_\alpha; \boldsymbol{\mathcal{R}}\rangle = V_\alpha(\boldsymbol{\mathcal{R}})|\Psi_\alpha; \boldsymbol{\mathcal{R}}\rangle \qquad \textbf{Eq. 115}$$

Puis, la seconde étape consiste à résoudre l'équation de Schrödinger pour les noyaux (ce qui est obtenu par des calculs de dynamique quantique) dans le champ moyen adiabatique créé par les électrons, $V_\alpha(\boldsymbol{\mathcal{R}})$. Cette approximation est appelée l'approximation de Born-Oppenheimer pour un état électronique α donné.

On peut généraliser cette approche en deux étapes à un jeu fini d'états électroniques interagissant entre eux;

$$\left|\Psi^{\text{mol}}(t,\boldsymbol{\mathcal{R}})\right\rangle = \sum_{\alpha} \psi_{\alpha}^{\text{nuclear}}(t,\boldsymbol{\mathcal{R}})\left|\Psi_{\alpha};\boldsymbol{\mathcal{R}}\right\rangle \qquad \textbf{Eq. 116}$$

$$i\hbar\frac{\partial}{\partial t}\psi_{\alpha}^{\text{nuclear}}(t,\boldsymbol{\mathcal{R}}) = \sum_{\beta}\left[\delta_{\alpha\beta}\hat{T}(\boldsymbol{\mathcal{R}}) + \delta_{\alpha\beta}V_{\alpha}(\boldsymbol{\mathcal{R}}) + \widehat{\Lambda}_{\alpha\beta}(\boldsymbol{\mathcal{R}})\right]\psi_{\beta}^{\text{nuclear}}(t,\boldsymbol{\mathcal{R}}) \qquad \textbf{Eq. 117}$$

où $\widehat{\Lambda}_{\alpha\beta}$ est l'opérateur de couplage cinétique.

Le mouvement des noyaux induit des couplages non-adiabatiques, $D_{\alpha\beta}^{I}$, (aussi appelés couplages vibroniques) qui s'ecrivent au premier ordre:

$$D_{\alpha\beta}^{I}(\boldsymbol{\mathcal{R}}) = \left\langle \Psi_{\alpha};\boldsymbol{\mathcal{R}}\middle|\frac{\partial}{\partial\mathcal{R}^{I}}\Psi_{\beta};\boldsymbol{\mathcal{R}}\right\rangle, \qquad \textbf{Eq. 118}$$

et qui interviennent dans l'expression de $\widehat{\Lambda}_{\alpha\beta}$.

Les processus photoinduits impliquent souvent des couplages vibroniques qui sont responsables des processus de déclin ultrarapide entre un état électronique vers un état électronique plus bas en énergie (typiquement, une conversion interne entre états électroniques de même spin ; on parle de croisement intersystème entre états électroniques de spins différents mais le couplage est alors de type spin-orbite). Dans ce type de situation, l'excès d'énergie qui est donné à la molécule à travers l'absorption de la lumière et l'excitation électronique sont transformés en excitation vibrationnelle. Ce type de processus est gouverné par ce qu'on appelle des couplages non-adiabatiques entre la structure électronique et le mouvement des noyaux qui sont par définition au delà de l'approximation Born-Oppenheimer (adiabatique) [1,21,48,67,68]. Ces effets deviennent importants quand la différence d'énergie entre les deux états électroniques est du même ordre de grandeur que l'énergie vibrationnelle. De plus, les couplages non-adiabatiques divergent quand il y a dégénérescence (intersection conique, voir Fig. 115).

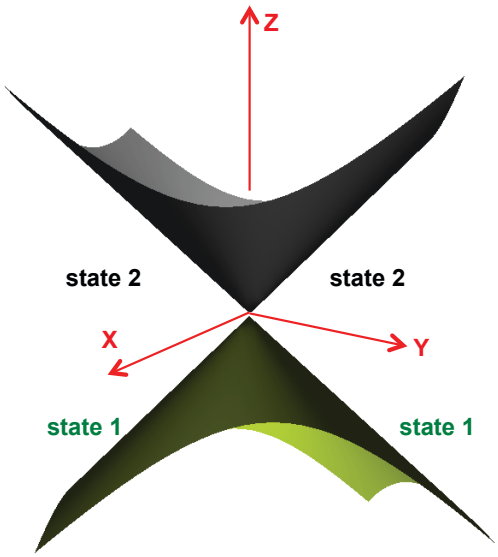

Fig. 115 Schéma du double cône d'une intersection conique entre les énergies de deux états électroniques dans un repère cartésien. Axe *z*: énergie, les axes *x* et *y* sont des coordonnées spécifiques définies dans la suite.

Pour cette raison (divergence du couplage non-adiabatique au point de dégénérescence), il est préférable de travailler dans une nouvelle base de représentation des états électroniques, appelé base diabatique, qui a pour particularité d'annuler le couplage cinétique pour le rendre potentiel. En d'autres termes, dans la base diabatique, l'hamiltonien électronique n'est plus diagonal,

$$H_{ij}^{\text{diab}}(\boldsymbol{\mathcal{R}}) = \left\langle \Phi_i; \boldsymbol{\mathcal{R}} \middle| \widehat{H}^{\text{elec}}(\boldsymbol{\mathcal{R}}) \middle| \Phi_j; \boldsymbol{\mathcal{R}} \right\rangle. \qquad \textbf{Eq. 119}$$

mais l'opérateur $\widehat{\Lambda}_{\alpha\beta}$ est négligeable.

Une intersection conique est donc un point $\boldsymbol{\mathcal{R}_0}$ où il y a dégénérescence entre deux états électroniques de même spin. La levée de dégénérescence est définie par deux vecteurs spécifiques:

$$\frac{\partial}{\partial \mathcal{R}^I} \Delta H(\boldsymbol{\mathcal{R}_0}) = x_I^{0(12)1}(\boldsymbol{\mathcal{R}_0}) \qquad \textbf{Eq. 120}$$

$$= \frac{\left\langle \Psi_2^0; \boldsymbol{\mathcal{R}_0} \middle| \frac{\partial}{\partial \mathcal{R}^I} \widehat{H}^{\text{elec}}(\boldsymbol{\mathcal{R}_0}) \middle| \Psi_2^0; \boldsymbol{\mathcal{R}_0} \right\rangle - \left\langle \Psi_1^0; \boldsymbol{\mathcal{R}_0} \middle| \frac{\partial}{\partial \mathcal{R}^I} \widehat{H}^{\text{elec}}(\boldsymbol{\mathcal{R}_0}) \middle| \Psi_1^0; \boldsymbol{\mathcal{R}_0} \right\rangle}{2},$$

$$\frac{\partial}{\partial \mathcal{R}^I} H_{12}(\boldsymbol{\mathcal{R}_0}) = x_I^{0(12)2}(\boldsymbol{\mathcal{R}_0}) = \left\langle \Psi_1^0; \boldsymbol{\mathcal{R}_0} \middle| \frac{\partial}{\partial \mathcal{R}^I} \widehat{H}^{\text{elec}}(\boldsymbol{\mathcal{R}_0}) \middle| \Psi_2^0; \boldsymbol{\mathcal{R}_0} \right\rangle.$$

$x_I^{0(12)1}$ est la difference des gradients et $x_I^{0(12)2}$ est le gradient du couplage. Ces deux vecteurs définissent un plan appelé espace de branchement.

Il faut savoir que les intersections coniques ne sont pas des points isolés sur la surface d'énergie potentielle mais qu'elles sont reliées par ce qu'on appelle une « couture », comme illustré dans la Fig. 2, où la dégénérescence est conservée.

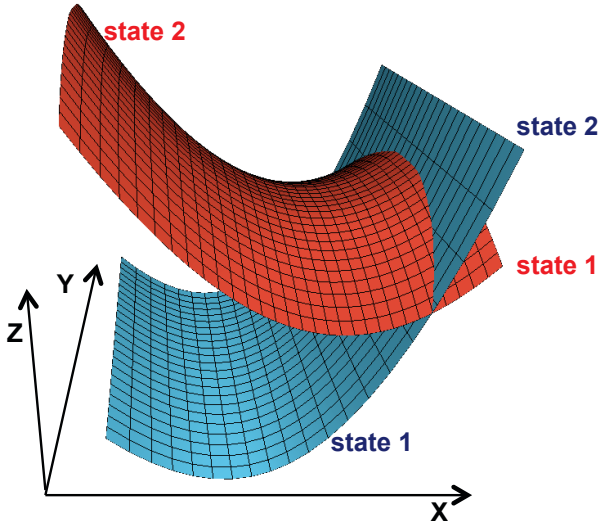

Fig. 116 Schéma d'une couture entre les deux états électroniques :*state 1* et *state 2* le long de deux coordonnées judicieuses *X* et *Y*, *Z* étant l'énergie.

Les intersections coniques peuvent être classifiées en deux types: « sloped » (Fig. 3, à gauche) et « peaked » (Fig. 3, à droite).

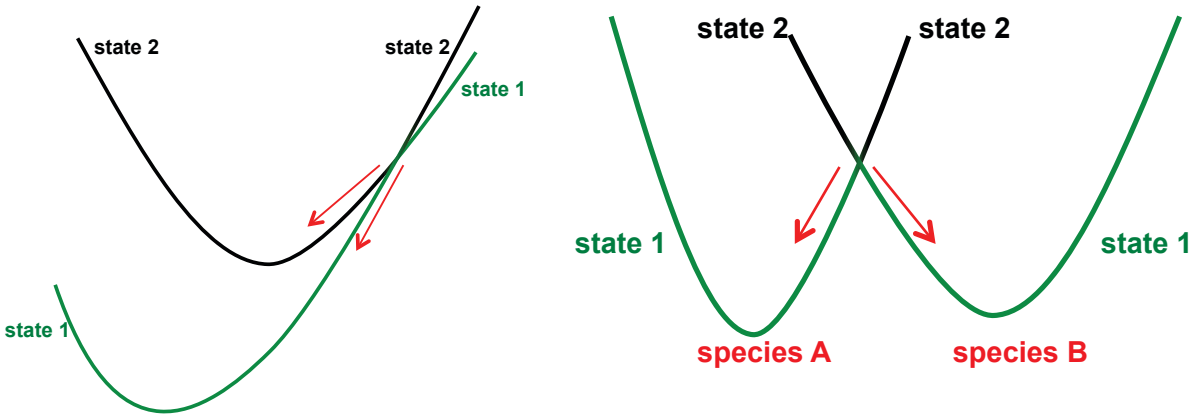

Fig. 117 A gauche: schéma d'une intersection conique « sloped ». A droite: schéma d'une intersection conique « peaked ».

2- Methodes

2-1. Chimie Quantique

Les méthodes de chimie quantique utilisées lors de ce travail de thèse, telles que le CASSCF ou la TD-DFT, ont pour particularité d'être adaptées à la description des états électroniques excités. Concernant la représentation du solvant, nous nous somme limités à un modèle de continuum diélectrique appelé PCM qui ne rend pas compte de la dynamique de relaxation du solvant et n'est pas adapté à la description d'interactions soluté-solvant fortes de type liaison hydrogène par exemple.

2-2. Dynamique Quantique

Concernant la dynamique quantique, comme nous l'avons déjà mentionné dans l'Introduction Générale, nous avons utilisé une méthode de dynamique, appelée ML-MCTDH, adaptée à la description de processus non-adiabatiques pour des systèmes de grande taille. Sa force réside dans l'écriture récursive de la fonction d'onde nucléaire comme une somme de produit de fonction à une dimension où les coefficients d'expansion sont dépendants du temps.

La première étape lorsque l'on fait de la dynamique quantique sur grille est de devoir choisir un jeu de coordonnées. Nous avons travaillé en coordonnées curvilignes; ceci permet ainsi de décrire les mouvements de grande amplitude (comme par exemple des torsions) d'une manière plus adaptée que si l'on utilisait des coordonnées rectilignes (ce choix de coordonnées permet donc de réduire les couplages dans l'expression du potentiel).

Cependant en coordonnées curvilignes l'expression de l'operateur énergie cinétique pour les noyaux n'est plus triviale (par rapport à son expression en coordonnées

rectilignes, cartésiennes par exemple). Nos opérateurs énergie cinétique des noyaux sont générés automatiquement dans n'importe quel jeu de coordonnées curvilignes à l'aide des programmes Tnum (expression numérique) [165] et Tana (expression analytique) [159,160]. Ces programmes ont été développés par D. Lauvergnat et M. Ndong du Laboratoire de Chimie Physique d'Orsay, France.

Chapitre II Modèle Quasidiabatique

Un des point principaux de ces travaux de thèse est le développement d'une méthodologie systématique et la plus automatique possible (mise en œuvre sous la forme du code PAnDA, i.e. Potentiel Analytique Diabatique Adiabatique) pour générer des surfaces d'énergie potentielle non-adiabatiques en toutes dimensions et ce afin de faire des calculs de dynamique quantique dans l'objectif d'étudier des processus photochimiques dans des molécules de grande taille.

Notre stratégie est fondée sur le modèle d'hamiltonien vibronique [20,110–112]. Nous l'avons étendu d'une manière similaire aux développements qui avaient préalablement été réalisés au sein de l'équipe de Montpellier par Loïc Joubert-Doriol et Joaquim Jornet-Somoza [205–207].

L'originalité de ce travail de thèse est d'avoir évité d'être dépendant du nombre de dimensions du système (nombre de degrés de liberté nucléaires). En d'autres termes, nous voulions éviter une méthodologie où la dimension du système devient la principale limitation comme cela peut s'avérer le cas dans les procédures de « fit » (méthode utilisée en général pour obtenir les paramètres du modèle) où le nombre de paramètres à « fitter » peut exploser avec la dimensionnalité du problème ; par exemple, pour un système à 12 dimensions dans un problème à deux niveaux électroniques, si on utilise un polynôme d'ordre quatre pour les expression des surfaces d'énergie potentielle et une expression linéaire pour le couplage électronique, le nombre de paramètres nécessaires est de 1924 [208]).

Pour pouvoir accomplir cette tâche, nous avons mis en place des relations analytiques entre la matrice hamiltonienne et ses dérivées exprimées dans la base quasidiabatique d'une part (utilisée pour les calculs de dynamique quantique) et la base adiabatique d'autre part (obtenue par les calculs de chimie quantique). Ainsi, une fois les calculs de chimie quantique nécessaires effectués, l'obtention des paramètres du modèle quasidiabatique est automatique et immédiate avec l'utilisation du programme PAnDA développé au cours de ce travail de thèse.

La description de paysages énergétiques complexes a demandé des modifications du modèle original d'hamiltonien vibronique le long de directions spécifiques ainsi que la définition de paramètres additionnels.

Chapitre III Colorants de type 3-HydroxyChromone

Nous avons effectué une étude théorique et computationnelle de la dynamique photoinduite du 3-HC (3-HydroxyChromone) en phase gaz ainsi que du 2T-3HC en solvant polaire et non polaire afin de proposer une rationalisation des observations expérimentales: Le 3-HC et le 2T-3HC (2-Thionyl-3-HydroxyChromone) présentent deux constantes de réaction pour le processus d'ESIPT (Excited States Intramolecular Proton Transfer) alors qu'une seule constante de réaction est observée pour le 2T-3HC en solvant non polaire. L'étude du 2T-3HC fait partie d'un projet en collaboration avec des expérimentateurs, Dr. Thomas Gustavsson (CEA, France) et Prof. Rajan Das (Tata Institute of Fundamental Research, India) [travaux de recherche en cours].

Nous avons fait des calculs de TD-DFT pour décrire la topographie des surfaces d'énergie potentielle du premier état électronique excité impliqué dans le processus photoinduit. Nous avons caractérisé une nouvelle intersection conique entre les états électroniques ππ* et nπ* qui est de géométrie plane et de symétrie C_s. Cette intersection conique a été localisée le long d'une direction approximativement parallèle à la coordonnée de relaxation du point de Franck-Condon (FC) vers le minimum énol (i.e. cis*).

Dans le 3-HC l'intersection conique « peaked » est dans la région de FC et on s'attend que le système passe à travers (ou tourne autour) de ce point de croisement pour, dans un second temps, effectuer l'isomérisation cis-trans de la forme énol. Ceci ouvre donc une nouvelle voie ultrarapide de conversion interne qui permet de peupler l'état nπ*.

En utilisant nos modèles en toutes dimensions de surfaces d'énergie potentielle couplées s'appuyant sur des énergies et géométries obtenues à l'aide de la méthode TD-DFT, nous avons réalisé des calculs de dynamique quantique avec la méthode ML-MCTDH [200]. Nos résultats indiquent clairement que l'état quasidiabatique nπ* est peuplé quasiment instantanément après la photoexcitation, ce qui montre donc que les couplages non-adiabatiques dans la région de FC sont cruciaux pour comprendre la dynamique du processus d'ESIPT. Il est à prévoir que cette caractéristique soit encore plus marquée en solvant polaire qu'en phase gaz grâce à la différence de stabilisation des états électroniques en fonction de leurs moments dipolaires. L'isomérisation cis-trans de la forme énol serait plus accessible (cette étude est actuellement en cours et demandera une meilleure description de la torsion de l'hydrogène dans les modèles de surfaces d'énergie potentielle).

Nos résultats sont cohérents avec les récentes observations expérimentales de Chevalier et al. [220], où l'implication possible de l'espèce trans à été mentionnée. Ceci suggère que le processus d'ESIPT, impliquant des mouvements se produisant dans le plan de la molécule soit en compétition avec l'isomérisation cis-trans de la forme énol (mouvement hors du plan).

Au contraire, dans le 2T-3HC l'intersection conique est « sloped » et n'est pas accessible depuis le point de FC; en d'autres termes, elle est trop haute en énergie pour avoir un impact notable sur le processus photoinduit. De plus, nos calculs en solvant polaire et non polaire ont permis de décrire le comportement spectral mais non la réactivité. Nous suspectons que les effets du solvant sur la barrière de réaction d'ESIPT demandent une approche plus sophistiquée que la méthode PCM pour être décrits correctement.

Chapitre IV Transfert de Charge Intramoléculaire dans l'Aminobenzonitrile

Lors de cette étude, nous avons effectué une étude théorique et computationnelle sur l'aminobenzonitrile (ABN) en phase gaz et dans le solvant acétonitrile afin de corroborer ou écarter l'hypothèse de Park et al. [343] et d'apporter des informations sur la nature des processus ultrarapides qui peuplent l'état électronique localement excité (LE) quasiment immédiatement après la photoexcitation initiale.

Ce travail fait partie d'un projet collaboratif avec le groupe du Dr. Mar Reguero et Pedro J. Castro de l'Universitat Rovira i Vigili in Tarragona, Espagne. Nous avons réalisé des calculs CASSCF(12,11)//CASPT2 afin de décrire la topographie des deux surfaces d'énergie potentielle couplées impliquées dans les premières étapes du processus de transfert de charge intramoléculaire (ICT). Une nouvelle intersection conique à été caractérisée entre les états électroniques S_2-CT (transfert de charge) et S_1-LE. Cette intersection conique est totalement plane et de symétrie C_{2v}. Elle a été optimisée le long d'une direction approximativement parallèle à la coordonnée de relaxation du point de FC vers le minimum plan de l'état S_2-CT (i.e. PICT).

Ceci ouvre donc une nouvelle voie ultrarapide de population de l'état LE par conversion interne. En utilisant les modèles en toutes dimensions de surfaces d'énergie potentielle couplées que nous avons développés lors de ce travail de thèse, qui dans un premier temps on été obtenus à l'aide de données CASSCF et ensuite raffinés à l'aide de données CASPT2, et ce en phase gaz et dans l'acetonitrile, nous avons ensuite effectué des calculs de dynamique quantique à l'aide de la méthode ML-MCTDH [200]. Nos résultats nous ont indiqué que l'espèce PICT se peuple directement après photoexcitation, pour ensuite peupler l'espèce LE par déclin non radiatif (sans émission de photon) à travers la nouvelle intersection conique plane, montrant ainsi l'absence du mouvement de « bending » dans le processus non radiatif. Il est à prévoir que cette caractéristique soit encore plus marqué en solvant polaire qu'en phase gaz grâce à la forte stabilisation de l'état à transfert de charge : l'intersection conique va donc être plus proche de la région de FC. Nos résultats sont cohérents avec les récentes observations expérimentales de

Park et al. [31] sur le système parent DMABN (diméthyle-ABN) où la première étape de désactivation est attribuée à un mouvement quasiplan qui va induire une conversion interne ultrarapide et la formation par voie directe de l'espèce LE en moins de 30 fs.

Ceci suggère que la voie de désactivation à travers la nouvelle intersection conique plane écarte la nécessité de mouvements hors du plan ou l'implication de l'état électronique πσ* dans le processus de transfert de charge intramoléculaire, au moins pendant les premières étapes de la réactivité.

Conclusion Générale

A l'occasion de cette thèse nous avons mis en place une méthodologie systématique pour générer des surfaces d'énergie potentielle couplées sous forme de modèles d'hamiltoniens vibroniques. Celle-ci a été appliquée à l'étude de la réactivité de processus photo-induits à l'aide de simulations utilisant une approche de dynamique quantique en cours de développement appelée ML-MCTDH spécifiquement dédiée au traitement des systèmes de grande taille.

L'originalité de ce travail de thèse a été de mettre en place une méthodologie permettant l'obtention automatique des paramètres du modèle (base diabatique) à l'aide de relations analytiques explicites impliquant directement les données obtenues par les calculs de chimie quantique (représentation adiabatique). Cette stratégie permet ainsi de s'affranchir de certaines limitations des modèles d'hamiltoniens vibroniques, notamment concernant la dimensionnalité du problème. En effet, ce dernier point peut s'avérer l'étape limitante dans les procédures plus habituelles d'ajustement non linéaire de paramètres (*fits*). Au contraire, notre méthodologie n'est pas limitée par le nombre de degrés de liberté du système et peut ainsi être appliquée à l'étude de la réactivité par dynamique quantique de systèmes considérés comme étant de grande taille (i.e. plus d'une dizaine de degrés de liberté). Ceci nous a mené à développer le code PAnDA qui permet de générer automatiquement les surfaces d'énergies potentielles couplées dans un format adapté à la méthode de dynamique quantique que nous avons utilisée (i.e. ML-MCTDH).

D'un point de vue technique, nos modèles s'inspirent des modèles d'hamiltoniens vibroniques développés par Köppel et al. [20,110–112] dans lesquels les surfaces d'énergie potentielle en représentation diabatique sont en général exprimées comme des formes quadratiques (deuxième ordre). Cependant, en l'état, de tels modèles sont limités à la description de processus (quasi)harmoniques. Pour le traitement de cas moins harmoniques, nous avons étendu cette description et mis en place différentes stratégies pour modifier le modèle diabatique quadratique initial en introduisant une certaine part d'anharmonicité. Comme il est visible dans les chapitres d'applications (Chapitres III et IV), les modèles ont été élaborés dans l'optique d'être facilement adaptables à la description de différents types de paysages énergétiques, plus ou moins complexes. Ils ont donc ainsi permis la production dans un temps "raisonnable" d'une étude prenant en compte toutes les dimensions du système et les effets quantiques des noyaux sur la photo-reactivité du processus non-adiabatique en question. Ces stratégies sont présentées formellement dans les Chapitres I et II, et appliquées à l'étude de deux processus photo-induits: le transfert de charge dans l'aminobenzonitrile et le transfert de proton du 3-hydroxychromone.

L'étude du transfert de charge dans l'aminobenzonitrile à été réalisée en collaboration avec le groupe du Dr. Mar Reguero et Pedro J. Castro (Universitat Rovira i Vigili, Tarragona, Espagne) qui ont réalisé une partie des calculs de chimie quantique. Lors de cette étude, nous avons mis en place un modèle qui a permis la description d'une "couture" (*seam*) connectant deux types différents d'intersections coniques entre les deux mêmes états électroniques. D'un point de vue dynamique, ce type de modèle nous a permis de comparer l'efficacité des deux types de chemins photo-réactionnels. Ceci nous a mené à l'une des conclusions majeures de ce chapitre vis-à-vis de la chimie du système: le chemin réactionnel majoritairement responsable du transfert de population non-radiatif entre les deux premiers états excités n'est pas le chemin de plus basse énergie. La dynamique (i.e. description du mouvement des noyaux) est donc un outil essentiel à la compréhension de la réactivité des processus photo-induits.

Nous avons également étudié l'effet du solvant sur le processus en question. Rappelons ici que l'état qui absorbe à FC est un état à transfert de charge ; il va donc être stabilisé

en présence d'un solvant polaire, ce qui va induire une plus grande accessibilité (énergies plus basses) des intersections coniques au cours de la photo-réaction. Nous avons pu observer que dans les limites de notre description (solvant implicite décrit avec la méthode PCM), la présence du solvant accentuait les résultats obtenus en phase gaz mais que cependant la stabilisation de l'état à transfert de charge n'était pas assez importante pour modifier la réactivité d'un point de vue qualitatif : l'intersection conique n'a pas de changé de nature et la topographie des surfaces d'énergie potentielle est restée globalement la même (et ce, que le solvant soit relaxé ou non sur l'état excité).

L'étude du transfert de proton photo-induit du 3-hydroxychromone nous a demandé une analyse préliminaire de chimie quantique, ce qui nous a permis de mettre en évidence pour la première fois l'existence d'une intersection conique dans la région de FC mais aussi de rationaliser le processus d'isomérisation cis-trans qui s'avère plus complexe que ce que la littérature pouvait sous-entendre. La question posée lors de cette étude concernait l'observation expérimentale de deux temps de réaction pour le transfert de proton. Nous avons pu rationalisé ceci à l'aide de calculs de dynamique quantique. Nous avons pu montrer que la présence d'une intersection conique dans la région de FC avait un impact non négligeable sur la réactivité car les couplages non-adiabatiques entre S_1 et S_2 y sont non négligeables. Ceci va donc induire un retard d'une partie du système qui va partiellement se délocaliser le long de l'isomérisation cis-trans. En d'autres termes, nos calculs ont montré qu'effectivement l'isomérisation cis-trans était un chemin en compétition avec le transfert de proton comme le supposait la littérature. En revanche, ce mécanisme, plus complexe que prévu, implique plus d'états électroniques que ce qui pouvait être attendu.

Cependant, le modèle d'hamiltonien électronique utilisé pour obtenir ces résultats ne décrit pas l'isomérisation cis-trans dans sa totalité. En effet, le mouvement associé à cette isomérisation (torsion de l'hydrogène) n'est, à l'heure actuelle, pas décrit dans notre modèle comme un mouvement périodique mais comme un mouvement lié. Cette étape nécessite d'adapter les expressions analytiques des paramètres du modèle diabatique, ce qui est actuellement un travail en cours.

Comme nous venons de le souligner, ces modèles nécessitent encore un certain nombre de développements qui s'orientent principalement vers : comme déjà suggéré, l'implémentation de fonctions périodiques et la possibilité de décrire plusieurs intersections coniques entre des états électroniques différents (la difficulté concerne l'impossibilité de séparer simplement l'hamiltonien électronique diabatique comme une série de problèmes à deux états indépendants). Ce point permettrait de pouvoir augmenter le nombre d'état diabatiques pour décrire un même état adiabatique (Cf. *Conclusion and Outlooks* Chaptitre IV sur l'aminobenzonitrile) et ainsi de développer une nouvelle stratégie de description de l'anharmonicité. Ceci pourrait également assurer une meilleure description locale des intersections coniques et de leurs espaces de branchement (*branching spaces*) et donnerait, en tout état de cause, plus de flexibilité dans la description des surfaces d'énergie potentielle couplées ayant des topographies complexes.

Une des perspectives à long terme sur le développement de ce type de méthodologie serait de pouvoir la combiner avec d'autres méthodes pour continuer à aller vers le traitement de systèmes de plus grande taille et plus complexes (i.e. en interaction forte avec un environnement intra et/ou intermoléculaire). On peut ainsi concevoir une stratégie hiérarchisée avec une description précise du système et une modélisation plus approchée de la dynamique cet environnement et de ses effets sur le système (par des méthodes de dynamique quantique utilisant des modes effectifs ou par des méthodes de dynamique plus approximatives dans le traitement quantique des noyaux du type DD-vMCG ou « ab initio multiple spawning »).

Appendix F- Paper on the Intramolecular Charge Transfer in Aminobenzonitrile

THE JOURNAL OF PHYSICAL CHEMISTRY Letters

Letter

pubs.acs.org/JPCL

Intramolecular Charge Transfer in 4-Aminobenzonitrile Does Not Need the Twist and May Not Need the Bend

Aurelie Perveaux,[†,‡] Pedro J. Castro,[§] David Lauvergnat,[†] Mar Reguero,*[,§] and Benjamin Lasorne*[,‡]

[†]Laboratoire de Chimie Physique (UMR 8000), CNRS, Université Paris-Sud, 91405 Orsay, France

[‡]Institut Charles Gerhardt (UMR 5253), CNRS, Université de Montpellier, 34095 Montpellier, France

[§]Departament de Química Física i Inorgànica, Universitat Rovira i Virgili, 43007 Tarragona, Spain

Supporting Information

ABSTRACT: A study combining accurate quantum chemistry and full-dimensional quantum dynamics is presented to confirm the existence of an ultrafast radiationless decay channel from the charge-transfer state to the locally excited state in 4-aminobenzonitrile. This intramolecular charge-transfer pathway proceeds through a newly found planar conical intersection, and it is shown to be more efficient in the presence of acetonitrile than in the gas phase. Our results are consistent with recent experimental observations.

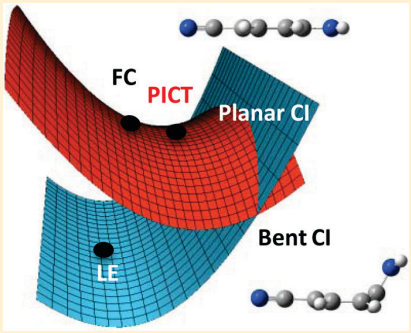

Intramolecular charge transfer (ICT) in electron donor−acceptor molecules is a process of high interest that has given place to a strong debate over the last decades. A large amount of experimental and theoretical studies have been devoted to this kind of systems, often focused on the aminobenzonitrile family and particularly on the parent system, 4-aminobenzonitrile (ABN), and on its *N*-dimethyl derivative, DMABN.[1] The small size and simple architecture of ABN and DMABN have made them prototype systems for studying ICT phenomena. They are particularly interesting because, despite their similarity, their luminescent patterns are quite different; while ABN only shows the normal fluorescence band in any environment, DMABN exhibits normal fluorescence in nonpolar solvents but dual fluorescence in polar ones.[2,3] This indicates that the different photochemical behaviors are not due to different characters of the electronic states but to changes induced by the polar environment.

Despite the large amount of time and effort invested in their study, there is still a very lively controversy involving these systems. It is well-established that the normal band is originated from a locally excited (LE) state, while the anomalous band is due to a charge-transfer (CT) state of high dipole moment that is stabilized in polar solvent environments. The exact structures of the species responsible for the anomalous band and the mechanism that populates them are unclarified questions due to contradictory arguments based on both experimental observations and theoretical calculations, which support different models and hypotheses.

Mainly, three models are in the lead of the controversy regarding the structure of the luminescent CT species: the planar ICT model (PICT),[4] the twisted one (TICT),[5] and the partially twisted or pretwisted one (pTICT).[6] It seems sufficiently proved that the PICT and TICT species do in fact correspond to two minimum-energy points of the potential energy surface (PES) of the excited CT state in both ABN and DMABN, but their role in the fluorescence spectra is less clear. A fourth model, the rehybridized ICT (RICT),[7] is thought to be a stable species of a $\pi\sigma^*$ excited state but is nowadays discarded as a luminescent species.

Regarding the ICT mechanism, it is well-established that the initial excitation populates first the S_2 state of CT character. The subsequent sequence of steps along the LE or CT PES until the luminescent species are populated is still under discussion. Computational works indicate the existence of a conical intersection (CI) seam between the LE and CT PES that allows internal conversion to occur over a large range of molecular geometries.[8] Experimental works suggest initial population of the LE state and later equilibration with a CT state.[9] It has even been suggested the involvement of the $\pi\sigma^*$ state in the early stages of the ICT process,[10] but recent works present arguments to discard this possibility.[11,12] This is in fact a point that deserves to be clarified.

Park et al. have published a recent paper reporting a study of highly time-resolved fluorescence spectra (TRFS) over the whole emission region of DMABN in acetonitrile.[13] The precise measurements of this study give information about the dynamics of the ICT process free from the interferences of the

Received: January 27, 2015
Accepted: March 24, 2015

DOI: 10.1021/acs.jpclett.5b00162
J. Phys. Chem. Lett. 2015, 6, 1316−1320

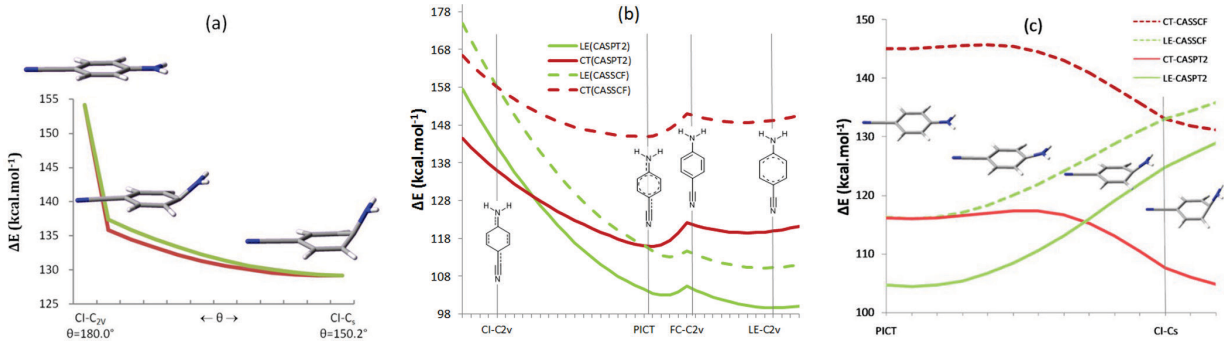

Figure 1. SA2-CASSCF energy profiles of the two lowest-energy excited states along the S_2/S_1 CI seam joining CI-C_{2v} and CI-C_s (panel a). CASSCF and CASPT2 energy profiles of the CT and LE states along the C_{2v} pathway (panel b) and from PICT to CI-C_s (panel c). Gray lines show the location of the geometries of the critical points optimized at the CASSCF level, used as fixed points for the interpolations.

solvent reorganization and vibrational relaxation dynamics that occur on the same time scale. The experimental techniques used in that work also give access to an analysis of the ultrafast events that occur within the first few femtoseconds. From their observations, it is concluded that, after photoexcitation to the S_2 state, both the CT and LE states are populated in less than 30 fs for geometries that are still quasiplanar. This early internal conversion process is the main focus of the present Letter. Subsequent processes from the initial LE and ICT species lead to the formation of partially twisted and fully twisted ICT species that give place to the anomalous fluorescence band. A similar ultrafast interval conversion was also proposed in a previous work by McCamant et al.[14,15]

Computational studies carried out on ABN and DMABN have shown that the topographies of the PESs of the low-lying states of both systems are similar, but small energetic changes induce a different interplay between the LE and CT species that leads to different luminescent patterns. The initial steps of the photochemistry, though, are expected to be analogous in both systems; therefore, the experimental conclusions derived by Park et al. for DMABN must hold in a qualitative way also for ABN, at least during the early stages when only quasiplanar deformations are involved.

In this Letter, we have performed a computational study on ABN in the gas phase and acetonitrile in order to corroborate or discard the hypothesis of Park et al. and provide further information about the ultrafast process that populates the LE state almost immediately after the initial photoexcitation. We have carried out a CASSCF(12,11)/cc-pVDZ study to describe the topography of both coupled PESs involved in the initial steps of the process using the Gaussian 09 package[16] In this way, we have established the paths and regions of the surfaces that determine the mechanism of the ultrafast process under study (<30 fs). The energies of these regions were then recalculated at the CASPT2 level with the Molcas 7 package[17] to include the effect of dynamic correlation in the calculations. Using full-dimensional models of coupled PESs, first based on CASSCF energies and geometries and further refined to match CASPT2 data, both in the gas phase and in acetonitrile, we have run quantum dynamics simulations with the multilayer version[18] of the multiconfiguration time-dependent Hartree[19] (ML-MCTDH) method (computational details are provided in the Supporting Information (SI)).

A new CI has been characterized between the S_2-CT state and the S_1-LE one for totally planar geometries (C_{2v} symmetry), along a direction approximately parallel to the relaxation coordinate from the Franck−Condon (FC) point to the S_2-CT minimum. This opens a new channel for an ultrafast population of the LE state upon internal conversion, that could discard the need for out-of-plane motions or the involvement of the $\pi\sigma^*$ state in the CT process, at least during its early stages.

First, CASSCF/CASPT2 calculations in the gas phase show that light absorption occurs from a double-well region in the ground-state PES. The two equivalent minima, denoted FC-C_s, have a wagged geometry belonging to C_s point group symmetry. Both points are connected through a planar C_{2v} transition state (TS), for which the transition vector corresponds mainly to the pyramidalization of the amino group. This planar TS, named FC-C_{2v}, has a small energy barrier of 1.4 kcal·mol^{-1} (0.06 eV; 490 cm^{-1}, CASPT2 energies) (see Tables S1 and S2 in the SI). As aforementioned, S_1 and S_2 in the FC region correspond to the LE and CT states, respectively. Their electronic characters are determined by their orbital populations and confirmed with the values of their dipole moments (5.02 [5.30] D for S_1-LE and 11.30 [11.51] D for S_2-CT; CASSCF values within square brackets). The S_1-LE PES also has a double-well shape. The corresponding TS (LE-C_{2v}) is 1.3 kcal·mol^{-1} (0.06 eV; 455 cm^{-1}) higher than the LE wagged minima, which are 101.9 kcal·mol^{-1} (4.42 eV; dipole: 5.11 [5.40] D) above the ground-state ones. The S_2-CT PES shows a flat single well with a planar C_{2v} minimum denoted PICT, 118.8 kcal mol^{-1} (5.15 eV; dipole: 11.71 [11.91] D) above the ground state FC-C_s minima (PES cuts along the pyramidalization coordinate for the three states are depicted in Figure S1 of the SI). The large oscillator strength found for the transition to S_2-CT (from the FC-C_{2v} TS as well as from the FC-C_s wagged minima; see Table S1, SI) indicates that this is the most optically active one. The corresponding excitation energies (107.8 and 125.5 kcal mol^{-1} in the gas phase for LE and CT, respectively; $\Delta E(S_1-S_2)$ = 17.7 kcal mol^{-1}) are in reasonable agreement with experimental results (108.8 kcal mol^{-1} maximum of the absorption band and $\Delta E(S_1-S_2)$ = 13.6 kcal mol^{-1} in *n*-hexadecane).[20] Initial relaxation on the S_2-CT state (the FC gradient obtained at the CASSCF level depicted in Figure S2 of the SI) is governed mainly by an in-plane quinoidal coordinate and leads directly to the PICT species located 6.7 kcal·mol^{-1} (0.29 eV) below the excitation energy.

Previous works have reported a minimum-energy CI point between the S_1-LE and S_2-CT states[8,21] of nonplanar C_s geometry (CI-C_s; see Figure S3 of the SI) with a bent ring and a slightly pyramidalized amino group. Here, we report a new CI belonging to C_{2v} point group symmetry with a planar

DOI: 10.1021/acs.jpclett.5b00162
J. Phys. Chem. Lett. 2015, 6, 1316−1320

geometry, denoted CI-C_{2v}. This point has been optimized at the CASSCF level, but its position and energy slightly shift when recalculating the energy profiles at the CASPT2 level. The relocated crossing point is 3.8 kcal·mol^{-1} (0.16 eV) above the energy of the S_2-CT state at the FC-C_s geometry and 10.5 kcal·mol^{-1} (0.45 eV) above the PICT minimum (see Table S2 for CASPT2 energies and Figure S4 for CASSCF results, SI). We have checked that the initial relaxation that leads from FC-C_{2v} on S_2-CT to the PICT minimum (see Figure S2 of the SI) further leads to CI-C_{2v}. This indicates that access to this CI is favored due to the momentum acquired by the nuclei during initial relaxation. This new CI is thus easily accessible according to both energetic and geometric criteria, and deactivation through this point is expected to be ultrafast.

Given that the CI-C_s point (optimized at the CASSCF level and also relocated at the CASPT2 level) is 14.2 kcal.mol^{-1} (0.62 eV) lower than the CI-C_{2v} point, it is relevant to characterize the CI seam that joins these two points. This was achieved along a relaxed-interpolated coordinate, optimizing CIs for fixed values of the bending angle (defined by the out-of-plane motion of the carbon atom bonded to the amino group). This was calculated at the CASSCF level only because such optimizations are not available at the CASPT2 level. However, we can safely assume that the landscape does not change qualitatively when dynamic correlation is included, as proved by the existence of both CI-C_{2v} and CI-C_s relocated points at the CASPT2 level. Figure 1a shows that the CASSCF seam is continuous and decreases monotonically as both points belong to the same degenerate subspace. The S_1-LE and S_2-CT states are B_2 and A_1 at the C_{2v} geometries, respectively (using Mulliken's convention where the x-axis is perpendicular to the molecular plane). The bending deformation that lowers the symmetry to C_s is B_1, such that S_1-LE and S_2-CT become A″ and A′, respectively, with no further coupling. The derivative coupling is a B_2/A″ Kekulé-like motion all over the seam (see Figure S5 of the SI). Internal conversion can thus take place at any point of the seam and implies activation of motions that break the left/right symmetry of the molecule. However, the topographies of both crossings are different; CI-C_{2v} is sloped (see Figure 1b), whereas CI-C_s is peaked (see Figure 1c). These characteristics have been determined from the profiles of the PESs of the LE and CT states calculated between the geometries of the critical points optimized at the CASSCF level. Including electron dynamic correlation (CASPT2 calculations) induces an energy shift all along each surface that is not constant but quite smooth for both. This results in relative stabilization of the CT state with respect to the LE state. Consequently, the critical points at the CASPT2 level are not located at the same geometries as those at the CASSCF level. The most affected ones are the CIs (see Figure S6 of the SI for comparison of results). The shape of the surfaces, though, is quite similar at both levels, as shown in Figure 1b,c. In addition, CASPT2 calculations show that the CI-C_{2v} region is even more accessible from the FC region compared to CASSCF calculations. In any case, the different topographies of both CI-C_s and CI-C_{2v} crossings and the fact that the CI-C_s geometry is farther from the FC region than the CI-C_{2v} one are expected to make the bent deactivation pathway though CI-C_s occur later than the planar one through CI-C_{2v} and less in favor of populating the LE minimum.

Describing experimental conditions more accurately requires the solvent environment to be taken into account. We modeled the acetonitrile solvent using the polarizable continuum model (PCM) approach. Modeling solvent effects in nonadiabatic phenomena has an additional difficulty given the different time scales of the various processes undergone by the solute and the finite relaxation time required by the solvent to equilibrate with the changing geometry or electronic distribution of the solute. To account for different situations, in the PCM model, the reaction field is partitioned into a fast component, always equilibrated, and a slow component, only equilibrated for stable species or slow processes. Vertical transitions are considered instantaneous; therefore, it is assumed that only the fast component of the solvent field will be able to equilibrate with the new electronic distribution of the state reached after the transition. This is considered as an extreme case (as opposed to the equilibrated solvent) that can be properly addressed computationally, and this is the model assumed in this work to compute excitation energies. On the other hand, the relaxation and subsequent processes that take place on the excited state (for example, internal conversion) can proceed on the same time scale as the solvent reequilibration, which makes impossible an adequate modeling. Given that we want to study the evolution of our system along the CT PES populated after the initial excitation, we have opted for equilibrating the solvent for this excited state and calculated the LE energies with the fast component equilibrated for this state but the slow component equilibrated for the CT state. The profiles of Figure 1b recalculated at both CASSCF and CASPT2 levels using this model (see Figure S7 of the SI) show that the global shape of the surfaces is not changed by the solvent, although the CT state is stabilized preferentially due to its larger dipole moment.

Optimizing a CI within the PCM approach is not an available technique at the moment. We thus identified a shifted crossing point by recomputing the energies in the presence of acetonitrile along a linear interpolation pathway from the FC point to the CI-C_{2v} point obtained in the gas phase (see Figure 2). Our results show that the solvent stabilizes the CT state

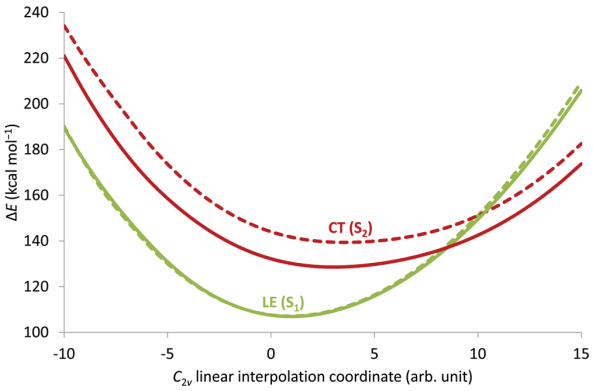

Figure 2. C_{2v} pathway along a linear interpolation coordinate Q linking the FC point (Q = 0) to the CI-C_{2v} point (Q = 10) in the gas phase (dashed lines) and in acetonitrile (plain lines). Energy differences are given with respect to the ground-state minimum. Level of theory: SA2-CASSCF(12,11)/cc-pVDZ.

with respect to the LE state by about 5 kcal·mol^{-1} (0.2 eV). This effect is not strong enough to invert the energies, and the PICT minimum still belongs to the S_2 state. In addition, the energy of the CI-C_{2v} point with respect to the FC point is lower than that in the gas phase.

DOI: 10.1021/acs.jpclett.5b00162
J. Phys. Chem. Lett. 2015, 6, 1316−1320

Consequently, the shifted CI-C_{2v} point appears even closer to the PICT minimum when the effect of the solvent is considered. Thus, internal conversion from PICT to LE is expected to be faster in acetonitrile than that in the gas phase. To check this hypothesis, quantum dynamics calculations were run in full dimensionality (39 internal degrees of freedom) with ML-MCTDH.[18] The electronic Hamiltonian matrix was expressed using a vibronic coupling Hamiltonian model[22] whereby quasidiabatic PESs and coupling terms are expressed as quadratic expansions along the nuclear coordinates (further details are provided in the SI). Time-resolved electronic populations were calculated over 160 fs for coupled PESs based on CASSCF data and over 70 fs for coupled PESs based on CASPT2 data. They are depicted in Figures 3 and 4, respectively, both in the gas phase and in acetonitrile.

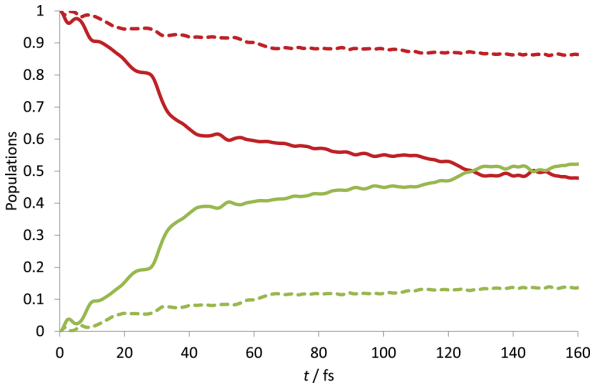

Figure 3. Evolution of the electronic populations (red: CT; green: LE) as functions of time in the gas phase (dashed lines) and in acetonitrile (plain lines). Coupled PESs based on CASSCF data.

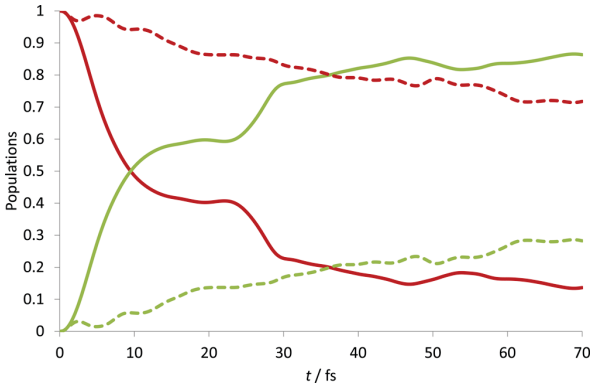

Figure 4. Evolution of the electronic populations (red: CT; green: LE) as functions of time in the gas phase (dashed lines) and in acetonitrile (plain lines). Coupled PESs based on CASPT2 data.

Figures 3 and 4 show that internal conversion starts immediately in all situations. Including electron dynamic correlation (CASPT2 data) only amplifies the conclusions that could be drawn from a less accurate description based on CASSCF data. The CI-C_{2v} point is reached very rapidly (after a few fs), and we observe significant ultrafast radiationless decay from PICT to LE (transfer of population) within the planar channel. The solvent makes the transfer of population more efficient than that in the gas phase; inversion of population (50%:50%) is observed around 10 fs in acetonitrile, while the population of LE has only reached 6% in the gas phase (CASPT2-based results; see Figure 4).

Our calculations for ABN in the gas phase and in a polar solvent environment clearly indicate that the PICT species is populated right after photoexcitation where it can radiationlessly decay to the LE species very early through a newly found, planar CI. This process is even more efficient in the presence of acetonitrile than that in the gas phase. Such computational results are consistent with the recent experimental observations of Park et al. on the parent system DMABN, where the first deactivation step is attributed to quasiplanar motions inducing ultrafast internal conversion and direct formation of LE in less than 30 fs.

■ ASSOCIATED CONTENT

Supporting Information

Additional quantum chemistry data calculated at the CASSCF and CASPT2 levels of theory and further details on the coupled PES models used to perform quantum dynamics simulations. This material is available free of charge via the Internet at http://pubs.acs.org.

■ AUTHOR INFORMATION

Corresponding Authors

*E-mail: mar.reguero@urv.cat (M.R.).
*E-mail: benjamin.lasorne@univ-montp2.fr (B.L.).

Notes

The authors declare no competing financial interest.

■ ACKNOWLEDGMENTS

P.J.C. and M.R. thank the financial support provided by the Spanish Administration (CTQ2011-23140), the Generalitat de Catalunya (2014SGR199 and Xarxa d'R+D+I en Química Teòrica i Computacional, XRQTC), and the European Union (COST Action CODECS CM1002).

■ REFERENCES

(1) Grabowski, Z. R.; Rotkiewicz, K.; Rettig, W. Structural Changes Accompanying Intramolecular Electron Transfer: Focus on Twisted Intramolecular Charge-Transfer States and Structures. *Chem. Rev.* **2003**, *103*, 3899−4032.

(2) Rettig, W. Charge Separation in Excited States of Decoupled Systems—TICT Compounds and Implications Regarding the Development of New Laser Dyes and the Primary Process of Vision and Photosynthesis. *Angew. Chem., Int. Ed. Engl.* **1986**, *25*, 971−988.

(3) Gómez, I.; Castro, P. J.; Reguero, M. Insight into the Mechanisms of Luminescence of Aminobenzonitrile and Dimethylaminobenzonitrile in Polar Solvents. An Ab Initio Study. *J. Phys. Chem. A* **2015**, *119*, 1983−1995.

(4) Zachariasse, K. A.; Grobys, M.; von der Haar, Th.; Hebecker, A.; Il'ichev, Yu. V.; Jiang, Y.-B.; Morawski, O.; Kühnle, W. Intramolecular Charge Transfer in the Excited State. Kinetics and Configurational Changes. *J. Photochem. Photobiol., A* **1996**, *102*, 59−70.

(5) Rotkiewicz, K.; Grellmann, K. H.; Grabowski, Z. R. Reinterpretation of the Anomalous Fluorescence of p-N,N-Dimethylamino-benzonitrile. *Chem. Phys. Lett.* **1973**, *19*, 315−318, 212.

(6) Coto, P. B.; Serrano-Andres, L.; Gustavsson, T.; Fujiwara, T.; Lim, E. C. Intramolecular Charge Transfer and Dual Fluorescence of 4-(Dimethylamino)benzonitrile: Ultrafast Branching Followed by a Two-Fold Decay Mechanism. *Phys. Chem. Chem. Phys.* **2011**, *13*, 15182−15188.

(7) Sobolewski, A. L.; Domcke, W. Charge Transfer in Aminobenzonitriles: Do They Twist? *Chem. Phys. Lett.* **1996**, *250*, 428−436.

DOI: 10.1021/acs.jpclett.5b00162
J. Phys. Chem. Lett. 2015, 6, 1316−1320

(8) Gómez, I.; Reguero, M.; Boggio-Pasqua, M.; Robb, M. A. Intramolecular Charge Transfer in 4-Aminobenzonitriles Does Not Necessarily Need the Twist. *J. Am. Chem. Soc.* **2005**, *127*, 7119−7129.
(9) Druzhinin, S. I.; Ernsting, N. P.; Kovalenko, S. A.; Lustres, L. P.; Senyushkina, T. A.; Zachariasse, K. A. Dynamics of Ultrafast Intramolecular Charge Transfer with 4-(Dimethylamino)benzonitrile in Acetonitrile. *J. Phys. Chem. A* **2005**, *110*, 2955−2969.
(10) Ramos, R. C.; Fujiwara, T.; Zgierski, M. Z.; Lim, E. C. Photophysics of Aromatic Molecules with Low-Lying $\pi\sigma^*$ States: Excitation-Energy Dependence of Fluorescence in Jet-Cooled Aromatic Nitriles. *J. Phys. Chem. A* **2005**, *109*, 7121−7126.
(11) Galván, I. F.; Martín, M. E.; Aguilar, M. A. On the Absorption Properties of the Excited States of DMABN. *Chem. Phys. Lett.* **2010**, *499*, 100−102.
(12) Zachariasse, K. A.; Druzhinin, S. I.; Kovalenko, S. A.; Senyushkina, T. Intramolecular Charge Transfer of 4-(Dimethylamino)benzonitrile Probed by Time-Resolved Fluorescence and Transient Absorption: No Evidence for Two ICT States and a $\pi\sigma^*$ Reaction Intermediate. *J. Chem. Phys.* **2009**, *131*, 224313.
(13) Park, M.; Kim, C. H.; Joo, T. Multifaceted Ultrafast Intramolecular Charge Transfer Dynamics of 4-(Dimethylamino)-benzonitrile (DMABN). *J. Phys. Chem. A* **2012**, *117*, 370−377.
(14) Rhinehart, J. M.; Mehlenbacher, R. D.; McCamant, D. Probing the Charge Transfer Reaction Coordinate of 4-(Dimethylamino)-benzonitrile with Femtosecond Stimulated Raman Spectroscopy. *J. Phys. Chem. B* **2010**, *114*, 14646−14656.
(15) Rhinehart, J. M.; Challa, J. R.; McCamant, D. W. Multimode Charge-Transfer Dynamics of 4-(Dimethylamino)benzonitrile Probed with Ultraviolet Femtosecond Stimulated Raman Spectroscopy. *J. Phys. Chem. B* **2012**, *116*, 10522−10534.
(16) Frisch, M. J.; Trucks, G. W.; Schlegel, H. B.; Scuseria, G. E.; Robb, M. A.; Cheeseman, J. R.; Scalmani, G.; Barone, V.; Mennucci, B.; Petersson, G. A.; et al. *Gaussian 09*, revision D.01; Gaussian, Inc.: Wallingford, CT, 2009.
(17) Aquilante, F.; De Vico, L.; Ferré, N.; Ghigo, G.; Malmqvist, P. Å.; Neogrády, A.; Bondo Pedersen, T.; Pitoňák, M.; Reiher, M.; Roos, B. O.; et al. Software News and Update. MOLCAS 7: The Next Generation. *J. Comput. Chem.* **2010**, *31*, 224−247.
(18) Vendrell, O.; Meyer, H.-D. Multilayer Multiconfiguration Time-Dependent Hartree Method: Implementation and Applications to a Henon−Heiles Hamiltonian and to Pyrazine. *J. Chem. Phys.* **2011**, *134*, 044135.
(19) Beck, M. H.; Jäckle, A.; Worth, G. A.; Meyer, H.-D. The Multiconfiguration Time-Dependent Hartree (MCTDH) Method: A Highly Efficient Algorithm for Propagating Wavepackets. *Phys. Rep.* **2000**, *324*, 1−105.
(20) Druzhinin, S. I.; Demeter, A.; Galievsky, V. A.; Yoshihara, T.; Zachariasse, K. A. Thermally Activated Internal Conversion with 4-(Dimethylamino)benzonitrile, 4-(Methylamino)benzonitrile, and 4-Aminobenzonitrile in Alkane Solvents. No Correlation with Intramolecular Charge Transfer. *J. Phys. Chem. A* **2003**, *107*, 8075−8085.
(21) Amatatsu, Y. Theoretical Study on the Photochemical Behavior of 4-(Dimethylamino)benzonitrile. *J. Phys. Chem. A* **2005**, *109*, 7225−7235.
(22) Köppel, H.; Domcke, W.; Cederbaum, L. S. Multimode Molecular Dynamics Beyond the Born−Oppenheimer Approximation. *Adv. Chem. Phys.* **1984**, *57*, 59−246.

DOI: 10.1021/acs.jpclett.5b00162
J. Phys. Chem. Lett. 2015, 6, 1316−1320

Supplementary Information to: Intramolecular Charge Transfer in 4-Aminobenzonitrile Does Not Need the Twist and May Not Need the Bend

Aurelie Perveaux, Pedro J. Castro, David Lauvergnat, Mar Reguero,* and Benjamin Lasorne.*

DOI: 10.1021/acs.jpclett.5b00162

A. Quantum Chemistry

Table S1. Energies in kcal.mol^{-1} (eV) and oscillator strengths calculated at the CASSCF(12,11)/cc-pVDZ level of theory for various critical points of ABN in the gas phase.

	FC-C_s		FC-C_{2v}		LE-C_s		LE-C_{2v}	PICT		CI-C_s	CI-C_{2v}
	ΔE	*f*	ΔE	*f*	ΔE	*f*	ΔE	ΔE	*f*	ΔE	ΔE
GS	0.0 (0.00)	-	1.8 (0.08)	-	4.6 (0.20)	-	6.3 (0.27)	10.1 (0.44)	-	-	-
LE	110.4 (4.79)	0.01	111.4 (4.83)	0.01	105.8 (4.59)	0.01	106.9 (4.64)	112.8 (4.89)	0.02	129.6 (5.62)*	154.6 (6.71)*
CT	150.8 (6.54)	0.43	147.1 (6.38)	0.49	147.6 (6.40)	0.39	144.9 (6.28)	141.0 (6.11)	0.66	129.6 (5.62)*	154.7 (6.71)*

* Energies calculated using SA2-CASSCF(12,11)/cc-pVDZ

Table S2. Energies in kcal.mol^{-1} (eV) and oscillator strengths calculated at the CASPT2/cc-pVDZ level of theory for various critical points of ABN in the gas phase.

	FC-C_s		FC-C_{2v}		LE-C_s		LE-C_{2v}	PICT		CI-C_s	CI-C_s	CI-C_{2v}	CI-C_{2v}
	ΔE	*f*	ΔE	*f*	ΔE	*f*	ΔE	ΔE	*f*	ΔE*	ΔE*†	ΔE*	ΔE*†
GS	0.0 (0.00)	-	1.4 (0.06)	-	2.3 (0.10)	-	3.6 (0.16)	6.1 (0.26)	-	-	-	-	-
LE	107.8 (4.67)	0.01	106.9 (4.64)	0.01	101.9 (4.42)	0.01	101.2 (4.39)	105.9 (4.59)	0.02	124.8 (5.41)*	116.0 (5.03)	142.4 (6.18)	129.6 (5.62)
CT	125.5 (5.44)	0.43	124.1 (5.38)	0.49	122.4 (5.31)	0.39	121.5 (5.27)	118.8 (5.15)	0.66	107.6 (4.67)*	115.1 (5.00)	136.0 (5.90)	129.3 (5.61)

* Energies calculated using MS2-CASPT2/cc-pVDZ † Energy at crossing point geometry at the CASPT2 level (non-optimized)

Table S3. Energies in kcal.mol^{-1} (eV) calculated at the CASPT2/cc-pVDZ level of theory for various critical points of ABN in acetonitrile.

	FC-C_s	FC-C_{2v}	LE-C_s	LE-C_{2v}	PICT	CI-C_{2v}	CI-C_{2v}
	ΔE	ΔE	ΔE	ΔE	ΔE	ΔE*	ΔE*†
GS	0.0 (0.00)	1.0 (0.04)	1.9 (0.08)	2.8 (0.12)	4.2 (0.18)	39.4	8.8
LE	108.3 (4.69)	106.0 (4.59)	102.0 (4.42)	100.1 (4.34)	104.6 (4.53)	140.3 (6.09)	110.4 (4.79)
CT	120.8 (5.24)	117.9 (5.11)	116.8 (5.07)	114.7 (4.97)	112.8 (4.89)	129.6 (5.62)	110.0 (4.77)

* Energies calculated using MS2-CASPT2/cc-pVDZ † Energy at crossing point geometry at the CASPT2 level (non-optimized)

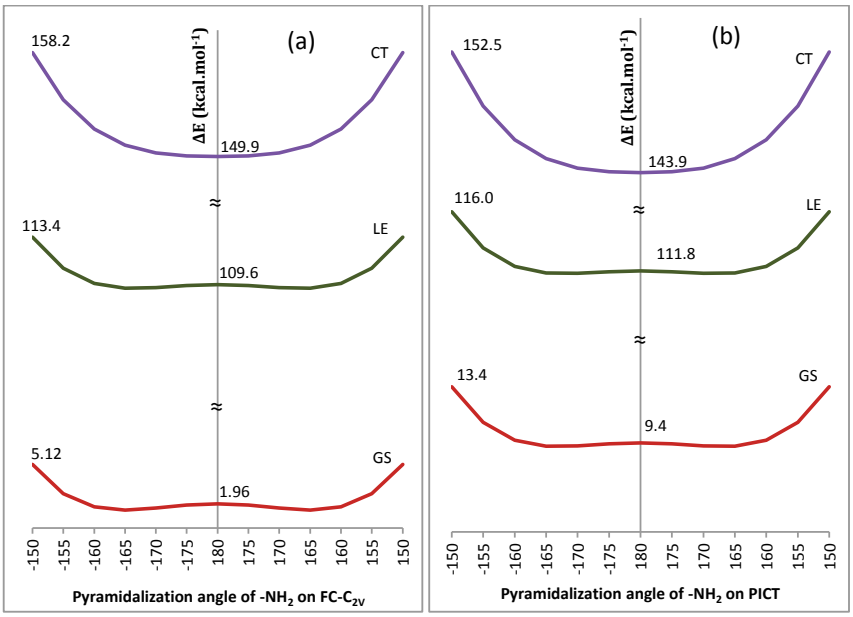

Figure S1. SA4-CASSCF/cc-pVDZ scans for the first three electronic states along the NH_2-pyramidalization coordinate, from FC-C_{2v} (a) and PICT (b). Energies in kcal.mol^{-1}.

Figure S2. Qualitative relaxation vector from S_2-CT to PICT.

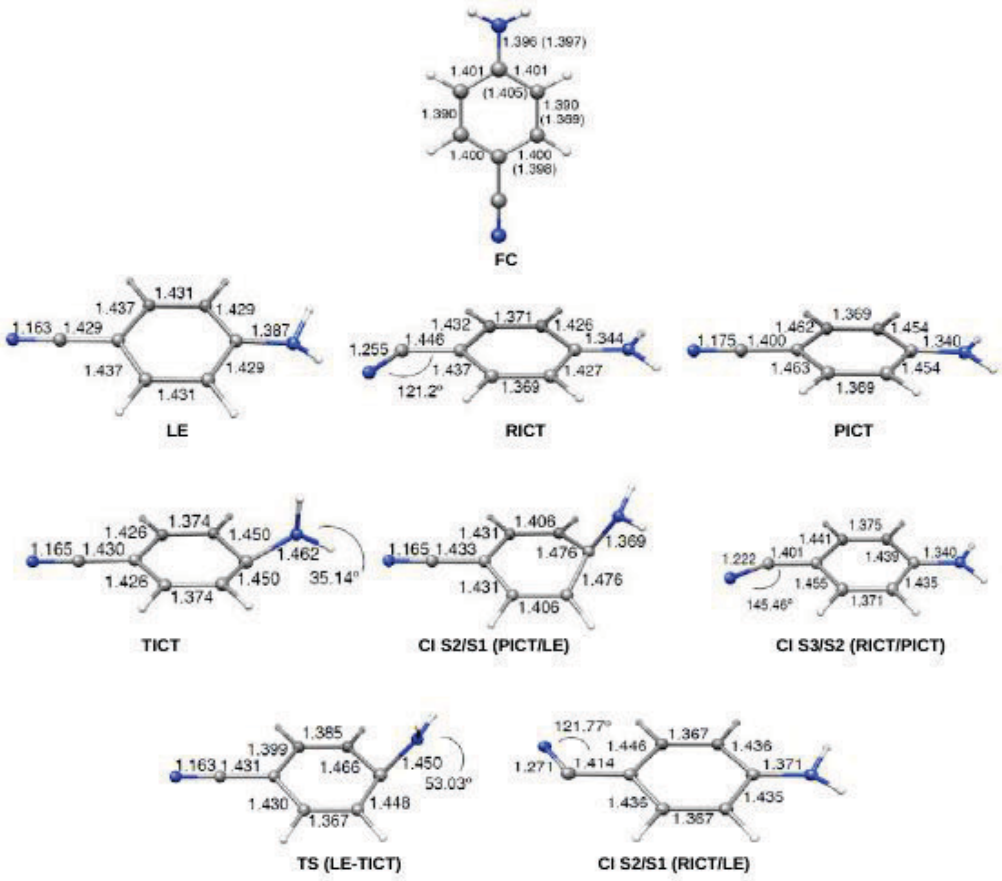

Figure S3. Critical points characterized in previous studies.

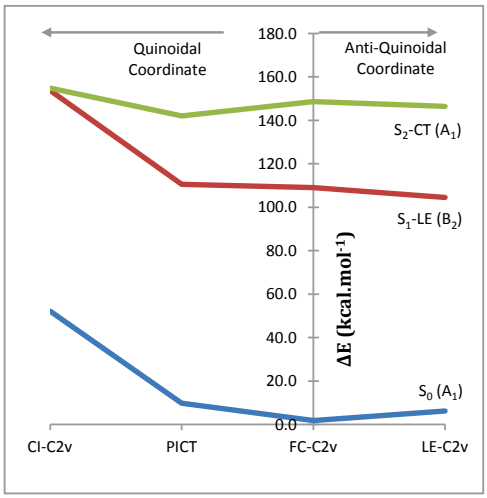

Figure S4. Energies of the critical points of C_{2v} symmetry, obtained at theSA3-CASSCF(12,11)/cc-pVDZ level of theory. The irreducible representation of each state is indicated within parentheses.

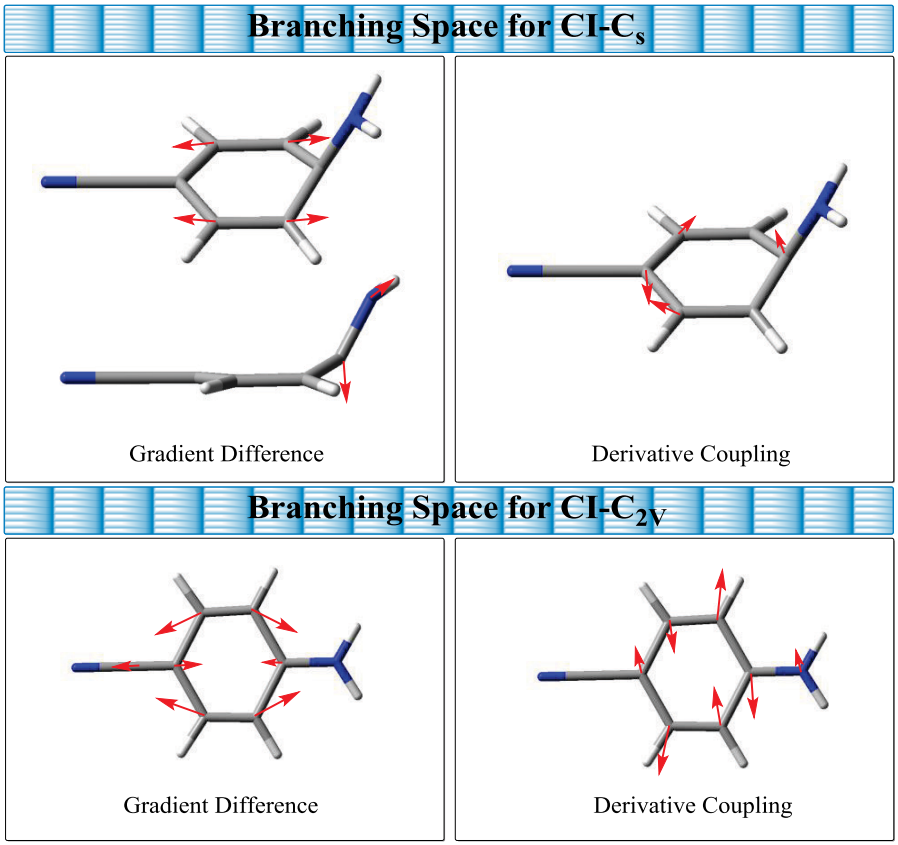

Figure S5. Gradient-difference and derivative-coupling vectors at both conical intersections.

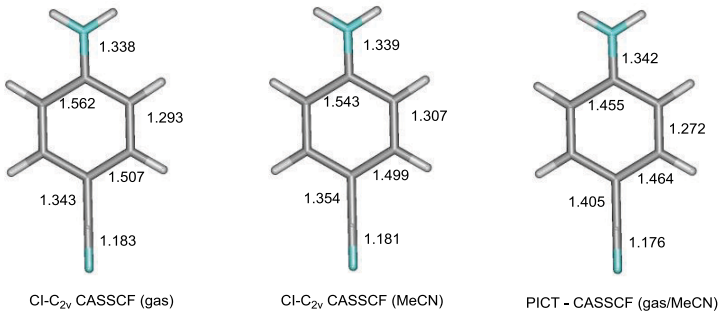

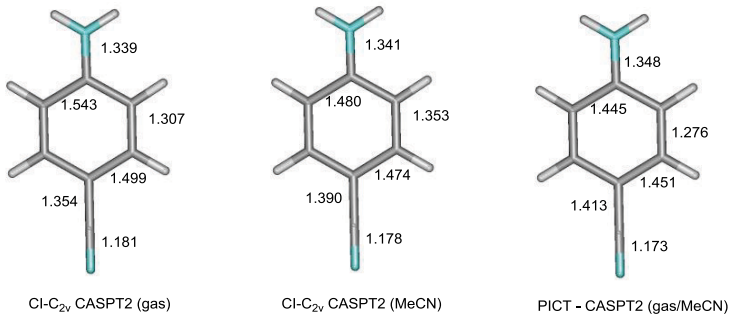

Figure S6. Geometries for CI-C_{2v} and PICT at different levels of theory. Variations with respect to PICT within brackets.

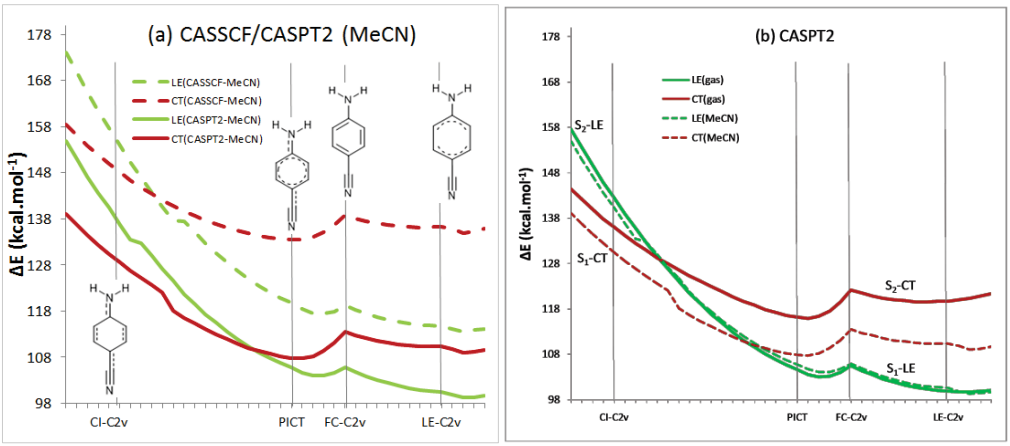

Figure S7. a) CASSCF and CASPT2 energy profiles of the CT and LE states in acetonitrile along the C_{2v} pathway. b) CASPT2 profiles of the CT and LE states in the gas phase and acetonitrile along the C_{2v} pathway. Grey lines show the location of the geometries of the critical points optimized at the CASSCF level, used as fixed points for the interpolations. The discontinuities observed in the CASPT2 profiles are due to the inversion of states at different levels of calculation (CASSCF vs. CASPT2 and vacuum vs. acetonitrile) at those points.

B. Quantum Dynamics

We represented the PES and non-adiabatic couplings with a vibronic-coupling Hamiltonian model (1) based on three quasidiabatic states. It consists in a real symmetric matrix $\mathbf{H}(\mathbf{Q})$ made of three diagonal potential energy functions: $H_{11}(\mathbf{Q})$, $H_{22}(\mathbf{Q})$, and $H_{33}(\mathbf{Q})$, and three off-diagonal electronic couplings, $H_{12}(\mathbf{Q})$, $H_{13}(\mathbf{Q})$, and $H_{23}(\mathbf{Q})$, where $\mathbf{Q}$ denotes the set of nuclear coordinates. In the Franck-Condon region the three quasidiabatic states coincide with the relevant adiabatic states: state 1 (S_0/GS), state 2 (S_1/LE), and state 3 (S_2/CT). Each diagonal entry, $H_{ii}(\mathbf{Q})$, is expanded quadratically around a reference geometry, $\mathbf{Q}_{ref,ii}$, corresponding to the relevant C_{2v} stationary points: $\mathbf{Q}_{GS} = \mathbf{Q}_{ref,11}$, $\mathbf{Q}_{LE} = \mathbf{Q}_{ref,22}$, and $\mathbf{Q}_{PICT} = \mathbf{Q}_{ref,33}$.

The non-adiabatic coupling terms between S_0 and the two other states can be neglected. In other words, $H_{11}(\mathbf{Q})$ corresponds to the S_0PES, and the electronic couplings $H_{12}(\mathbf{Q})$, $H_{13}(\mathbf{Q})$ are set to zero. The remaining coupling, $H_{23}(\mathbf{Q})$, is expanded linearly around $\mathbf{Q}_{CI}$, the geometry of the C_{2v} conical intersection between S_1 and S_2. Its parameters are obtained using the two vectors of the branching space and the PICT minimum is used as a reference point for setting the value of the arbitrary mixing angle between both degenerate states so as to satisfy $H_{23}(\mathbf{Q}_{PICT}) = 0$.

The curvatures of the diagonal entries, $H_{ii}(\mathbf{Q})$, were obtained through a second-order Jahn-Teller procedure (whereby the difference between adiabatic and quasidiabatic second derivatives is considered as a second-order effect of the non-adiabatic coupling). However, the curvatures along the two directions $\mathbf{Q}_{LE}$-$\mathbf{Q}_{CI}$ and $\mathbf{Q}_{PICT}$-$\mathbf{Q}_{CI}$ were slightly adjusted to make sure that the two diabatic PES $H_{22}(\mathbf{Q})$and $H_{33}(\mathbf{Q})$ cross exactly at $\mathbf{Q}_{CI}$ and do so with the right energy.

The following figure (Fig. S8) shows the agreement between the ab initio energies and the ones of the vibronic model along the$\mathbf{Q}_{PICT}$-$\mathbf{Q}_{CI}$ direction when using CASSCF data.

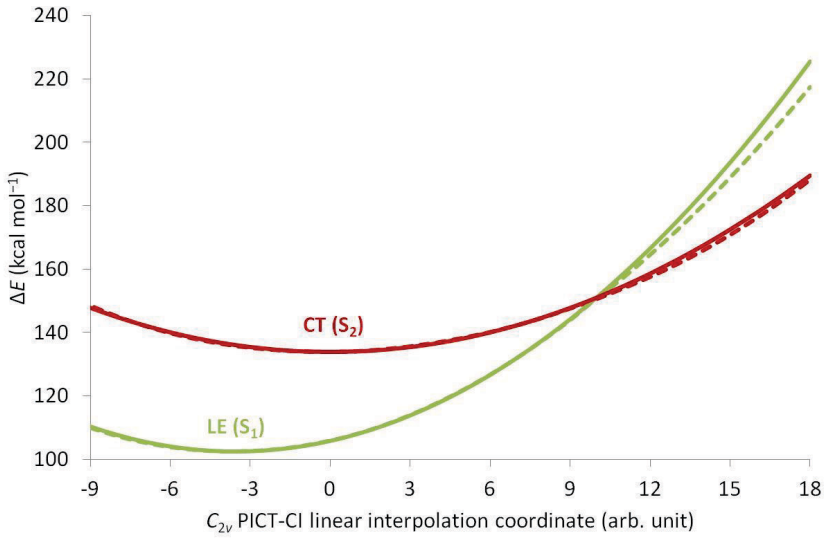

Figure S8. C_{2v} pathway along a linear interpolation coordinate Q linking thePICT point (Q = 0) to the CI-C_{2v} point (Q = 10), in the gas phase. Energy differences are given with respect to the ground-state minimum. Dashed lines: ab initio; plain lines: vibronic model. Ab initio level of theory: CASSCF(12,11)/cc-pVDZ with variable SA weights (single-state calculations on each state at Q = 0; 0.5:0.5 weights on S_1/S_2 at Q = 10; linear interpolation in between).

All parameters of the model were extracted from ab initio calculations (CASSCF(12,11)/cc-pVDZ) at the four relevant geometries, $\mathbf{Q}_{GS}$, $\mathbf{Q}_{LE}$, $\mathbf{Q}_{PICT}$, and $\mathbf{Q}_{CI}$ (SA2 was used at the conical intersection only). The solvent (acetonitrile) effect was taken into account with the PCM (polarizable continuum model). It is important to note that the C_{2V} LE stationary point is not a minimum but a planar transition state. However, the negative curvature associated to the imaginary frequency is very small (flat surface), and within our propagation time (160 fs), this did not cause any trouble during the wavepacket propagation.

A more accurate model of coupled PES (based on CASPT2 data) was further obtained by shifting the geometries and energies of the relevant relocated points (minima and crossings). Again, the curvature was slightly adjusted along the linear interpolation coordinate to make sure that the curves along this direction go through the relevant points (Fig. S9).

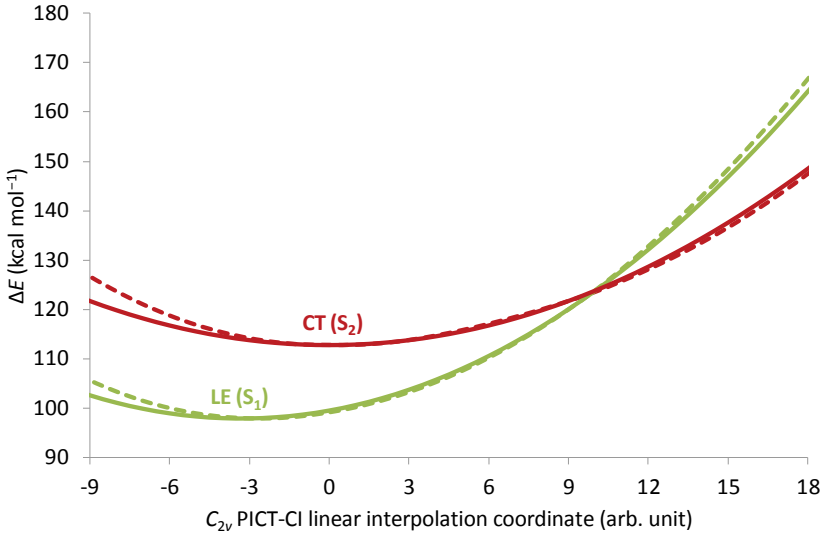

Figure S9. *Same as Figure S8 but based on CASPT2 data*.

In quantum dynamics, the selection of an optimal set of coordinates is a crucial step. Indeed, this enables to minimize considerably the couplings in the potential energy between the modes and

thus to reduce the computational resources (CPU time and memory). In the present study, we used a set of polyspherical coordinates with several subsystems (in red, blue,and pink) (2,3,4).

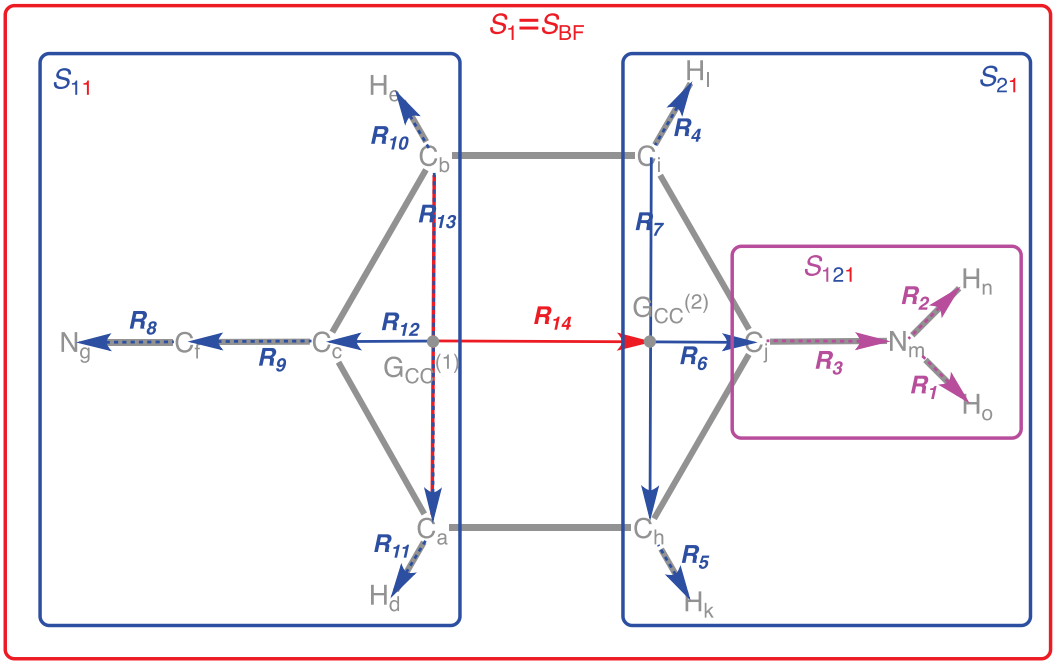

Figure S9. Polyspherical coordinates used in the vibronic model and to perform the dynamics.

These coordinates were carefully selected to describe the relevant motions involved in the photoprocess. In particular, the quinoidal stretching and the symmetric CC stretching on the amino side are represented with a combination of the norms of several vectors ($\mathbf{R_{14}}$, $\mathbf{R_{13}}$, and $\mathbf{R_7}$) and the norm of $\mathbf{R_6}$, respectively.

The kinetic energy operator (KEO) required to perform the dynamics was obtained numerically and exactly with the Tnum program (5). In addition, we assumed a constant metric tensor (calculated at the ground-state geometry). This approximation enables to preserve the main features of the KEO and to considerably reduce the number of terms in the Hamiltonian operator.

Finally, the quantum dynamics calculations were performed with the multilayer version (6) of MCTDH (ML-MCTDH) of the Heidelberg package (7). Indeed, this approach gives access to dealing with a large number of degrees of freedom with a highly compact and flexible basis set. Our system, with 39 coordinates, was described with an eight-layer wavefunction, and, for each layer, 6 single-particle functions (SPF) were used except for the last layer. As usual, we used the discrete variable representation (DVR) for the primitive basis sets (last layer) with (i) 40 DVR grid points for the harmonic-oscillator basis sets associated with the distances (vector norms) and the out-of-

plane angles; (ii) 80 DVR grid points for the sine basis sets associated with the in-plane angles.The vibrational ground state on S_0 was obtained with the relaxation approach implemented in ML-MCTDH.

(1) H. Köppel, W. Domcke, L.S. Cederbaum, *Adv. Chem. Phys.* **1984**, *57*, 59.

(2) F. Gatti and C. Iung, *Phys. Rep.* **2009**, *484*, 1.

(3) M. Ndong, A. Nauts, L. Joubert-Doriol, H.-D. Meyer, F. Gatti and D. Lauvergnat, *J. Chem. Phys.* **2013**, *139*, 204107.

(4) M. Ndong, L. Joubert-Doriol, H.-D. Meyer, A. Nauts, F. Gatti, D. Lauvergnat, *J. Chem. Phys.* **2012**, *136*, 034107.

(5) D. Lauvergnat, A. Nauts, *J. Chem. Phys.* **2002**, *116*, 8560.

(6) O. Vendrell, H.-D. Meyer, *J. Chem. Phys.* **2011**, *134*, 044135.

(7) M.H. Beck, A. Jäckle, G.A. Worth, H.-D. Meyer, *Phys. Rep.* **2000**, *324*, 1.

Bibliography

[1] F.C. De Schryver, S. De. Feyter, G. Schweitzer, *Femtochemistry. with the Nobel Lecture of A. Zewail*, Wiley-VCH, 2001.

[2] P. Hockett, C.Z. Bisgaard, O.J. Clarkin, A. Stolow, *Nat. Phys*. **7** (2011) 612.

[3] F. Krausz, M.Y. Ivanov, *Rev. Mod. Phys*. **81** (2009) 163.

[4] E. Goulielmakis, Z.-H. Loh, A. Wirth, R. Santra, N. Rohringer, V.S. Yakovlev, S. Zherebtsov, T. Pfeifer, A.M. Azzeer, M.F. Kling, S.R. Leone, F. Krausz, *Nature* **466** (2010) 739.

[5] R.J. Saykally, G.A. Blake, *Science.* **259** (1993) 1570.

[6] O.V Boyarkin, M. Kowalczyk, T.R. Rizzo, *J. Chem. Phys*. **118** (2003) 93.

[7] D. Romanini, A. Campargue, *Chem. Phys. Lett*. **254** (1996) 52.

[8] M. Lapert, Y. Zhang, M.A. Janich, S.J. Glaser, D. Sugny, *Sci. Rep*. **2** (2012) 589.

[9] A.K. Hansen, M.A. Sørensen, P.F. Staanum, M. Drewsen, *Angew. Chemie Int. Ed.* **51** (2012) 7960.

[10] C.B. Madsen, L.B. Madsen, S.S. Viftrup, M.P. Johansson, T.B. Poulsen, L. Holmegaard, V. Kumarappan, K.A. Jørgensen, H. Stapelfeldt, *Phys. Rev. Lett.* **102** (2009) 73007.

[11] L. Holmegaard, J.L. Hansen, L. Kalhoj, S. Louise Kragh, H. Stapelfeldt, F. Filsinger, J. Kupper, G. Meijer, D. Dimitrovski, M. Abu-samha, C.P.J. Martiny, L. Bojer Madsen, *Nat Phys* **6** (2010) 428.

[12] R.J. Levis, G.M. Menkir, H. Rabitz, *Science* **292** (2001) 709.

[13] H.L. Bethlem, G. Berden, F.M.H. Crompvoets, R.T. Jongma, A.J.A. van Roij, G. Meijer, *Nature* **406** (2000) 491.

[14] T. Brixner, N.H. Damrauer, P. Niklaus, G. Gerber, *Nature* **414** (2001) 57.

[15] B.W Shore, *Manipulating Quantum Structures Using Laser Pulses,* Cambridge University Press, New York, 2011.

[16] M. Shapiro, B. Brumer. *Principe of the Quantum Control of Molecular Processes*. Eds Wiley-Interscience, 2001.

[17] H. Ihee, V. Lobastov, U. Gomez, B. Goodson, R. Srinivasan, C.-Y. Ruan, A.H. Zewail, *Science* **291** (2001) 385.

[18] Z.F. Liu, K. Hashimoto, A. Fujishima, *Nature* **347** (1990) 658.

[19] I. Willner, S. Rubin, *Angew. Chemie, Int. Ed. English* **35** (1996) 367.

[20] H. Köppel, H.W. Domcke, L.S. Cederbaum, *Adv. Chem. Phys*. **57** (1984) 59.

[21] D.R. Yarkony, *Rev. Mod. Phys*. **68** (1996) 985.

[22] G. A. Worth, L.S. Cederbaum, *Annu. Rev. Phys. Chem.* **55** (2004) 127.
[23] J.C. Tully, *J. Chem. Phys*. **137** (2012) 22A301.

[24] P. Wolynes, *Proc. Natl Acad. Sci. USA* **106** (2009) 17247.

[25] A. de la Lande, J. Řezáč, B. Lévy, B.C. Sanders, D.R. Salahub, *J. Am. Chem. Soc*. **133** (2011) 3883.

[26] J. Quenneville, M. Ben-Nun, T.J. Martínez, *J. Photochem. Photobiol. A* **144** (2001) 229.

[27] M. Ben-nun, T.J. Martínez*, Ab Initio Quantum Molecular Dynamics, Advances in Chemical Physics,* **121** (2002).

[28] M.D. Hack, A.M. Wensmann, D.G. Truhlar, M. Ben-Nun, T.J. Martínez, *J. Chem. Phys.* **115** (2001) 1172.

[29] G.A. Worth, M.A. Robb, I. Burghardt, *Faraday Discuss*. **127** (2004) 307-323.

[30] G.A. Worth, M.A. Robb, B. Lasorne*, Mol. Phys*. **106** (2008) 2077-2091.

[31] H.-D. Meyer, F. Gatti, G.A. Worth, eds., *Multidimensional Quantum Dynamics. MCTDH Theory and Application*, Wiley-VCH, Weinheim, 2009.

[32] C. Woywod, W. Domcke, A.L. Sobolewski, H. Werner, *J. Chem. Phys*. **100** (1994) 112.

[33] S. Krempl, M. Winterstetter, H. Plöhn, W. Domcke, *J. Chem. Phys.* **100** (1994) 926.

[34] G.A. Worth, H.-D. Meyer, L.S. Cederbaum, *J. Chem. Phys.* **109** (1998) 3518.
[35] A. Raab, G. A. Worth, H.-D. Meyer, L.S. Cederbaum, *J. Chem. Phys.* **110** (1999) 936.

[36] M. Döscher, H. Köppel, P.G. Szalay, *J. Chem. Phys.* **117** (2002) 2645.

[37] H. Köppel, M. Döscher, I. Bâldea, H.-D. Meyer, P.G. Szalay, *J. Chem. Phys*. **117** (2002) 2645.

[38] C. Cattarius, G.A. Worth, H.-D. Meyer, L.S. Cederbaum, *J. Chem. Phys*. 115 (2001) 2088.

[39] H. Köppel, *Chem. Phys. Lett.* **205** (1993) 361.

[40] G.G. Dyadyusha, E.S. Kryachko, *Int. J. Quantum Chem*. **19** (1981) 251.

[41] W. Fuß, *Chem. Phys*. **425** (2013) 96.

[42] R. Schneider, W. Domcke, H. Köppel, *J. Chem. Phys*. **92** (1990) 1045.

[43] A. Kühl, W. Domcke, *Chem. Phys*. **259** (2000) 227.

[44] E. Gindensperger, I. Burghardt, L.S. Cederbaum, *J. Chem. Phys*. **124** (2006) 144103.

[45] E. Gindensperger, H. Köppel, L.S. Cederbaum, *J. Chem. Phys*. **126** (2007) 034106.

[46] Á. Vibók, A. Csehi, E. Gindensperger, H. Köppel, G.J. Halász, *J. Phys. Chem. A* **116** (2012) 2629.

[47] I. Burghardt, E. Gindensperger, L.S. Cederbaum, *Mol. Phys*. **104** (2006) 1081.

[48] A.W. Jasper, C. Zhu, S. Nangia, D.G. Truhlar, *Faraday Discuss*. **127** (2004) 1.

[49] M. Olivucci, M. Garavelli, F. Bernardi, *A Computational Strategy for Organic Photochemistry*, *reviews in computational chemistry* K. B. Lipkowitz and D. B. Boyd Editors, Wiley-VCH: New-York, 2000.

[50] J.C. Tully, *Faraday Discuss*. **127** (2004) 463.

[51] M. Desouter-Lecomte, C. Galloy, J.C. Lorquet, M.V. Pires, *J. Chem. Phys.* **71** (1979) 3661.

[52] R.A. Marcus, *J. Chem. Phys*. **24** (1956) 966.

[53] T.A. Barckholtz, *Int. Rev. Phys. Chem*. **17** (1998) 435.

[54] Isaac C. Bersuker, *The Jahn-Teller Effects*, Cambridge University Press, New York, 2010.

[55] E. Teller, *J. Phys.Chem.* **41** (1937) 109.

[56] T. Förster, *Pure Appl. Chem*. **24** (1970) 443.

[57] H.E. Zimmerman, *J. Am. Chem. Soc*. **88** (1966) 1566.

[58] S.H. Lin, A.A. Villaeys, Y. Fujimura, *Advances in Multi-Photon Processes and Spectroscopy*, **19** (2014).

[59] F. Jensen, *Introduction to Computational Chemistry second edition*, John Wiley & Sons, Chichester, 2007.

[60] K.. Lawley, *Ab-initio Methods in quantum chemistry– Part I*. Ed. John Wiley & Sons Great Britain, 1987.

[61] E.R. Davidson, *J. Am. Chem. Soc.* **99** (1977) 397.

[62] G. Herzberg, H.C. Longuet-Higgins, *Discuss. Faraday Soc*. **35** (1963) 77.

[63] C.A. Mead, *J. Chem. Phys*. **78** (1983) 807.

[64] C. Gonzalez, H.B. Schlegel, *J. Chem. Phys*. **90** (1989) 2154.

[65] J. Born, M and Oppenheimer, *Ann. Phys*. **20** (1927) 457.

[66] M. Born, K. Huang, *Dynamical Theory of Crystal Lattices*, Ed. N. F. Mott E. C. Bullard, D. H. Wilkinson Oxford University Press, London, 1954.

[67] F. Bernardi, M. Olivucci, M. A. Robb, *Chem. Soc. Rev*. **25** (1996) 321.

[68] W. Domcke, D.R. Yarkony, H. Köppel, *Conical Intersections: Electronic Structure, Dynamic & Spectroscopy*, *Advanced Series in Physical Chemistry* **15** (2004).

[69] L.S. Cederbaum, H. Köppel, W. Domcke, *International Journal of Quantum Chemistry : Quantum Chemistry Symposium,* **15** (1981) 251.

[70] M. Baer, C.-Y. Ng, *State-selected and state-to-state-ion-molecule reaction dynamics Part 2. Theory. Advances in Chemical Physics* **82** (1992).

[71] X. Yang, K. Liu, *Modern Trends in Chemical Reaction Dynamics: Experiment and Theory (part I), Advanced series in Physical Chemistry* **14** (2012).

[72] D.R. Yarkony, *J. Chem. Phys*. **123** (2005) 204101-204110.

[73] H. Köppel, B. Schubert, *Mol. Phys*. **104** (2006) 1069-1079.

[74] J. Katriel, E.R. Davidson, *Chem. Phys. Lett*. **76** (1980) 259-262.

[75] S. Matsika, D.R. Yarkony, *J. Phys. Chem. A*. **106** (2002) 2580-2591.

[76] M.S. Schuurman, D.R. Yarkony, *J. Chem. Phys*. **124** (2006) 124109-124120.

[77] M. Assmann, G.A. Worth, L. González, *J. Chem. Phys*. **377** (2012) 86-95.

[78] G.J. Atchity, S.S. Xantheas, K. Ruedenberg, *J. Chem. Phys*. **95** (1991) 1862-1876.

[79] J.C. Juanes-Marcos, S.C. Althorpe, E. Wrede, *Science* **309** (2005) 1227-1230.

[80] B.E. Applegate, T. A. Barckholtz, T. A. Miller, *Chem. Soc. Rev.* **32** (2003) 38-49.

[81] M. Garavelli, *Theor. Chem. Acc.* **116** (2006) 87-105.

[82] E.R. Davidson, W.T. Borden, *J Phys Chem* **87** (1983) 4784-4790.

[83] G.J. Atchity, K. Ruedenberg, *J. Chem. Phys*. **110** (1999) 4208-4212.

[84] M. Ben-Nun, T. Martínez, *Chem. Phys. Lett.* **298** (1998) 57-65.

[85] M. Boggio-Pasqua, M.J. Bearpark, P.A. Hunt, M.A. Robb, *J. Am. Chem. Soc*. **124** (2002) 1456.

[86] M. Boggio-Pasqua, M.J. Bearpark, F. Ogliaro, M.A. Robb, *J. Am. Chem. Soc.* **128** (2006) 10533.

[87] M. Boggio-Pasqua, M. Ravaglia, M.J. Bearpark, M. Garavelli, M.A. Robb, *J. Phys. Chem. A* **107** (2003) 11139.

[88] H.C. Longuet-Higgins, *Adv. Spectrosc*. **2** (1961) 429.

[89] O.E. Alon, L.S. Cederbaum, *Phys. Rev. B* **68** (2003) 033105.

[90] G.J. Atchity, S.S. Xantheas, K. Ruedenberg, *J. Chem. Phys*. **95** (1991) 1862.

[91] R.A. Ogg, Jun, P. M., *Trans. Faraday Soc*. **31** (1935) 1375.

[92] H. Hellman, J.K. Syrkin, *Acta Physicochim. U.R.S.S*. **2** (1935) 433.

[93] M. Baer, *Chem. Phys. Lett*. **35** (1975) 112.

[94] M. Baer, *Chem. Phys*. **15** (1976) 49.

[95] C.A. Mead, *J. Chem. Phys*. **77** (1982) 6090.

[96] M. Desouter-Lecomte, D. Dehareng, B. Leyh-Nihant, M.T. Praet, A. J. Lorquet, J.C. Lorquet, J. *Phys. Chem*. **89** (1985) 214.

[97] M. Desouter-Lecomte, D. Dehareng, J.C. Lorquet, *J. Chem. Phys*. **86** (1987) 1429.

[98] F.X. Gadea, F. Spiegelmann, M. Pelissier, J.P. Malrieu, *J. Chem. Phys*. **84** (1986) 4872.

[99] T. Pacher, H. Köppel, L.S. Cederbaum, *J. Chem. Phys*. **95** (1991) 6668.

[100] H.-J. Werner, *J. Chem. Phys*. **74** (1981) 5802.

[101] D. Simah, B. Hartke, H.-J. Werner, *J. Chem. Phys*. **111** (1999) 4523.

[102] H. Nakamura, D.G. Truhlar, *J. Chem. Phys*. **115** (2001) 10353.

[103] C. Evenhuis, T.J. Martínez, *J. Chem. Phys*. **135** (2011) 224110.

[104] A Thiel, H. Köppel, *J. Chem. Phys*. **110** (1999) 9371.

[105] C.S.M. Allan, B. Lasorne, G. A. Worth, M. A. Robb, *J. Phys. Chem. A* **114** (2010) 8713.

[106] J. Vura-Weis, M.D. Newton, M.R. Wasielewski, J.E. Subotnik, *J. Phys. Chem. C* **114** (2010) 20449.

[107] R. Hoffmann, S. Shaik, P.C. Hiberty, *Acc. Chem. Res*. **36** (2003) 750.

[108] F. Bernardi, M. Olivucci, M. A. Robb, *J. Am. Chem. Soc*. **114** (1992) 1606.

[109] F. Bernardi, M. Olivucci, M. A. Robb, *Acc. Chem. Res*. **23** (1990) 405.

[110] L.S. Cederbaum, W. Domcke, *Chem. Phys. Lett*. **25** (1974) 357.

[111] L.S. Cederbaum, W. Domcke, *J. Chem. Phys*. **64** (1976) 603.

[112] L.S. Cederbaum, W. Domcke, H. Köppel, W. Von Niessen, *Chem. Phys*. **26** (1977) 169.

[113] R.H. A. Eade, M. A. Robb, *Chem. Phys. Lett*. **83** (1981) 362.

[114] H.B. Schlegel, M. A. Robb, *Chem. Phys. Lett*. **93** (1982) 43.

[115] F. Bernardi, A. Bottoni, J.J.W. McDouall, M. a. Robb, H.B. Schlegel, *Faraday Symp. Chem. Soc.* **19** (1984) 137.

[116] M. Frisch, I.N. Ragazos, M. A. Robb, H. Bernhard Schlegel, *Chem. Phys. Lett*. **189** (1992) 524.

[117] N. Yamamoto, T. Vreven, M. A. Robb, M.J. Frisch, H. Bernhard Schlegel, *Chem. Phys. Lett*. **250** (1996) 373.

[118] F. Bernardi, A. Bottoni, M. Field, M.F. Guest, I.H. Hillier, M. A. Robb, A. Venturini, J. *Am. Chem. Soc.* **110** (1988) 3050.

[119] F. Bernardi, A. Bottoni, M. Olivucci, M. A. Robb, H.B. Schlegel, G. Tonachini, *J. Am. Chem. Soc.* **110** (1988) 5993.

[120] F. Bernardi, A. Bottoni, M. a Robb, A. Venturini, *J. Am. Chem. Soc*. **112** (1990) 2106.

[121] G. Tonachini, H.B. Schlegel, F. Bernardi, M. A. Robb, *J. Am. Chem. Soc.* **112** (1990) 483.

[122] I.J. Palmer, M. Olivucci, F. Bernardi, M. A. Robb, *J. Org. Chem*. **57** (1992) 5081.

[123] I.J. Palmer, I.N. Ragazos, F. Bernardi, M. Olivucci, M.A. Robb, *J. Am. Chem. Soc*. **116** (1994) 2121.

[124] T. Vreven, F. Bernardi, M. Garavelli, M. Olivucci, M. A. Robb, H.B. Schlegel, *J. Am. Chem. Soc.* **119** (1997) 12687.

[125] J. Andzelm, E. Wimmer, *J. Chem. Phys*. **96** (1992) 1280.

[126] A.D. Becke, *J. Chem. Phys*. **96** (1992) 2155.

[127] P.M.W. Gill, B.G. Johnson, J. A. Pople, M.J. Frisch, *Chem. Phys. Lett.* **197** (1992) 499.

[128] J. Perdew, J. Chevary, S. Vosko, K. Jackson, M. Pederson, D. Singh, C. Fiolhais, *Phys. Rev. B* **48** (1993) 4978.

[129] G.E. Scuseria, *J. Chem. Phys*. **97** (1992) 7528.

[130] A.D. Becke, *J. Chem. Phys*. **97** (1992) 9173.

[131] J. Perdew, Y. Wang, *Phys. Rev. B* **45** (1992) 13244.

[132] P. Hohenberg, W. Kohn, *Phys. Rev*. **136** (1964) B864.

[133] W. Kohn, L.J. Sham, *Phys. Rev*. **140** (1965) A1133.

[134] J.P. Perdew, K. Burke, M. Ernzerhof, D. of Physics, *Phys. Rev. Lett*. **77** (1996) 3865.

[135] A.D. Becke, *J. Chem. Phys*. **98** (1993) 1372.

[136] A.D. Becke, *J. Chem. Phys*. **98** (1993) 5648.

[137] M.E. Casida, C. Jamorski, K.C. Casida, D.R. Salahub, *J. Chem. Phys*. **108** (1998) 4439.
[138] R. Bauernschmitt, R. Ahlrichs, *Chem. Phys. Lett*. **256** (1996) 454.

[139] R.E. Stratmann, G.E. Scuseria, M.J. Frisch, *J. Chem. Phys*. **109** (1998) 8218.

[140] C. Van Caillie, R.D. Amos, *Chem. Phys. Lett*. **308** (1999) 249.

[141] C. Van Caillie, R.D. Amos, *Chem. Phys. Lett*. **317** (2000) 159.

[142] F. Furche, R. Ahlrichs, *J. Chem. Phys*. **117** (2002) 7433.

[143] G. Scalmani, M.J. Frisch, B. Mennucci, J. Tomasi, R. Cammi, V. Barone, *J. Chem. Phys*. **124** (2006) 94107.

[144] J. Tomasi, B. Mennucci, R. Cammi, *Chem. Rev*. **105** (2005) 2999.

[145] G. Scalmani, M.J. Frisch, *J. Chem. Phys*. 132 (2010) 114110.

[146] M. Cossi, G. Scalmani, N. Rega, V. Barone*, J. Chem. Phys*. **117** (2002) 43.

[147] L. Onsager, *J. Am. Chem. Soc*. **58** (1936) 1486.

[148] R. Fukuda, M. Ehara, H. Nakatsuji, R. Cammi, *J. Chem. Phys*. **134** (2011) 104109.

[149] D.M. Dennison, *Rev. Mod. Phys*. (1929) 280.

[150] E.B. Wilson, J.C. Decius, P.C. Cross, *Molecular Vibrations : The Theory of Infrared and Raman Vibrational Spectra* (1955).

[151] P. Atkins, R. Friedman. *Molecular Quantum Mechanics Fith edition*. Oxford University Press, New York, 2011

[152] Y.F. Zhang, S.J. Klippenstein, R. A. Marcus, *J. Chem. Phys*. **94** (1991) 7319.

[153] C. Leforestier, A Viel, F. Gatti, C. Muñoz, C. Iung, *J. Chem. Phys*. **114** (2001) 2099.

[154] L. Joubert-Doriol, B. Lasorne, F. Gatti, M. Schröder, O. Vendrell, H.-D. Meyer, *Comput. Theor. Chem.* **990** (2012) 75.

[155] F. Gatti, C. Iung, *Phys. Rep*. **484** (2009) 1.

[156] F. Gatti, C. Muñoz, C. Iung, *J. Chem. Phys*. **114** (2001) 8275.

[157] C. Iung, F. Gatti, A. Viel, X. Chapuisat, *Phys. Chem. Chem. Phys*. **1** (1999) 3377.

[158] T. Carrington, X.-G. Wang, *Wiley Interdiscip. Rev. Comput. Mol. Sci*. **1** (2011) 952.

[159] M. Ndong, A. Nauts, L. Joubert-Doriol, H.D. Meyer, F. Gatti, D. Lauvergnat, *J. Chem. Phys.* **139** (2013) 204107.

[160] M. Ndong, L. Joubert-Doriol, H.-D. Meyer, A. Nauts, F. Gatti, D. Lauvergnat, *J. Chem. Phys.* **136** (2012) 034107.

[161] F. Gatti, C. Iung, J. Theor. Comput. Chem. 02 (2003) 507.

[162] X. Chapuisat, C. Iung, *Phys. Rev. A* **45** (1992) 6217.

[163] A. Nauts, X. Chapuisat, *Mol. Phys*. **55** (2006) 1287.
[164] B. Podolsky, *Phys. Rev*. **32** (1928) 812.

[165] D. Lauvergnat, A. Nauts, *J. Chem. Phys*. **116** (2002) 8560.

[166] F. Gatti, Y. Justu, M. Menou, A. Nauts, X. Chapuisat, *J. Mol. Spec.,* **181** (1997) 403.

[167] D. Lauvergnat, A. Nauts, Y. Justum, X. Chapuisat, *J. Chem. Phys*. **114** (2001) 6592.

[168] D. Lauvergnat, Y. Justum, M. Desouter-Lecomte, X. Chapuisat, *J. Mol. Struct. Theochem* **577** (2002) 1.

[169] X. Chapuisat, C. Saint-Espès, C. Zuhrt, L. Zülicke, *Chem. Phys*. **217** (1997) 43.

[170] E.L. Sibert, W.P. Reinhardt, J.T. Hynes, *J. Chem. Phys*. **81** (1984) 1115.

[171] L. Halonen, T. Carrington, *J. Chem. Phys*. **88** (1988) 4171.

[172] L. Lespade, S. Rodin, D. Cavagnat, S. Abbate, D. Cavgnat, C. Laboratoire, S. Molbculaire, C. Universitb, T. Cedex, N. Sauro, F. Form, I. The, *J. Phys. Chem*. **97** (1993) 6134.

[173] D.J. Rush, K.B. Wiberg, *J. Phys. Chem. A* **101** (1997) 3143.

[174] J.R. Durig, W. Zhao*, J. Phys. Chem*. **98** (1994) 9202-9206.

[175] S. Sakurai, N. Meinander, J. Laane, *J. Chem. Phys*. **108** (1998) 3537.

[176] D. Luckhaus, *J. Chem. Phys*. **113** (2000) 1329.

[177] E. Mátyus, G. Czakó, A.G. Császár, *J. Chem. Phys*. **130** (2009) 134112.

[178] Y. Scribano, D.M. Lauvergnat, D.M. Benoit, *J. Chem. Phys*. **133** (2010) 094103.

[179] H.-D. Meyer, U. Manthe, L.S. Cederbaum, *Chem. Phys. Lett*. **165** (1990) 73.

[180] U. Manthe, H.-D. Meyer, L.S. Cederbaum, *J. Chem. Phys*. **97** (1992) 3199.

[181] M.H. Beck, A. Jäckle, G.A. Worth, H.-D. Meyer, *Physics Reports* **324** (2000) 1.

[182] H.-D. Meyer, G.A. Worth, *Theor. Chem. Acc*. **109** (2003) 251.

[183] A. Raab, G.A. Worth, H.-D. Meyer, L.S. Cederbaum, *J. Chem. Phys*. **110** (1999) 936.

[184] A. Markmann, G.A. Worth, S. Mahapatra, H.-D. Meyer, H. Köppel, L.S. Cederbaum, *J. Chem. Phys*. **123** (2005) 204310.

[185] L.J. Doriol, F. Gatti, C. Iung, H.-D. Meyer, *J. Chem. Phys*. **129** (2008) 224109.

[186] O. Vendrell, F. Gatti, H.-D. Meyer, *J. Chem. Phys*. **127** (2007) 184303.

[187] F. Richter, F. Gatti, C. Léonard, F. Le Quéré, H.-D. Meyer, *J. Chem. Phys*. **127** (2007) 164315.

[188] C. Iung, F. Gatti, H.-D. Meyer, *J. Chem. Phys*. **120** (2004) 6992.

[189] S. Sukiasyan, H.-D. Meyer, *J. Chem. Phys*. **116** (2002) 10641.

[190] F. Otto, F. Gatti, H.-D. Meyer, *J. Chem. Phys*. **128** (2008) 064305.
[191] R. van Harrevelt, G. Nyman, U. Manthe, *J. Chem. Phys*. **126** (2007) 084303.

[192] S. Bhattacharya, A.N. Panda, H.-D. Meyer, *J. Chem. Phys*. **132** (2010) 214304.

[193] R. van Harrevelt, U. Manthe, *J. Chem. Phys*. **121** (2004) 3829.

[194] C. Crespos, H.-D. Meyer, R.C. Mowrey, G.J. Kroes, *J. Chem. Phys*. **124** (2006) 074706.

[195] P. Jungwirth, R.B. Gerber, *J. Chem. Phys*. **102** (1995) 6046.

[196] R.B. Gerber, *J. Chem. Phys*. **77** (1982) 3022.

[197] R.H. Bisseling, R. Kosloff, R.B. Gerber, M. A. Ratner, L. Gibson, C. Cerjan, *J. Chem. Phys.* **87** (1987) 2760.

[198] P. Jungwirth, R.B. Gerber, *J. Chem. Phys.* **102** (1995) 8855.

[199] Z. Bihary, R.B. Gerber, V. A. Apkarian, *J. Chem. Phys*. **115** (2001) 2695.

[200] O. Vendrell, H.-D. Meyer, *J. Chem. Phys*. **134** (2011) 044135.

[201] U. Manthe, *J. Chem. Phys*. **128** (2008) 164116.

[202] Q. Meng, H.-D. Meyer, *J. Chem. Phys*. **138** (2013) 014313.

[203] T. Westermann, R. Brodbeck, A.B. Rozhenko, W. Schoeller, U. Manthe, *J. Chem. Phys*. **135** (2011) 184102.

[204] Q. Meng, H.-D. Meyer, *J. Chem. Phys*. **138** (2013) 014313.

[205] L. Joubert-Doriol, B. Lasorne, D. Lauvergnat, H.-D. Meyer, F. Gatti, *J. Chem. Phys*. **140** (2014) 044301.

[206] B. Lasorne, M. A. Robb, H.-D. Meyer, F. Gatti, *Chem. Phys*. **377** (2010) 30.

[207] J. Jornet-Somoza, B. Lasorne, M. a. Robb, H.-D. Meyer, D. Lauvergnat, F. Gatti, *J. Chem. Phys.* **137** (2012) 084304.

[208] L.J. Doriol, *Control of Benzopyran Photochemistry. Theoretical Strategy Coupling Quantum Chemistry and Quantum Dynamics*., Université Montpellier 2, 2012.

[209] R.G. Pearson, *J. Mol. Struct. Theochem* **103** (1983) 25.

[210] L. Salem, *Chem. Phys. Lett*. **3** (1969) 99.

[211] R.G. Pearson, *J. Am. Chem. Soc*. **91** (1969) 4947.

[212] R.G. Pearson, *J. Am. Chem. Soc*. **91** (1969) 4947.

[213] D. Lauvergnat, E. Baloïtcha, G. Dive, M. Desouter-Lecomte, *Chem. Phys*. **326** (2006) 500.

[214] J. Schirmer, A. Dreuw, *Phys. Rev. A* **75** (2007) 022513.

[215] B.F.E. Curchod, U. Rothlisberger, I. Tavernelli, *Chem. Phys. Chem*. **14** (2013) 1314.

[216] B.G. Levine, C. Ko, J. Quenneville, T.J. MartÍnez, *Mol. Phys.* **104** (2006) 1039.

[217] A.S. Klymchenko, V.G. Pivovarenko, T. Ozturk, A.P. Demchenko, *New J. Chem*. **27** (2003) 1336.

[218] A.S. Klymchenko, T. Ozturk, V.G. Pivovarenko, A.P. Demchenko, *Tetrahedron Lett*. **42** (2001) 7967.

[219] D. Svechkarev, A. Doroshenko, V. Baumer, B. Dereka, *J. Lumin*. **131** (2011) 253.

[220] K. Chevalier, A. Gru, A. Stamm, Y. Schmitt, M. Gerhards, R. Diller, *J. Phys. Chem. A*. **117** (2013) 11233.

[221] A.S. Klymchenko, V. V Shvadchak, D. a Yushchenko, N. Jain, Y. Mély, *J. Phys. Chem. B* **112** (2008) 12050.

[222] A.J.G Strandjord, P.F. Barbara. *Chem. Phys. Lett*. **98** (1983) 21.

[223] A.J.G. Strandjord, P.F. Barbara. *J. Phys. Chem*. **89** (1985) 2355.

[224] B.J. Schwartz, L.A. Peteanu, C.B. Harris*, J. Phys. Chem*. **96** (1992) 3591.

[225] S. Ameer-Beg, S.M. Ormson, R.G. Brown, P. Matousek, M. Towrie, E.T.J. Nibbering, P. Foggi, F.V.R. Neuwahl, *J. Phys. Chem. A* **105** (2001) 3709.

[226] P.T. Chou, S.C. Pu, Y.M. Cheng, W.S. Yu, Y.C. Yu, F.T. Hung, W.P. Hu, *J. Phys. Chem. A* **109** (2005) 3777.

[227] Y.M. Cheng, S.C. Pu, Y.C. Yu, P.T. Chou, C.H. Huang, C.T. Chen, T.H. Li, W.P. Hu, J*. Phys. Chem. A* **109** (2005) 11696.

[228] C.C. Lin, C.L. Chen, M.W. Chung, Y.J. Chen, P.T. Chou, *J. Phys. Chem. A* **114** (2010) 10412.

[229] A.D. Roshal, J. A. Organero, A. Douhal, *Chem. Phys. Lett*. **379** (2003) 53.

[230] P. Chou, M.L. Martinez, J.H. Clements, *J. Phys. Chem*. **97** (1993) 2618.

[231] P.T. Chou, Y.C. Chen, W.S. Yu, Y.M. Cheng, *Chem. Phys. Lett*. **340** (2001) 89.

[232] V. V. Shynkar, A.S. Klymchenko, C. Kunzelmann, G. Duportail, C.D. Muller, A.P. Demchenko, J.M. Freyssinet, Y. Mély, *J. Am. Chem. Soc*. **129** (2007) 2187.

[233] R. Das, A.S. Klymchenko, G. Duportail, Y. Mély, *J. Phys. Chem. B* **112** (2008) 11929.

[234] Y. Kimura, M. Fukuda, K. Suda, M. Terazima, *J. Phys. Chem. B* **114** (2010) 11847.

[235] K. Suda, M. Terazima, H. Sato, Y. Kimura, *J. Phys. Chem. B* **117** (2013) 12567.

[236] A.N. Bader, V.G. Pivovarenko, A.P. Demchenko, F. Ariese, C. Gooijer, *J. Phys. Chem. B* **108** (2004) 10589.

[237] R. Das, A.S. Klymchenko, G. Duportail, Y. Mély, *Photochem. Photobiol. Sci*. **8** (2009) 1583.

[238] R. Das, G. Duportail, A. Ghose, L. Richert, A. Klymchenko, S. Chakraborty, S. Yesylevskyy, Y. Mély, *Phys. Chem. Chem. Phys*. **16** (2014) 776.

[239] F. Parsapour, D.F. Kelley, *J. Phys. Chem*. **100** (1996) 2791.

[240] P. Chou, *Journal of the Chinese Chemical Society* **48** (2001) 651.

[241] J.A. Organero, L. Tormo, M. Sanz, L. Santos, A. Douhal, *J. Incl. Phenom. Macrocycl. Chem.* **56** (2006) 161.

[242] J.A. Organero, L. Tormo, M. Sanz, A. Roshal, A. Douhal, *J. Photochem. Photobiol. A Chem.* **188** (2007) 74.

[243] M. Sanz, J.A. Organero, A. Douhal*, Chem. Phys*. **338** (2007) 135.

[244] T.C. Swinney, D.F. Kelley, *J. Chem. Phys*. **99** (1993) 211.

[245] S.M. Ormson, R.G. Brown, F. Vollmer, W. Rettig, *J. Photochem. Photobiol. A Chem*. **81** (1994) 65.

[246] D. Dziuba, I.A. Karpenko, N.P.F. Barthes, B.Y. Michel, A.S. Klymchenko, R. Benhida, A.P. Demchenko, Y. Mély, A. Burger, *Chem. - A Eur. J*. **20** (2014) 1998.

[247] A. Roshal, A. Grigorovich, *J. Phys. Chem. A* **102** (1998) 5907.

[248] A.D. Roshal, A.V Grigorovich, A.O. Doroshenko, V.G. Pivovarenko, A P. Demchenko, *J. Photochem. Photobiol. A Chem*. **127** (1999) 89.

[249] A.S. Klymchenko, A.P. Demchenko, *J. Am. Chem. Soc*. **124** (2002) 12372.

[250] J.R. Dharia, K.F. Johnson, J.B. Schlenoff, *Macromolecules* **27** (1994) 5167.

[251] R. Das, G. Duportail, L. Richert, A. Klymchenko, Y. Mély, *Langmuir* **28** (2012) 7147.

[252] M. Sarkar, J. Guha Ray, P.K. Sengupta, *Spectrochim. Acta Part A Mol. Biomol. Spectrosc.* **52** (1996) 275.

[253] A.S. Klymchenko, A.P. Demchenko, *Langmuir* **18** (2002) 5637.

[254] G. M'Baye, A.S. Klymchenko, D.A. Yushchenko, V.V Shvadchak, T. Ozturk, Y. Mély, G. Duportail, *Photochem. Photobiol. Sci*. **6** (2007) 71.

[255] S.M. Dennison, J. Guharay, P.K. Sengupta, *Spectrochim. Acta Part A Mol. Biomol. Spectrosc*. **55** (1999) 1127.

[256] G. Duportail, A. Klymchenko, Y. Mély, A. Demchenko, *FEBS Lett*. **508** (2001) 196.

[257] N.A. Nemkovich, J.V. Kruchenok, A.N. Rubinov, V.G. Pivovarenko, W. Baumann, *J. Photochem. Photobiol. A Chem.* **139** (2001) 53.

[258] A.S. Klymchenko, G. Duportail, T. Ozturk, V.G. Pivovarenko, Y. Mély, A.P. Demchenko, *Chem. Biol*. **9** (2002) 1199.

[259] A. Sytnik, D. Gormin, M. Kasha, *Proc. Natl. Acad. Sci. U. S. A*. **91** (1994) 11968.

[260] A.V. Strizhak, V.Y. Postupalenko, V.V. Shvadchak, N. Morellet, E. Guittet, V.G. Pivovarenko, A.S. Klymchenko, Y. Mély, *Bioconjug. Chem*. **23** (2012) 2434.

[261] M. Spadafora, V.Y. Postupalenko, V.V. Shvadchak, A.S. Klymchenko, Y. Mély, A. Burger, R. Benhida, *Tetrahedron* **65** (2009) 7809.

[262] D. Dziuba, V.Y. Postupalenko, M. Spadafora, A.S. Klymchenko, V. Guérineau, Y. Mély, R. Benhida, A. Burger, *J. Am. Chem. Soc*. **134** (2012) 10209.

[263] S. Ash, S.P. De, H. Beg, A. Misra, *Mol. Simul*. **37** (2011) 914.

[264] C.A. Kenfack, A.S. Klymchenko, G. Duportail, A. Burger, Y. Mély, *Phys. Chem. Chem. Phys.* **14** (2012) 8910.

[265] G. Estiú, J. Rama, A. Pereira, R.E. Cachau, O.N. Ventura, *J. Mol. Struct. Theochem* **487**

(1999) 221.

[266] A.P. Demchenko, K.-C. Tang, P.-T. Chou, *Chem. Soc. Rev*. **42** (2013) 1379.

[267] A.D. Laurent, C. Adamo, D. Jacquemin, *Phys. Chem. Chem. Phys*. **16** (2014) 14334.

[268] A.J. Aquino, H. Lischka, C. Hättig, *J. Phys. Chem. A* **109** (2005) 3201.

[269] R. De Vivie-Riedle, V. De Waele, L. Kurtz, E. Riedle, *J. Phys. Chem. A* **107** (2003) 10591.

[270] A.L. Sobolewski, W. Domcke, *Phys. Chem. Chem. Phys*. **1** (1999) 3065.

[271] C. Adamo, V. Barone, *J. Chem. Phys*. **110** (1999) 6158.

[272] D. Jacquemin, E. a. Perpète, G.E. Scuseria, I. Ciofini, C. Adamo, *J. Chem. Theory Comput.* **4** (2008) 123.

[273] A.D. Quartarolo, E. Sicilia, N. Russo, *J. Chem. Theory Comput*. **5** (2009) 1849.

[274] K.S. Thanthiriwatte, E.G. Hohenstein, L. a. Burns, C.D. Sherrill, *J. Chem. Theory Comput*. **7** (2011) 88.

[275] S. Gozem, F. Melaccio, A. Valentini, M. Filatov, M. Huix-rotllant, N. Ferre, L.M. Frutos, C. Angeli, A.I. Krylov, A.A. Granovsky, R. Lindh, M. Olivucci, *J. Chem. Theory Comput*. **10** (2014) 3074.

[276] M. Böckmann, N.L. Doltsinis, D. Marx, *J. Phys. Chem. A* **114** (2010) 745.

[277] M. Svensson, S. Humbel, R.D.J. Froese, T. Matsubara, S. Sieber, K. Morokuma, *J. Phys. Chem.* **100** (1996) 19357.

[278] J.Z. Zhang, B.J. Schwartz, J.C. King, C.B. Harris, *J. Am. Chem. Soc*. **114** (1992) 10921.

[279] J. Zhao, S. Ji, Y. Chen, H. Guo, P. Yang, *Phys. Chem. Chem. Phys*. **14** (2012) 8803.

[280] L.M. Tolbert, K.M. Solntsev, *Acc. Chem. Res*. **35** (2002) 19.

[281] J. Waluk, *Acc. Chem. Res*. **36** (2003) 832.

[282] T.E. Dermota, Q. Zhong, A.W. Castleman, *Chem. Rev.* **104** (2004) 1861.

[283] K. Fukui, *The Role of Frontiere Orbitals in Chemical Reactions*. Nobel Lecture (1981).

[284] G. Zhang, C.B. Musgrave, *J. Phys. Chem. A* **111** (2007) 1554.

[285] Q. Zhao, R.C. Morrison, R.G. Parr, *Phys. Rev. A* **50** (1994) 2138.

[286] R. Stowasser, R. Hoffmann, *J. Am. Chem. Soc*. **121** (1999) 3414.

[287] H. Köppel, L.S. Cederbaum, W. Domcke, *J. Chem. Phys*. **89** (1988) 2023.
[288] M. Döscher, H. Köppel, P.G. Szalay, *J. Chem. Phys*. **117** (2002) 2645.

[289] H. Köppel, M. Döscher, I. Bâldea, H.-D. Meyer, P.G. Szalay, *J. Chem. Phys*. **117** (2002) 2657.

[290] A.B. Burrill, Y.K. Chung, H.A. Mann, P.M. Johnson, *J. Chem. Phys*. **120** (2004) 8587.

[291] R. Lindner, E. Wedum, K. Haber, *Science* **271** (1996) 1698.

[292] H. Koppel, W. Domcke, L.. Cederbaum, *Mol. Phys*. **43** (1981) 851.

[293] L. Seidner, G. Stock, A.L. Sobolewski, W. Domcke *J. Chem. Phys*. **96** (1992) 5298.

[294] E. Brémond, *Simulation Ab Initio de Spectres UV-Visibles*, Université Pierre et Marie Curie, 2012.

[295] Y. Carissan, D. Hagebaum-reignier, N. Goudard, S. Humbel. *J. Phys. Chem. A.* **112** (2008) 13256.

[296] D. Hagebaum-Reignier, R. Girardi, Y. Carissan, S. Humbel, *J. Mol. Struct. Theochem* **817** (2007) 99.

[297] S. Humbel, *J. Chem. Educ*. **84** (2007) 1056.

[298] R. Spezia, I. Burghardt, J.T. Hynes, *Mol. Phys*. **104** (2006) 903.

[299] I. Burghardt, J.T. Hynes, *J. Phys. Chem. A* **110** (2006) 11411.

[300] A. Dreuw, J.L. Weisman, M. Head-Gordon, *J. Chem. Phys*. **119** (2003) 2943.
[301] D.J. Tozer, *J. Chem. Phys.* **119** (2003) 12697.

[302] O. Gritsenko, E.J. Baerends, *J. Chem. Phys*. **121** (2004) 655.

[303] S. Shaik, A. Shurki, *Angew. Chemie - Int. Ed*. **38** (1999) 586.

[304] J. Olsen, B.O. Roos, P. Jørgensen, H.J.A. Jensen, *J. Chem. Phys*. **89** (1988) 2185.

[305] M. Klene, M.A. Robb, L. Blancafort, M.J. Frisch, *J. Chem. Phys*. **119** (2003) 713.

[306] Q. Li, B. Mennucci, M.A. Robb, L. Blancafort, C. Curutchet, *J. Chem. Theory Comput*. **11** (2015) 1674.

[307] F. Ding, D.B. Lingerfelt, B. Mennucci, X. Li, *J. Chem. Phys*. **142** (2015) 034120.

[308] F. Lipparini, G. Scalmani, L. Lagardère, B. Stamm, E. Cancès, Y. Maday, J.-P. Piquemal, M.J. Frisch, B. Mennucci, *J. Chem. Phys*. **141** (2014) 184108.

[309] S. Caprasecca, B. Mennucci, *J. Phys. Chem. A* **118** (2014) 6484.

[310] G.W. Richings, I. Polyak, K.E. Spinlove, G. a. Worth, I. Burghardt, B. Lasorne, *Int. Rev. Phys. Chem.* **34** (2015) 269.

[311] A. Warshel, M. Karplus, *Chem. Phys. Lett*. **32** (1975) 11.

[312] R. Car, M. Parrinello, *Phys. Rev. Lett*. **55** (1985) 2471.

[313] I.S.Y. Wang, M. Karplus, *J. Am. Chem. Soc*. **85** (1973) 8160.

[314] Z.R. Grabowski, K. Rotkiewicz, W. Rettig, *Chem. Rev.* **103** (2003) 3899.

[315] W. Rettig, *Angew.Chem*. **98** (1986) 969.

[316] I. Gómez, P.J. Castro, M. Reguero, *J. Phys. Chem. A* **119** (2015)1983.

[317] S.I. Druzhinin, N.P. Ernsting, S.A. Kovalenko, L.P. Lustres, T.A. Senyushkina, K.A. Zachariasse, *J. Phys. Chem. A* **110** (2006) 2955.

[318] K.A. Zachariasse, T. Von Der Haar, A. Hebecker, U. Leinhos, W. Kuhnle, *Pure Appl. Chem*. **65** (1993) 1745.

[319] J.R. Lakowicz, *Principles of Fluorescence Spectroscopy*, 3rd Edition, Joseph R. Lakowicz, Editor, 2006.

[320] M. Bedoya, G. Orellana, M.C. Moreno-Bondi, *Helv. Chim. Acta* **84** (2001) 2628.

[321] G. Orellana, A.M. Gomezcarneros, C. Dedios, A.A. Garciamartinez, M.C. Morenobondi, *Anal. Chem*. **67** (1995) 2231.

[322] A.P. De Silva, H.Q.N. Gunaratne, T. Gunnlaugsson, A.J.M. Huxley, C.P. McCoy, J.T. Rademacher, T.E. Rice, *Chem. Rev*. **97** (1997) 1515.

[323] J.J. La Clair, *Angew. Chemie - Int. Ed. English* **37** (1998) 325.

[324] K. Rotkiewicz, K.H. Grellmann, Z.R. Grabowski, *Chem. Phys. Lett*. **19** (1973) 315.

[325] E. Lippert, Angew. Chem. 21 (1961) 695.

[326] W. Schuddeboom, S.A. Jonker, J.M. Warman, *J. Phys. Chem*. **96** (1992) 10809.

[327] W.M. Kwok, C. Ma, D. Phillips, P. Matousek, A.W. Parker, M. Towrie, *J. Phys. Chem. A.* **104** (2000) 4188.

[328] K.A. Zachariasse, M. Grobys, T. Von Der Haar, A. Hebecker, Y. V. Il'ichev, Y.B. Jiang, O. Morawski, W. Kühnle, *J. Photochem. Photobiol. A Chem*. **102** (1996) 59.

[329] J. Dreyer, A. Kummrow, *J. Am. Chem. Soc*. **122** (2000) 2577.

[330] C.J. Jamorski, H.P. Lüthi, *J. Chem. Phys*. **119** (2003) 12852.

[331] D. Rappoport, F. Furche, *J. Am. Chem. Soc*. **126** (2004) 1277.

[332] A. Köhn, C. Hättig, *J. Am. Chem. Soc*. **126** (2004) 7399.

[333] K. Rotkiewicz, Z.R. Grabowski, A. Krówczyński, W. Kühnle, *J. Lumin*. **12-13** (1976) 877.

[334] A.-D. Gorse, M. Pesquer, *J. Phys. Chem*. **99** (1995) 4039.

[335] G. Berden, J. van Rooy, W. Leo Meerts, K.A. Zachariasse. *Chem. Phys. Lett*. **278** (1997) 373.

[336] K.A. Zachariasse, *Chem. Phys. Lett*. **320** (2000) 8.

[337] W. Sudholt, A.L. Sobolewski, W. Domcke, *Chem. Phys*. **240** (1999) 9.

[338] C. Chudoba, A. Kummrow, J. Dreyer, J. Stenger, E.T.J. Nibbering, T. Elsaesser, K.A. Zachariasse, *Chem. Phys. Lett*. **309** (1999) 357.

[339] A.L. Sobolewski, W. Domcke, *Chem. Phys. Lett*. **250** (1996) 428.

[340] P.B. Coto, L. Serrano-Andrés, T. Gustavsson, T. Fujiwara, E.C. Lim, *Phys. Chem. Chem. Phys.* **13** (2011) 15182.

[341] I. Fdez. Galván, M.E. Martín, M.A. Aguilar, *Chem. Phys. Lett*. **499** (2010) 100.

[342] K.A. Zachariasse, S.I. Druzhinin, V.A. Galievsky, S. Kovalenko, T.A. Senyushkina, P. Mayer, M. Noltemeyer, M. Boggio-pasqua, M.A. Robb, *J. Phys. Chem. A* **113** (2009) 2693.

[343] M. Park, C.H. Kim, T. Joo, *J. Phys. Chem. A* **117** (2013) 370.

[344] J.M. Rhinehart, R.D. Mehlenbacher, D. McCamant, *J. Phys. Chem. B* **114** (2010) 14646.

[345] Y. Amatatsu*, J. Phys. Chem. A* **109** (2005) 7225.

[346] Y. V Il'ichev, W. Kühnle, K.A. Zachariasse, *J. Phys. Chem. A* **102** (1998) 5670.

[347] L. Serrano-Andrés, M. Merchán, B.O. Roos, R. Lindh, *J. Am. Chem. Soc*. **117** (1995) 3189.

[348] A.B.J. Parusel, G. Köhler, *J. Phys. Chem. A*. **103** (1999) 4056.

[349] R.C. Ramos, T. Fujiwara, M.Z. Zgierski, E.C. Lim, *J. Phys. Chem. A* **109** (2005) 7121.

[350] K.A. Zachariasse, S.I. Druzhinin, W. Bosch, R. Machinek, *J. Am. Chem. Soc*. **126** (2004) 1705.

[351] C. Jamorski Jödicke, H.P. Lüthi, *J. Chem. Phys.* **117** (2002) 4157.

[352] A.L. Sobolewski, W. Sudholt, W. Domcke, *J. Phys. Chem. A* **102** (1998) 2716.

[353] T. Gustavsson, P.B. Coto, L. Serrano-Andrés, T. Fujiwara, E.C. Lim, *J. Chem. Phys*. **131** (2009) 031101.

[354] I. Gómez, M. Reguero, M. Boggio-Pasqua, M.A. Robb, *J. Am. Chem. Soc*. **127** (2005) 7119.

[355] J.M. Rhinehart, J.R. Challa, D.W. McCamant, *J. Phys. Chem. B* **116** (2012) 10522.

[356] S.I. Druzhinin, A. Demeter, V.A. Galievsky, T. Yoshihara, K.A. Zachariasse, *J. Phys. Chem. A* **107** (2003) 8075.

[357] A. Perveaux, P.J. Castro, D. Lauvergnat, M. Reguero, B. Lasorne, *J. Phys. Chem. Lett*. **6** (2015) 1316.

[358] M. Ndong, A. Nauts, L. Joubert-Doriol, H.D. Meyer, F. Gatti, D. Lauvergnat, *J. Chem. Phys.* **139** (2013) 204107.

[359] J. Doriol, *Control of benzopyran photochemistry. Theoretical strategy coupling quantum chemistry and quantum dynamics*. Université Montpellier 2 (2012).

[360] J. Jornet-Somoza, B. Lasorne, M. a Robb, H.-D. Meyer, D. Lauvergnat, F. Gatti, *J. Chem. Phys.* 137 (2012) 084304.

[361] B. Lasorne, J. Jornet-Somoza, H.-D. Meyer, D. Lauvergnat, M.A. Robb, F. Gatti, *Spectrochim. Acta. A. Mol. Biomol. Spectrosc*. **119** (2014) 52.

[362] B.H. Lengsfield, D.R. Yarkony, *Adv. Chem. Phys*. **82** (1992) 1.

[363] H. Köppel, B. Schubert, *Mol. Phys*. **104** (2006) 1069.

[364] G. Pasin, F. Gatti, C. Iung, H.-D. Meyer, *J. Chem. Phys.* **124** (2006) 194304.

[365] W. Fuβ, K. K. Pusha, W. Rettig, W. E. Schmid, S. A. Trushin, *Photochem. Photobiol. Sc*i. **1** (2002) 255.

université PARIS-SACLAY

ÉCOLE DOCTORALE
Sciences chimiques : molécules, matériaux, instrumentation et biosystèmes

Titre : Etude de processus photochimiques par une approche couplant chimie quantique et dynamique quantique

Mots clés : Photochimie non-adiabatique, intersections coniques, modèles vibroniques

Résumé : Ces dernières années, les progrès des techniques expérimentales combinées avec les simulations théoriques ont donné accès à l'étude et au contrôle des réactions photochimiques dans des systèmes moléculaires de grande taille. Ceci permet d'envisager de nouvelles applications technologiques. Par exemple, les molécules de la famille du 3-hydroxychromone et de l'aminobenzonitrile sont des types de systèmes où les spectres de fluorescence vont présenter des différences importantes selon l'environnement du système et en fonction des substituants utilisés. Ce type de propriété est crucial dans le domaine des matériaux organiques, afin de pouvoir comprendre, prédire et élaborer des matériaux qui présentent des propriétés optiques spécifiques tels que les marqueurs fluorescents dans le domaine médical par exemple.
Notre stratégie pour étudier la réactivité photochimique a été la suivante : * Explorer les surfaces d'énergie potentielle et optimiser les points spécifiques avec des calculs de chimie quantique ; nous avons utilisé des méthodes CASSCF/CASPT2 et TD-DFT (états fondamental et excités) et l'approche PCM pour décrire implicitement les effets de solvant. * Génération des surfaces d'énergie potentielle exprimées sous forme de fonctions analytiques de toutes les coordonnées nucléaires (modèle vibronique quasidiabatique). * Résolution de l'équation de Schrödinger dépendante du temps pour les noyaux et pour les états électroniques couplés à l'aide de la méthode de dynamique quantique *multilayer multiconfiguration time-dependent Hartree* (ML-MCTDH).

Title: Study of photoinduced processes with an approach combining quantum chemistry and quantum dynamics methods

Keywords: Non-adiabatic photochemistry, conical intersections, vibronic models

Abstract: Over the last decades, progress in experimental techniques combined with theoretical simulations has given access to studying and controlling the photochemical reactivity of large molecular systems with numerous technological applications. Derivatives of the 3-hydroxychromone and aminobenzonitrile molecules are examples where different fluorescence patterns are observed, depending on the solvent or on the substituents. Such properties are crucial in the field of organic materials to understand, predict, and design materials with specific optical properties such as fluorescent markers.
Our strategy to study photochemical reactivity is summarized as follows: * Exploring the potential energy surfaces and optimizing specific points with quantum chemistry calculations; these were run with the CASSCF/CASPT2 and TD-DFT methods (ground and excited states) and the solvent effect was described implicitly with the PCM approach. * Generating the full-dimensional potential energy surfaces as analytical functions of the nuclear coordinates (quasidiabatic vibronic model). * Solving the time-dependent Schrödinger equation for the nuclei and the coupled electronic states with the multilayer multiconfiguration time-dependent Hartree (ML-MCTDH) quantum dynamics method.

Université Paris-Saclay
Espace Technologique / Immeuble Discovery
Route de l'Orme aux Merisiers RD 128 / 91190 Saint-Aubin, France